Below-Ground Root Structure and Ecophysiological Controls of Plant Water Flux During Drought: From Individual to Ecosystem

by

Elizabeth Agee

A dissertation submitted in partial fulfillment
of the requirements for the degree of
Doctor of Philosophy
(Environmental Engineering)
in the University of Michigan
2019

Doctoral Committee:

Associate Professor Valeriy Y. Ivanov, Chair
Professor Nikolaos D. Katopodes
Assistant Professor Gretchen Keppel-Aleks
Professor Rafael S. Oliveira, Universidade Estadual de Campinas

Elizabeth Agee

lizagee@umich.edu

ORCID: 0000-0002-2331-3056

DEDICATION

This work is dedicated to my children, Jackson and Penelope Agee. You are by the far the best result I can ever hope to achieve.

ACKNOWLEDGEMENTS

This work was supported by the Victor L. Streeter Fellowship, the Blue Waters Graduate Fellowship (NSF OCI-0725070 and ACI-1238993), the NASA Earth and Space Science Fellowship (award 17-EARTH17F-84), Google Earth Engine Research Award to a project “Evapotranspiration of the Green Ocean Amazon,” and GOAmazon (DOE OBER Grant DE-SC0011078). Additional funding support for field activities was provided by the Lewis & Clark Field Exploration Grant, the International Institute Individual Fellowship, the Tinker Foundation Field Research Grant, the Rackham International Research Award, the J. B. and Marilyn McKenzie Graduate Fellowship, and the Rackham Research Grant.

There are not enough words to express my gratitude for my fearless advisor and mentor, Prof. Valeriy Ivanov. He took a chance on a physics student from a small university in Indiana and empowered her to develop into a scientist that is comfortable both at the helm of complex computational models and in the midst of the sweltering forests of a different continent. As we left the forests of Tapajós for the final time, you told me that we do not own the places, just our memories of them. Thank you for giving me so many fond memories to hold to for many years to come. You have supported me at every turn and I am proud to be your student.

Thank you to the members of my committee, Gretchen Keppel-Aleks, Nikolaos Katopodes, and Rafael Oliveira. Each of you have taught me a great deal and I value your wisdom and guidance.

I am indebted to the members of the HydroWIT lab: Lingli He, Donghui Xu, Greg

Ewing, Parisa Shahbaz, Frank Sedlar, Jongho Kim, Wenbo Zhou, Weichen Huang, Weina Zhang, Chuanli Ni, Katya Rakhmatulina, and the various scholars who have stayed with us over the years. I am especially grateful to my “lab brother” Chase Dwelle, who has provided me with countless hours of mentorship and friendship over the past six years. Thank you also to my undergraduate mentees for your patience and hard work: Jia Yu, Maeve Gillis, Avi Patel, Sophia Pryor, Alecsander de la Rosa, and Stepp Mayes.

I have been very fortunate to have had support and mentorship from many people during my graduate career. Thank you to Profs. Jeremy Semrau, Brian Ellis, Avery Demond, Steve Wright, Aline Cotel, Branko Kerkez, Allison Steiner, and Rose Cory. Thank you to my peer mentors Susan Cheng, Sara Rimer, and Yang Li. I have been fortunate enough to collaborate with many people who have been more than patient with me as I’ve learned the ropes and have juggled many projects and parenthood. Thank you to Gautam Bisht, Valentin Couvreur, Félicien Meunier, Christopher Gough, Gil Bohrer, Mauro Brum, the entire UNICAMP Lab, Scott Saleska, Tyeen Taylor, Marielle Smith, Neill Prohaska, Loren Albert, Brad Christoffersen, Marciel Ferreira, Simone Fatichi, Phoebe Aron, and Natalia Restrepo-Coupe. A special thank you goes to Ashley Matheny and Jeff Atkins (you know why). Thank you to the student community in CEE (there are far too many to list them all!) who have been nothing but kind all of these years.

Thank you finally to my family. You have given so much to get me where I am and I can only hope to earn it. And even if I cannot, I will never stop trying.

TABLE OF CONTENTS

LIST OF TABLES

LIST OF FIGURES

ABSTRACT

Shifting patterns of precipitation and rising temperatures have highlighted forest vulnerability to heat- and drought-induced stress. For systems that face water-limitation, either from short-term, seasonal dry periods or longer-term droughts, plasticity of root system function establishes the ability of individuals to meet atmospheric demand and maintain physiological function. This functional plasticity is determined by an individual's intrinsic properties and their interactions within the community and environment. Given limitations to *in situ* measurement, improved model representation of below-ground structural and functional complexity has provided means for exploring these ecophysiological feedbacks between drying soil and trees across biomes. This research addresses individual, ecosystem, and basin scale responses to water limitation by examining (i) the role of below-ground structure and ecophysiological controls on water uptake across functional gradients (i.e., low diversity vs. high diversity ecosystems); (ii) identifying and expanding the utility of novel proxies of hydraulic function; and (iii) exploring the feasibility of monitoring drought response at large scales using a parsimonious model of surface energy partitioning.

Modeled root water uptake from both temperate and tropical systems highlight that independent of functional strategy, root lateral interactions at the tree scale directly impact the depth distribution of water uptake and plant hydraulic status. A newly developed index of root system interaction provides an amenable axis with which to explore the tradeoffs between structural investment and resource acquisition. Laboratory and field analysis show that conventional technologies used to measure sap flow velocity may contain hidden information

regarding a tree's hydraulic state. This low frequency signal may also serve well as a proxy for below-ground response to the drying soil, providing valuable validation for future modeling efforts. Finally, the feasibility of hourly, basin scale estimates of the land-surface energy budget partition are tested. The Maximum Entropy Production model is successfully applied to the Amazon River Basin, a highly complex region prone to strong seasonal droughts, elucidating avenues of future research needed to more fully link ecosystem and hydrologic processes. The methodologies developed and expanded in this work provide new avenues for assessing tree-scale water fluxes and hydraulic state, providing a means for observing and testing hypotheses related to ecophysiological response across spatiotemporal scales.

Chapter 1 - Literature Review and Meta-analysis of Root Trait Space

1.1 Introduction and Scope of Doctoral Research

1.1.1 Motivation

Shifting patterns of precipitation and rising temperatures have highlighted forest vulnerability to heat- and drought-induced stress. Drought stress has been linked to decreases in productivity (Ciais et al., 2005; Zhao & Running, 2010); altered biogeochemistry (Schlesinger et al., 2016); increased rates of disturbance from fire, insect infestation, and disease (Kolb et al., 2016; Littell et al., 2016; Preisler et al., 2017); and, in extreme cases, mass mortality (Allen et al., 2010). While the impact of prolonged exposure to water limitation is readily apparent, factors contributing to individual and stand response are nonlinear and difficult to disentangle (Phillips et al., 2016). The subsurface, namely**,** interactions between the soil and root systems, is particularly complex given variability in both soil (Ivanov et al., 2010) and root (Kramer-Walter et al., 2016; McCormack et al., 2017; Weemstra et al., 2016) structure and response. Despite these challenges, there is a]general consensus that improved understanding and representation of subsurface dynamics are needed to fully describe water, nutrient, and ecosystem dynamics for vegetated ecosystems (McDowell et al., 2013).

For systems that face water-limitation, either from short-term, seasonal dry periods or longer-term droughts, plasticity of root water uptake (RWU) establishes the ability of individuals to meet atmospheric demand and maintain physiological function. This plasticity is determined by both intrinsic properties of individuals and interactions within the community and environment. Of particular interest is how the spatial distribution of root structural and hydraulic properties contribute to the plasticity of root water uptake.

As trees in forest systems grow relatively slowly, they will configure such that they reach individual optimality for a given set of nutrient and water availability conditions. Optimality could be defined as the ability to meet physiological demands for water uptake, while controlling water stress within the bounds of the individual's safety margin (Yang et al., 2016). A variant of optimality theory draws analogues from economic theory, with individual traits manifesting as unique cost-benefit strategies in line with the "plant economic spectrum" (Reich, 2014). This framework has been examined at the organ level – leaf, wood, and root – but as of yet, coordination between above- and below-ground traits has not been concretely established, with suggestions that coordination of root traits may be more multidimensional than leaf traits (Kramer-Walter et al., 2016b; Weemstra et al., 2016). Some of this may be attributable to measurement bias towards more readily accessible above-ground features and lack of clear focus in both measurement standards and execution for below-ground traits (McCormack et al., 2017; Weemstra et al., 2016).

1.1.2 Dissertation Outline

Chapter 1 provides an extensive background and review of the role of plant hydraulic processes in terrestrial water cycling. It begins with a summary of the plant economic spectrum and continues with an extensive review of root system structure and function.

Chapter 2 investigates the interplay of root system structure and interaction under water limitation for a temperate forest system. This chapter uses observational evidence from the University of Michigan Biological Station, located in northern Lower Michigan to parameterize a model of root water uptake. The model is used to explore multiple scenarios of root system morphology to identify thresholds of benefit gained by the expansion of root system area. As roots explore more soil, they gain access to additional soil water reserves, but also increase their level of interaction with other root systems. A new metric of root system interaction was developed and used to characterize system scale responses to water limitation. It further demonstrates the importance of lateral interaction for temporal evolution of soil moisture and plasticity of water uptake processes. The analysis presented in this chapter provides valuable insights on how structure influences function in a low diversity system, providing a jumping off point for the high diversity system explored in Chapter 3 - 5.

Chapter 3 explores the below-ground contribution to individual and community response to water limitation for a high diversity tropical rainforest system. Set against the backdrop of the 2015-2016 El Niño dry season, water uptake processes are explored for trees of different canopy classes. Observational data from the Tapajós National Forest, located in the Eastern Amazon rainforest, is used to quantify below-ground structure and to parameterize the model. Scenarios are used to test hypotheses of below-ground structure and function proposed by previous observational and modeling studies conducted for the area.

Chapter 4 presents analysis of above-ground response to the 2015-2016 El Niño. Methodology is developed that field calibrates a new low-power sap flow sensor used to observe differences in above-ground hydraulic response to the extreme dry season. This chapter examines and quantifies the sensitivity of sap flow measurements to changes in wood moisture content.

Chapter 5 takes a broader view of the system by utilizing remotely sensed climate variables to examine the spatiotemporal shifts in evapotranspiration (ET) for the entire Amazon River Basin. The maximum entropy production (MEP) model is used to partition surface energy fluxes for the entire basin at an hourly timescale. The model is forced using surface radiation products derive from the GOES geostationary satellite.

Chapter 6 summarizes the key findings and propose directions for future research.

1.2 Below-ground structure and ecophysiological background

1.2.1 Below-ground structure

The development and maintenance of root systems constitutes a significant carbon investment for an individual plant or tree, playing an important role for both local and system scale biogeochemical feedbacks. The distribution of vegetation drives individual water and nutrient acquisition and influences the spatiotemporal evolution of state variables like soil moisture at the system scale (Ivanov et al., 2010; Orfánus et al., 2016; Vivoni et al., 2008; Wang et al., 2015). “Below-ground structure”, or the distribution of roots within the soil medium, is nearly impossible to determine without extensive disturbance to the system. Non-invasive technologies such as ground penetrating radar (GPR) so far have limited utility in distinguishing individual root structures and are affected by soil composition (Ferrara et al., 2017). As such, we rely primarily on destructive means—excavations, soil cores, and trenches (Smit, 2000)—to deduce system morphology (see review by (Danjon & Reubens, 2007)).

Figure 1.1 (Left) Exposed coarse root architecture for a tropical tree on the banks of the seasonally flooded Amazon River, Pará, Brazil (photo credit: Joseph Xu). (Right) Fine root “mat” sampled from the surface soil layer at FLONA Tapajós, Pará, Brazil.

Root system morphology describes the arrangement and structure of vascular pathways. Roots are classified in to two major categories: coarse roots (> 2-5 mm) and fine roots (< 2-5 mm) (Fig. 1.1). Coarse roots provide structural stability for trees and are the main transport pathways for water and nutrients acquired by the fine roots. The smaller, more absorptive fine roots comprise a majority of root system biomass. While root structural information is relatively scarce, the following sections outline the components of root system structure and their variability across ecosystem types.

1.2.1.1 Coarse Root Morphology

Coarse root morphology is characterized by general forms or *archetypes* that describe the general shape of the root system. The most common forms are tap, combination or dimorphic, and lateral (Fig 1.2) (R. F. Fisher & Binkley, 2012; Sutton & Tinus, 1983). Contrasting forms may be found within a given species, representing a phenotypic response to soil conditions and competition dynamics (Brown et al., 1961). Uncertainties surrounding coarse root form and morphology boil down to a simple question: what is the spatial extent of an individual root system? Spatial extent is described by two major metrics, representing the horizontal and vertical axes: lateral spread and rooting depth.

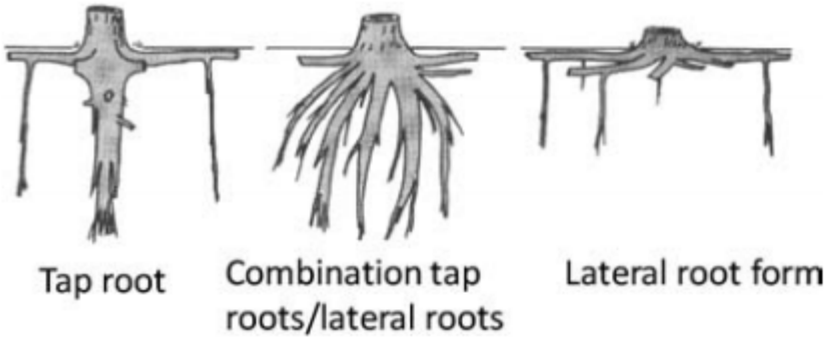

Figure 1.2 General coarse root forms found in forest trees. Tap roots are deep-rooting structures that contrast with the lateral form, which rely on shallow lateral roots to provide stability. An intermediate form, sometimes called the heart root form, combines both lateral and tap forms. (R. F. Fisher & Binkley, 2012)

Lateral spread (or extent) defines the maximum radial distance roots extend from the stem. A common operational assumption is that root structure mirrors above-ground canopy structure, with lateral roots extending to the edge of the tree crown. This assumption has been challenged by several studies examining root architecture (Casper et al., 2003; Meinen et al., 2009; Sinacore et al., 2017; Stone & Kalisz, 1991). Stone and Kalisz (1991) found in their examination of 200+ species that in the absence of restrictive substrate, many species form long lateral roots, with observed maximum spreads exceeding 20 m. This finding is corroborated by Casper et al. (2003) who established that while lateral spread is indeed correlated with canopy spatial extent, it is not limited to it. Using a global dataset, Casper et al. (2003) developed an allometric relationship between the lateral spread and canopy volume:

$$\log(Lmax) = \mathrm{a} + \mathrm{b}\log(C_v) \;, \tag{1.1}$$

where constant parameters *a* and *b* are dependent upon the aridity of the system (Figure 1.3). Root systems in arid environments, faced with more frequent bouts of water limitation, explore a larger subsurface area per crown volume than those in semi-arid and humid systems. While they have a smaller subsurface area per crown volume, root systems in semiarid to humid environments are able to support greater crown volumes, facilitating large lateral spreads, upwards of 20-30m.

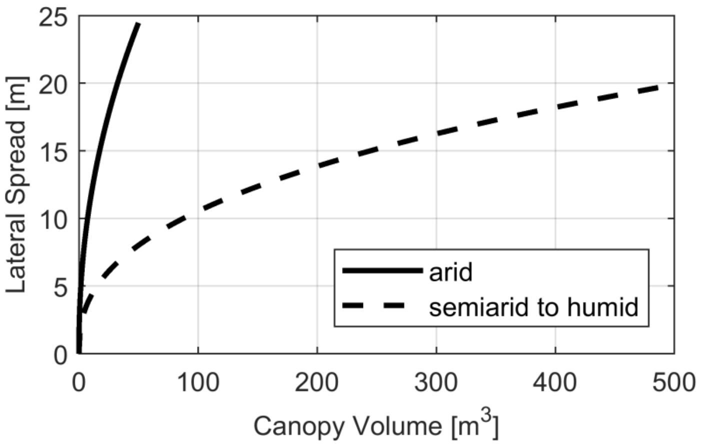

Figure 1.3 Allometric relationships for lateral spread as a function of canopy volume for arid and semi-arid to humid sites. Allometric scaling constants taken according to Casper et al. (2003). The presented relationship assumes a maximum crown volume of 50 m^3 for arid systems and a maximum of 500 m^3 for the semi-arid to humid system, based on back of the envelope approximations.

Rooting depth plays a critical role in individual and community hydrological and biogeochemical cycling (Pierret et al., 2016) and is a key variable for many ecohydrologic and biogeochemical models because of its effect on energy budget partition and element (i.e., nutrient, carbon) cycling in the environment (Yang et al., 2016). Observational and modeling evidence support species specific rooting depth as a principal hydraulic strategy for maintaining uptake during short- or long-term water limitation (Brum et al., 2018; Matheny et al., 2017; Mathias et al., 2016; Paz et al., 2015). In a global meta-analysis, Canadell et al. (1996) found that tree species, aggregated across all ecosystem type, have a mean maximum rooting of ca. 7 m (Figure 1.4). When assessed by ecosystem type, tropical evergreen trees had the deepest roots, with a mean maximum of 6.45 m, while temperate broadleaf trees had the shallowest, with a mean maximum of 2.95 m.

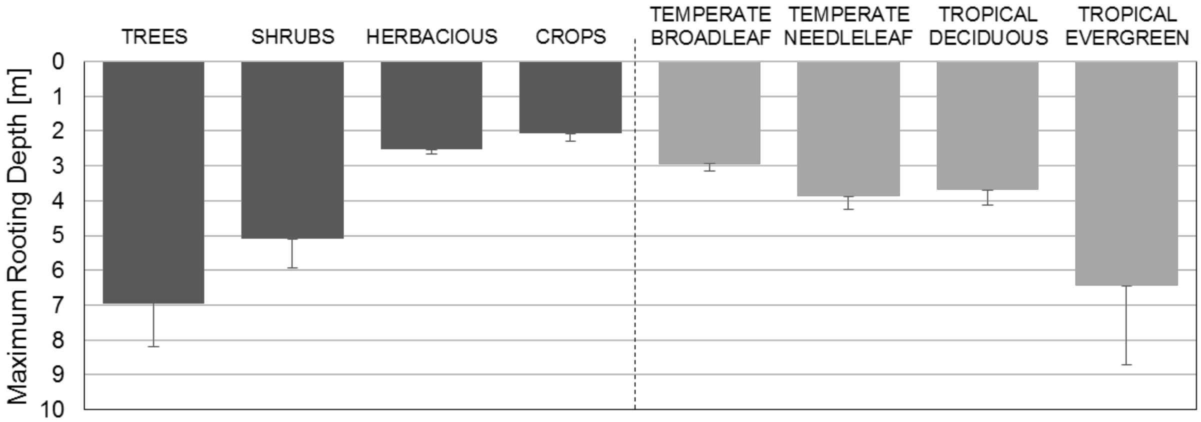

Figure 1.4 Mean maximum rooting depth across plant function groups (left) and broken down by forest ecosystem type (right). SE is given as an error whisker. Plot and data were digitized or taken after Canadell et al. (1996).

It is important to note that while lateral spread and rooting depth are important to defining the spatial extent of root system architecture, they do not fully describe how biomass is partitioned within the soil. Partitioning of roots along stratified depths may allow root systems to maintain adequate soil water supply during periods of water limitation (Brum et al., 2018; Ivanov et al., 2012).

1.2.1.2 Fine Root Morphology

Fine roots are the site of water and nutrient absorption and represent the majority of biomass within the root system. While microscale morphology (e.g., branching structure) is important at the local scales (e.g., pore- or centimeter-scale), this discussion will focus primarily on larger bulk properties important for tree- and ecosystem-scale water transport processes.

Fine root distributions are quantified as root biomass or length per unit soil volume. *Root biomass density* (RBD) is easily measured with soil cores and the most readily available. Root length and surface area, however, represent the actual root-soil interface and are preferred for plant water relations but the data are scarce. Root length can either be directly measured from soil cores using image analysis or derived from root biomass using specific root length. *Specific root length* (SRL) is a functional trait which relates length to biomass (SRL = root length/dry root biomass). Analogous to specific leaf area (SLA), SRL has been identified as a key functional trait as it directly links plant carbon structural investment to water uptake capacity (Cornelissen et al., 2003). *Root length density* (RLD) varies greatly (orders of magnitude) among ecosystems as a function of water availability, with higher RLD found in arid climates (Fig. 1.5). Regardless of actual rooting depth, the majority of root density is typically found within the top 1 m of soil. RLD is a bulk metric, providing insights to community level root distribution, but lacks the fidelity needed to discern individual fine root distribution.

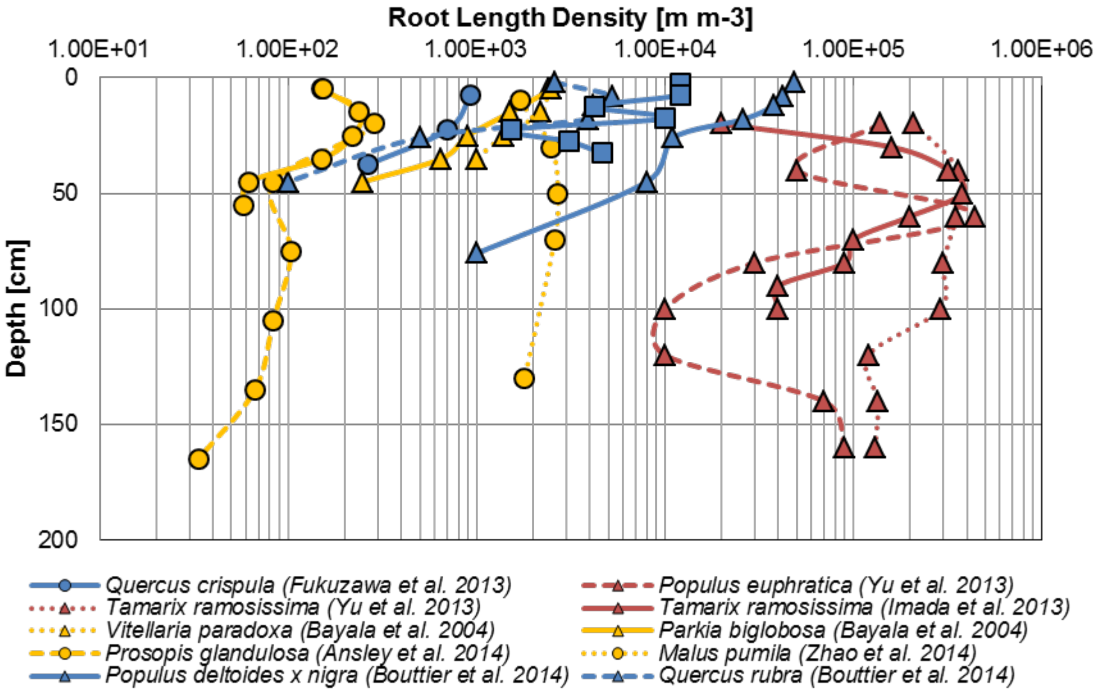

Figure 1.5 Comparison of root length density profiles collected from literature for various tree species across climate types. Line color corresponds to climate type with blue as temperate, yellow as semi-arid, and red as arid. Marker style denotes the bulk soil characteristics with circle as fine, triangle as medium, and square as coarse.

1.2.2 Ecophysiological controls

The response of trees to water limitation is governed by the expression of functional traits that as a whole, may contribute to individual's "hydraulic strategy". Hydraulic strategies can be classified in several ways, but at their core, define the regulation of water uptake such that an individual may assimilate carbon, while maintaining whole system hydraulic function. As soil dries, the water potential within a tree decreases. If this value drops too low, emboli may form in xylem vessels, obstructing the flow of water. If an individual invests heavily in resistant anatomy, then they require less regulation at the leaf level as they are able to withstand these lower water potentials without the danger of embolism. On the other hand, other trees may favor regulation at the leaf level, preferring to store carbon in other labile forms than invest in emboli resistant anatomy.

1.2.2.1 Root hydraulic conductivity

For transport through porous media, hydraulic efficiency or capacity is characterized by hydraulic conductivity and conductance. Hydraulic conductivity is an *intrinsic property*, quantifying flow per energy gradient, normalized by the surface of interest. Hydraulic conductance is an *extrinsic property*, dependent on an individual's structure and is the scaled value of hydraulic conductivity (Hunt et al., 1991). For roots, which experience flow within xylem and through surface tissues (i.e., soil to xylem), conductivity is divided into two components: 1) root axial hydraulic conductivity which quantifies flow per unit energy within the xylem, normalized by root length, [L^3 T^{-1} P^{-1} L^{-1}]; and 2) root radial hydraulic conductivity which quantifies flow per unit energy for the soil-root pathway, normalized by root surface area [L^3 T^{-1} P^{-1} L^{-2}].

Root radial hydraulic conductivity is orders of magnitude lower than axial conductivity, and is the rate limiting step for water acquisition. Radial conductivity varies in magnitude both within species and among species (

Table 1.1). Variability is attributed to complex interactions at the cellular level which have amplified effects at the bulk transport scale.

Table 1.1 Compiled literature values for root radial conductivity, organized by gross biome type. The mean and pooled STD are computed from values listed in the cited works, regardless of data collection method (listed). Studies that applied chemical inhibition treatments were excluded. PF = pressure-flow curves, HPFM = high pressure flow meter (Bogeat-Triboulot et al., 2002), RPP = root pressure probe (Steudle et al., 1987).

Species	**Mean ± STD (N) 10^{-8} [$m^3s^{-1}MPa^{-1}m^{-2}$]**	**Method(s)**	**Reference**
Temperate			
Pinus strobus	9.62 ± 5.51 (29)	PF	(Johnsen et al., 1988)
Pinus taeda	15.6 ± 14.1 (52)	PF	(Sands et al., 1982)
Populus tremuloides	5.96 ± 0.54 (20)	PF	(Wan et al., 1999)
Populus balsamifera	4.92 ± 2.55 (24)	PF	(Siemens & Zwiazek, 2008)
Quercus cerris	7.99 ± 0.96 (5)	HPFM	(Nardini & Tyree, 1999)
Quercus patraea	1.86 ± 0.66 (45)	HPFM, RPP	(Nardini & Tyree, 1999; Rasheed-Depardieu et al., 2015)
Quercus pubescens	3.72 ± 0.86 (5)	HPFM	(Nardini & Tyree, 1999)
Quercus robur	2.73 ± 1.07 (40)	HPFM, RPP	(Nardini & Tyree, 1999; Steudle & Meshcheryakov, 1996)
Quercus rubra	3.87 ± 1.89 (30)	PF	(Cheng, 2009; Kruger & Sucoff, 1989)
Quercus suber	3.94 ± 1.10 (5)	HPFM	(Nardini & Tyree, 1999)
Ulmus americana	0.763 ± 0.10 (28)	PF	(Cheng, 2009)
Betula papyrifera	7.15 ± 3.61 (6)	PF	(W. Zhang & Zwiazek, 2016)
Cornus sericea	72.7 ± 40.8 (6)	PF	(W. Zhang & Zwiazek, 2016)
Tropical			
Trichilia tuberculata	14.6 ± 2.92 (12)	PF	(Tyree et al., 1998)
Pouteria reticulata	8.13 ± 1.04 (12)	PF	(Tyree et al., 1998)
Gustavia superba	18.3 ± 3.96 (12)	PF	(Tyree et al., 1998)
Apeiba membranacea	24.2 ± 4.58 (12)	PF	(Tyree et al., 1998)
Miconia argentea	7.50 ± 1.04 (12)	PF	(Tyree et al., 1998)
Shorea balangeran	6.79 ± 1.61 (5)	PF	(Shimizu et al., 2005)
Shorea acuminate	3.84 ± 1.07 (5)	PF	(Shimizu et al., 2005)
Shorea johorensis	6.61 ± 1.96 (5)	PF	(Shimizu et al., 2005)
Shorea multiflora	4.29 ± 1.43 (5)	PF	(Shimizu et al., 2005)
Macaranga gigantean	4.73 ± 2.86 (5)	PF	(Shimizu et al., 2005)
Trema orientalis	2.05 ± 0.80 (5)	PF	(Shimizu et al., 2005)

1.3 Root structure and function in hydrological models

Connections between vegetation and land surface hydrology are long established. Gradmann (1928) first recognized that for an isothermal system, water potential is a gradient from soil to plant to atmosphere, where flow is proportional to the resistance of the component parts. His work was largely overlooked for twenty years until van den Honert (1948) reintroduced and refined it. Van den Honert described plant water transport as a catenary process, a chain where the soil-root interface and leaf-atmosphere interfaces formed the terminal ends of the soil-plant-atmospheric continuum (SPAC). Analogous to Ohm's law of electrical current, the portion of the system with the highest resistance governs the rate of the whole. Interactions between the rhizosphere and soil became a topic of research for many prominent soil physicists including J.R. Philip (1957), van Genuchten, and W.R. Gardner. Gardner (1960) is credited with one of the first model formulations for the movement of water from soil to root. Fiscus (1975) expanded the potential term to include the effect of solute concentrations on flow, as described by the osmotic potential. The combination of pressure and osmotic gradients helped explain non-linear pressure-flow relationships observed in previous experiments. Continued work on the role of root water uptake in both plant scale and climate models has varied in complexity, dependent on the respective scales of the problems considered.

Models have formed two distinct groups: empirically based *macroscopic* models which relate uptake to root distributions (Feddes et al., 2001; Ivanov et al., 2008; Jarvis, 2011), and the more physically-based *microscopic* models which examine uptake into individual root systems or branching segments (Doussan et al., 2006; Javaux et al., 2008; Landsberg & Fowkes, 1978; Schneider et al., 2010). In recent years, a third group has emerged which attempts to resolve root scale information at the macroscopic scale for use in large scale models (Couvreur et al., 2012;

de Jong van Lier et al., 2008).

1.3.1 Microscopic models

Microscopic models resolve flow at the scale of a single root segment or branch. Models which operate at the scale of a whole root system are also referred to as mesoscale models. Modeling flow into an individual root branch, Landsberg & Fowkes (1978) described flow along the potential gradient as being proportional to both the axial and radial hydraulic conductivity of the root. The radial component represents the resistance formed between the soil and the living cells of the root system. The axial component occurs within the non-living xylem vessels and is several orders of magnitude more conductive than the radial component (as such, is neglected in many models). This work was later expanded by Doussan et al., (2006) to include the branching network of an entire root system. Drawing from mathematical graph theory, he constructed an incidence matrix to describe the connections between individual root segments, also known as the root hydraulic architecture. Micro- and mesoscale conductance can then be calculated utilizing principles from electrical circuit theory. This formulation, when coupled with appropriate models of soil physics (Doussan et al., 2006; Javaux et al., 2008; Schneider et al., 2010), completes the pathway between soil and plant.

A major benefit of microscopic models is that they capture compensation mechanisms without any additional formulation. Compensation mechanisms are merely products of the potential gradients found within the system. For example, as soil layers dry, the water potential inside the plant decreases, increasing the gradient between sparsely populated, yet still moist, soil layers. This results in greater uptake from these layers. Hydraulic redistribution or lift, where water is redistributed to different soil layers via the root system, may occur when the water potential inside a root segment is higher than the surrounding soil layer (Burgess et al., 1998).

Microscopic models, due to their physical nature, are expected to need little to no calibration. This benefit is overshadowed by the complex parameterizations required in the form of root architecture and hydraulic parameterizations (Javaux et al., 2008, 2013). Data of this nature is scarce and highly variable, especially for natural systems. This limitation as confined studies to commercial species, primarily maize and sorghum.

1.3.2 Macroscopic models

Large scale macroscopic models, based primarily on root distribution parameters, were championed by Feddes et al. (1976) and have been included in terrestrial and global climate models. The Feddes-type model introduced a stress-factor β which inhibits root water uptake based upon current soil moisture conditions. Jarvis (1989) introduced an additional term to this stress function to account for compensation mechanisms. These account for changes in uptake regions or intensity based upon hydraulic gradients formed by heterogeneous soil moisture. $\frac{E_a}{E_p} = f(\alpha)$ when $f(\alpha) = 1,\ \alpha_c < \alpha < 1$ and $f(\alpha) = \frac{\alpha}{\alpha_c}\ ,\ \ 0 < \alpha < \alpha_c$ where α_c is the critical value of the weighted stress-index and is analogous to β in the Feddes formulation. In Jarvis's study of oats and other crops, this value was set to be 0.25, but it could be calibrated to the specific system in question. A criticism of this type of model is that these parameters cannot be directly measured, requiring calibration for individual environments. Semi-empirical approaches were suggested throughout the late 1990s and early 2000s and were reviewed by (Feddes & Raats, 2005). Feddes later recognized the limitations of the formulation to capture root water uptake under water limitation (2001).

1.3.3 Hybrid models

Proponents of the early microscopic formulations, J.R. Philip and Gardner, both indicated skepticism for microscopically scaled formulations of macroscopic models. Within the past decade, a number of formulations have arisen which aim to balance root system structure and function with computational tractability. Hybrid micro/macroscopic models attempt to fill that middle space by incorporating morphological or hydraulic information from the individual root systems, but with terms that are amenable for larger scale modeling. de Jong van Lier et al. (2008) developed a one-dimensional hybrid that has been used by Tron et al. (2015) to model water use efficiency in crops. Additional attempts at hybrid models were made by Raats (2007) and Jarvis (2011) by approximating numerical solutions to root water uptake by hydraulic architectures.

A three-dimensional approach was developed by Couvreur et al. (2012) that relies heavily on the previous work of Doussan et al. (1998). Specifically, Doussan et al. (1998) introduced a connected graph matrix that incorporates radial and axial root conductances and is used to find instantaneous RWU for non-uniform and uniform conditions. These envelope conditions are used to formulate what Couvreur et al. (2012) called a *standard sink fraction* and a *compensatory conductance* term. The standard sink fraction is an aggregated quantity at the level of the soil voxel, which represents the proportion the roots in the soil voxel contribute to water uptake under normal, well-watered conditions. The compensatory conductance, is a bulk parameter which quantifies the conductance of the whole root system under water-limited conditions. The Couvreur et al. (2012) model was incorporated into the CLM model by (Sulis et al., 2019) and the PFLOTRAN model by (He, 2014).

Chapter 2 – Root Lateral Interaction and Below-Ground Structural Impacts on Water Uptake in a Temperate Forest

2.1 Introduction

Over the past decade, there has been a unified drive to increase representation of root zone processes in models across spatial scales and disciplinary foci. A number of reviews have highlighted current implementations and opportunities for improvement (Fatichi et al., 2015; Javaux et al., 2013; Warren et al., 2015). As the community moves away from bulk parameterization of the below-ground system and towards more mechanistic representations of root system structure and function, questions regarding below-ground competition may be more fully addressed (Casper & Jackson, 1997). Specifically, how does root interaction and competition impact water uptake processes during water limitation? While pioneering studies have examined water uptake for overlapping root systems (Manoli et al., 2014), they typically examine only a limited number of individuals with minimal representation of root topology or architecture.

Horizontal segregation of root systems, as an analogue to vertical segregation or niche separation, has been suggested as a potential mechanism for efficient resource utilization (Schenk et al., 1999). However, studies looking at competition and fine root dynamics in both monospecific and mixed-species stands have found strong evidence supporting overlapping root systems in forest systems (Lang et al., 2010; Leuschner et al., 2001; Meinen et al., 2009; Valverde-Barrantes et al., 2015). While dependent on species and local environmental factors (e.g., soil and nutrient distribution), maximum root lateral extents have been observed as far as

20-40m from tree stems (Meinen et al., 2009; Stone & Kalisz, 1991). These extents all but guarantee lateral interaction among neighboring individuals. Yet the impact such interactions can have on water acquisition in natural forest ecosystems is largely unaddressed. Given inherent difficulties to *in situ* measurement of below-ground processes, physically-based computational models of soil and root water dynamics provide an opportunity to quantify the role of root spatial interactions without the need for destructive field measurements.

This chapter is driven by the following research questions: (1) How does root lateral interaction affect the spatiotemporal evolution of soil moisture? (2) Does investment in root lateral structure improve the ability of individuals to meet atmospheric demand during water limitation? These are addressed through the fusion of data collected from a temperate forest site with a three-dimensional model of root water uptake for overlapping root systems. The objectives of this work are to quantify the role of root structure and lateral interactions in water uptake processes. To meet this objective, spatiotemporal patterns of uptake, soil moisture, and plant water status are compared for a range of root lateral spread scenarios, architectures, and hydraulic properties. Finally, I explore the implications that carbon investment in rooting structure may have on forest systems under future water limitation.

2.2 Theory and Background

2.2.1 Root hydraulic architecture

2.2.1.1 Root system structure

Root system architecture varies among and within species, with axes of variation arising from both physiological and environmental factors. Typically, system topology can be classified as one of three archetypes: flat (or lateral), tap, or dimorphic. As the actual root architecture could not be verified without destructive measures, simulations using both flat and tap archetypes were performed. While a given ecosystem may contain multiple topologies, each scenario in this study was assigned a single archetype. By choosing opposing topologies for comparison, an envelope of potential system solutions is developed.

Three-dimensional root structures were generated using RootBox (Leitner et al., 2010), a dynamic root growth model which utilizes Lindenmeyer system (L-system) strings (Lindenmayer, 1977) to generate branching segments along predefined production rules (Appendix 2A). Production parameters were defined to generate two general root archetypes: tap roots and flat (or lateral) roots. Tap roots are defined as ‘carrot-like’ structures with a single root descending from the stem, with subsequent branches extending laterally. Flat or lateral root are dominated by lateral roots located near the surface, with secondary roots reaching deeper into the soil. The flat root archetype does not have a significant tap root, with coarse structure residing in the superficial soil layers.

2.2.1.2 Hydraulic parameterization

Root hydraulic parameterization is accomplished through a hybrid macroscale approach (Couvreur et al. 2012). The approach uses special cases of *microscale* root water uptake equations (Doussan et al., 2006) to generate *macroscale* parameters that are computationally tractable for large domain simulations, yet maintain microscale hydraulic information. Specifically, for each modeled root architecture, root segments are assigned intrinsic hydraulic conductivities that quantify the ease with which water flows from soil to root. The microscopic RWU is solved for two special cases of soil water potential distribution with depth: (1) uniform and (2) hydrostatic. From case (1), the relative contribution of each root segment to overall water uptake is determined and described as standard uptake fraction, *SUF*, defined by Couvreur et al.

(2012). The *SUF* values depend on the specific root architecture and root hydraulic properties and are independent of the distribution of soil water potential or transpiration rate.

Case (2) characterizes the root system's response to non-uniform soil water potential. The compensatory conductance, K_{comp}, is a macroscopic parameter that quantifies the degree to which total uptake is enhanced due to non-uniform potential gradients between the soil and root segments. When soil water potential distribution is uniform, compensatory root water uptake is equal to zero. Like the *SUF*, K_{comp} depends on specific root architecture and hydraulic properties. These macroscale quantities are used in a coupled root and soil water physics model to simulate water uptake at a larger, plot-size scale.

2.2.2 PFLOTRAN-Root Water Uptake

PFLOTRAN, a massively parallel flow and reactive transport model (Hammond et al., 2014; Lichtner et al., 2017), is used to solve the three-dimensional Richards equation (Richards, 1931) to describe flow in variably saturated soil. Root water uptake is described as a source/sink term in the Richards equation the above macroscale parameterization (Couvreur et al., 2012). The evolution of soil moisture at a point is described as

$$\frac{d\theta}{dt} = \nabla\big(K(\phi)\nabla(\phi + z)\big) - S(x, y, z, t), \tag{2.1}$$

where K [L/T] is the unsaturated soil hydraulic conductivity as a function of soil water potential (φ [L]) and S [1/T] is the sink or source due to root water uptake.

The domain is discretized into grid cells, represented as finite volumes with defined soil properties, hereto after referred to as soil grid cells. Multiple root systems may occupy the soil grid cell, each contributing to the overall uptake rate. At the soil grid volume, k, the total sink is expressed by Couvreur et al. (2012) as

$$S_{k,p} = T_{act,p}SSD_{k,p} + K_{comp,p}\left(H_{s,k} - \sum_{j=1}^{M} H_{s,j}SSD_{j,p}\right)SSD_{k,p}, \tag{2.2}$$

where $S_{k,p}$ is the generated sink term for a root system p (p= 1, … N); $T_{act,p}$ is the actual transpiration (or total uptake) for root system p; $H_{s,k}$ is the soil water potential of the grid cell k; M is the total number of soil elements that root system p occupies; K_{comp} is compensatory conductance [m^2 s^{-1}] and *SSD* is the standard sink density [-]. *SSD* is the aggregated value of *SUF* for all microscale root nodes (n=1, …, N) occupying soil grid cell k,

$$SSD_{k,p} = \sum_{n=1}^{N} SUF_{n,k} . \tag{2.3}$$

K_{comp} and *SUF* are determined from macroscopic parameterization routines and are specific to individual root systems, which is summarized in section 2.2. The total sink for a grid cell k, S_k, is the sum of all water uptake rates from roots occupying the cell.

$$S_k = \sum_{p=1}^{P} S_{k,p} \tag{2.4}$$

Water potential at the root collar, H_{collar}, is used to determine the overall water potential status of the stem. H_{collar} is defined as

$$H_{collar,p} = \sum_{j=1}^{M} H_{s,j}SSD_{j,p} - \frac{T_{act,p}}{K_{comp,p}} , \tag{2.5}$$

where $H_{collar,p}$ is the water potential at the root collar for root system p. A threshold water potential, H_{th}, is set to constrain water uptake at negative water potentials, mirroring stomatal response to water limitation. T_{act} is then expressed as a conditional function

$$T_{act,p} = \begin{cases} K_{comp}\left(\sum_{j=1}^{M} H_{s,j} SSD_j - H_{th,p}\right) & if \ \left|H_{collar,p}\right| > \left|H_{th,p}\right| \\ T_{potential,p} & if \ \left|H_{collar,p}\right| < \left|H_{th,p}\right| \end{cases} \qquad (2.6)$$

where $H_{th,p}$ is the water potential threshold at the root collar for root p and $T_{potential,\,p}$ is tree-scale potential transpiration.

2.3 Data and Methods

2.3.1 Site description

The study uses data collected at the University of Michigan Biological Station in Northern Michigan, USA (45.56° N, 84.71° W). A temperate deciduous forest, the canopy is dominated by big-tooth aspen (*Populus grandidentata*) and birch (*Betula paprifera*), with an understory consisting of red oak (*Quercus rubra*), maple (*Acer rubrum, Acer sacchrum*), and pine (*Pinus strobes*, *Pinus resinous*). The mean annual precipitation is 805 mm with mean annual temperature of 6.8°C. Soils are well-drained Haplorthods of the Rubicon, Blue Lake or Cheboygan series with 92.2% sand, 6.5% silt and 0.6% clay (Nave et al., 2011). Tree census data were used to define tree locations in the vicinity of the Ameriflux UMB tower (He et al., 2014).

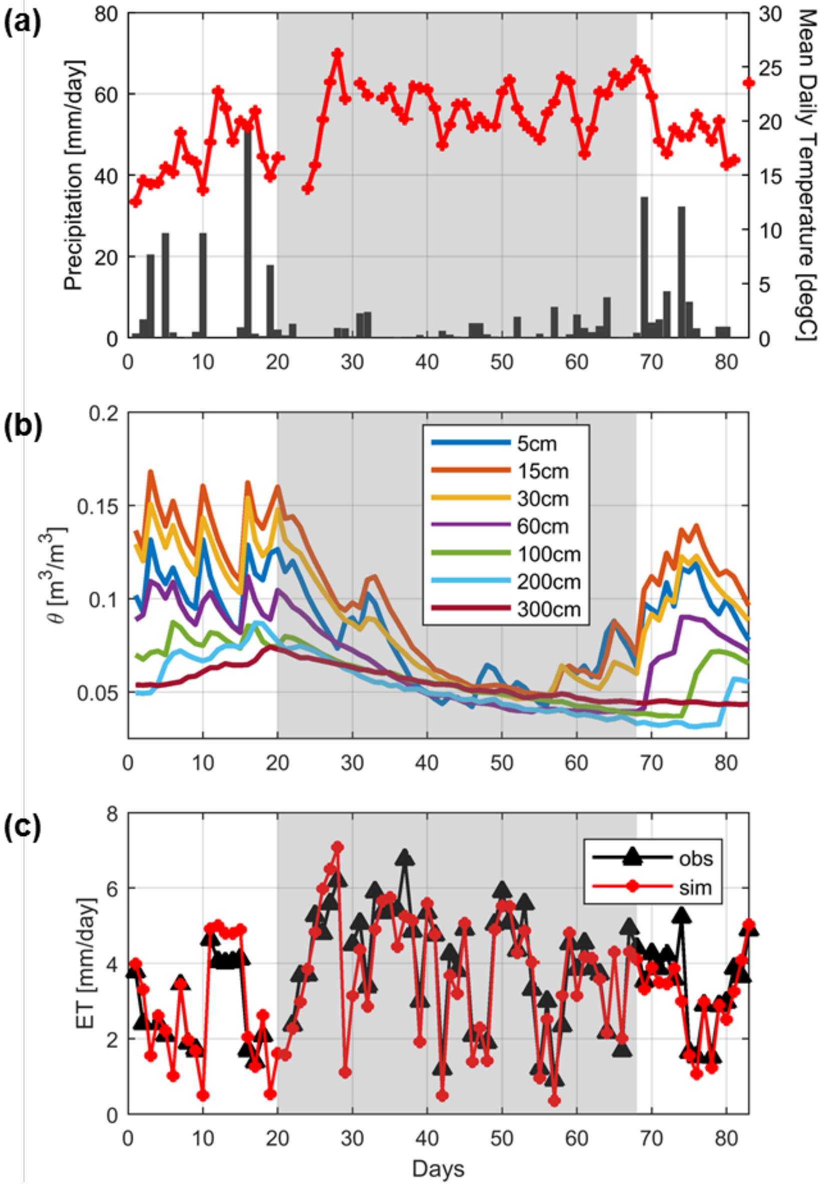

Figure 2.1 Site conditions and forcing for the simulation period 06/07/2010 – 08/23/2010. (a) Precipitation and mean daily temperature, (b) observed soil water content from different depths near the UMBS AmeriFlux tower. (c) observed evapotranspiration and potential evapotranspiration as generated from tRIBS-VEGGIE.

2.3.2 Tree size and allometry

During the 2011 growing season, a 50m by 50m plot was surveyed in the footprint of the UMBS-AmeriFlux eddy covariance tower. The area was used as the analysis domain and diameter at breast height (DBH) and recorded spatial coordinates of all trees were used to specify ‘root collar’ locations. During post-processing, individuals with DBH ≤10cm and within 2m of each other were assumed to share the same root system and aggregated to form a single stem. To prevent domain edge effects, the computational area was expanded by 25m on all sides, with additional trees added at random according to plot derived distributions of stem density and size. The entire computational domain is thus 100m x 100m x 2m and contains 574 trees with DBH values from 5 to 73.5cm. Allometric relationships from previous studies were used to approximate tree height, crown diameter, and crown height (Table 2.1). Crowns were assumed to be ellipsoids for the purposes of determining crown volume.

Table 2.1 Allometric equations used to describe stem and root zone size characteristics. Equations describe tree height H [m], diameter at breast height DBH [cm], crown diameter W [m], crown height H’ [m], stem fraction D [-], crown volume V [m3], and lateral spread LS [m].

Tree Allometry		
Parameter	**Equation**	**Source**
Tree Height	$H = 9.97 \times \log[DBH] - 12.61$	[Garrity et al., 2012]
Crown Diameter	$W = 2.67 \times \log[DBH] - 1.90$	[Garrity et al., 2012]
Crown Height	$H' = D \cdot H$, where D = 0.6	[Canham, 2005]
Crown Volume	$V = \frac{\pi}{6} H' W^2$	Volume of ellipsoid
Scenarios of lateral spread		
1	$LS = W/2$)	
2	$\log[LS] = -0.202 + 0.406 \log[V]$	[Casper et al., 2003]
3	$\log[LS] = 0.2978 + 0.406 \log[V]$	[Casper, correspondence]

2.3.3 Forcing data

Time variant boundary conditions, specifically net precipitation and potential transpiration (T_{pot}), were generated for a subset of the 2010 growing season (06/07/2010 – 08/23/2010) (Figure 2.1) using the tRIBS+VEGGIE model (Ivanov et al., 2008a; Ivanov et al., 2008b), an ecohydrologic model that represents water and energy processes and essential regulatory processes for vegetation. Ecosystem scale T_{pot} was determined by imposing ample soil moisture conditions to ensure that water uptake was never constrained. T_{pot} was downscaled among tree individuals in proportion to their crown volume and fraction of root system that resided within the 100 m x 100 m plot,

$$T_{pot,p} = T_{pot}\, A \frac{F_{root,p}\, V_p}{\sum_{p=1}^{N} F_{root,p}\, V_p} \qquad (2.9)$$

where $T_{pot,p}$ is the potential transpiration for stem p [kg s^{-1}], T_{pot} is the ecosystem scale potential transpiration per unit area [kg s^{-1} m^{-2}], A is the simulation domain area [m^2], $F_{root,p}$ is the fraction of root system p which resides within the simulation domain [-], and V_p is the crown volume of stem p [m^3].

2.3.4 Soil hydraulic properties

Soil saturation and pressure were characterized using van Genuchten soil characteristic curves (van Genuchten 1980). Parameters defining the shape of the curve were taken from He et al. (2014) and derived from Rajkai & Várallyay (1992) to define two soil saturation curves. The two soil conditions represent two potential profiles for the observed soil composition. The soil properties used are sand 92%, silt 7%, clay 1%, organic content 0.94%, with a bulk density (ρ_b) of 1.28 g cm^{-3}. Multiple pedotransfer functions were compared (Fig. 2.2) using the CalcPTF program from the USDA (https://www.ars.usda.gov/northeast-area/beltsville-md-barc/beltsville-agricultural-research-center/emfsl/docs/environmental-transport/calcptf/). The two soil conditions selected for the study represent the two extrema of potential soil water retention curves.

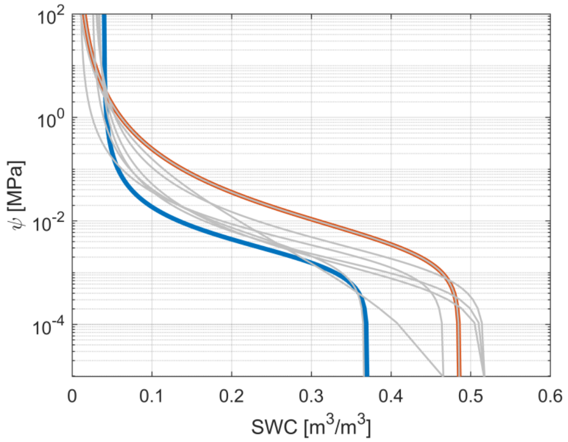

Figure 2.2 Two soil water retention curves were used in this study, soil 1 (blue) and soil 2 (orange). Other potential models are highlighted in gray and were calculated using the CalcPTF software that models multiple pedotransfer functions.

Table 2.2 Soil hydraulic parameters used to define the van Genuchten (1980) soil characteristic curves. Soil 1 properties were taken from (He et al., 2014) and soil 2 properties were derived from (Rajkai & Várallyay, 1992).

Soil Hydraulic Properties			
Parameter	**Soil 1**	**Soil 2**	**Unit**
K_s, Saturated hydraulic conductivity	350	350	mm h^{-1}
θ_s, Saturated volumetric soil moisture content	0.3700	0.4856	m^{3}m^{-3}
θ_r, Residual volumetric soil moisture content	0.0400	0.0056	m^{3}m^{-3}
α, Shape parameter of van Genuchten (1980)	-0.0052	-0.0029	mm^{-1}
n, Shape parameter of van Genuchten (1980)	1.68	1.38	-

2.3.5 Root distributions and zones of uptake

Root length density (*RLD*) is an important metric used to describe the length of root per soil volume available for uptake. Length does not linearly scale with the more commonly measured biomass and therefore requires additional metrics for conversion, such as root diameter distribution (Fig. 2.3a). Root biomass density (*RBD*) was measured by soil cores at 20cm intervals to a depth of 80cm, described previously by (He et al., 2013). While species were not identified, samples were taken across the monitored plot and the resulting distribution assumed to be representative of the study area. Specific root length (*SRL*), the ratio of root dry mass to root length, was measured for root diameters ≤ 2mm. Fine root distribution was divided into four diameter classes (0-0.05 mm, 0.05-0.1mm, 0.1-0.15mm, and 1.5-2.0mm) based on fractions reported for similar temperate forest sites (Makita et al., 2009; Montagnoli et al., 2012). The RLD profile is described by

$$RLD(z) = \sum_{i=1}^{N} f_i RBD(z) SRL_i \tag{2.10}$$

where RBD(z) is root biomass density [g m-3] as a function of depth z, SRL is specific root length for diameter class i [m g-1], f is the fractional percentage of diameter class i, and N=4 is the number of root diameter classes.

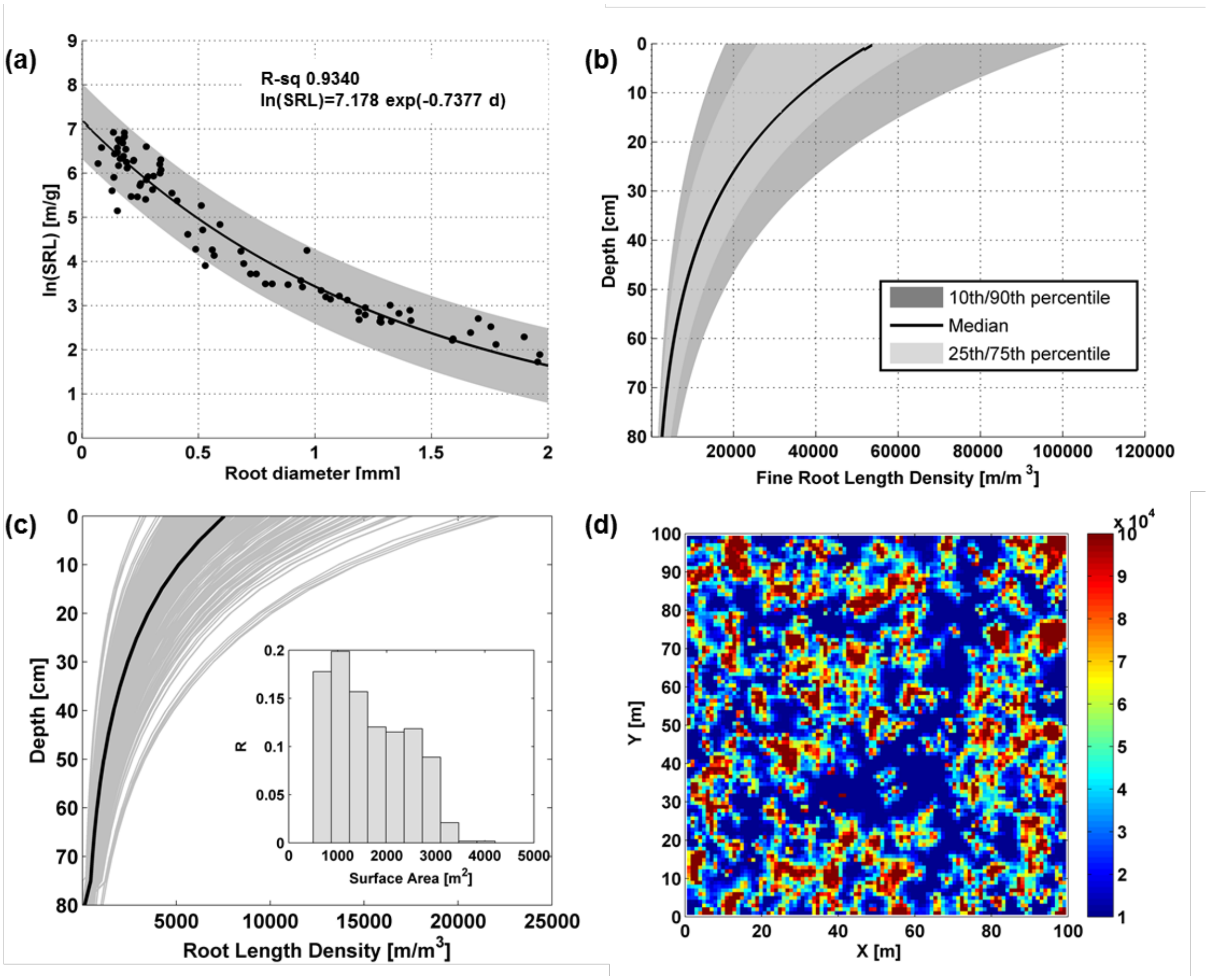

Figure 2.3 (a) Natural log of specific root length as a function of fine root diameter with non-linear regression giving ln(SRL)=7.178 exp(-0.7337d), with R-square of 0.9340. (b) The calculated profile of RLD for UMBS. The dark gray shaded region encompasses the 10th – 90th percentiles, the light shaded region encompasses the 25th – 75th percentiles, and black line is the median. (c) RLD profile for 574 trees with each line representing an individual root system (within the cylindrical volume defined by root lateral spread and depth), with the dark black line representing the median RLD profile. Inset: Relative frequency of total root surface area for root systems in the domain. (d) Spatial distribution (plan view) of surface (maximum, top 0-10cm) RLD for the domain.

The centroid of root water uptake characterizes the "center of mass" of soil moisture sink density distribution due to individual's transpiration flux. If water uptake is proportional to the root length density distribution, the centroid of uptake will occur at the root system's center of mass, which is equal to 0.385 m for the root distribution in Fig. 2.3b. If the centroid shifts above the center of mass, this indicates roots in shallow layers are contributing proportionately more to uptake than deeper roots. The reverse is true for when the centroid shifts below the root distribution center of mass. To compare values across the different scenarios with variable magnitudes of cumulative uptake, each individual's centroid was weighted by its daily uptake.

2.3.6 Lateral spread scenarios

Three scenarios of lateral spread were designed to examine the relationship between root spatial interactions and tree water status (Figure 2.4). Scenario 1 (Sc1) acts as a 'lower bound' in which root system extent mirrors the projection of leaf crown extent onto the horizontal plain. Scenarios 2 and 3 (Sc2 and Sc3) utilize root allometric relationships from Casper et al. (2003) to determine lateral spread as a function of crown volume. While the coarse architecture of the root systems expand, fine roots are spatially redistributed such that each scenario maintains the same median root length density profile (Figure 2.3, , Figure 2.5).

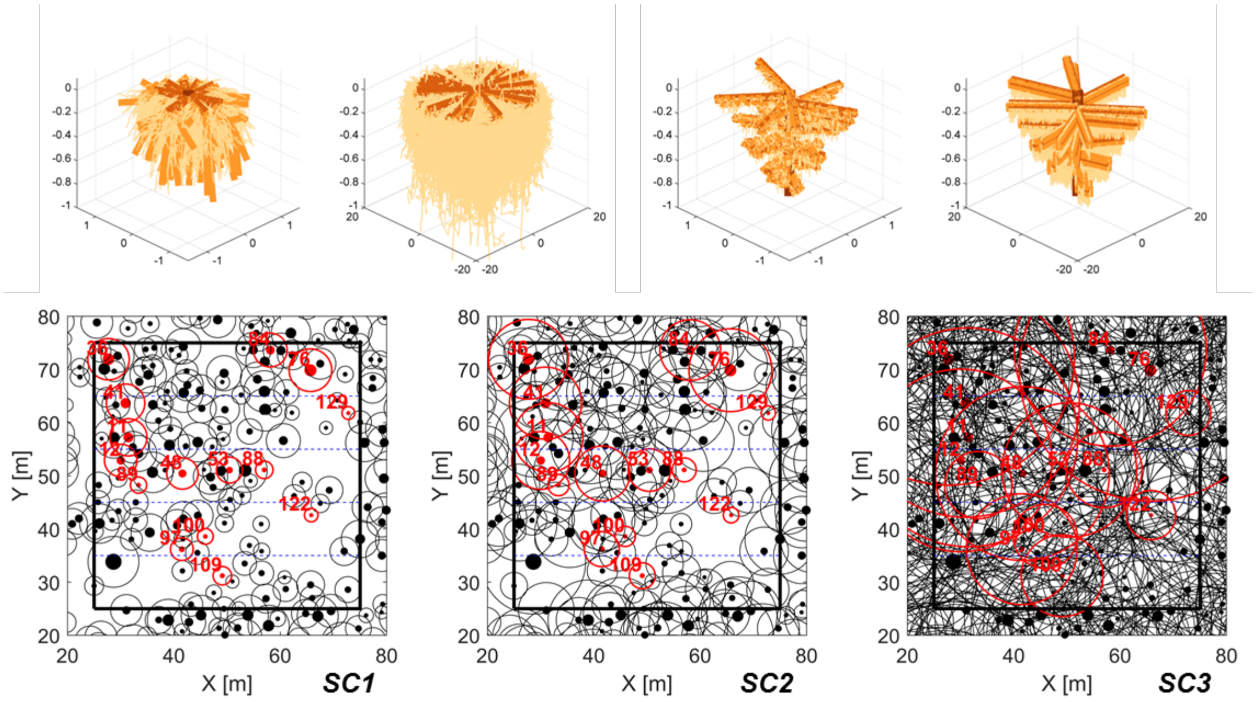

Figure 2.4 (Top) Root architectures generated with the RootBox model (flat and tap root archetypes) for lateral spreads of 1m and 20m, with fixed rooting depth of approximately 80cm. Fourth and fifth branching order roots are not shown. (Bottom) Three scenarios of lateral spread with an increasing degree of interactions from left to right. Representative individuals (Sec. 3.8) are marked in red.

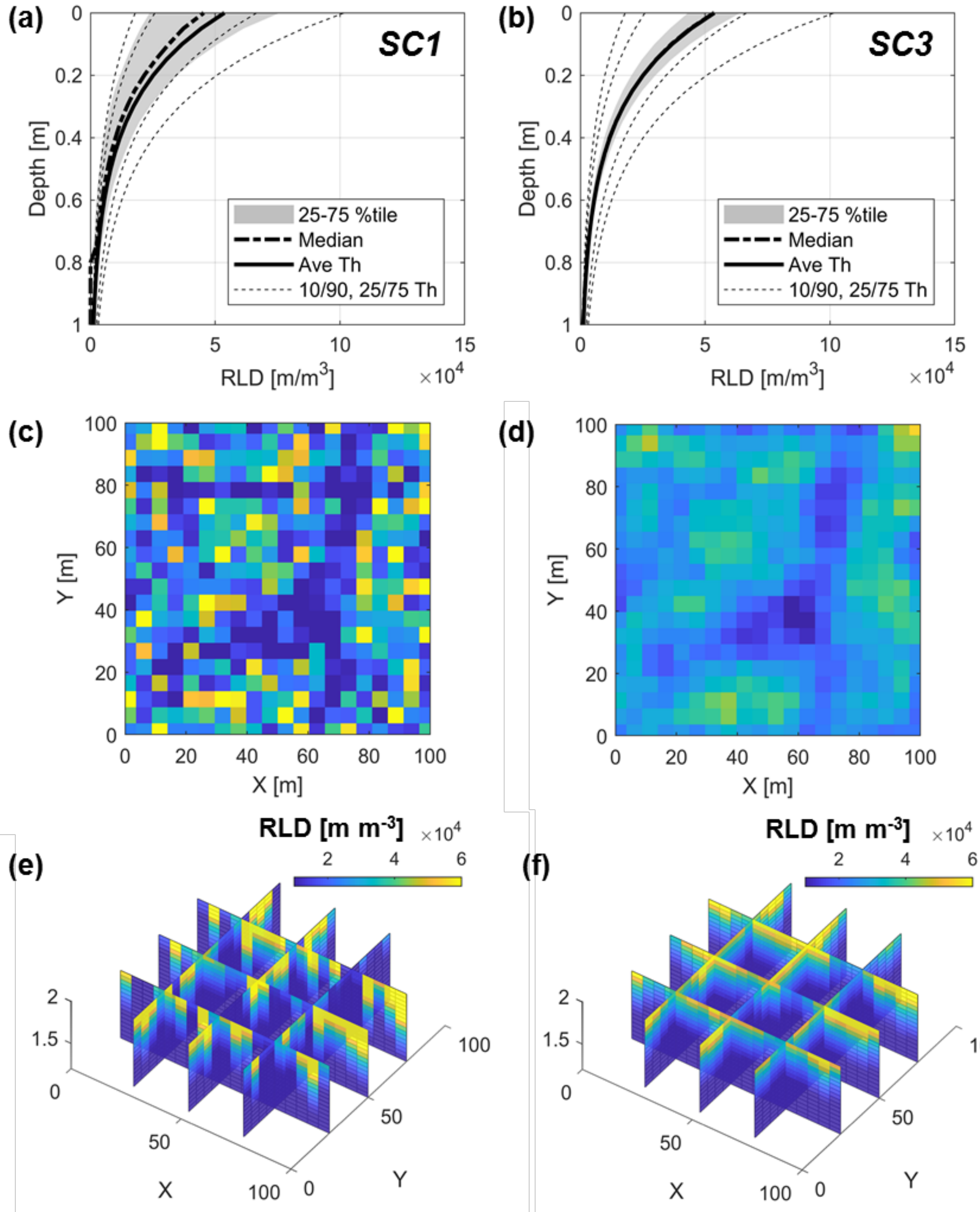

Figure 2.5 Illustration of root lateral interactions for SC1 (a, c, e) and SC3 (b, d, f). (a – b) Domain scale RLD for the extrema scenarios with the simulated median (black dashed lined) and 25-75th percentile range (shaded gray) shown against the observed profile percentiles (10th, 25th, 75th, and 90th in light gray dashes; average profile black solid line). (c – d) Areal view of 90th percentile RLD at 5m x 5m scale. (e – f) 3D domain slices showing RLD wth depth across simulation domain at 0.05m depth scale. Color scales are uniform across (c – f)

2.3.7 Root competition index

Tree size is frequently used to extrapolate system scale behavior from local measurements. While size plays a large role in determining the area from which individuals acquire water and nutrients, it does not account for competition from neighboring individuals. To account for both system size *and* spatial interactions, we adapted above-ground competition metrics (Arney, 1973) to develop a "Root Competition Index" (RCI). The RCI is given by

$$RCI_i = 100\left(\frac{\sum_{j=1}^{n} a_{ij} + RA_i}{RA_i}\right) \tag{2.11}$$

where a_{ij} is the area of root zone overlap between subject tree I and competitor j, RA_i is plan area of root system I, and n is the number of competitors as defined by area overlap.

2.3.8 Representative individuals

To characterize water uptake and water potential status of the forested patch, representative individuals were selected for observation using k-means cluster analysis (Lloyd, 1982). For each lateral spread scenario Sc1-Sc3, clusters ($k = 4$) were obtained according to DBH and RCI. Each cluster partition was assigned a value (1-4) that ranked its degree of interaction *relative* to the other partitions. For example, a value of 1 would indicate low spatial interaction relative to the other clusters, while 4 would indicate a high degree of spatial interaction relative to the other clusters. These rankings were summed across the three lateral spread scenarios to determine an aggregate or "total rank", with values ranging from 3-12. The aggregate rank accounts for nonlinear changes in root system overlapped areas across the scenarios and unites the scenarios under one metric.

Cluster analysis was repeated for the aggregate rank and DBH, identifying four distinct groups: low interaction, moderate interaction, high interaction, and large trees (Fig. 2.6). RCI takes into account only root area overlap, not the size of the trees sharing the root space. Tree size is needed to quantify the demand for water in the shared root space. The three "interaction" groups encompass individuals with DBH ≤30cm with different values of the rank metric. 'Low', 'moderate', and 'high' clusters have ranks ranging from 3-5, 5-8, and 9-12, respectively. The 'large tree' cluster encompasses individuals with DBH ≥15cm with ranks ranging from 6-10. Representative individuals from each cluster (N=3-5) were randomly selected and used in the subsequent analysis.

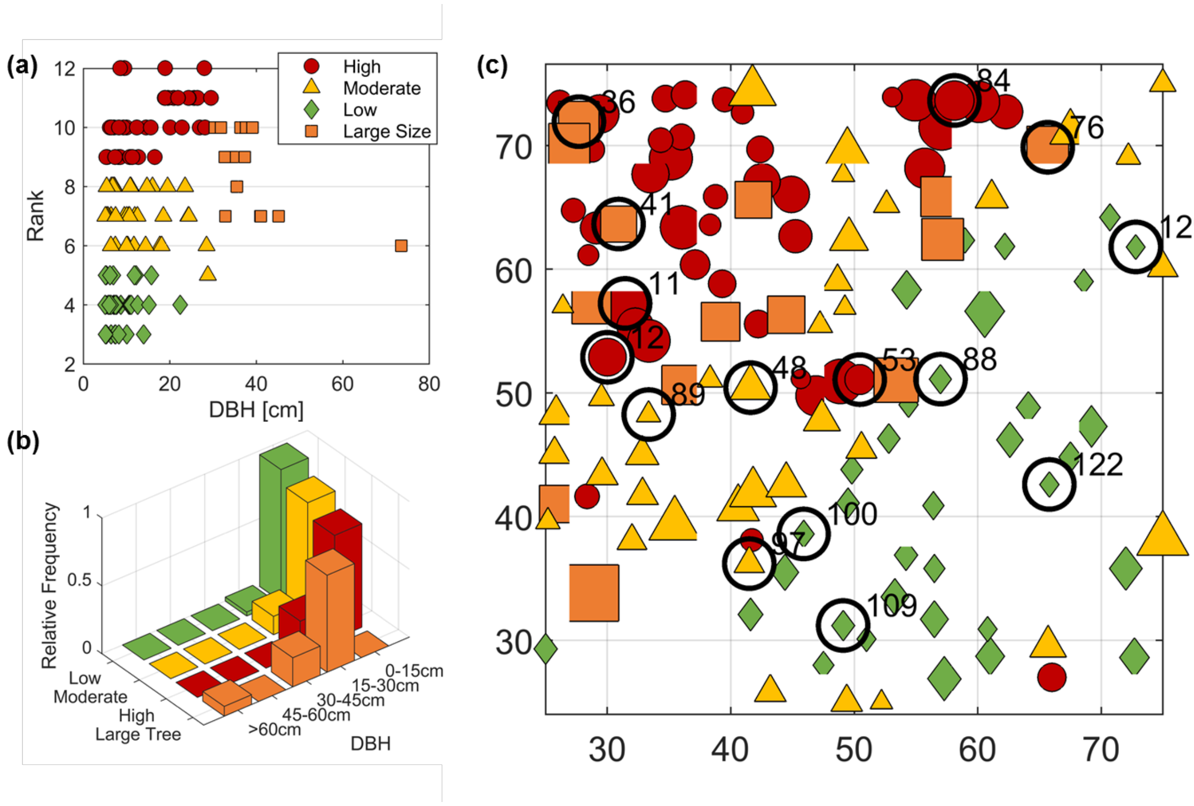

Figure 2.6 (a) K-means cluster analysis for all 127 individuals of the inner 50m x 50m plots based on aggregate rank and DBH. (b) Relative frequency per size class for each representative group. (c) Representative groups within the simulation domain, with randomly selected individuals marked by black circles and their simulation identifier. In all plots, groups are represented as low interaction (green diamond), moderate interaction (yellow triangle), high interaction (red circle), and large size (orange square).

2.4 Results

2.4.1 Magnitude of uptake

The growing season was marked by consistent rainfall events until simulation day 22 when precipitation events decreased in magnitude and frequency (Figure 2.1). The mid-season dry period ended on day 68, when more frequent precipitation resumed. A comparison of eddy-covariance measured latent heat fluxes with domain scale T_{pot} indicate that despite relative soil dryness, T_{act} was not constrained (Figure 2.1), with a cumulative total of 281mm over the period.

Table 2.3 Compilation of representative individuals and their simulation statistics.

Root ID	Classification	PET [mm]	Flat SC1 [mm]	Tap SC1 [mm]	%Diff	Flat SC3 [mm]	Tap SC3 [mm]	%Diff
11	High Interaction	0.50	0.50	0.51	-0.89	0.84	0.82	1.41
12	High Interaction	0.50	0.50	0.48	2.70	0.55	0.54	1.36
53	High Interaction	0.17	0.17	0.19	-6.93	0.29	0.29	0.24
84	High Interaction	0.38	0.38	0.37	1.09	0.66	0.62	4.01
36	Large Tree	0.70	0.70	0.61	5.60	1.25	1.22	2.09
41	Large Tree	0.74	0.74	0.65	7.89	0.93	0.92	1.29
76	Large Tree	1.06	1.06	0.96	5.83	1.54	1.46	4.49
88	Low Interaction	0.07	0.07	0.08	-11.24	0.08	0.08	-0.86
100	Low Interaction	0.05	0.05	0.05	0.00	0.05	0.05	-1.02
109	Low Interaction	0.10	0.10	0.10	-0.22	0.10	0.10	0.45
122	Low Interaction	0.03	0.03	0.03	0.00	0.03	0.03	0.00
129	Low Interaction	0.02	0.02	0.02	0.00	0.02	0.02	-1.20
48	Moderate Interaction	0.47	0.47	0.47	-0.34	0.50	0.51	-1.59
89	Moderate Interaction	0.06	0.06	0.06	-0.95	0.05	0.05	-0.02
97	Moderate Interaction	0.20	0.20	0.20	-0.13	0.19	0.19	-0.63

Under Soil 1, T_{act} does not meet T_{pot} due to excessive drying of the soil across Sc1-Sc3 (Fig. 2.6a). As root lateral spread increases, accessible soil water reservoirs grow, elevating T_{act} from 183 to 233mm. For Soil 2, which had higher porosity and overall soil water content, uptake was not constrained and T_{pot} was met across all three scenarios.

The influence of root structural archetype (e.g., flat roots vs. tap roots) was examined across all lateral spread scenarios. The cumulative difference in growing season uptake for individuals varied from 0 – 11.2% and 0 – 4.5% for SC1 and SC3 respectively (Figure 2.57). for an individual breakdown). Averaged across the representative groups, variations were most pronounced for large trees in Sc1 and to a lesser extent, those experiencing high competition (). Given the similarity between flat and tap root results, results and discussion will refer to flat roots unless otherwise noted.

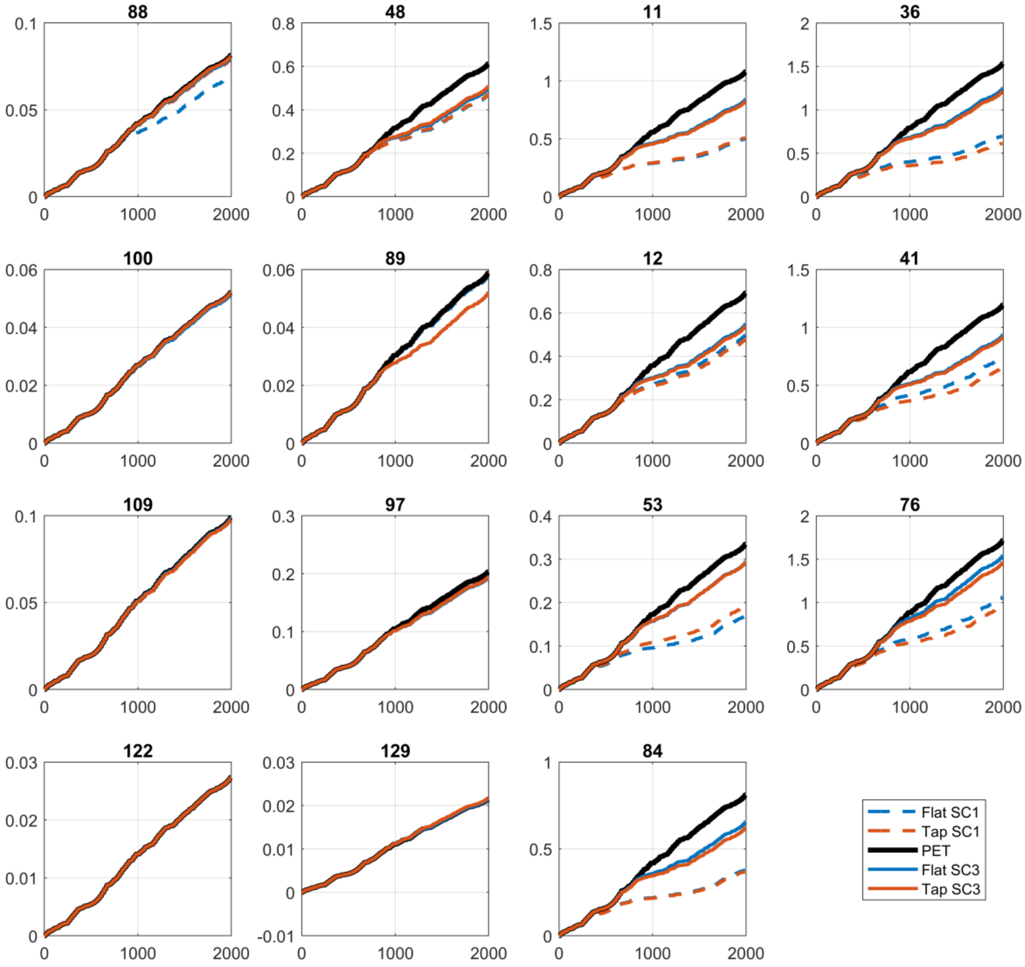

Figure 2.7 Cumulative water uptake (mm) for representative root systems. Each subplot is titled with the root's

identification number (Table 2.3). Sc1 is shown in dashed lines, Sc3 in solid lines, and potential transpiration in black. See legend for color specifications and table for interaction group.

Table 2.4 Mean percent difference of cumulative uptake between root archetypes for the extrema lateral spread scenarios

Classification	**Sc1 Mean**	**Std**	**Sc3 Mean**	**Std**
Low Interaction	-2.29	4.48	-0.53	0.64
Moderate Interaction	-0.47	0.17	-0.75	0.65
High Interaction	-1.01	0.12	1.76	1.39
Large Tree	6.44	1.03	1.20	1.36

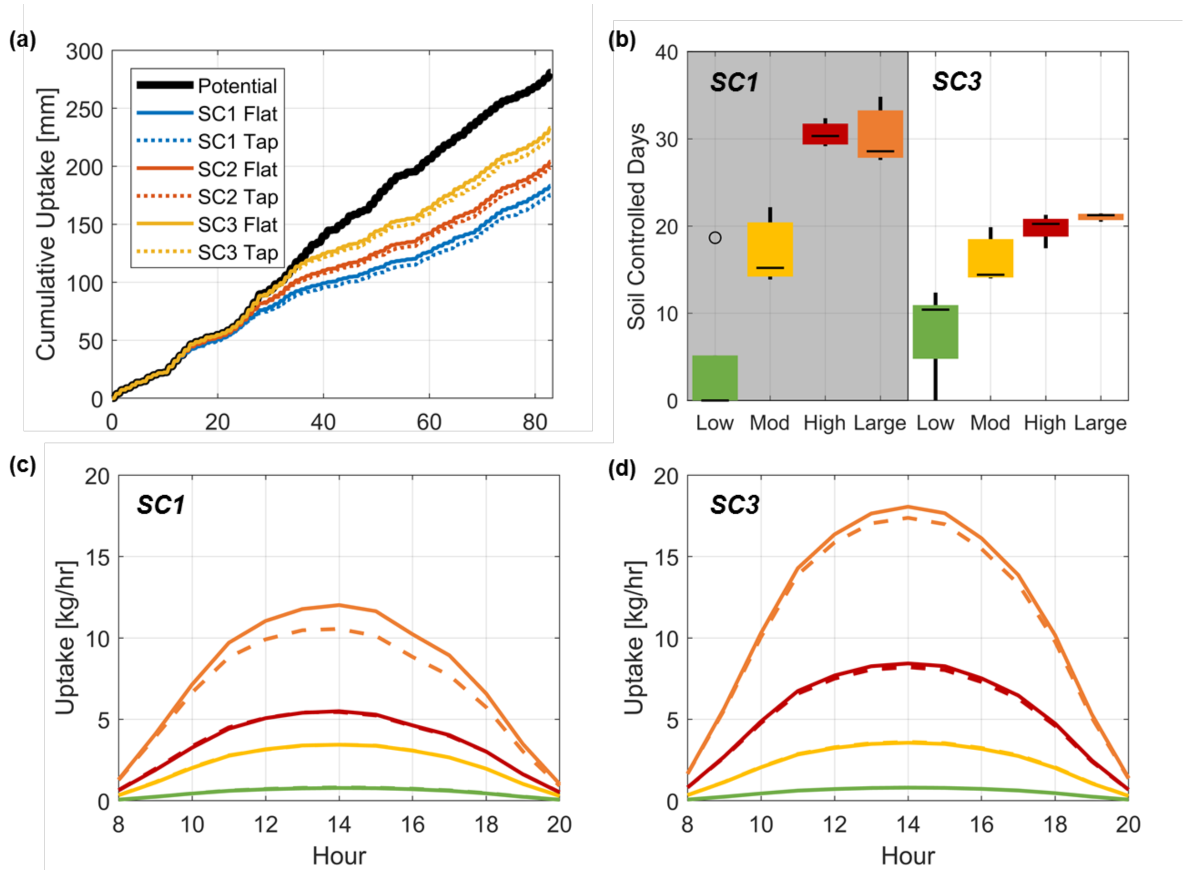

Figure 2.8 (a) Cumulative system-scale uptake [mm] for Sc1-Sc3 under water-limited conditions. Cumulative system-scale uptake for Soil 2 was equal to the potential transpiration which is shown in black. (b) Number of "soil controlled days" (e.g., days when dry soil limits water uptake) for the representative clusters for the extrema scenarios. Quartile ranges are given by the box length, range by the whisker, median by the black interior line, and outlier by the open marker. (c – d) Mean daily uptake [kg/hr] for the representative clusters for the extrema lateral scenarios. Solid lines represent the flat root archetype and dashed lines represent the tap root. Colors follow the color scheme previously introduced and shown in (b).

2.4.2 Shifting zones of water uptake

Under water limitation (Soil 1), individual uptake during the mid-period shifts away from the root system's center of mass into deeper soil layers (Figure 2.69, left panel). The centroid responds quickly to small pulses of rainfall, returning to the center of root mass distribution or to surface layers as water infiltrates through the soil column. The mid-period rainfall events were not large enough to saturate the entire soil column, with the centroid returning to deeper layers as the pulse was depleted. As lateral interactions increase (Sc1→ Sc3), the magnitude of the centroid shift increases across all representative groups. Without water limitation (Soil 2, Figure 2.7, right panel), there are no significant shifts away from the center of root mass distribution.

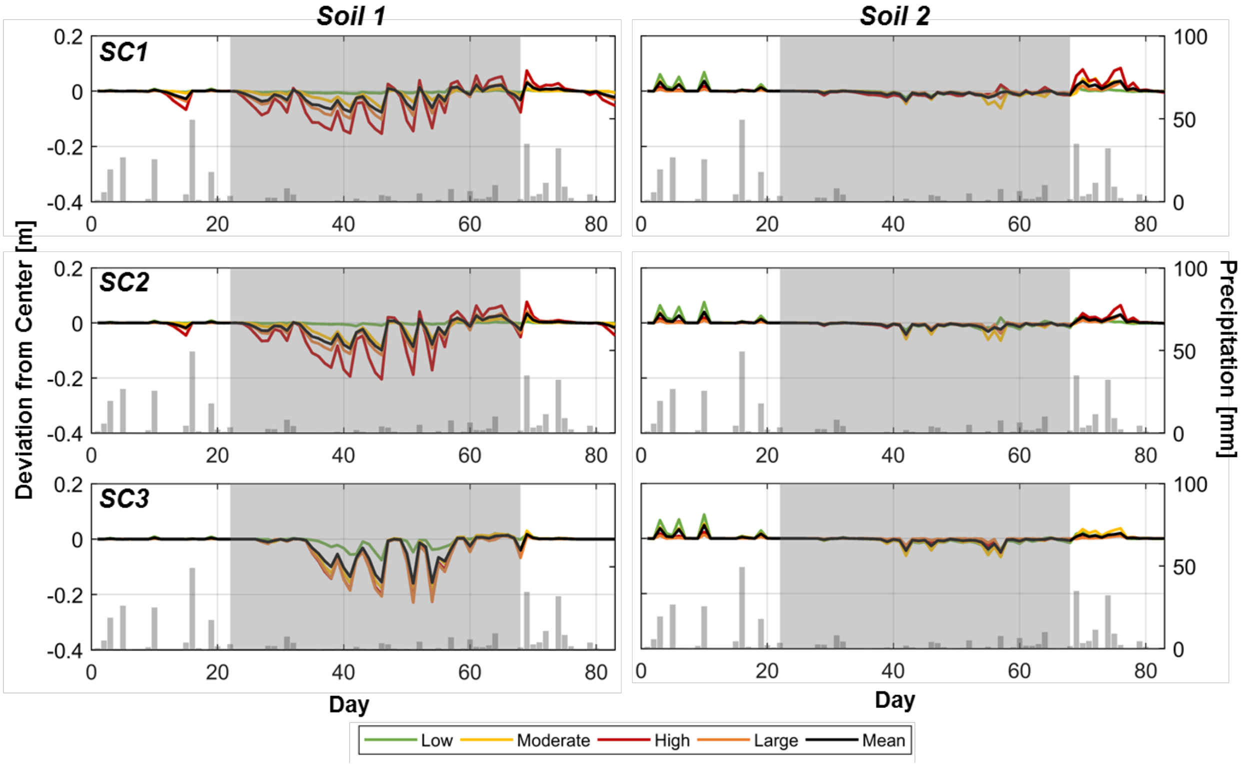

Figure 2.9 (left panel) The shift of the weighted centroid of water uptake away from the center of root mass distribution (0.385 m) for Soil 1 for the three interaction scenarios. (right panel) The shift of the weighted centroid of uptake away from the center of mass for Soil 2 for the same interaction scenarios. In all plots, interaction groups are given by the legend, gray bars are daily precipitation [mm], and the shaded gray is the observed "dry period".

At the system scale, water uptake from characteristic wet (days 22-26) and dry (days 34-38) periods were compared for four soil layers (Fig 2.10). During the well-watered period, the relative contribution of different soil layers is fairly consistent, mirroring the root length density distribution. However, as these layers dry and water limitation sets in, the relative contribution of deeper soil layers (specifically, 40-60cm and 60-80cm) increases significantly. These shifts are seen across all lateral interaction scenarios, but at varying intensity.

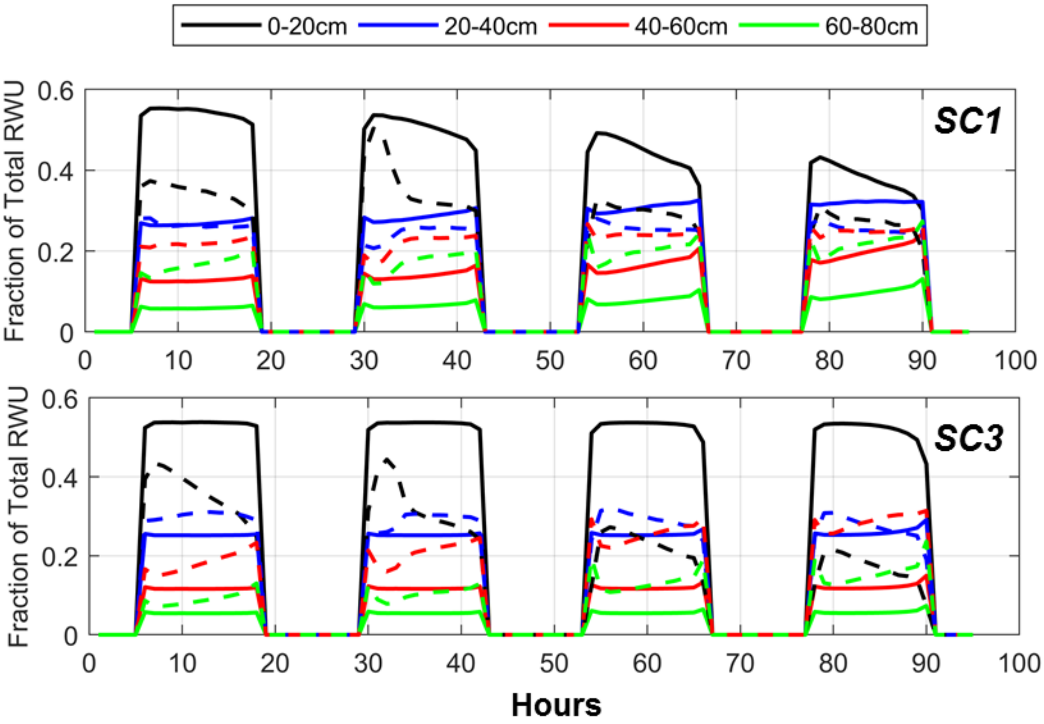

Figure 2.10 (top) The relative contribution of the various soil layers (see the legend) to domain scale water uptake for Sc1 and (bottom) Sc3. The simulation results for the characteristic wet period is denoted with the solid lines and for the characteristic dry period with the dashed lines. The results correspond to Soil 1.

2.4.3 Soil moisture

Mean soil water content in the root zone (top 80cm) decreased from 0.20 $m^3 m^{-3}$ in the early growing season to <= 0.10 $m^3 m^{-3}$ in the mid-season dry period. As rain events became more frequent, mean water content rose above 0.10 $m^3 m^{-3}$. Mean soil water content values were comparatively lower during the dry period for Sc3, indicative of the higher rates of cumulative uptake (Fig. 2.11a). Spatial patterns of soil moisture closely track root system distributions (Fig. 2.11c,d), with Sc1 displaying higher heterogeneity than Sc3. This is especially apparent when examining the coefficient of variation (Cv) of root zone soil water potential across the simulation period (Fig. 2.11b). Sc1 and Sc2, with similar root density distributions show similar patterns of Cv, with values exceeding 1 during the dry period, indicating that the standard of deviation is higher than mean. Cv for Sc3 was significantly lower, never exceeding 1, even during the mid-season dry period.

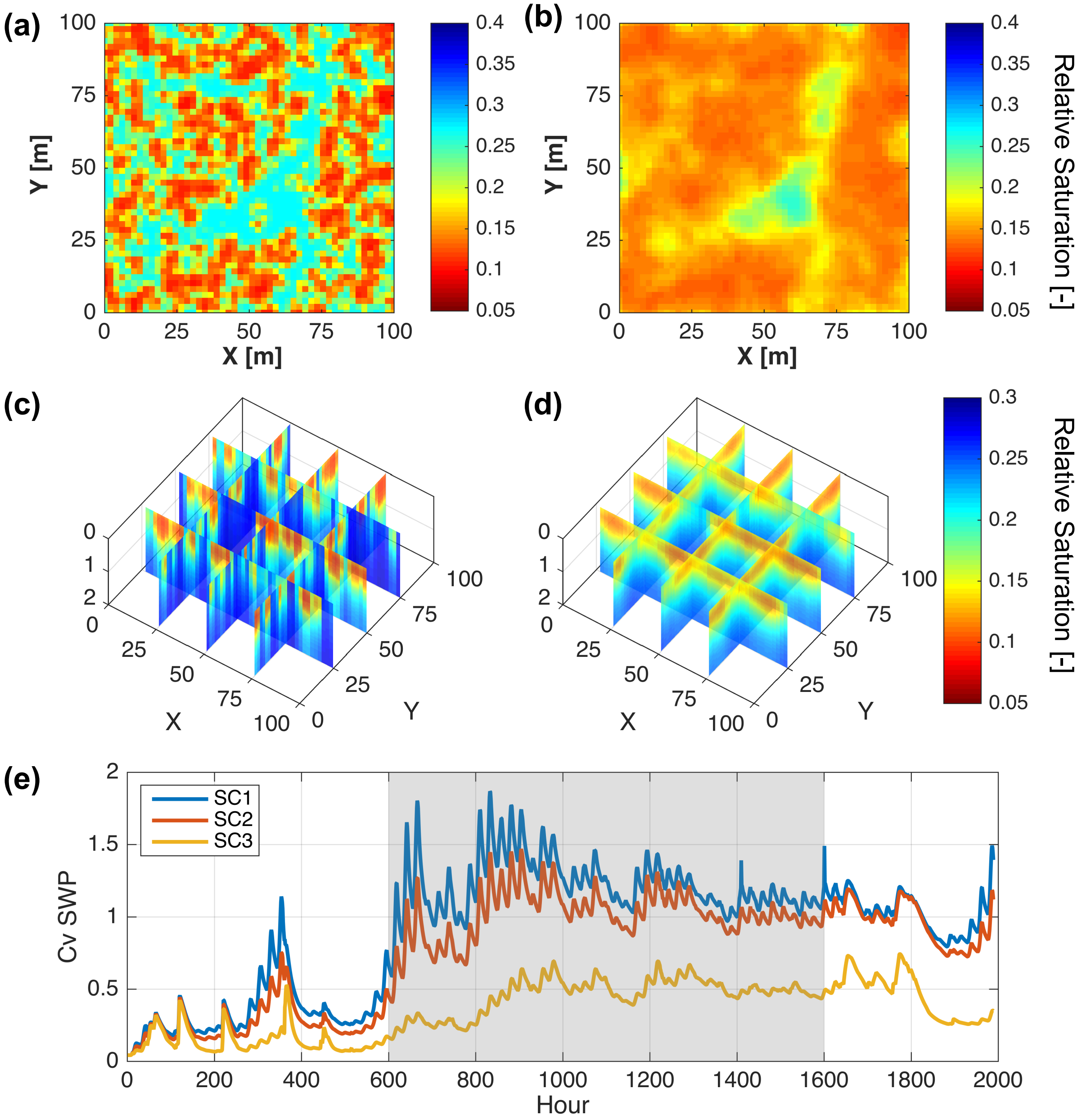

Figure 2.11 (a – b) Areal view of mean relative saturation, averaged across dry period, for Sc1 and Sc3 respectively

at 2 x 2 m scale. (c – d) Mean relative saturation, averaged across the dry period, for Sc1 and Sc3 respectively at 0.05 m scale. (e) Coefficient of variation for soil water potential for Sc1 – Sc3 across the simulated period, with dry period indicated as shaded gray.

Hourly mean soil water content for SC1 and SC3 show similar patterns across the simulation period, but overall soil moisture was lower for SC3. This can be explained by root distributions. In SC3, roots occupied every soil cell in the surface layers, while in SC1 some cells in the top 80cm had no roots. Soil moisture patterns and magnitudes agree relatively well with observations from the study plot (Figure 2.10, 2.12), but do not quite reach the same residual values.

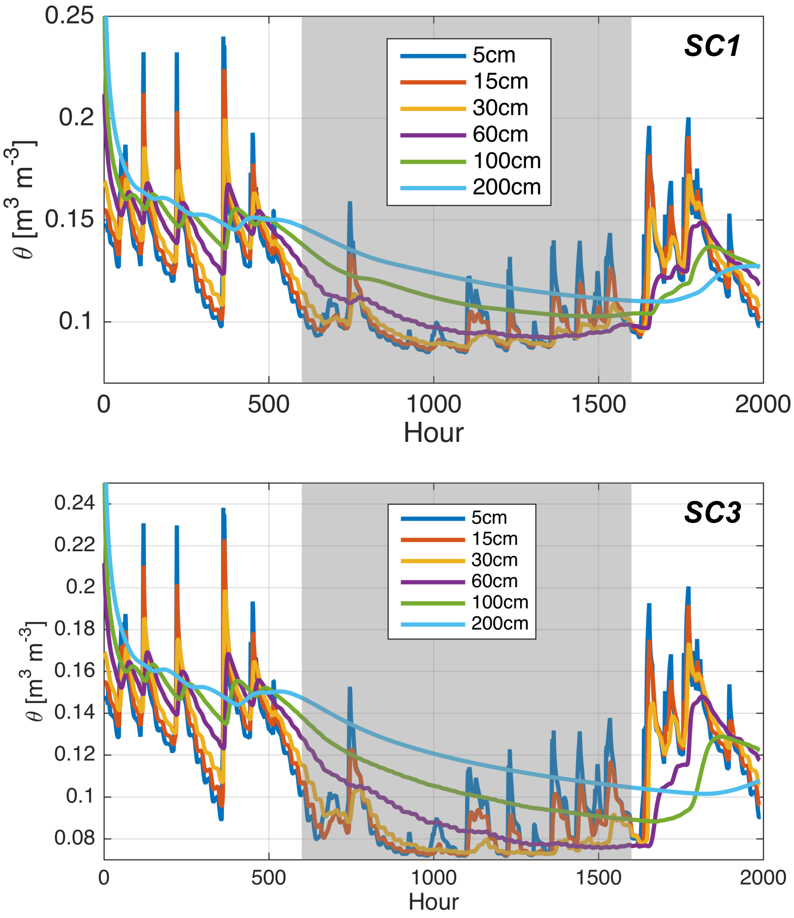

Figure 2.12 Hourly mean soil water content at 5, 15, 30, 60, 100, and 200cm for (top) soil 1, Sc1 and (bottom) soil 1, Sc3 averaged across the simulation domain.

2.4.4 Sensitivity of root hydraulic architecture

Beyond root structure, sensitivity to hydraulic parameterization was also tested. Increasing root system conductivity can result in increased rates of water uptake. These increases plateau as the system reaches a limit of water availability (not shown). The increases in conductivity also increase the rate of water moving from root to soil. As the source function is not limited in volume the same way the sink function is, HR scales exponentially with increased values of K_{comp}. Similar increases in HR with high root hydraulic conductivity were observed by (Quijano & Kumar, 2015), but in this study, these increased rates did not translate to alleviation of water stress.

A further analysis of the sensitivity of K_{comp} to microscale properties (e.g., surface area and root hydraulic conductivity) was performed using traits from dominant species found at the UMBS (Table 2.5). Measurements were placed in consistent units and checked for compatible normalization. Axial conductivity is normalized per unit root length basis and has the units [$m^3s^{-1}MPa^{-1}m^{-1}$] or [$m^2s^{-1}MPa^{-1}$]. Radial conductivity is normalized per root surface area basis and has the units of [$m^3s^{-1}MPa^{-1}m^{-2}$]. It is important to note there are multiple methodologies for measuring hydraulic conductivity in woody tissues, and further, the compatibility of the various methods is still under scrutiny (Cochard et al., 2013). For the purposes of this work, the various protocols were assumed compatible and temporal changes in hydraulic conductivity (due to age or environmental factors) were not accounted for. Where multiple studies existed for a single species, the means and variances were pooled using unbiased least squares estimation.

Table 2.5 Compilation of root radial hydraulic conductivity values from the literature.

Species	Radial hydraulic conductivity [$m^3s^{-1}MPa^{-1}m^{-2}$] (n)	Source

Betula papyrifera	7.15E-08 ± 3.61E-08 (6)	(W. Zhang & Zwiazek, 2016)
Pinus strobus	9.62E-08 ± 5.51E-08 (29)	(Johnsen et al., 1988)
Populus tremuloides	21.7E-08 ± 18.2E-08 (48)	(Siemens & Zwiazek, 2003; Wan et al., 2001)
Quercus rubra	3.87E-08 ± 1.89E-08 (30)	(Cheng, 2009; Kruger & Sucoff, 1989)
Ulmus Americana	0.76E-08 ± 0.10E-08 (28)	(Cheng, 2009)

K_{comp} was computed for the range of radial root hydraulic conductivity values for flat and tap root archetypes. K_{comp} was found to have a log-linear relationship with radial hydraulic conductivity, Kr (Figure 2.13). This relationship held even if each branching root order was assigned a different value of Kr. Changing axial conductivity, Kx, which is typically assumed much larger than Kr, merely shifted the intercept, but had no impact on the slope. At the lower range of conductivities some instability in the computation of K_{comp} develops but values in this range are lower than typical observations of root conductance and were not used in this study.

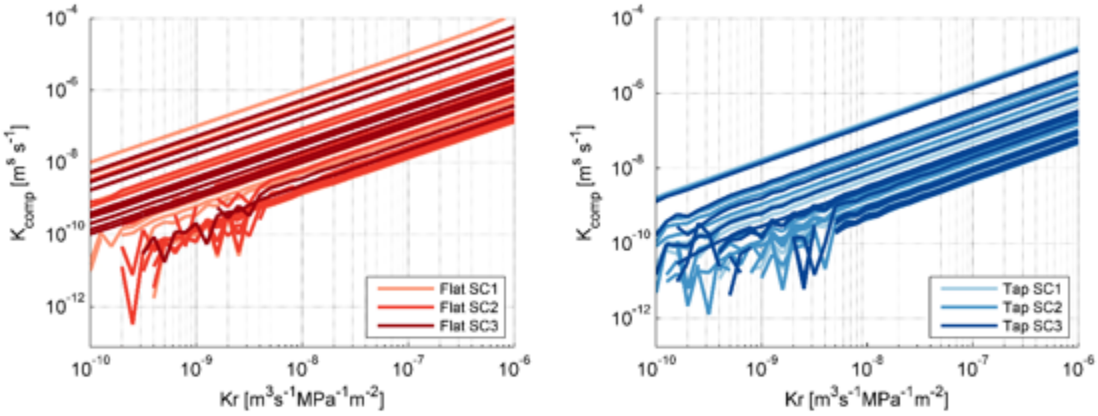

Figure 2.13 (left) Sensitivity of K_{comp} to radial conductivity, K_r, for flat root architectures. (right) Sensitivity of K_{comp} to radial conductivity, K_r, for tap root architectures.

2.4.5 Root collar potential

The water potential at the root collar was computed for the representative individuals across the simulation period (Figure 2.14). Root collar potential is a function of both soil water potential and atmospheric demand. Diurnal shifts from the baseline are due to atmospheric demand, with larger trees experiencing higher fluctuations – as seen by trees 36 and 76 in the sample plot. Higher interaction individuals experience greater soil drying, causing shifts in baseline soil water potential, as seen by trees 97 and 100. The baseline water potential is analogous to predawn leaf water potential (a metric frequently used in ecophysiological studies to assess gradual changes in plant hydraulic state during drought spells) while the diurnal swings are analogous to mid-day leaf water potentials (indicative of plant hydraulic function).

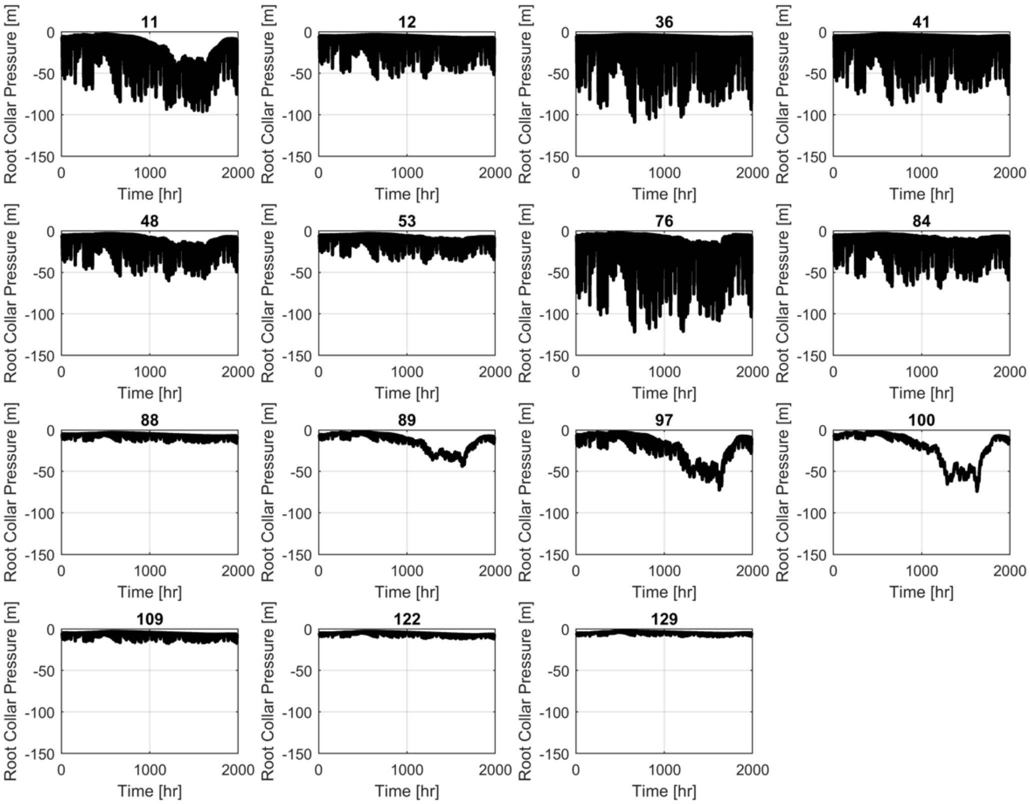

Figure 2.14 Hourly root collar potential for the representative trees for the entire simulation period. Tree numbers are given as subplot titles.

2.5. Discussion

2.5.1 The carbon cost and water benefit of interaction

The primary focus of this study has been to examine the impacts of root lateral expansion and peer interaction on root water uptake – where expansion refers only to extension of the coarse root architecture. System scale fine root density was kept constant across all tested scenarios. Coarse roots (>2-5mm in diameter, depending on source) provide structural stability for the absorptive fine roots and are the primary transport pathways for water to the stem. Individuals incur a greater carbon cost, both from construction and maintenance, as roots extend horizontally or vertically through soil layers (Fig. 2.15a, b). This growth increases the size of an individual's soil water reservoir, but realized benefits to water uptake are nonlinear. As new water reserves are accessed, peer interaction and demand likewise increase, potentially reducing the actual water available to the individual.

In the lowest interaction scenario (Sc1), "large trees" (>25cm) constrain uptake more often and earlier than smaller trees, unable to meet their proportionately larger atmospheric demands. Large expansions in lateral spread (Sc3) improve uptake during the dry period, but do not completely allay constrained uptake. While the lateral spreads of Sc3 (as high as 30m for the largest individuals) provide ample supply in the absence of peers, increased rates of interaction and competition counteract this benefit, with individuals still unable to meet demand (Fig. 2.15c "Large trees"). "High interaction" root systems also experience the impacts of water limitation more strongly than other groups (Fig. 2.15c "Low Interaction" and "Moderate Interaction"). These individuals represent a range of tree sizes that experience high levels of root zone overlap (i.e., high RCI) across all scenarios. Again, increasing lateral spread alleviates constrained uptake to a degree, but individuals are still unable to meet the full atmospheric demand (Fig. 2.15c "High Interaction").The "large tree" and "high interaction" groups both show increasing relative carbon costs across Sc1-3. Despite these high relative costs, additional benefit is not gained, as seen by the plateau in AI.

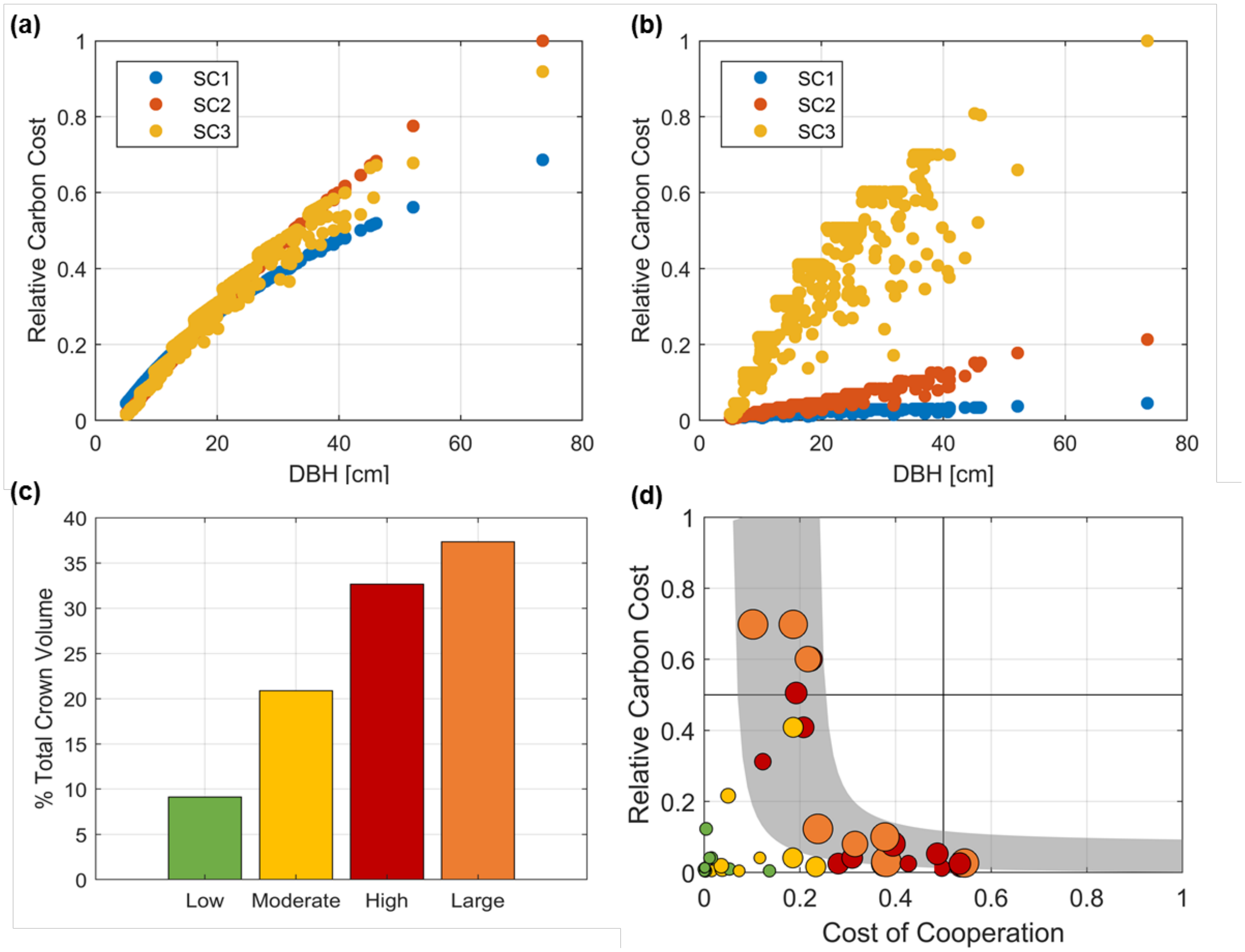

Figure 2.15 (a) The relative carbon cost of fine roots for Sc1 – Sc3. (b) The relative carbon cost of coarse root architecture for Sc1 – Sc3. (c) Relative crown volume of each representative group. (d) The relative structural carbon cost (Y-axis) versus the ability to meet atmospheric demand (X-axis) under Soil 1 for the four representative tree groups. The gray shaded region encompasses the majority of trees as illustrated by the combined crown volumes of high interaction and large trees presented in (c).

An alternative viable strategy to ameliorate drought stress is to access deeper soil water. Deep rooting has long been proposed as a coping mechanism for water limitation in some species (e.g., (Barbeta et al., 2015; Nepstad et al., 1994; Thomsen et al., 2013)). We instituted a uniform rooting depth of 80cm, a depth which encompasses a majority of the fine root profile, to isolate the impact of lateral spread. With this limit, mean soil water content in deep soil layers (>=1m) remained greater than 0.10 m^3 m^{-3} across the simulated period. Observations from the UMBS show extremely dry deep soil layers, with soils from 1-3m maintaining values close to residual saturation (0.03-0.04 $m^3\ m^{-3}$) for the majority of the growing season (Figure 2.1). This suggests that further deep soil drying to occur in simulation, a deeper rooting profile would be required. This is supported by empirical evidence of deep water uptake by species during dry periods as means of maintaining the transpiration stream. For example, in Matheny et al. (2014) deep-rooted red oaks (*Quercus rubra*) were able to meet atmospheric demand during dry periods while shallow-rooted red maples (*Acer rubrum*) were not. To cope with water limitation, individuals with high atmospheric demand and those with high competitive pressure or lateral interaction must optimize both lateral spread and rooting depth, if they wish to maintain water uptake during dry periods. Our analysis supports other studies that highlight the importance of both tree size and spatial proximity in assessing drought resilience (Larocque et al., 2012; Lechuga et al., 2017).

2.5.2 Homogenization of soil moisture

Spatial patterns of soil moisture track closely with root spatial distributions, becoming more homogeneous across the scenarios. As shallow soil layers (0-30cm) are more uniformly depleted, the centroid of uptake across all representative groups is driven further below the center of mass. This is most evident when inspecting the "low" and "moderate" interaction groups. In Sc1, these groups have relatively "exclusive" access to water reserves in the surrounding soil, averting extreme drying from shallow layers. Uptake instead occurs across the entire root profile, the centroid close to the center of root system biomass. As lateral interactions increase and the once exclusive soil water reserves are now shared spaces, "low" and "moderate" individuals must dynamically adjust their uptake to deeper soil layers.

From a physical standpoint, the homogenization of soil moisture by vegetation represents a minimization of the free energy of the system. Heterogeneous fields represent a non-optimal energy state which consist of sharp soil water potential gradients and unutilized pockets of moisture. The consequences of extreme soil water potential gradients may be the cavitation of root xylem vessels. Fine roots, often described as a plant's 'surge protector,' may protect the rest of the hydraulic system by cavitating, preventing embolism from spreading further into the system and reducing overall tension on the water column.

2.5.3 Emergent system properties

Implementation of root water uptake and root system structure in terrestrial models is still a large area of opportunity for the research community (Warren et al., 2015). Yet, three-dimensional representation of individual root architecture and simulation of water uptake requires a substantial data and time investment. While the hybrid macroscale formulation of the model significantly reduces computational load, post-processing of 574 root systems at the hourly timescale would constitute a large computational effort, while gaining minimal additional information. As such, aims were taken to identify individuals which could elucidate the higher level, system scale impacts of root system structure and function. Representative individuals were chosen with a cluster analysis that accounts for both the size of an individual and their positions in the community structure.

The representative groups showed divergent behavior in their response to water limitation in terms of zones of uptake and ability to meet potential demand. Individuals of the same size, but with different degrees of interaction, responded differently, with higher degrees of interaction driving water uptake into deeper soil layers.

2.6. Summary

The degree of spatial interaction between root systems is a contributing factor to dynamic root water uptake, with increased interaction contributing to shifting uptake to deeper soil layers under drying conditions. As the lateral spread of root systems expand and interactions increase, the soil moisture field is homogenized, minimizing the free energy in the field, but generating additional construction and maintenance costs for the system. Our work shows that beyond rooting depth, lateral or horizontal interactions are an important dimension to consider when examining uptake, especially under conditions of water limitation.

Appendix 2A Root Architecture Parameters

RootBox was used to generate root architectures for the simulation domain. Two general archetypes were assumed: flat root and tap root systems. Roots were grown to desired lateral spreads by exploiting the relationship between total branch length (k) and inter-branching distance (*ln*), $k = ln(nob - 1) + la + lb$, where *nob* is the number of children branches to be spawned, la is the apical segment length, and lb is the basal segment length. Additional root orders were added to increase total root length and surface area. Example parameters for the flat and tap roots are given in Table . While RootBox incorporates natural stochasticity in spawning branch angles (e.g., parameter β in Leitner et al. 2010), we selected for architectures that are naturally symmetric. Symmetry is defined as architectures with a planar center of mass near the origin.

Table 2.6 RootBox parameters for tap root with 8m lateral spread, 0.8m rooting depth.

Parameter	**Order 1**	**Order 2**	**Order 3**	**Order 4**	**Order 5**	**Unit**
***r*, growth Rate**	d/LS	1.0	5.0	5.0	5.0	[L/T]
***lb*, length of basal zone**	0	0	0	0	0	[L]
***la*, length of apical zone**	0.1	0	0	0	0	[L]
***nob*, number of branches**	33	801	3	3	1	[-]
***a*, root radius**						[L]
θ, angle between order and predecessor	0	π/2	π/4	π/4	π/4	[rad]
maximum root deviation due to tropism	0	0	0	0	π/3	[rad]
***dx*, axial resolution**	1	1	1	1	1	[L]

Table 2.7 . RootBox parameters for a Flat Root – 8m lateral spread, 0.8m rooting depth

Parameter	**Order 1**	**Order 2**	**Order 3**	**Order 4**	**Order 5**	**Unit**
***r*, growth Rate**	10	10	10	10	10	[L/T]
***lb*, length of basal zone**	0	0	0	0	0	[L]
***la*, length of apical zone**	0	0	0	0	0	[L]
***nob*, number of branches**	27	32	20	11	3	[-]
***a*, root radius**						[L]
θ, angle between order and predecessor	0	π/2	π/4	π/2	π/4	[rad]
maximum root deviation due to tropism	0	0	π/2	π/4	π/3	[rad]
***dx*, axial resolution**	1	1	1	1	1	[L]

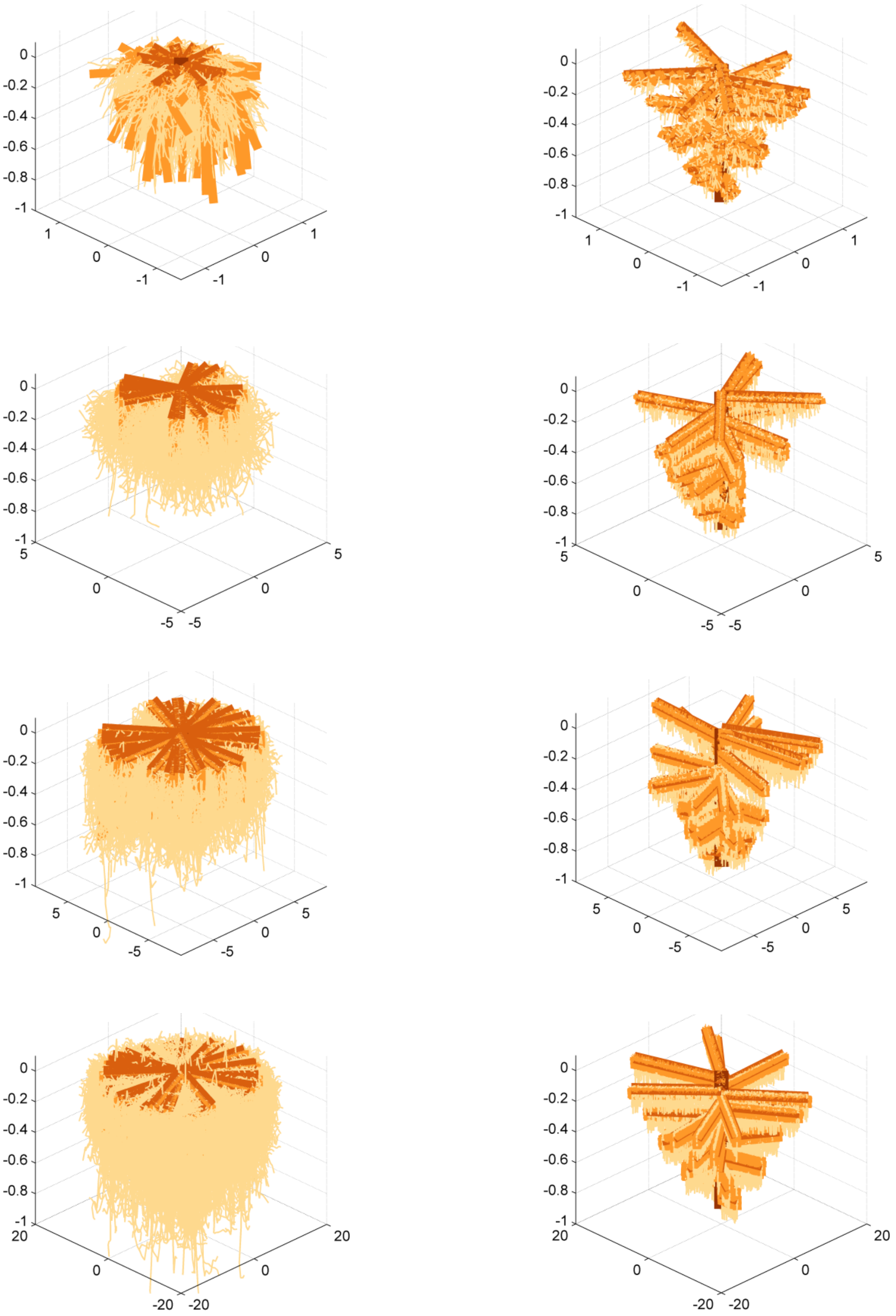

Figure 2.16 (Left, from top to bottom) Flat root systems for lateral spreads 1.5, 5, 9, and 20-m with 0.8m rooting depth. (Right, from top to bottom) Tap root systems for lateral spreads 1.5, 5, 9, and 20-m with 0.8m rooting depth. For visualization, only four of the five root orders are shown.

Chapter 3 – Feedbacks of Root Functional Diversity on Water Uptake in a Tropical Rainforest

3.1 Introduction

The tropical rainforests of the Amazon Basin region play a significant role in global energy, carbon, and water cycling, with climatic influences extending as far as North America (Medvigy et al., 2011, 2013). The increased frequency and severity of drought events in the region has highlighted the potential vulnerability of rainforests to heat and drought-induced stress (Phillips et al., 2009; Xu et al., 2011). Yet, current projections of forest fate are belied by model uncertainties that have been unable to fully capture observed physiological responses to water-limitation (Sitch et al., 2008). Water uptake processes by root systems have been identified as an area of critical import to reducing overall uncertainty and improving the ability of land surface models to quantify forest response to extended dry season and drought events (McDowell et al., 2013; Sperry & Love, 2015).

For individual trees, the response to abiotic stress is determined by the expression of functional traits that regulate internal biochemical and biophysical processes. Analogous to an economic market analysis, a tree's behavior is driven by cost-benefit analysis where individual investment in and regulation of shared resources follow distinct and varied evolutionary strategies (Reich, 2014). This 'plant economic spectrum' provides an amenable axis with which to explore how these investment strategies evoke varied responses to changing patterns of precipitation**.** Those trees that favor continual carbon uptake at the cost of system safety are termed "risky," while those who conserve water at the cost of taking up carbon are termed “conservative” (Skelton et al., 2015). Each strategy poses inherent risk, as those who conserve water for extended periods of time without adequate carbohydrate reserves run the risk of carbon starvation, while those who continually take up carbon during extreme drought conditions can suffer permanent damage to hydraulic pathways due to embolization of xylem conduits (McDowell et al., 2008). How these strategies coexist within an ecosystem remains an open question to which the root zone function plays a vital, yet often ignored role.

For the rainforests of the Amazon, which contain more than 11,000 woody species and over 270 hyper-dominant species (ter Steege et al., 2013), a wide range of functional strategies for water uptake likely exists. These strategies are driven by both root structural (Ivanov et al., 2012; Nepstad et al., 1994) and ecophysiological controls (Barros et al., 2019; Brum et al., 2018; Oliveira et al., 2005). Chapter 2 explored the impacts of root lateral interaction on water uptake during water limitation in a temperate forest. The temperate forest system represents a low diversity system with a handful of functional strategies. This chapter builds upon this previous work to explore the impact of root functional strategy on water uptake by addressing the following research questions: (1) How does diversity of hydraulic strategy contribute to the maintenance of the transpiration stream during water limitation? And (2) what root structural and physiological traits are important in determining drought response?

These research questions are addressed in the context of the unprecedented ENSO 2015-2016 event which caused record-breaking warming and drought across much of the Amazon River Basin (Jiménez-Muñoz et al., 2016). Data were collected and synthesized from a highly seasonal rainforest located in the eastern Amazon River Basin and used to parameterize the coupled soil-root water uptake model presented in Chapter 2. The model is used as testing bed to explore the role of various below-ground structural and ecophysiological controls on root water uptake during the 2015-2016 ENSO dry season.

3.2 Methods

3.2.1 Site description

This study uses data from the highly seasonal Tapajós National Forest (TNF), located in the eastern portion of the Amazon River basin. Measurements and supporting data were collected at or in the vicinity of the ‘KM67’ eddy covariance tower (FluxNet: BR-SA1). The climatology is moist tropical, receiving ~1,920 mm per year of precipitation, with a pronounced dry season (monthly precipitation <100 mm) from July through November (Parotta et al., 1995). The soils are deeply weathered clay Oxisols, with no impeding layers in the upper 12 m (Nepstad et al., 2007). The monitored area is on a plateau approximately 250m above the Tapajós River, with deep water table.

3.2.2 Structural relationships

3.2.2.1 Tree census

During the 2014 field season, an intensive survey of individual species, size, and location was conducted within the sap flow monitoring area. Large anchor trees formed the vertices of triangular parcels. Within the triangular parcels, the distance between individuals and two anchor trees were measured using flexible measuring tapes. A subset of these tape measurements were verified using a laser rangefinder. X-Y coordinates were generated for the anchor trees and parcel members using multidimensional scale mapping (MDS-mapping) (Oh et al., 2010) and a “sweeping points” algorithm (Appendix 3A).

3.2.2.2 Above-ground allometry

Allometric relationships developed for K67 and similar sites were used to characterize above-ground canopy structure as a function of tree diameter at breast height (Table 3.1). A subsample of trees were measured at K67 in January 2017 using a laser range finder and a hand clinometer and compared to the LIDAR based allometric measurements (Appendix 3B).

Table 3.1 Above-ground allometry for K67 field site.

Variable	Allometric Equation	Equation	Source
Tree height (*H*)	$H = 4.268\ \mathrm{DBH}^{0.5129}$	(3.1)	(Hunter et al., 2013)
Crown radius (*C_r*)	$C_r = -0.367 + 0.741\sqrt{\mathrm{DBH}}$	(3.2)	(Gonçalves, 2014)
Tree Height (*H*)	$H = -17.514 + 12.191\sqrt{\mathrm{DBH}}$	(3.3)	(Gonçalves, 2014)
Crown height (*C_h*)	$C_h = -1.347 + 1.903\sqrt{\mathrm{DBH}}$	(3.4)	(Gonçalves, 2014)
Crown volume (ellipsoid)	$C_v = \frac{4}{3}\pi C_r^2 C_h$	(3.5)	

Incident light attenuates through the canopy based on the canopy structure. This can produce non-linear forcing of potential transpiration throughout the canopy. To partition canopy forcing, tree heights were binned into five classes: 0-10, 10-20, 20-30, 30-40, and >40 m. Individuals were organized into five height classes, binned by 10 m increments. Fraction of incident light at each canopy height was derived using observational data collected by Stark et al. (2012).

3.2.2.3 Below-ground allometry

Root lateral spread was determined using allometry for non-arid sites presented in Casper et al. (2003). For non-arid sites, root lateral extent is given as a function of crown volume as $\log LS = 0.3949 \log C_v + 0.2328$, where lateral spread, LS, is in [m] and crown volume, C_V, is in [m^3]. As explored in Chapter 2, a general assumption is that tree roots extend to the “drip line” or the crown radius. As such, the allometric lateral spread was compared to potential lateral spreads based on factors of C_R (Table 3.1).

Rooting depth, especially in the tropics, is an important vegetation characteristic, but little observational evidence exists with which to constrain it. As such, different scenarios of rooting depth are imposed to test hypotheses regarding water acquisition under water limitation (Table 3.2). (1) The uniform rooting scenario follows the relatively shallower root scenario from Ivanov et al. (2012) with all root systems, regardless of size, sharing a common rooting depth of 6m. (2) The effective rooting depth scenario (EFRD) was derived from Brum et al. (2018) based on isotopic analysis performed at K67 under dry season conditions. EFRD describes the effective area of uptake for an individual based on size, with small trees (<10 cm) operating in the surface layers. As such, actual rooting depths were adjusted to a minimum of 1m. (3) The linear model is a simplified model of rooting depth that assumes rooting depth is linearly scaled of DBH.

Table 3.2 Rooting depth scenarios used for structural analysis and RWU modeling.

Depth Scenario	**Rooting depth**	**Equation**
Uniform	$D = 6$ m	(3.6)
Effective Rooting Depth	$D = \exp\left[-\frac{k}{n}(1 - exp(-rDBH)) - \frac{m}{n}\right]$ *	(3.7)
Linear	$D = 0.214$ DBH	(3.8)

* m = -3.810, n = -0.562, k = 5.52235, r = 0.05591

3.2.2.4 Root profiles and species specific data

Fine roots were collected in September 2015 at 5 randomly selected locations within the surveyed area at depths of 0, 5, 10, 25, 40, and 60 cm. A sharpened, hollow core was driven into the ground and 5 cm cores extracted. Live roots were separated from the soil and dyed with methylene blue. Additional samples were collected during January 2017 and targeted individual species. Surficial roots of four species were traced and excised, with 3-4 samples taken for each individual. Samples were stored in brown paper bags and transported back to the lab within 12 hours where they were washed and placed in a solution of crystal violet dye for 24 hours. After being dyed, samples from both collections were photographed using a high-resolution DSLR camera (Canon 80D, Japan), then dried for over 48 hours at 70 °C and weighed (0.001 g precision).

Roots were imaged and root length was determined using ImageJ (Appendix 3C). One-dimensional profiles of root length density (RLD) were used to characterize the root length per soil volume available for root water uptake. Methodology was developed in Chapter 2 for the conversion of one-dimensional root biomass density (RBD) profiles to RLD profiles using specific root length (SRL) was applied here.

3.2.2.5 Root system architecture

Observations from K67 indicate that a large number of ‘terra firme’ (i.e., upland) species utilize a dimorphic root structural archetype. Dimorphic roots are a combination system which invest both in coarse lateral roots and elongated tap roots. Given the lack of species level information, all individuals within the domain were assigned the dimorphic root archetype. Root architectures were modeled to the computed lateral and depth dimensions using the RootBox model (v.5e) developed by Leitner et al. (2010) and described in detail in Chapter 2. Unique coarse root architectures were generated at 1m lateral spread intervals for each rooting depth class. Root architectures were “planted” in the domain using the surveyed coordinates of tree stems.

3.2.3 Climate forcing

Functional responses to the extreme dry season were tested using the PFLOTRAN-Root model, previously described in Chapter 2. The computational domain was 150 m x 80 m x 30 m using structured grids of 5 m x 5 m x 0.10 m resolution. Climate forcing was derived using observational data from the K67 eddy covariance tower and previous modeling and observational studies conducted at the field site.

3.2.3.1 Soil properties

Soil saturation and pressure are characterized using van Genuchten soil characteristic curves (van Genuchten, 1980). Soil parameterization scenarios were presented by Ivanov et al. (2012) and include measured and inferred soil properties (Table 3.3). The multiple soil water retention curves address uncertainty in measured properties and help ensure the robustness of results. The simulation results presented in this study utilize the TH soil characterization.

Table 3.3 Soil hydraulic parameterization including saturated hydraulic conductivity, K_s, saturated volumetric water content, θ_s, residual volumetric water content, θ_r, and van Genuchten fitting parameters n and α.

Scenario	K_s [mm h^{-1}]	θ_s [m^3 m^{-3}]	θ_r [m^3 m^{-3}]	n [-]	α [mm^{-1}]
CO-surface	35.6	0.647	0.225	1.237	-0.0883
CO-deep	14.1	0.578	0.291	1.413	-0.00674
TH*	14.1	0.696	0.315	1.687	-0.0224
MRE	26.9	0.604	0.283	1.0623	-0.0213

3.2.3.2 Potential transpiration

Potential transpiration was estimated using the Hargreaves-Samani (HS) method (Hargreaves & Samani, 1985). Compared to conventional models of ET (e.g., Priestley-Taylor and Penman-Monteith), HS relies on minimal forcing information and parameterization, making it a feasible choice for the tropics, where such information is scarce or highly variable. The HS potential evapotranspiration (ET_o) equation is given by

$$ET_o = C \cdot [0.0135\, K_T R_A\, (T + B)\, (T_{max} - T_{min})^{0.5}] \qquad (2.9)$$

where B and C are calibration factors (originally given as $C = 1$ and $B = 17.68$ by Hargreaves & Samani (1985)), R_A is extraterrestrial radiation, T is hourly temperature [^{o}C], T_{max} is the maximum daily temperature [^{o}C], T_{min} is the minimum daily temperature [^{o}C], and K_T is a conversion parameter. Calibrated forms of the HS equation have shown to be effective in sub-humid regions of Brazil (Lima et al., 2013). For K67, HS uses temperature data from the upper canopy temperature sensor and was calibrated using tower measured latent heat fluxes.

For the purposes of forcing, transpiration was assumed to be the dominant component of ET and thus, PET and potential transpiration were assumed equal. Potential transpiration (T_{pot}) was partitioned to the five canopy classes following the fraction of light available to the respective canopy class (i.e., the percentage of total potential transpiration assigned each layer was equal to the percentage of incident light for said layer). For the individuals within the canopy class, T_{pot} was further partitioned proportional to the relative crown volume, following methodology presented in Chapter 2.

3.2.3.3 Precipitation

Precipitation forcing was derived from corrected K67 EC rain gage observations. Raw observations were corrected using a simple scaling relationship derived from a more reliable gage installed on a nearby walk-up tower (Appendix 3B). Corrected tower observations were favored over the walk-up tower due to the length of the data record. Interception is assigned as 15% of precipitation across both the wet season and dry seasons (Fig. 3.1). While more sophisticated models of canopy storage and interception exist, the limited amount of rainfall during the modeling period preclude the need for the additional computational expenditure.

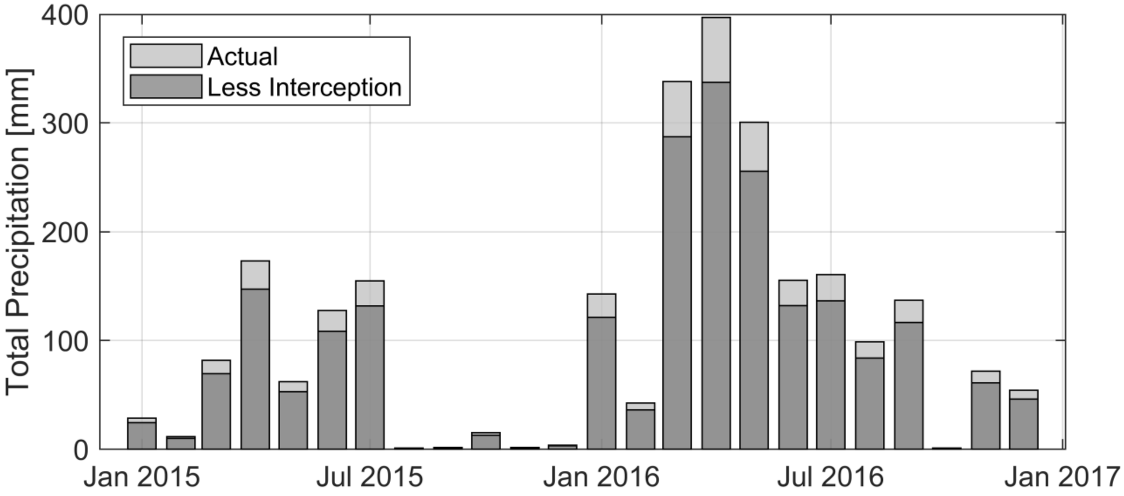

Figure 3.1Total monthly precipitation at K67 tower from 1/1/2015 – 12/31/2016 where actual precipitation is given as the light gray bar and estimated through fall is given as the dark gray bar.

Rainfall totals for the month of July were >100mm, the accepted threshold for dry season conditions (Restrepo-Coupe et al., 2013). To simplify the simulation, soil moisture was initialized with a Direchlet initial condition at near saturation ($\theta = 0.65$). As uptake occurs concurrently with rainfall events, this assumption is a simplification and may delay the onset of water stress. To account for this, a no recharge was set for precipitation events less than 10mm were discarded.

3.3 Results

3.3.1 Location survey

A total of 1,054 trees were surveyed, ranging in DBH from 0.5 – 150.7 cm, with a mean of 7.9 ± 12.0 cm (Fig. 3.2, black markers). The MDS-Mapping algorithm placed 39 “anchors”, (N=1000 iterations, RMSE = 1.4 m). Where previously unrecorded, anchor tree species were identified by local guides. The sweeping point algorithm placed 982 trees within the parcels formed by the anchors. An additional buffer of 2,292 trees were generated for a 80 m x 150 m area, with locations drawn from a standard uniform distribution and diameters drawn from a gamma distribution with shape parameters *a* = 0.4 and *b* = 14, developed from the surveyed individuals. Diameters less than actual measured DBH were excluded, with the final computational domain containing 3,346 individuals with a stem density of 2,788 stems ha^{-1}.

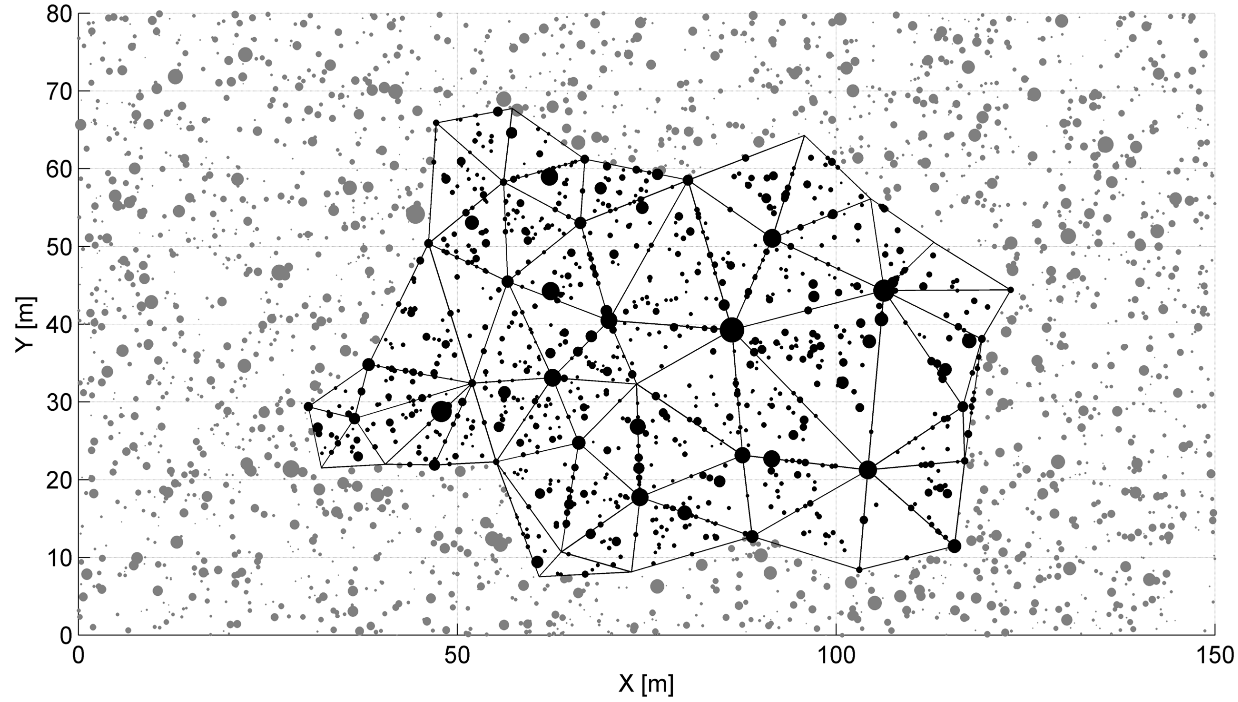

Figure 3.2 Black marker circles represent surveyed trees and gray circles representing planted buffer trees. Marker size is scaled relative to tree diameter at breast height (DBH). Black lines are parcel edges and connect anchor nodes.

3.3.2 Above-ground structure

Tree height and canopy fractions for the survey area are summarized in Table 3.4 and shown in (Fig. 3.3). While large canopy trees (individuals more than 20-30 m tall) are the lowest fraction of the community (~8%), they receive the highest amount of incident radiative forcing (~59%).

Table 3.4 Binned canopy classes with their actual DBH range, light fraction received, and relative population fraction within the domain.

Canopy Class	Height [m]	DBH [cm]	Light Fraction [-]	Relative Fraction [%]
1	0 – 10	0.4 – 5.3	0.17	58.86
2	10 – 20	5.4 – 20.3	0.24	33.27
3	20 – 30	20.4 – 44.4	0.26	6.64
4	30 – 40	44.5 – 77.5	0.25	1.05
5	≥ 40	≥ 77.6	0.08	0.18

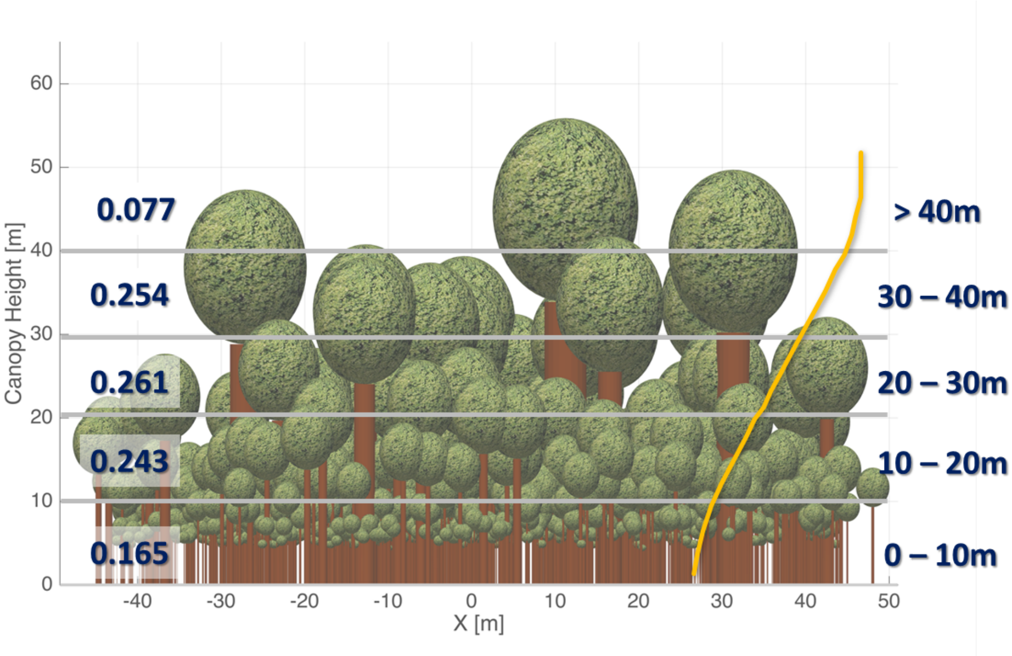

Figure 3.3 Visual schematic of canopy bins. Gray lines demarcate the canopy bins, with heights given on the right. The light fraction is given as values on the left and the yellow line represents the attenuation of incident light throughout the canopy (ranging from [1, 0]).

3.3.3 Below-ground structure

3.3.3.1 Root system spatial extent

Lateral spread was computed for the survey area. Canopy allometry developed by Gonçalves, (2014) (e.g., crown diameter and radius) used a sampling threshold of 10 cm DBH that does not hold for small samples with DBH < 2.5 cm. Consequently, such individuals were assigned a minimum lateral spread of 2 m. As lateral spread is often assumed to be directly correlated with crown radius, allometry-derived lateral spread (Section 3.2.2.3) was compared to multiplicative factors of crown radius (Fig. 3.4a). Allometry-derived lateral spread followed with 3 times the crown radius until ~10 cm DBH (~10 m lateral spread) when the two curves begin to diverge. Lateral spread ranged from 2 – 33.3 m with a mean of 4.33 ± 3.24 m. Approximately 59% of individuals were assigned lateral spread less than 5 m (Fig. 3.4b).

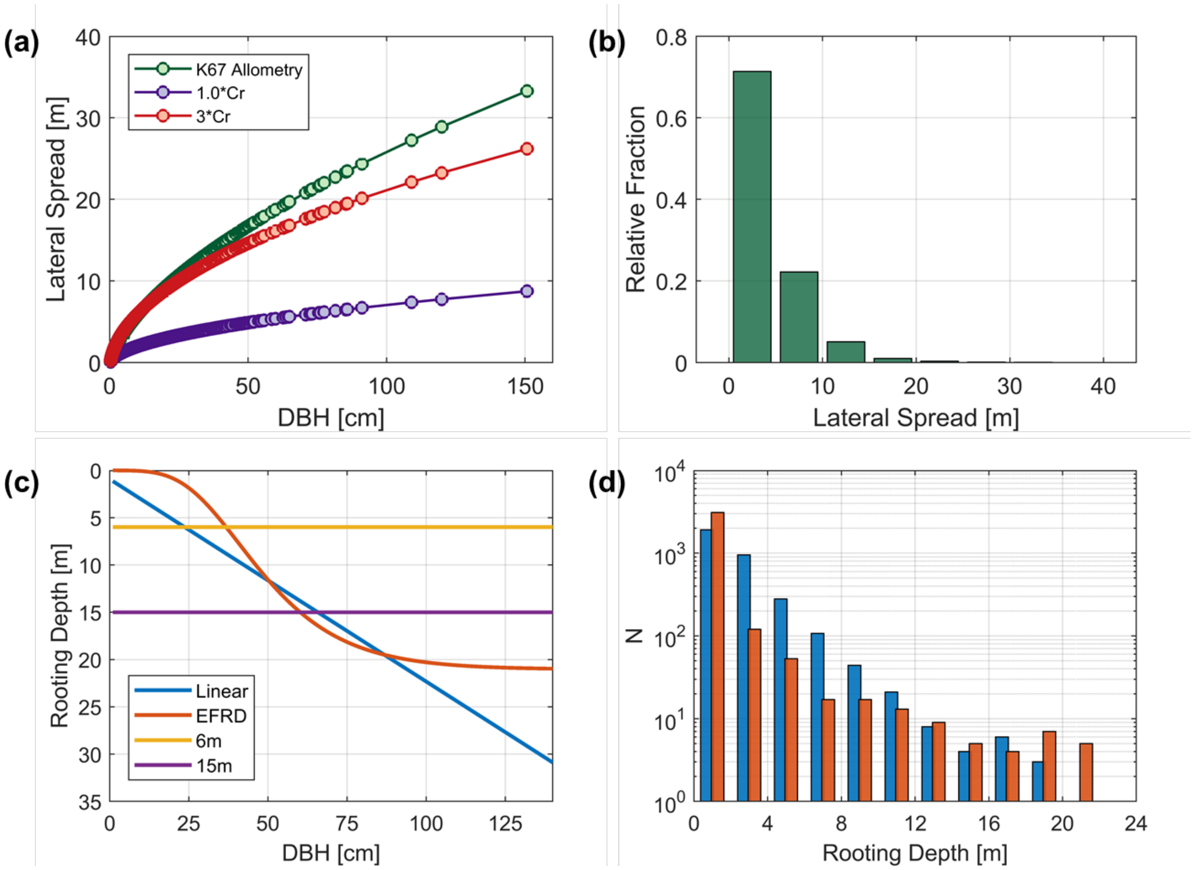

Figure 3.4 (a) A comparison of computed LS where (green) is the allometric LS, (red) is the crown radius multiplied by a factor of 3, and (purple) is the crown radius. (b) Relative fraction of allometric root lateral spreads within the surveyed area. (c) Rooting depth profiles as a function of DBH where (blue) is linear, (orange) is the effective rooting depth from Brum et al (2018), (yellow) is the constant shallow from Ivanov et al (2012), and (purple) is the constant mean from Brum et al.(2018). (d) Histogram of rooting depths for the (blue) linear and (orange) EFRD rooting profiles. Values are shown in log-scale for visual clarity, but the majority of individuals are rooted in the top 1m.

The frequency of linear and EFRD rooting depths are shown in (Fig. 3.4d). The two scenarios follow relatively similar distributions, but differ for depths <10m. The EFRD scenario places more individuals at the shallowest rooting depth of 1m, while the linear rooting scenario distributes these depths more evenly along the 2-8 m depth range. In both scenarios, the majority of the domain resides in the top 3 m of the soil with N ~ O(10^3).

Table 3.5 A random selection of trees across size classes to illustrate variability in lateral spread and rooting depth as a function of DBH.

ID	X [m]	Y [m]	DBH [cm]	LS [m]	EFRD [m]	LIN [m]	UNI [m]
13700	10.58	23.53	1.19	2.00	1.00	1.18	6
13874	40.08	6.77	4.43	3.21	1.01	1.87	6
10396	62.90	54.77	6.05	4.04	1.02	2.22	6
14052	42.59	66.56	8.59	5.19	1.05	2.76	6
13077	131.20	14.81	13.20	6.98	1.19	3.75	6
94	48.77	29.51	15.40	7.75	1.33	4.22	6
10292	91.72	59.09	18.14	8.65	1.60	4.81	6
13003	121.62	23.52	22.30	9.92	2.25	5.70	6
14172	118.58	76.32	23.03	10.13	2.40	5.85	6
14168	121.14	12.85	29.61	11.93	4.22	7.26	6
626	76.41	59.29	31.30	12.37	4.82	7.62	6
14238	119.31	66.63	36.84	13.74	7.01	8.81	6
14047	102.21	70.02	41.02	14.72	8.81	9.70	6
12338	91.30	8.03	43.73	15.33	9.98	10.28	6
14239	90.06	10.30	48.26	16.33	11.86	11.25	6
59	79.99	15.74	52.20	17.16	13.38	12.10	6
12119	56.11	68.96	58.53	18.45	15.50	13.45	6
13829	26.46	46.65	62.69	19.27	16.67	14.34	6
40	91.50	22.71	70.80	20.80	18.45	16.08	6
13786	28.03	21.41	72.43	21.10	18.74	16.42	6
619	62.30	44.27	81.50	22.72	19.99	18.37	6
46	104.19	21.28	85.80	23.46	20.41	19.29	6
14099	44.46	54.18	91.10	24.35	20.82	20.42	6
95	47.88	28.78	109.00	27.23	21.59	24.25	6
679	106.32	44.35	119.90	28.89	21.80	26.58	6
654	86.23	39.28	150.70	33.28	22.00	33.17	6

3.3.3.2 Root traits and distribution

These shallow rooting depths are consistent with observations of root biomass density

(RBD) at K67. Observations of RBD, collected in September 2015, ranged from near zero to ~6,000 g m^{-3}. Observations in the top 5 cm were most variable and subject to the highest error due to predominant root growth throughout the leaf litter layer on the forest floor. The median RBD profile was consistent with the profile reported in Ivanov et al. (2012), derived from data collected during the Nepstad campaigns (Fig. 3.5, left) (Nepstad et al., 2004; Nepstad et al., 1994).

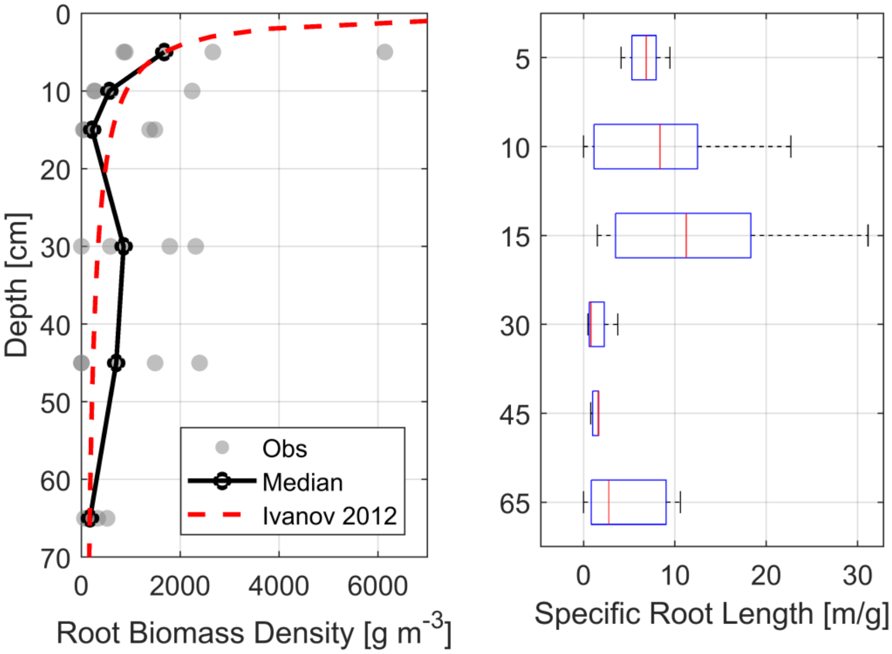

Figure 3.5 (Left) Observations of fine root biomass density with depth from five random locations with observations given as gray markers, with the median plotted as a black line. The observation derived biomass profile used in Ivanov et al. (2012) is in dashed red. (Right) Boxplots of SRL as a function of depth where the red line represents the median, the box boundaries are the 25th and 75th percentile, and the whiskers represent the range.

Specific root length (SRL) was measured concurrently with RBD and during a separate collection campaign in January 2017. SRL measurements done concurrently with soil coring was indiscriminate of species and taken as a bulk quantity (Fig. 3.5, right). Higher magnitudes and variability were observed in the top 15 cm of soil with median values ranging from 6.85-11.2 m

g^{-1}. SRL for 30-65 cm soil depth exhibited less variability and ranged 0.80-2.78 m g^{-1}. Species specific measurements of SRL were taken from excised surface fine roots taken from the top 15cm and are summarized in (Table 3.6). Mean values for the four species ranged from 3.79-11.41 m g^{-1}. The variability found at the species level strongly suggests large degrees of root interaction in the surface layers, consistent with the root distributions and depths previously mentioned.

Table 3.6 Species specific root length measurements collected during the January 2017 field campaign.

Species	DBH [cm]	ρ [g/cm^3]	N	SRL ± STD [m/g]
Erisma uncinatum	149.2	0.51	3	11.41 ± 13.19
Tachigali chrysophylla	77.9	0.57	4	5.55 ± 1.41
Endopleura uchi	46.8	0.79	4	5.90 ± 2.36
Chamaecrista xinguensis	59.8	0.91	4	3.79 ± 1.73

Roots collected during soil coring were photographed and analyzed for length using the ImageJ program. A subset of root lengths measured by the ImageJ macro were hand measured, with an overall root mean squared error of 2.95mm (Appendix 3C). A power regression, $RLD \sim a_1 D^{a_2}$, was fit to the observational median and the 25th-75th percentiles. The observed median SRL was used to convert the RBD profile from Ivanov et al. (2012) to RLD (Fig 3.5, left panel, red-dashed line). The resulting profiles show strong consistency between the two datasets, with RLD tapering strongly in the 10 cm, decreasing from $O(10^4)$ to $O(10^2\text{-}10^3)$ rapidly.

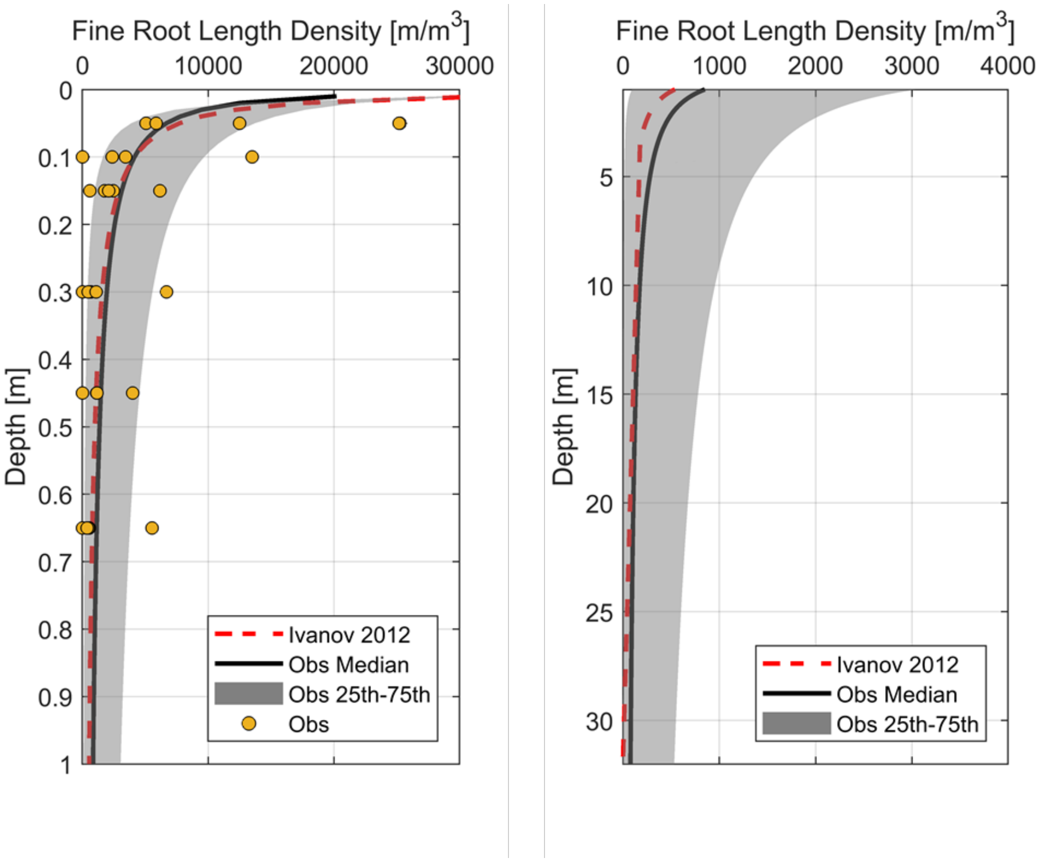

Figure 3.6 Fine root length density profiles for the top 1m (left) and 1-32m range (right). The RLD profile derived from the (Ivanov et al., 2012) RBD profile is in dashed red; the RLD profile derived from the median fit of RBD observations is in solid black, with with the 25-75th percentiles in shaded gray; point observations are given as yellow markers.

The results show a strong preference for roots in the shallow soil layers, greater than that found in the temperate forest system discussed in Chapter 2. The differences in soil texture (hardpan clay of the *terra firme* forest vs. sandy soil at UMBS) and low nutrient densities may contribute to these site-level differences.

3.3.3.3 Modeled root system distributions

Three rooting domains were generated using the derived depth scenarios. Modeled coarse root architectures were planted at surveyed tree locations. Additional fine root length was added to the structures following procedures outlined in Chapter 2. For visualization purposes, simulated RLD profiles are provided for the top 3 m. All simulated profiles fall within the 25-

75th observational profiles (Fig. 3.7) The EFRD shows the highest level of RLD in the surface layer, consistent with the large number of individuals rooted at ~ 1m. Simulated RLD at depths > 3m was < 10^2 m m^{-3} and within the confidence intervals of the given observations.

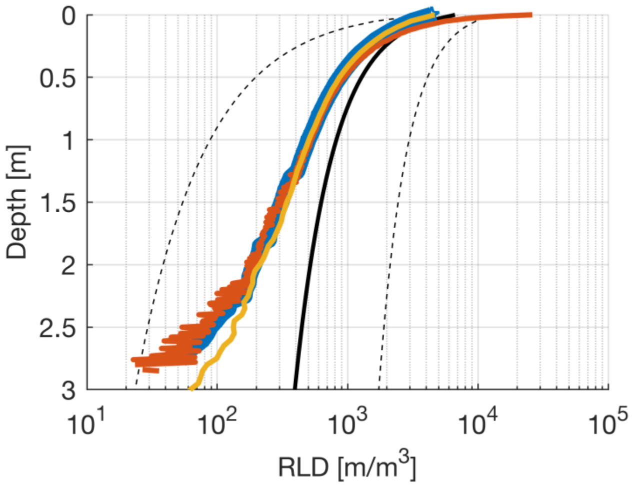

Figure 3.7 Simulated RLD profiles for the linear rooting depth (blue), EFRD (orange), and uniform rooting depth (yellow). The theoretical 25-75th percentiles are shown as black dashed lines and the mean is given in solid black. The RLD x-axis is given in log scale.

The surface spatial distribution of RLD (top 0.5 m) was relatively consistent across the three scenarios (Fig. 3.8). Lateral spread was kept consistent across the three rooting depth scenarios contributing to the similarity between surface spatial distributions. Differences in rooting depth result in some spatial variability in RLD at around 0.5 m which continues throughout the profile. As an illustrative example, volumetric slices are shown for two sample trees (root system IDs 95 and 10292 as summarized in Table 3.5) in Fig. 3.8. Profile slices taken through the sample locations show high magnitude of RLD clustered around stem locations which taper with depth, following the prescribed RLD profiles and a function of individual root architecture. A slice from the XY plane at D = 0.5 m shows some spatial heterogeneity of RLD, consistent with observed variability (Fig 3.6).

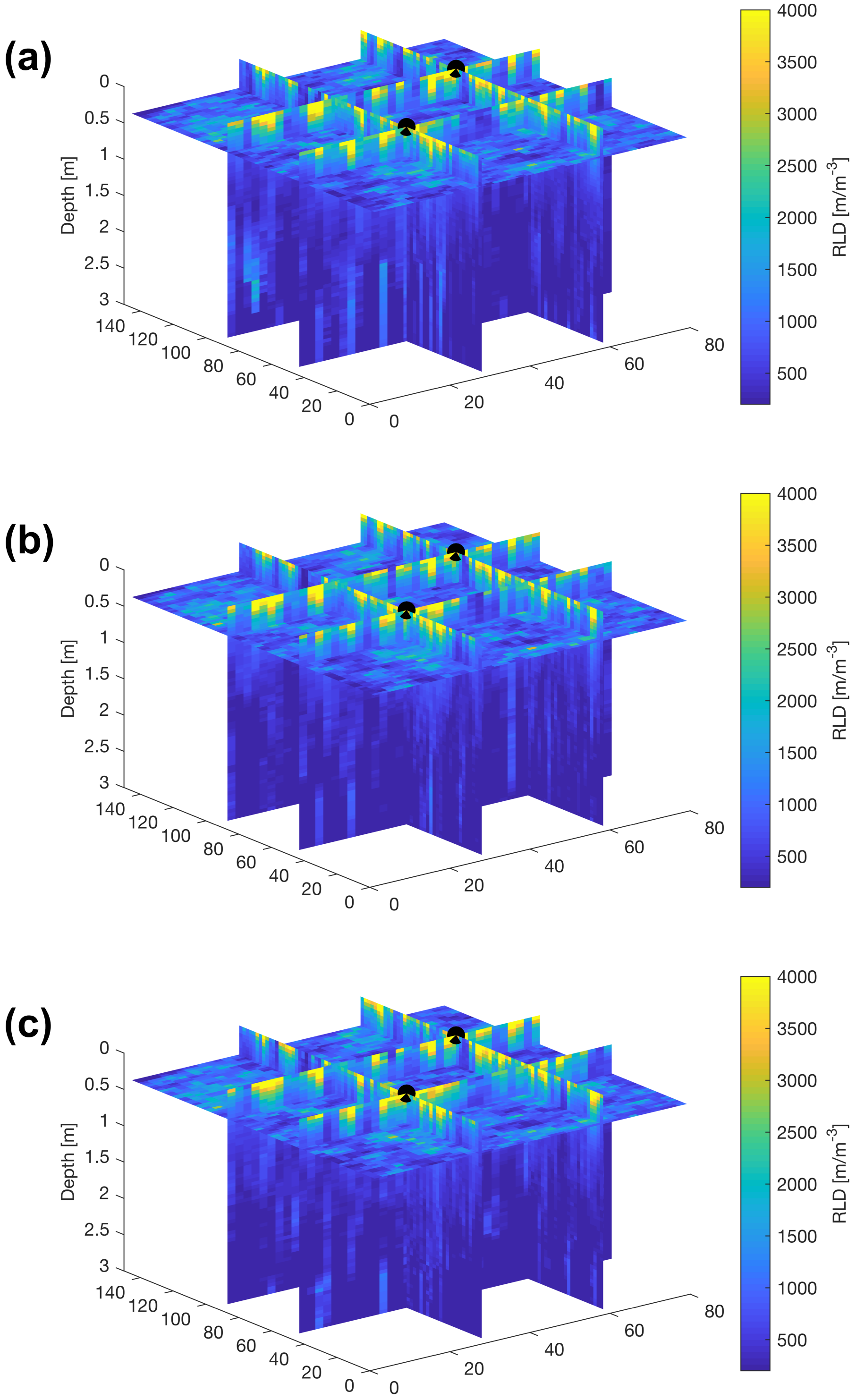

Figure 3.8 Three-dimensional root length density for three scenarios: (a) uniform rooting depth, (b) linear rooting depth, (c) effective rooting depth. The black markers indicate two representative individuals, IDs 95 and 10292 referenced in Table 3.5.

3.3.4 Potential transpiration

The HS PET formulation was used to compute potential evapotranspiration (PET) for K67. The model was calibrated using an objective function which maximized the determination coefficient for all data years available from the K67 eddy covariance tower (parameters: B = -20, C = 2.5). When compared to corrected actual ET from the tower, R-squared values ranging from 0.34-0.74 for the available data years (Fig. 3.9). The weakest performance was found for the simulation period with R^2 = 0.34. It is important to note that this formulation is producing *potential* transpiration given temperature and radiative forcing. Large differences result from periods of water limitation when trees are unable to meet atmospheric demand. The weak performance in 2015 highlights the impact of the 2015-2016 ENSO event on transpiration at K67.

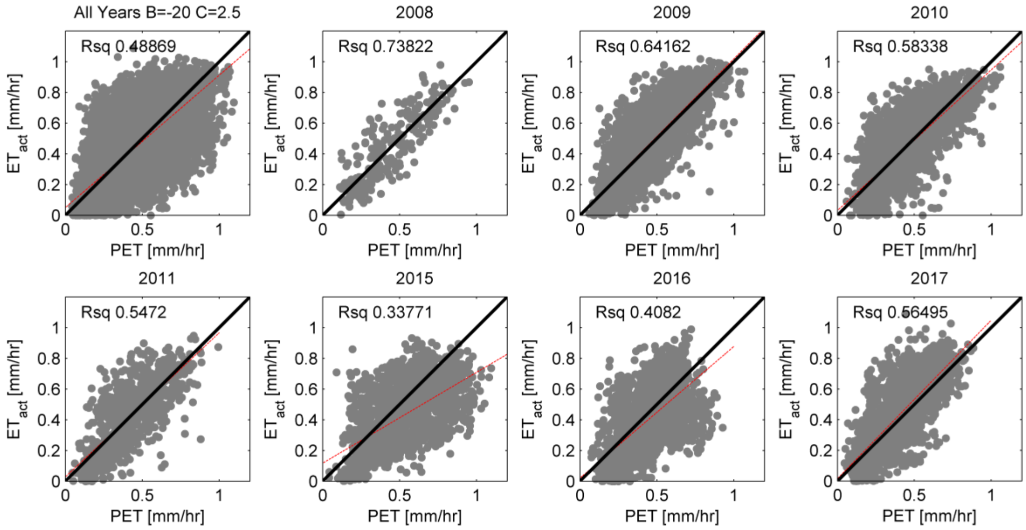

Figure 3.9 A comparison of modeled hourly potential evapotranspiration from the Hargreaves-Samani (HS) method to tower observations of ET for data available years. Data period is given by the plot title. The one-to-one reference line is given in black and a comparison regression line shown in red.

Potential transpiration is assumed to be equal to potential evapotranspiration for the closed canopy and evaporation from leaf storage is considered negligible. The time series of PET for the simulation period shows a steady increase in PET across the dry season period, consistent with increased temperature values which drive the model (Fig 3.10). Daily PET ranges from ~1.5-8 mm. Gaps in the data period were filled with seasonal diurnal mean and are evident in the daily time series as flat periods.

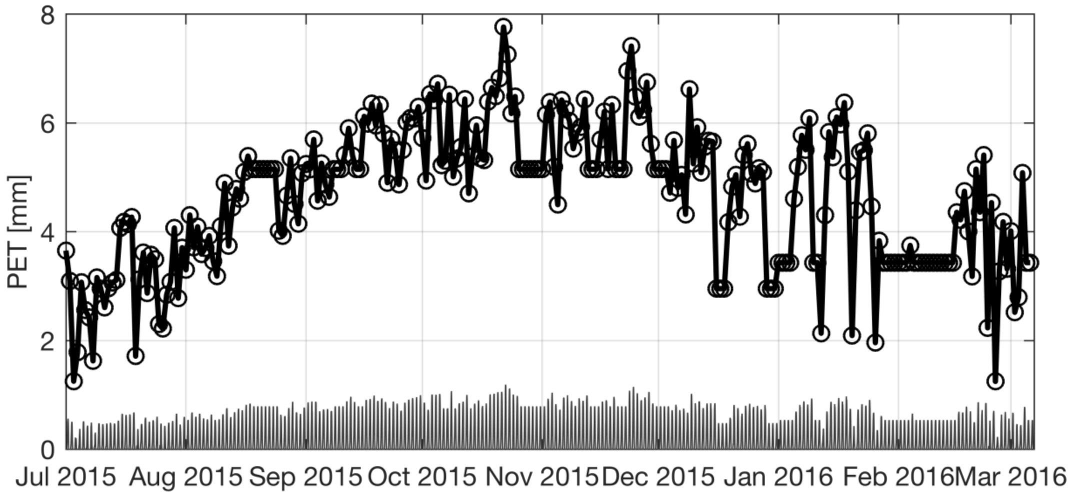

Figure 3.10 Simulated potential transpiration for July 2015 – March 2016. Hourly rates are shown at the plot bottom. Daily totals are given as the bold, markered line.

3.3.5 Simulated water uptake for three scenarios

Root water uptake was simulated using potential forcing from July 2015 – March 2016 for the three rooting scenarios described. Despite the lack of precipitation, atmospheric demand was met across all three scenarios until mid- to late-August (Fig 3.11). The onset of limitation resulted in a shaving of peak uptake magnitudes in the mid-day period from 10:00 – 15:00 local time. Uptake was maintained during water limitation, but at increasingly reduced rates. The onset of water stress first occurred for the linearly scaled scenario, but this difference in onset was only by a matter of a few days.

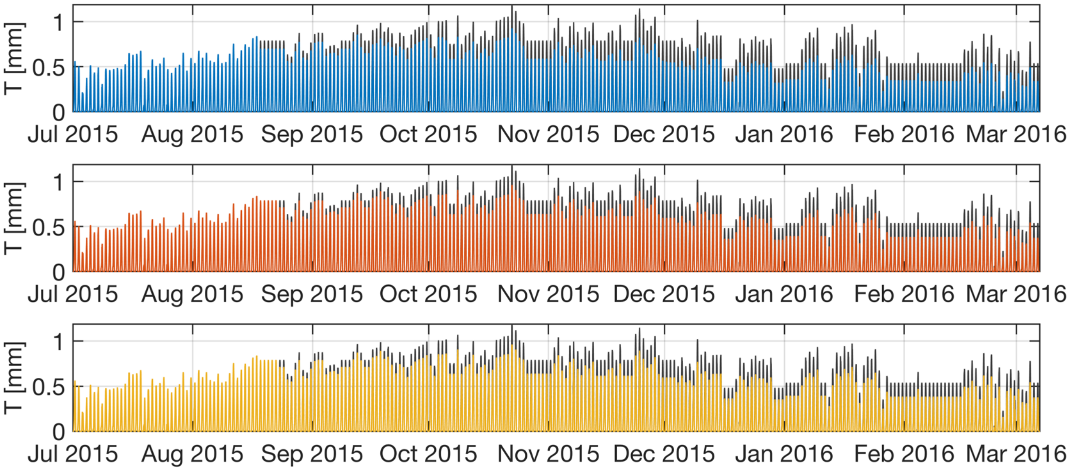

Figure 3.11 Time series of domain scale (all trees) water uptake for the simulation period with colors following previous presentations (linear – blue, EFRD – orange, uniform – yellow). Potential transpiration is given in gray, with different plots indicating scenario: linear (top), EFRD (middle), and uniform (bottom).

Mean diurnal cycles highlight differences in dry season impact of water limitation on the three rooting scenarios (Fig. 3.12). The EFRD scenario maintained the highest rates of uptake with mean daily maximum of 0.6 mm hr^{-1}, followed by the linear with 0.58 mm hr^{-1}, and the uniform at 0.49 mm hr^{-1}. The differences in scenarios are most evident at the highest potential forcing, with the uniform scenario reaching a maximum uptake rate of ~0.8 mm hr^{-1} while the EFRD scenario approaches 1 mm hr^{-1}.

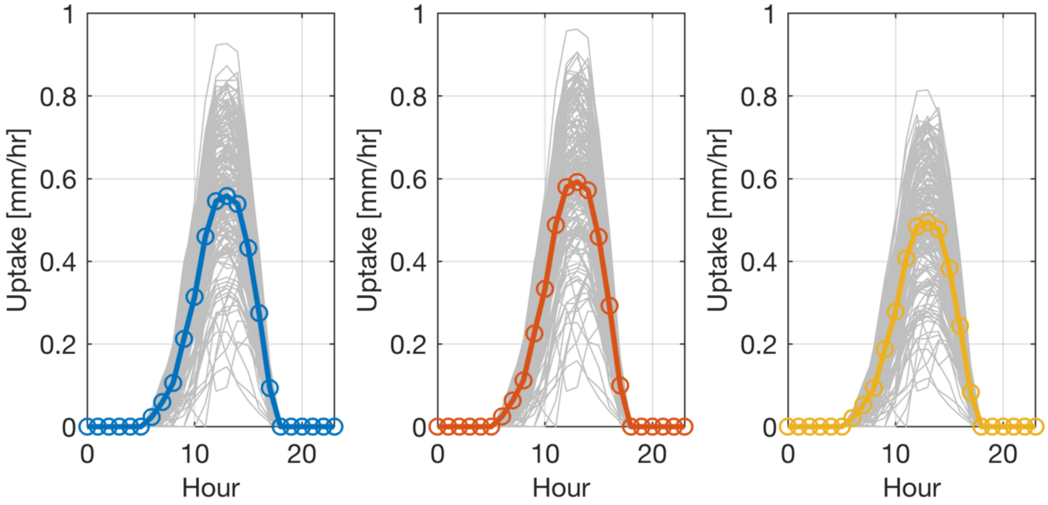

Figure 3.12 Mean domain scale diurnal uptake for the three rooting scenarios with line colors following previous presentations (linear – blue, EFRD – orange, uniform – yellow). Thin gray lines indicate actual diurnal profiles with the different panels representing the different scenarios: linear (left), EFRD (middle), uniform (right).

Reduced diurnal maxima had a significant impact on cumulative water uptake for the domain period (Fig. 3.13). The potential water uptake demanded by the atmosphere for the period was 1,152 mm. While none of the scenarios met this demand, the EFRD scenario met 83% with 956 mm, the linear scenario met 78% with 896 mm, and the uniform scenario met 69% with 800 mm. Divergence from potential was most evident around October, with differences widening across the simulation period.

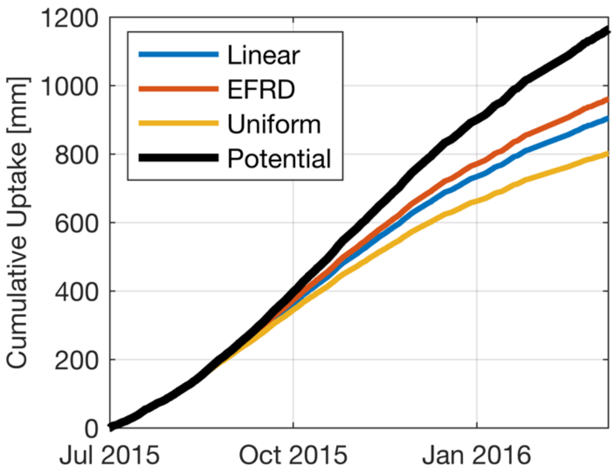

Figure 3.13 Cumulative water uptake across the simulation period for the three rooting scenarios with line colors

following previous presentations (linear – blue, EFRD – orange, uniform – yellow). Potential water uptake is given as the bold black line.

3.3.6 Simulated water potential

The water potential at the root collar was computed for individuals from the different size classes (root IDs 10396, 626, 14168, 59, 46, 654 from Table 3.5). Individuals ranged in size from 6.1 – 150.7 cm DBH with rooting depth ranges of 1.02 – 22.0 m for the EFRD scenario and 1.9 – 33.2 m for the linear scenario. Lateral spreads ranged from 3.21 – 33.28 m. The small trees (< 30 cm) show water potential most closely aligned with soil water potential as shown by the predominant shifting baseline of water potential in (Fig. 3.14). The largest trees, especially 654, show the largest swings in water potential at the root collar. These high magnitudes are consistent with the higher atmospheric demand placed on the canopy tree which is exposed to high levels of radiative forcing.

Between the scenarios, the uniform rooting depth experienced the lowest values of water potential, an accepted proxy of hydraulic stress. The separation of rooting depth and root distribution afforded by the linear and EFRD scenarios increased water potential, lower potential hydraulic stress. Differences in hydraulic state, especially for the small trees, was minimal between the linear and EFRD scenarios.

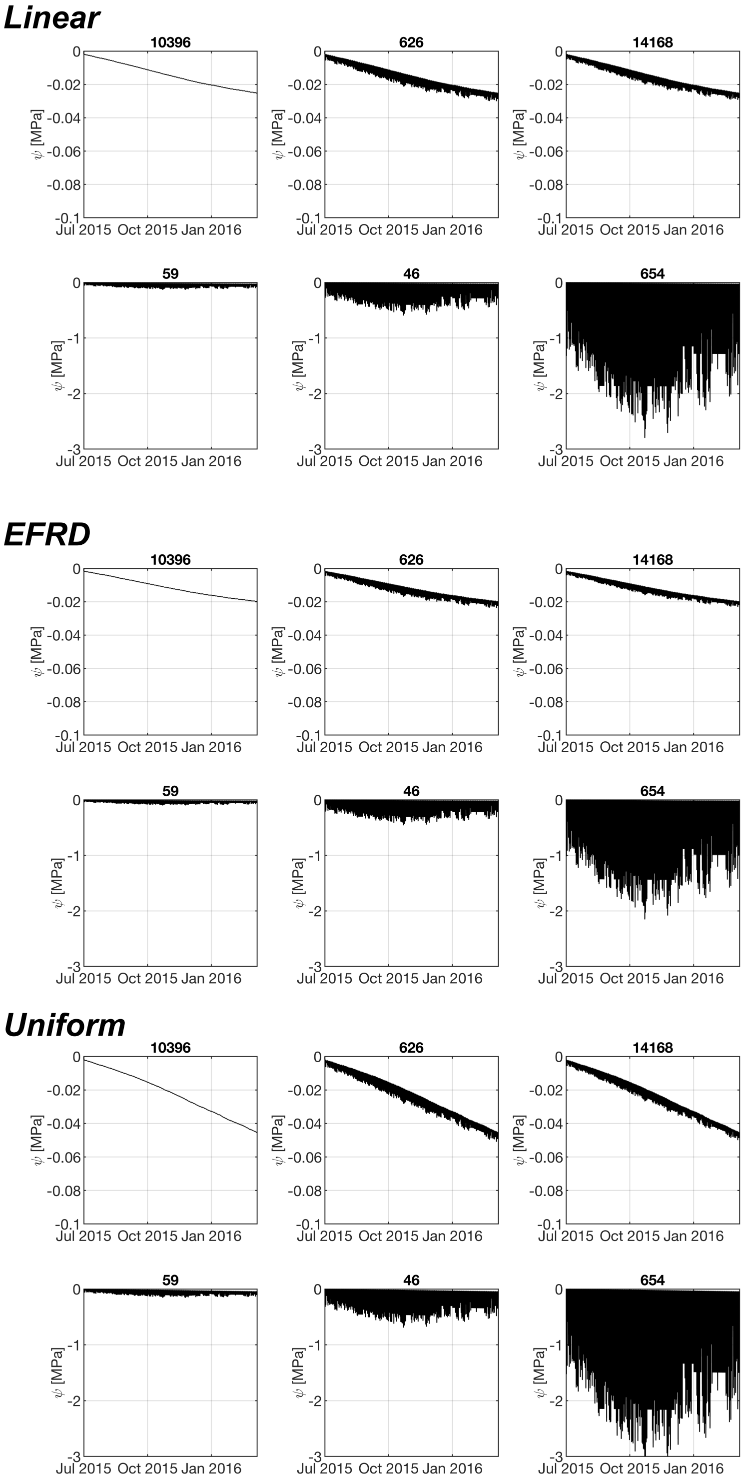

Figure 3.14 Hourly water potential at the root collar for 6 representative individuals. Plot titles give individual IDs referenced in Table 3.5. The different rooting scenarios are demarcated by the plot title, with each scenario showing 6 subplots.

3.3.7 Soil moisture

Soil water content at the beginning of the simulation period was influenced by the initial conditions that were approximated as near saturation, $\theta = 0.60$, with soil water potential values near zero $\psi_{soil} = -4.6E\text{-}6$ MPa. Given the lack of precipitation, mean soil water content experienced a steady decline as surface layers dried. The spatial variability of surface soil moisture varied little between the three depth scenarios, following the spatial distribution of RLD.

The temporal evolution of soil moisture with depth varied most significantly between the uniform rooting depth and the linear/EFRD scenarios. The relative difference [-] in soil water content between the uniform and EFRD scenarios is given by (Fig. 3.15) with the color bar indicating relative differences. The blue values show little difference between the scenarios, while warmer colors indicated where the EFRD was drier than the uniform, indicating a deeper exploitation of water. A demarcation in the temporal profile occurs near 7.5 m due to the uniform scenario's uniform rooting depth of 6 m.

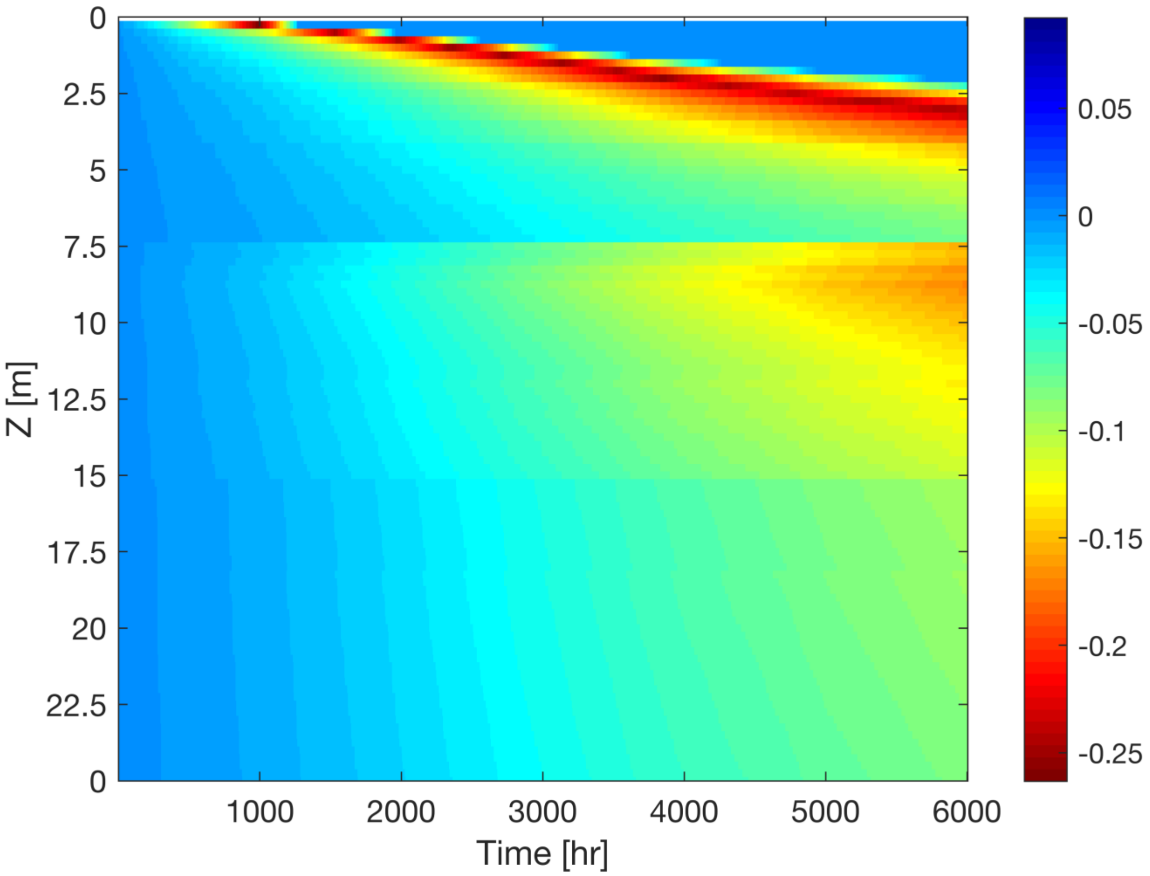

Figure 3.15 The temporal evolution of relative soil water content differences [-] between the uniform and EFRD scenarios. Negative values indicate when soil moisture in the EFRD was less than that found in the uniform scenario.

3.4 Discussion

3.4.1 The onset of water limitation

Consistent with above-ground observations of sap flow and latent heat fluxes the 2015-2016 dry season from K67, water uptake was constrained due to the onset of water limitation in the shallow soil layers. The onset of water limitation occurred approximately 1.5 months following the introduction of the no precipitation condition in the simulations with slight variations following rooting strategy. While it is unclear whether the precise timing of water limitation is congruent with actual site conditions, it provides a valuable estimation of potential limitation in the system. Potential differences can be attributed to initial conditions such as near saturated soil moisture (set as a uniform Dirichlet initial condition in the model) throughout the soil profile and forcing provided by the HS PET method.

Without precipitation to alleviate water stress, water uptake remained constrained during the simulation period. Given consistencies in surface layer soil moisture between the different scenarios, there were no appreciable differences in root system processes such as hydraulic distribution which could potentially alleviate some of the surface layer stress (Oliveira et al., 2005b). While the PFLOTRAN-Root model does capture hydraulic redistribution, large values caused by overly sharp potential gradients are constrained. Despite the limitations of the model, results are consistent with evidence of the 2015-2016 impact of the ENSO dry season on tree scale water dynamics (Brum et al., 2018).

3.4.2 Impact of functional strategy on stress

While the onset of water limitation occurred around the same time for all three rooting scenarios, the magnitude of impact was determined by the functional strategy of the individuals in the community. Segregation of rooting depth by either linear scaling or by the effective rooting depth scenario allowed individuals to tap access different soil water reserves at the different portions within the soil. This access did not allay constraint of water uptake, but instead reduced the overall impact of it by allowing individuals to maintain higher rates of uptake during this period. The shift of the centroid of uptake into deeper layers is a function of the potential gradients found within the soil and is shown to consistently contribute to water uptake during water limitation across climate types and soil textures.

In the previous chapter, root lateral spread was found to be a significant driver of water uptake into deeper layers of the soil. Site level allometry, coupled with the high stem density within this domain, found high degrees of lateral interaction across various lateral spreads (Fig 3.16). Given this degree of high interaction, lateral spread was kept constant across scenarios, an effort to isolate the impact that rooting depth has on water uptake within the domain.

Water potential at the root collar was not constrained in these simulations, meaning that no stomatal controls on water uptake were implemented. The high functional diversity of the tropical rainforests presents a variety of stomatal control strategies ranging from highly isohydric (maintaining a constant leaf water status under a changing soil water supply) to highly anisohydric (allowing leaf water status to vary as soil water supply varies) (Barros et al., 2019; Fisher et al., 2006; Fontes et al., 2018; Gimenez et al., 2019). The implementation of these controls could further constrain uptake for some individuals, while allowing others to capitalize on the increased soil water reserves left unexploited by those playing it safe during water limitation. This could be especially evident in the larger trees which experience larger swings in water potential at the root collar due to high atmospheric demand. The root collar potential of smaller trees are dominated by surface soil water potential rather than atmospheric demand. Uncertainty in soil water potential due to soil characterization or rooting distribution could further impact these results.

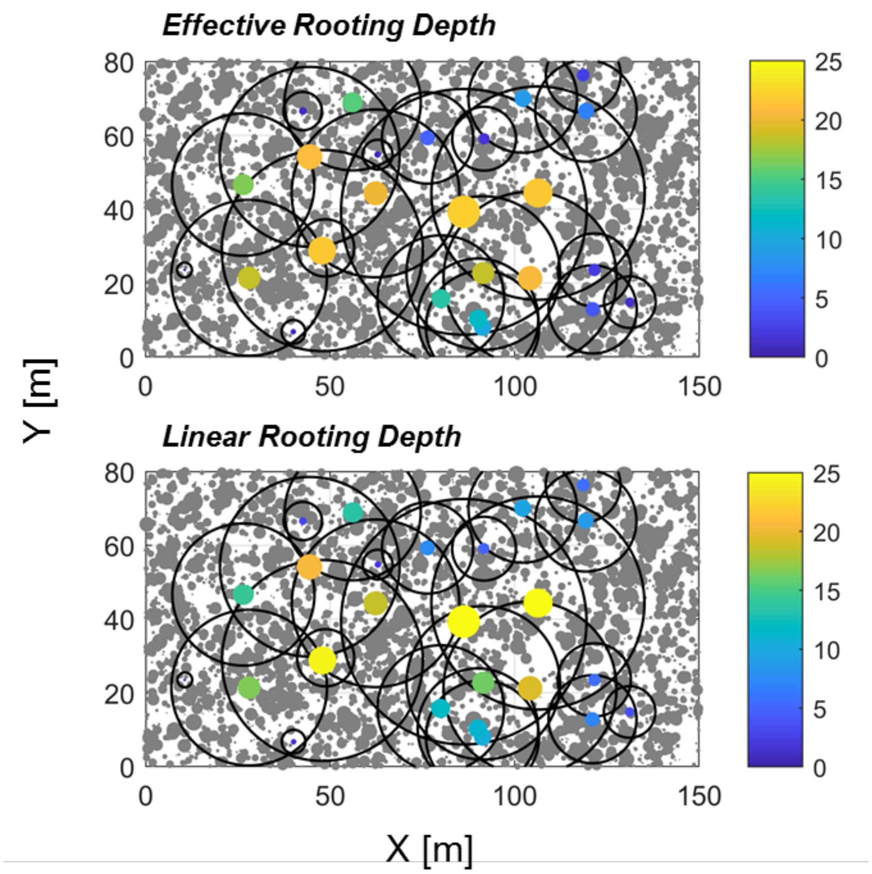

Figure 3.16 Illustrative example of computed root lateral spreads for sample trees given by Table 3.5. Gray markers indicate stem locations within domain with size relative to their DBH. Black circles indicate lateral spread and the colored markers indicate rooting depth for the listed scenarios, magnitudes as given by the color bar.

3.5 Summary

This chapter presents the impacts of root functional strategy on water uptake dynamics during the 2015-2016 ENSO dry season in a highly seasonal tropical rainforest. High stem density and functional diversity present large challenges for representing individual water uptake processes. Different scenarios of root structural diversity, largely represented through rooting depth, high differences in the onset of water limitation and the degree of impact dependent on strategy. Partitioning of roots into different depth classes dependent on size helps alleviate the impacts of water limitation by allowing individuals to tap into separate soil water reserves, reducing the overall hydraulic stress of the system as monitored by root collar potential.

Appendix 3A MDS-Mapping

Multidimensional scale mapping (MDS-Mapping) uses principles of graph theory to extract coordinates from completed connected graphs (Oh et al., 2010). In this case, each anchor tree represents a node and the parcel boundaries represent edges. The distance matrix, *D*, is a *n* x *n* matrix which gives the non-directional distance between graph nodes i and j.

$$D = \begin{bmatrix} d_{11} & \cdots & d_{1n} \\ \vdots & \ddots & \vdots \\ d_{n1} & \cdots & d_{nn} \end{bmatrix}$$

Given a complete distance matrix, we can extract X-Y coordinates (up to translation, rotation, and reflection) for all members of the matrix. Yet, as in this case, the exact distance between all anchors is unknown. When incomplete information exists, estimates of distance can be used in place of actual distances. The distance estimator matrix, $\widetilde{D_{ij}}$, uses the shortest path between nodes in place of an edge. The shortest path was determined using Dijkstra and is the sum of the connected edges which bridge two unconnected nodes. Random Gaussian noise was added to estimated distances to reduce error, such that $\widetilde{D_{ij}} = d_{ij}^2 + \varepsilon^2$, for $i \neq j$ and zero for $i = j$. The RMSE was calculated using distances from the generated X-Y coordinates and those measured in the field. The MDS-Map algorithm was iterated until RMSE was minimized. Additional rotational and translational adjustments were made, but these are superficial, and have no impact on the RMSE.

For individuals within the triangular parcel, insufficient data was available to apply MDS-Mapping or more common trilateration methods. Instead, a sweeping point algorithm was used which placed parcel trees by “sweeping” through all possible points created by the arc of the measured distances and using minimization to find the closest coordinate which satisfied the conditions of both measured distances. The parcel tree was placed at the midpoint of the distance between the two circles. If measurements were exact, this point would be the intersection of circles with radius of measured distance, but as the measurements have associated error, exact intersections do not exist which satisfy both distances.

The simulation domain was filled by planting buffer trees around the actual measured parcels. These buffer trees remove potential edge effects and provide spatial interactions for edge trees. Measured DBH was fit to a gamma distribution ($\bar{x}$ = 7.84cm, σ^2 = 47.05, a = 1.308, b = 5.998). X-Y coordinates were randomly selected from a uniform distribution, with DBH randomly pulled from the fit gamma distribution. DBH values < 0.35cm were excluded as this is outside the recorded range. Individuals were pulled until the stem density of the expanded domain matched the original measured area with 2788 stems ha^{-1}. A comparison of the relative frequency between randomly drawn and site measured DBH shows good agreement (Fig. 3.17)

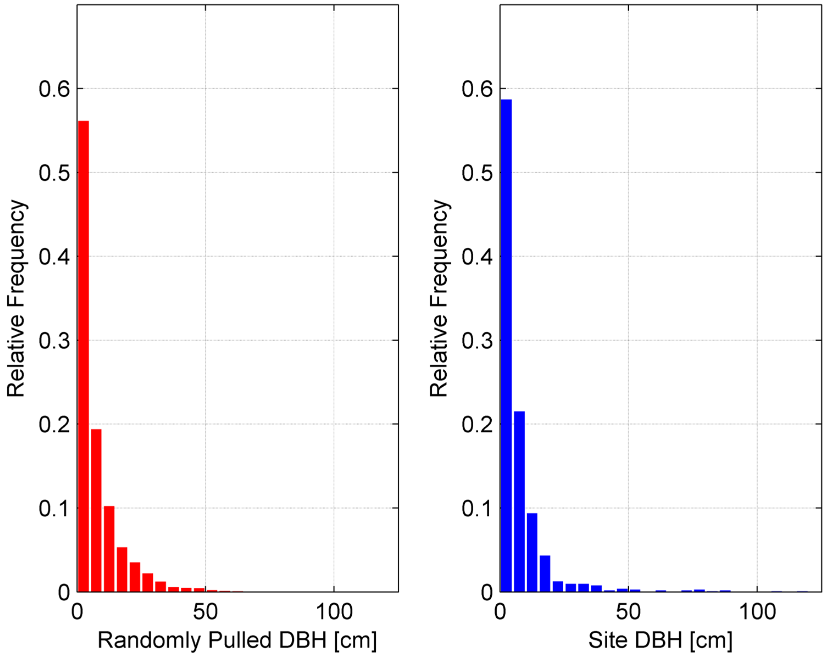

Figure 3.17 (Left) Relative frequency of tree DBH pulled from a gamma distribution fit to measured values. (Right) Relatively frequency of tree DBH as measured within the triangular parcels.

Appendix 3B Independent measurement verification

Domain mapping and structure

Tree height computed from allometry was compared to measurements taken at the K67 field site. Overall, measurement agreement was high, with the largest discrepancies occurring for larger trees (>25m). This disagreement can be partially attributed to the higher measurement error for large trees caused by tree-top occlusion, variability in ground slope, and obstacles in measuring distance (Hunter et al., 2013).

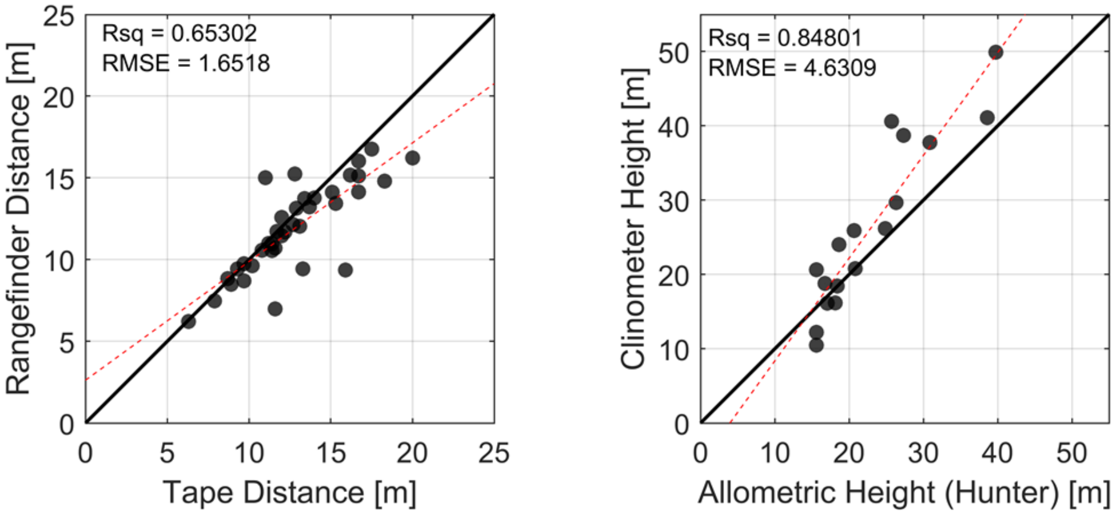

Figure 3.18 (Left) Comparison of distances measured by flexible tape and a laser rangefinder. (Right) Comparison of tree heights derived from allometric equations and those measured at the K67 site during the 2017 field season.

Precipitation adjustments

Two rain gages (Onset HOBO RG3-M) were installed on a canopy walk-up tower in the vicinity of the K67 EC tower. Output from the two gages (Fig. 3.19, right) and the EC tower rain gage were compared (Fig. 3.19, left). The two walk-up gages were in near perfect agreement, while the EC tower rain gage was found to be less reliable than the walkup gages. The EC tower rain gage overestimates daily precipitation, but has longer temporal coverage. To account for the overestimation, EC precipitation values were scaled using a simple linear regression between the EC tower rain gage and the walk-up tower rain gage, with slope 0.584 and intercept -0.053.

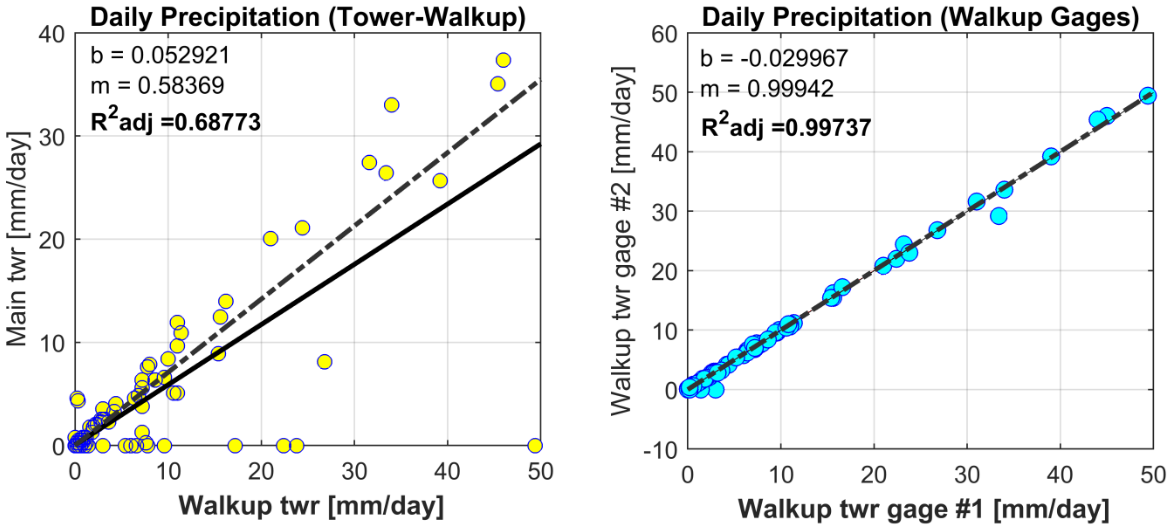

Figure 3.19 (Left) Linear scaling relationship between the walkup tower rain gage and the main EC tower rain gage. (Right) A comparison of the two walkup tower rain gages showing nearly perfect agreement.

Appendix 3C Root image analysis

Live roots were separated from the soil and dyed using methylene blue pigment. Roots were separated and placed in a tray filled with a shallow layer of water. Images were taken of the roots and a 5 cm forensic ruler using a Canon MODEL DSLR camera (Fig. 3.20, left). Images were analyzed using a plugin for the ImageJ (version 1.50i) program, IJRhizo (Pierret et al., 2013, https://www.plant-image-analysis.org/software/IJ_Rhizo). IJRhizo batch processes a collection of images, measuring individual segment length and diameter.

A subset of root images were selected for hand measurement to validate the results produced by IJRhizo. The following work was conceived and supervised by E. Agee and performed by J. Yu under the University of Michigan Undergraduate Opportunities Program. The initial results showed a gross inflation of root length compared to measurements obtained using the hand measurement tool available in ImageJ (Fig. 3.20, right). The gross inflation by IJRhizo was attributed to versioning errors which left certain thresholds and corrections (e.g., Kimura estimation) disabled. Without these thresholds in place, thicker diameter roots (~2 mm) produced erroneous micro segments which inflated total length. Linear scaling was an effective means of correction, reducing RMSE from 82.83 mm to 2.95 mm.

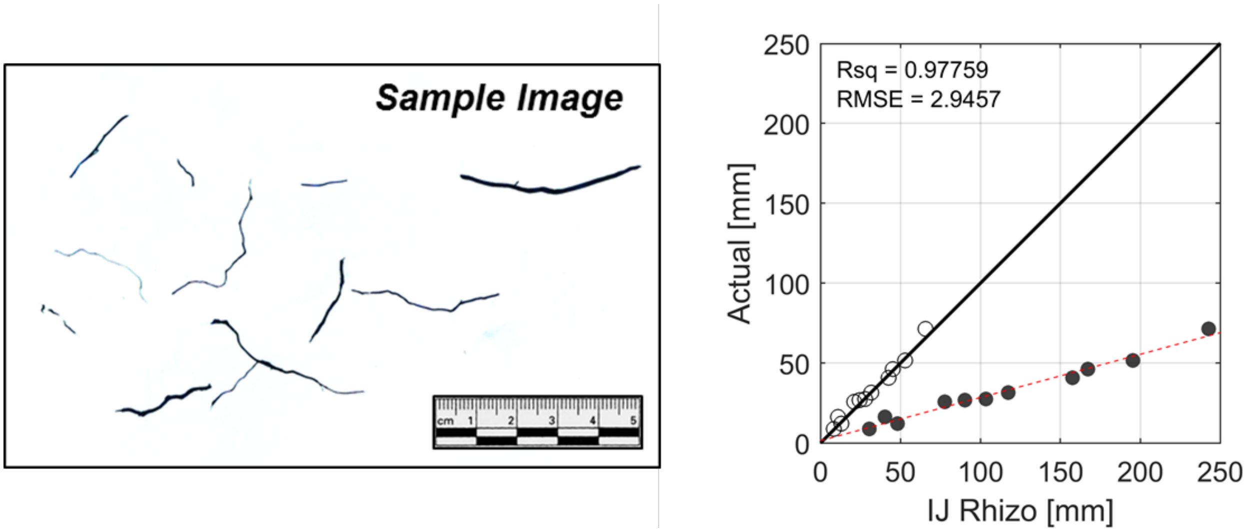

Figure 3.20 . (Left) Sample image of fine roots taken from soil core at K67. Images like this provide the input into IJRhizo. (Right) A comparison of results obtained by hand measurement and the IJRhizo plugin, where closed markers represent the actual comparison and open markers represent linear correction using the red-dashed linear relationship, m = 0.270, b = 1.456. Final RMSE was 2.95 mm, $R^2 = 0.98$, and $p < 0.001$.

As hand measurement of root lengths is time consuming and unique scaling calibrations may be required for each image set, the open-source IJRhizo macro was redeveloped to improve estimations without the need for linear scaling. The new macro uses the same principles as IJRhizo: the image is first pre-processed to remove impurities, roots are reduced to 1 pixel wide lines (i.e., skeletonized), the pixels counted, and then a pixel-length conversion applied (Fig. 3.21). While the underlying framework is the same, the new macro automatically identifies “problem roots” (i.e., thick diameter roots) and excludes them from initial measurement. These thick roots are marked for later measurement by hand. Results obtained from the new macro for the same subset of images further reduced RMSE to 0.33 mm.

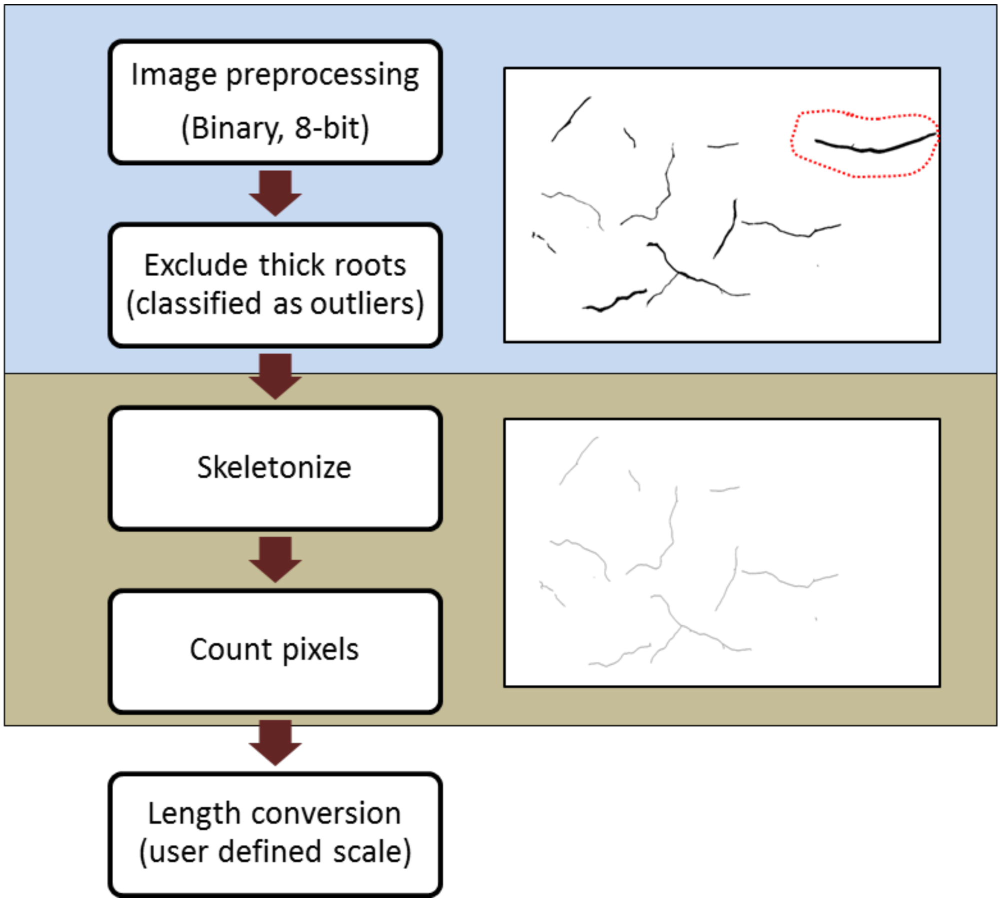

Figure 3.21Workflow of root image processing from raw image to file length measurement using the ImageJ macro developed by J. Yu.

Chapter 4 – Utilizing Sap Flow Technology as a Proxy for Plant Hydraulic State

4.1 Introduction

While it has been demonstrated that below-ground structure and function have coherent feedbacks with plant water uptake under water limitation, *in situ* measurements of below-ground processes are logistically difficult and infeasible. As such, we rely on above-ground proxies to deduce individual and system response to environmental stressors. The measurement of sap flow velocity has become a powerful tool for quantifying individual water usage and response to environmental conditions and has proliferated with the development of technologies that allow for large scale deployments at a relatively low cost (Davis et al., 2012; Miner et al., 2017) . The sap flow database, SAPFLUXNET, contains data for more than 160 species across 120 globally distributed sites (Poyatos et al., 2016), further highlighting the utility of such measurements across an array of climate types and species.

The measurement of sap flow is not without its challenges. Conversion of sap flow velocity to tree- and stand-scale transpiration is dependent on species-specific anatomy (Clearwater et al., 1999; James et al., 2002) and local environmental conditions (Oishi et al., 2008). A large body of research has been devoted to correcting raw signals for these factors, at diel and seasonal time scales (Reyes-Acosta et al., 2012; Vandegehuchte & Steppe, 2012; Vergeynst et al., 2014). Yet, it is these “dependencies” that contain information about the physical state of the system, beyond the quantification of water fluxes. The results from Chapter 3 illustrate that functional diversity is important for the maintenance of water uptake during water limitation, but the data available to assess this trait space is scarce and logistically challenging to measure. This chapter addresses the following research questions: (1) Given the inherent difficulties in assessing below-ground trait space, can we use more accessible above-ground traits as proxies for plant hydraulic state or strategy? (2) How do trees at the K67 site, with differing functional strategies, respond to the extreme 2015-2016 ENSO drought?

To address these questions, this chapter presents the current theoretical framework behind sap flow measurement and its potential relationship to plant hydraulic state. Laboratory experiments are used to provide experimental confirmation of the theory. Continuous measurements of sap flow from the K67 site are then deconstructed to illustrate how previous correction methods have masked a low-frequency signal that provides valuable information about the hydraulic status of the measured individual.

4.2 Sap Flux Theory

4.2.1 Thermal dissipation probes

The dual probe sap flow measurement system, also referred to as thermal dissipation probes (TDP), Granier, or the heat dissipation method, is based on liquid heat dissipation theory (Granier, 1985). Two small gauge needles, one heated and one not, are inserted into the sapwood of a tree approximately 10-15cm apart. Thermocouples within the needles measure the difference in temperature between the heated and unheated reference needle. The probes are at sufficient distance from each other that the reference needle does not detect heating caused by the heater needle. As flow velocities increase, heat is dissipated away from the reference needle with greater efficacy, decreasing the temperature difference between the two needles. At zero flow, the time when no transpiration is occurring, the temperature difference between the two needles is the highest as little heat is being dissipated away from the heater needle.

To translate measured temperature differences into sap velocities, Granier fit a weakly nonlinear regression, with coefficients determined by the heating power used and the medium. Average sap flow velocity, V, follows the form:

$$V = \alpha \left(\frac{dT_M - dT}{dT} \right)^{\beta} \tag{4.1}$$

where dT_M is the baseline or zero flow temperature difference, dT is the temperature difference of flowing sap, and α and β are fitting coefficients [-]. The variable α is a function of the heating power applied, while β is a fitting coefficient. The original calibration experiments performed by Granier using 0.2W heating power found the coefficients to follow:

$$V = 34.92 \left(\frac{dT_M - dT}{dT} \right)^{1.231} \tag{4.2}$$

where V is reported in units of [cm hr^{-1}]. These coefficients were corroborated by experiments summarized by Kostner et al. (1998) and have been used to determine sap flow velocity across many study sites and species (Matheny et al., 2014). Total volumetric sap flow is found by multiplying the average sap flow velocity by the cross-sectional area of sap conducting wood.

While initially proposed to be generic, Granier's coefficients have been found to underestimate sap velocities in several species. Species specific calibrations have been developed (Sun et al., 2012), along with general corrections that account for contact with inactive xylem elements (Clearwater et al., 1999; Paudel et al., 2013). Sun et al. (2012) found α coefficients ranging from 34.92-97.92 cm hr^{-1} and β coefficients from 1.336-2.572 for six juvenile temperate tree species. In general, the resulting calibration curves did not diverge greatly from Granier's proposed values, except for *Ulmus Americana*, which showed a strong nonlinear divergence from the original coefficient curve.

A standard heating power of 0.2W is used for TDP, a value which arises from the original work conducted by Granier (1985), a compromise between measurement sensitivity and the desire not to heat the reference needle (Lu et al., 2004). As such, calibrations in literature are generally specific to the 0.2W heating power. Reducing this heating power would reduce power consumption, a priority for remote deployments, but how lower heat affects signal is currently unknown and partially addressed by this work.

4.2.2 Thermal conductivity and sap flow signals

The transport of heat within the xylem and surrounding woody tissues is a function of internal tissue thermal conductivity. Thermal conductivity of wood is a function of stem water content, with moister tissues conducting heat more efficiently than drier tissues. However, stem water content has been shown to change at both diel and seasonal scales (Mares et al., 2016; Matheny et al., 2015; Vergeynst et al., 2014). Oishi et al. (2008) proposed a protocol for determining the zero baseline, dT_M, to correct for both this and potential nocturnal transpiration fluxes in long term time series. dT_M is selected by simultaneously satisfying conditions of minimal atmospheric water loss and stable maximum temperature difference, dT, across four measurement days.

Mean daily dT_M was compared to theoretical values derived from thermodynamic theory. (Vergeynst et al., 2014) presented the theoretical development for these changes as a function of wood dry density, ρ_d, and θ, and is summarized below. Water content of green wood is defined as the ratio between fresh wood mass, m, and dry wood mass, m_d:

$$\theta = \frac{m-m_d}{m_d} \tag{4.3}$$

From Vergeynst et al. (2014), the zero flow temperature difference, as a function of water content is defined as:

$$dT_{M,\theta} = \frac{Q}{4\pi l K_\theta} \ln\left[\frac{4K_\theta t}{r^2 \rho_\theta c_\theta}\right] - \frac{\gamma Q}{4\pi l K_\theta} \tag{4.3}$$

where Q is the heating power in [W], l is the length of the needle [m], K_θ is wood thermal conductivity [Wm^{-1} K^{-1}], ρ_θ is wood density [kg m^{-3}], c_θ is specific heat capacity [J kg^{-1} K^{-1}], $\gamma = 0.5772$ is Euler's constant. The specific heat capacity is given by:

$$c_\theta = \frac{\rho_d c_d + c_w(\rho_\theta - \rho_d)}{\rho_\theta} \tag{4.4}$$

where $c_d = 1200$ [J kg^{-1} K^{-1}] is the specific heat capacity of dry wood, and $c_w = 4186$ [J kg^{-1} K^{-1}] is the specific heat capacity of water. The thermal conductivity of wood above fibre saturation point is defined as:

$$K_\theta = K_w(\theta - \theta_{FSP})\left(\frac{\rho_d}{\rho_\theta}\right) + 0.04186(21.0 - 20.0\, F_{V,FSP}) \tag{4.5}$$

where void fraction at fiber saturation point is $F_{V,FSP} = 1 - G\left(\frac{\rho_\theta}{\rho_{CW}} + \theta_{FSP}\right)$, moisture content at fibre saturation point is $\theta_{FSP} = 0.2\left(\frac{\rho_d}{\rho_w}\right)^{-0.5}$, G is the specific gravity of wood or the ratio between dry mass over fresh volume over fresh wood density, the thermal conductivity of water is $K_W = 0.5984$, and cell wall density ρ_{CW} = 1530 [kg m^{-3}]. The fibre saturation point is the water content at which all free water has evaporated. For most wood fibre saturation point occurs at 25-30% gravimetric water content.

4.2 Methods

4.2.1 Adjustments for heating power

A low power TDP system was designed to reduce energy consumption for long-term, remote deployments (Dr. Yuriy Goykhman, electrical engineer). While the traditional Granier design uses a constant 0.2W heating source, the new system allows for smaller, user-defined heating powers, reducing overall power consumption for remote deployments. Onboard operational amplifiers boost raw signals (typical gain ~100), resolving potential signal attenuation across cable lengths and decreased heating powers. Control is resolved at the scale of individual trees, with each sap flow probe connected to an independent logging system. Data are recorded on flash media and operations controlled by a ATMega328P-based microcontroller (Arduino Uno Rev3).

To test the impact of variable heating on sensor output, an artificial stem apparatus was constructed using a 4” diameter PVC dry packed with fine sawdust. A 30 mm, a single thermocouple TDP (TDP30, Dynamax, USA) was installed in the side of the apparatus and connected to the self-manufactured data logger (Fig. 4.1a). The heating needle was installed reverse from field conditions to account for the reverse flow of the apparatus.

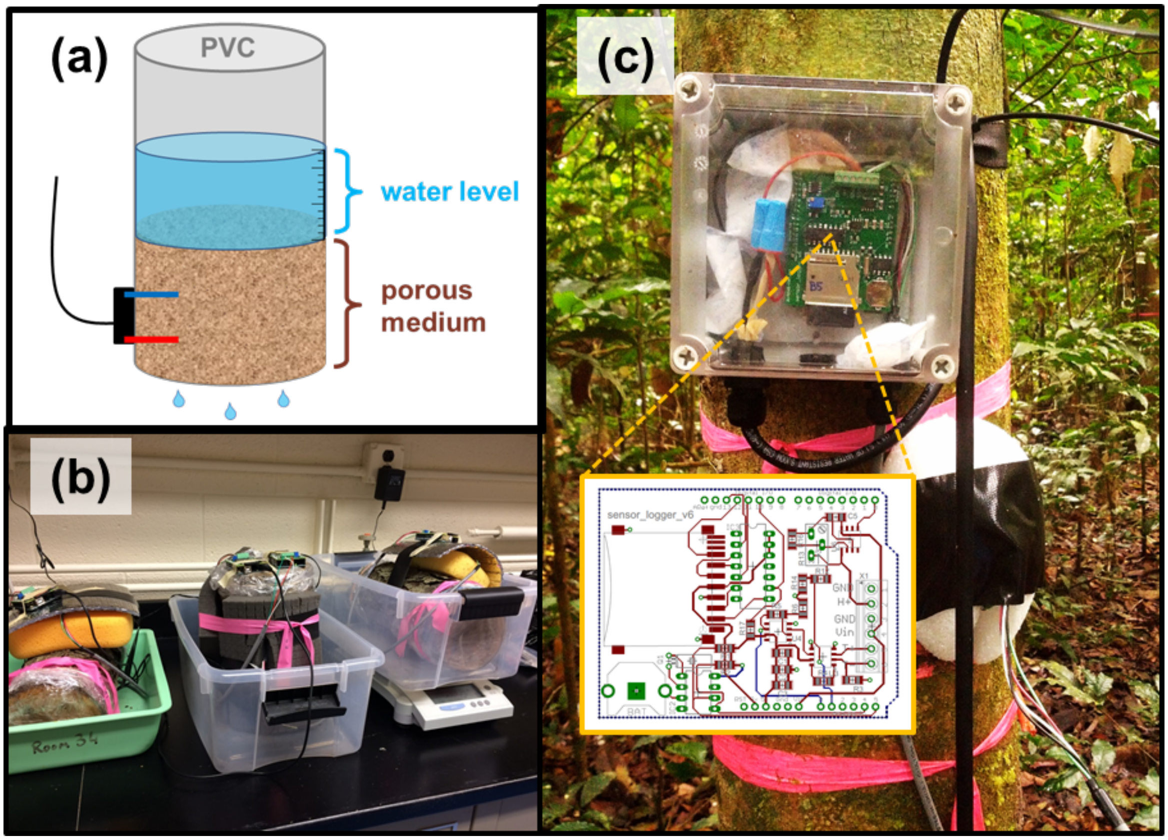

Figure 4.1 (a) Schematic for the artificial stem apparatus. (b) Instrumented, cut oak segments used in drying experiment. (c) Field installation of a TDP probe in Tapajos National Forest, Brazil (photo: Greg Ewing) with (inset) circuit board schematic from new low-power datalogger/control system (credit: Y. Goykhman).

A series of heating powers (0.018-0.170 W, variable step) were applied under no flow conditions. The stem column was saturated and flow obstructed at the base. Heating was applied for at least 15 minutes prior to data collection, allowing the system to reach thermal equilibrium. Sensor output was recorded at a 0.1 Hz for 2 minutes. dT_M was computed as the mean signal value for the 2 minute interval.

The original TDP sensor was calibrated using a heater power of 0.2W. Eq. 4.3 shows that the baseline voltage dT_M is scaled by the power Q. The scaling hypothesis is tested using data from the no flow experiment, which is assumed to be under saturated conditions. An adjustment factor can be presented as the ratio between the Granier heating power, $Q_G = 0.2\text{W}$, and the user-defined heating power, Q:

$$\tau = \frac{Q_G}{Q} \tag{4.6}$$

The adjustment factor accounts for differences in heating power across the experiments and places all measured values in a common basis.

4.2.2 Dehydration experiment

The moisture content of wood alters its thermal conductivity, with moister wood conducting heat more efficiently than dry wood. A large branch was removed from a healthy *Quercus* spp. tree, cut into smaller segments ranging from 27-35.5 cm (Table 4.1), and placed in dark plastic bags for transport. Within 24 hours of cutting, the segments were instrumented and the ends of the segments were covered with plastic film. TDP probes were installed at approximate center and covered with radiation shielding (Figure 4.1b). TDP probes were run continuously across the measurement period at constant heating power and output recorded every 1 minute. The segments were allowed to air dry and weighed at regular intervals. Segments were dried at 30°C for a period of 24 months until all free water was removed. Wood moisture content was calculated as:

$$\theta = \frac{m - m_{FSP}}{m_{FSP}} + \theta_{FSP} \tag{4.7}$$

where θ is wood moisture content, m is mass of the segment, m_{FSP} is the mass of the segment at fibre saturation point (after drying), and θ_{FSP} is the wood moisture content at fibre saturation point, the point where all free water is evaporated, given by $\theta_{FSP} = 0.2\left(\frac{\rho_d}{\rho_w}\right)^{-0.5}$.

Table 4.1 Description of samples used in the drying experiment

Sample	D [cm]	l [cm]	d_{sw} [cm]	P [W]	Θ_i [-]
1	14.00	35.50	1.50	0.138	0.68
2	12.75	30.25	1.20	0.138	0.69
3	14.25	27.00	1.75	0.288	0.78

Mean daily dT_M was compared to theoretical values derived from thermodynamic theory. Vergeynst et al. (2014) presented the theoretical development for these changes as a function of wood dry density, ρ_d, and θ, and is summarized above.

4.2.3 Field installation and calibration

In addition to controlled laboratory conditions, sensor performance was examined under field conditions at Tapajós National Forest, Brazil, previously described in Chapter 3. The self-made system (Figure 4.1c) was compared with a commercially available sap flow sensor (SFM1, ICT International, Australia) for N=4 individuals (see Table 4.2). The SFM1 sensor is based on the heat ratio method (HRM), a variation of the heat pulse velocity (HPV) method (S. S. Burgess et al., 2001). While a majority of sap flow technologies have been found to underestimate sap flow densities, the HPV method is considered to be one of the most accurate, with stronger performance than the more widely-used TDP method. In their comparison of sap flow technology performance, Steppe et al. (2012) found that HPV sensors underestimated sap flux density by 35% compared to 60% by the TDP sensors.

Table 4.2 TDP/HRM comparison information

Species	Field Location	Wood density [g/cm^3]	Power [W]	PSY1 Installation Height [m]
Tachigali chrysophylla	Tapajós, Pará, Brazil	0.690	0.185	25.5
Mezilaurus itauba		0.720	0.196	29.6
Endopleura uchi		0.700	0.226	24.4

Erisma uncinatum		0.510	0.145	26.5

A comparison of observations from the TDP and HRM sensors were used to develop *field calibration* curves, with V_S from the HRM acting as "ground-truth" for the TDP sensors. Granier calibration curves were fit following $V_S \sim \alpha K^{\beta}$ where $K = (dT_M - dT)/dT$ and α and β are fit coefficients as in Eq. (4.1). The HRM system measures sap flow velocity at slightly different locations within the stem than the TDP probe used – 12.5 and 27.5mm as opposed to 15mm. Sap flow velocity is not uniform throughout the stem, rather varying nonlinearly across multiple axes: radially, vertically, and circumferentially. To place measurements on the same basis for calibration, V_S from the HRM sensor was adjusted using a model that accounts for radial sap flow variation.

A number of statistical models have been developed to characterize radial variation using fitted probability distributions along the radial axis (Caylor & Dragoni, 2009; Gebauer et al., 2008). The Caylor & Dragoni (2009) model was used where V_S at a relative radial location r/R is given by:

$$V_s\left(\frac{r}{R}\right) = c_S \frac{1}{B(\omega,\zeta)} \left(\frac{r}{R}\right)^{\omega-1} \left(1 - \frac{r}{R}\right)^{\zeta-1} \qquad (4.9)$$

where r is absolute radial location measured from the center of the tree, R is the radius of the tree, c_s is the stem capacitance [cm hr^{-1}] , and $B(\omega, \zeta)$ is the beta function where ω and ζ are fitting the parameters of the beta distribution.

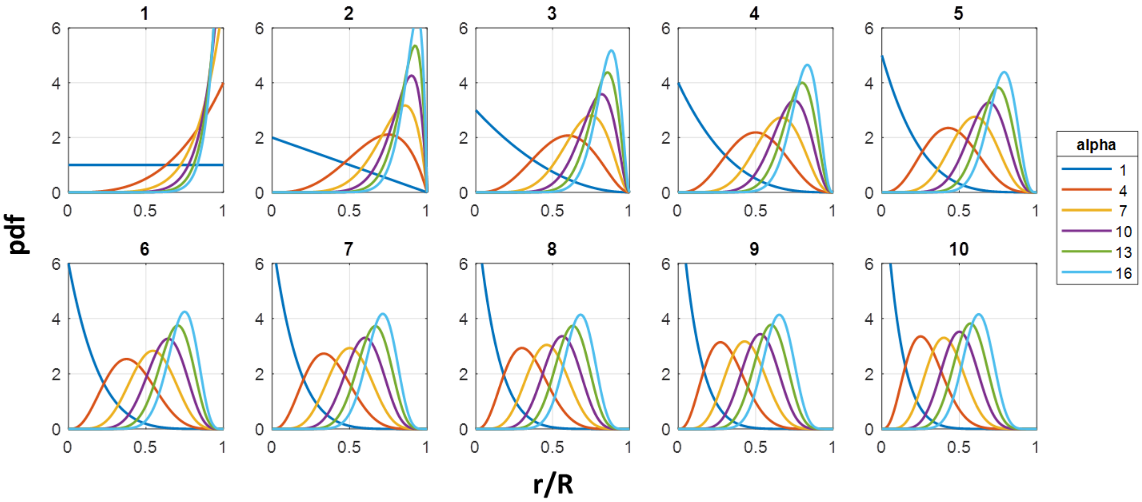

Figure 4.2 Variability of the radial sap flow distributions as a function of relative sapwood depth for different fit parameters. The title of each subplot represents the value of ζ while the legend gives values of ω. $r/R = 1$ represents the cambium-sapwood interface while $r/R = 0$ is the absolute center of the tree.

The dimensions of sapwood are important for both radial flow characterization and scaling of measured sap velocities to obtain volumetric flows. In the vicinity of the K67 study site, timber was collected from a selective logging program within the primary forest. Images of the timber cross-sections were taken and analyzed for total diameter, sapwood depth, and bark thickness using the ImageJ software package (v1.48). Photos were taken and initial analysis performed by G. Ewing and subsequent analysis and regression fitting performed by E. Agee. To account for irregularities in shape, multiple measurements were taken across the center point and averaged to compute effective diameters. An allometric relationship was fit to relate tree diameter, DBH [cm], to sapwood area, A_S [cm^2], in the form:

$$A_s \sim a_1 \mathrm{DBH}^{a_2} \tag{4.8}$$

where a_1 and *a,* are fit parameters.

The allometric relationship was used to estimate sapwood depth for the radial sap flow distribution model. Radial sap flow profiles were generated using daytime velocity observations taken from the HRM system at 12.5 (r = DBH – 12.5) and 27.5mm (r = DBH – 27.5) depth. Additional points of zero velocity were added at the sapwood/cambium interface (r = DBH) and at the sapwood/heartwood interface (r = DBH - d_s) where r is zero at the center of the tree. A large number ($N > 10^3$) of daytime profiles were fit for all species representing both wet and dry season profiles. The medians of the fitting parameters, $\widehat{\omega}$ and $\hat{\zeta}$, were used to build a general radial distribution model for each individual. The sap flow velocity at 15mm depth, $V_{s,15}$, was computed using the stem capacitance, c_s, from the sap flow velocity measured at 12.5mm depth – the measurement closest to the position of the TDP thermocouple.

4.2.4 Scaled sap fluxes

While radial sap flow variation is widely accepted, a majority of studies do not fully account for radial variability when scaling instantaneous sap velocity to volumetric flow. Instead, they assume homogenous flow or, at best, use a discrete weighted means approach (Hatton et al., 1990). That developed radial distribution was used to scale the point measured instantaneous sap flow velocity, V_S, to volumetric flux, F_S [$L^3\ T^{-1}$]. F_S is given by:

$$F_s(t) = 2\pi R^2 \frac{\omega}{\omega+\zeta}\left(\frac{V_s\left(\frac{r}{R};t\right)}{\rho_s\left(\frac{r}{R}\right)}\right), \tag{4.9}$$

where $\rho_s\left(\frac{r}{R}\right)$ is the value of the beta distribution at the relative xylem location, given as:

$$\rho_s\left(\frac{r}{R}\right) = \frac{1}{B(\omega,\zeta)} x^{\omega-1}(1-x)^{\zeta-1}, \tag{4.10}$$

where ω and ζ are the aforementioned fitting parameters described by (Caylor & Dragoni, 2009).

4.2.5 Stem water potential

Nocturnal no flow signals (dT_M) were compared to minimum and maximum daily stem water potential (ψ_{min} and ψ_{max}) at canopy height. Stem water potential (ψ) was measured using a chamber based thermocouple hygrometer or stem psychrometer (PSY1, ICT International, Australia). The stem psychrometer measures water potential using two welded chromel-constantan measuring junctions held within an insulated metal chamber (Dixon & Tyree, 1984). With one thermocouple in contact with the stem surface and the other monitoring chamber temperature, the chamber is cooled using a small pulse of electrical current (i.e., Peltier cooling) and the wet bulb temperature determined (Dixon & Tyree, 1984). This is used to determine the water potential within the stem, with the other thermocouple acting as a correcting factor. Calibrated stem psychrometers have shown strong agreement with leaf water potential as measured by pressure chamber in both laboratory and field settings (Dixon & Tyree, 1984; Nizinski et al., 2013). Leaf water potential is a widely used proxy for plant hydraulic state but is a destructive measurement that monitors a single point in time. The stem psychrometer allows for continuous monitoring of plant hydraulic status and is minimally invasive.

Prior to deployment, all stem psychrometers were calibrated according to factory instructions using NaCl solution of known osmotic potential. Calibration fit coefficients all had R^2 values > 0.98. Measurements were taken at sub-daily frequency, but only daily minimum and maximums were used in this analysis. Installation heights can be found in Table 4.2.

4.3 Results

4.3.1 Heating power shifts

For each heating power observed using the hydraulic apparatus (Section 4.2.1, Fig. 1a), the no flow signal output was averaged over the measurement interval (2 minutes, at 10 s sampling). The column was completely saturated for the entire trial. Within single trials, signal noise was small, with signal standard deviations ranging from 0.012 – 0.022 V, or roughly 1% of the average signal voltage. The averaged no flow signal, or dT_M, is linearly correlated with the heating power applied.

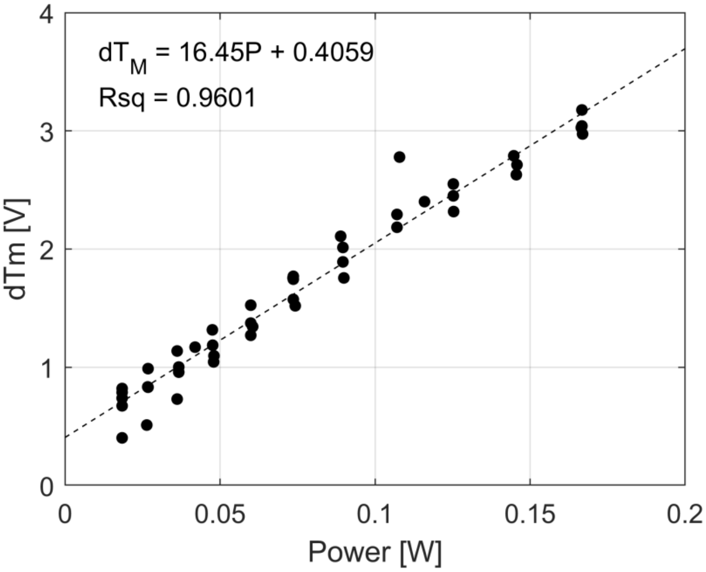

Figure 4.3 Mean zero flow (dT_M) signal voltage versus the heating power, P [W]. The resistance of the sensor was assumed to be 54 Ω for the Dynamax TDP30 probe.

For trials conducted on unchanged bedding (i.e., unaltered bulk density), variability was small (Fig. 4.4, left). It is important to note that when the bedding material was allowed to dry and sit for extended periods of time (e.g., more than one week), variability in baseline values increased (Fig. 4.4, right). This could be due to unobservable changes in the bedding matrix due to drying and rewetting. Over the course of the experimental trials, several materials and bulk densities were tested. Variations in bedding proportions and packing density resulted in different absolute values of *dTm* for the same heating voltage applied. Despite these differences in absolute values, each individual trial scaled with heating voltage applied, following the power law ($P = V^2/R$, where P is power [W], V is voltage, and R is electrical resistance [ohms]).

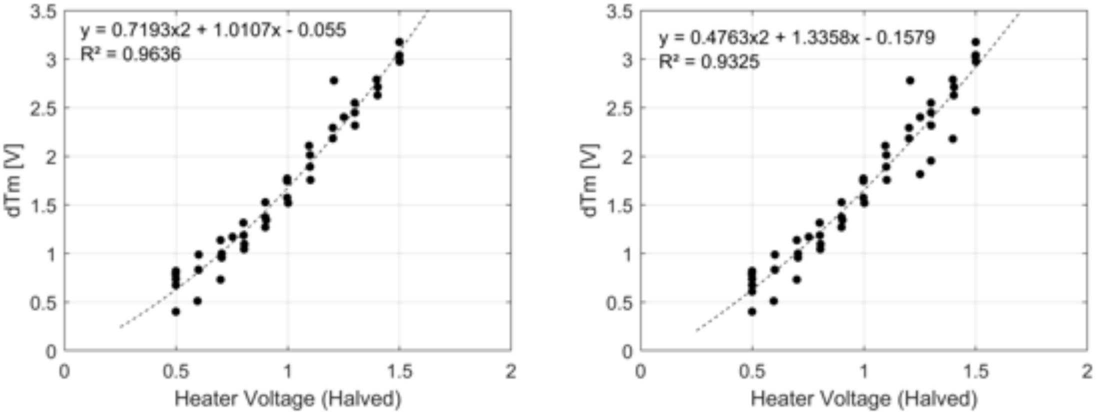

Figure 4.4 (left) Baseline values (dT_M) for halved heater voltages for August 13-21, 2018. (right) Baseline values (dT_M) for halved heater voltages for August 13 – September 8. The "halved heater voltages" are a legacy of the sensor design.

4.3.2 Stem water content

The cut segments were monitored for 200 days (06/27/2017 to 01/13/2018). Water content decreased from an initial mean value of 0.72 ± 0.05 to a mean value of 0.41 ± 0.02 across all three samples (Figure 4.5), a decrease of 43%. The sap flow sensor output, dT_M, was resampled at daily time scales, using the signal mean. Diurnal signal variability was less than 1-5%. Voltages were converted into temperature differences using a linear approximation for the Type-T thermocouple, $T = 2.927V + 0.14$. The absolute change in dT_M after 200 days was 1.4 ± 0.38V or 4.26 ± 1.11 ºC (Fig. 4.5, right). The highest change in dT_M was for segment 1, which was also the longest segment, with a length of 35.5 cm.

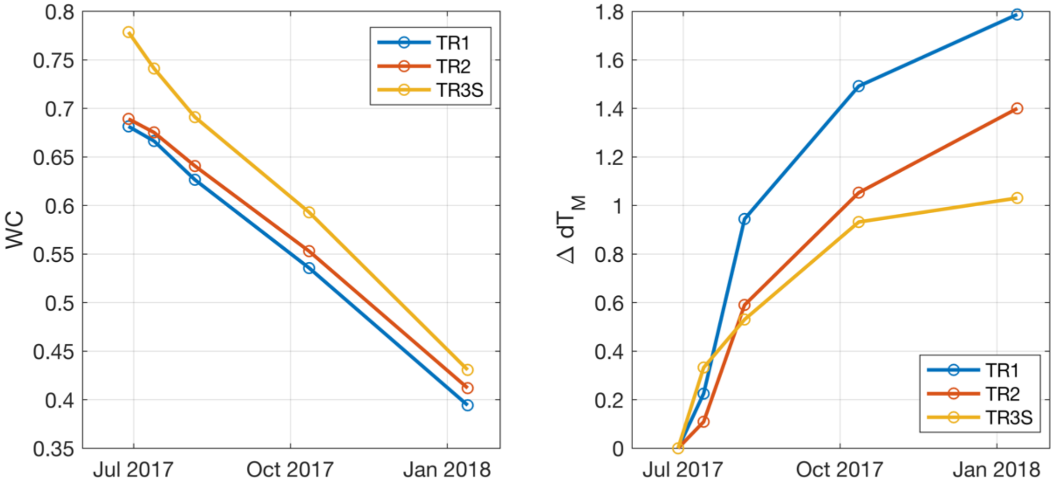

Figure 4.5 (left) Measured water content over the sample period. (right) Change in dT_M relative to the minimum, measured at the beginning of sampling. Line colors indicate the unique samples.

Change in absolute dT_M, when adjusted for differences in heating power, is linearly correlated with water content (Figure 4.6), $\Delta dT_M = -4.35\theta + 3.34$ ($R^2 = 0.77$, $p < 0.05$). The theoretical change in base voltage as a function of water content is nonlinear but weakly so. These results illustrate that changes in baseline voltage due to natural occurring variations in wood moisture content may be resolved using a linear approximation, reducing parameterization needs. Softwoods, with low dry wood densities, hold substantially more water than hardwoods, have a wider range of potential moisture contents.

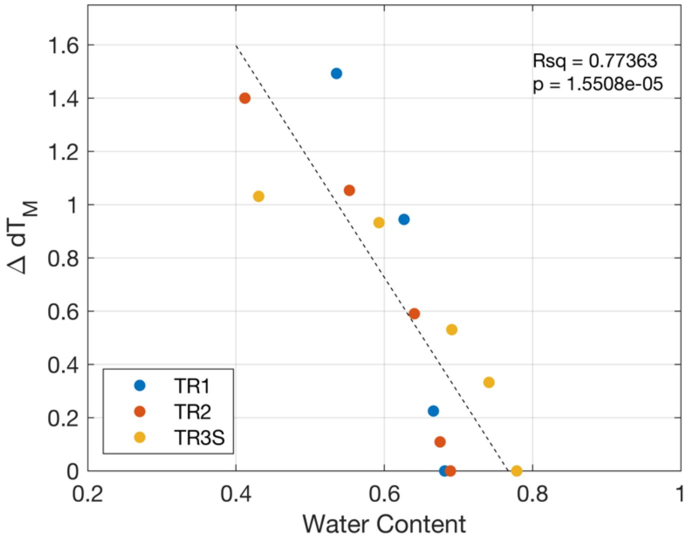

Figure 4.6 Change in baseline voltage (adjusted for heating power differences) for the three samples (see legend) as a function of measured wood moisture content.

4.3.3 Sapwood allometry

A total of 44 cross-section images, representing 7 unique species, were processed for diameter, sapwood depth, and sapwood area (Table 4.3). The species come from three different wood density classes: ~0.60 (29.6%), 0.80 (6.8%), and > 0.90 (63.6%) g cm^{-3}. Each image measurement was repeated 3 times and averaged, with variability of 0.2-5.3% of the total. Allometric relationships were developed that relate DBH to sapwood area and subsequently sapwood depth (Fig. 4.7). The fit parameters for A_S show good agreement with those from developed for a tropical evergreen rainforest near Manaus (a = 0.561, b = 1.783 at K67; a = 0.823, b = 1.781 at ZF2) (Aparecido et al., 2019).

Table 4.3 Species level results for sapwood image analysis.

Species	N	ρ_d [g cm^{-3}]	D [cm]	A_S [cm^2]	d_s [cm]	ρ_d Reference
Hymenaea courbaril	14	0.91	82.5 ± 17.1	1789 ± 544	15.1 ± 2.6	1
Astronium lecointei	3	0.80	64.7 ± 4.9	1182 ± 460	13.0 ± 5.4	2
Chrysophyllum lucentifolium	8	0.91	56.7 ± 9.3	958 ± 216	12.1 ± 2.0	3
Couratari stellata	1	0.62	143.8	979	4.4	3
Lecythis lurida	4	0.92	78.3 ± 13.6	1071 ± 405	9.0 ± 2.0	4
Protium spp.	11	0.63	61.6 ± 15.4	470 ± 167	5.3 ± 1.8	5
Manilkara huberi	3	0.93	76.7 ± 14.7	534 ± 90	4.8 ± 1.5	1

[1] http://www.wood-database.com/, [2] http://pre.fsc.dk/, [3] http://tropix.cirad.fr/, [4] http://www.industrial-resources.net/other_woods/woods21.html, [5] http://www.fpl.fs.fed.us/documnts/TechSheets/Chudnoff/TropAmerican/htmlDocs_tropamerican/Protiumspp.html

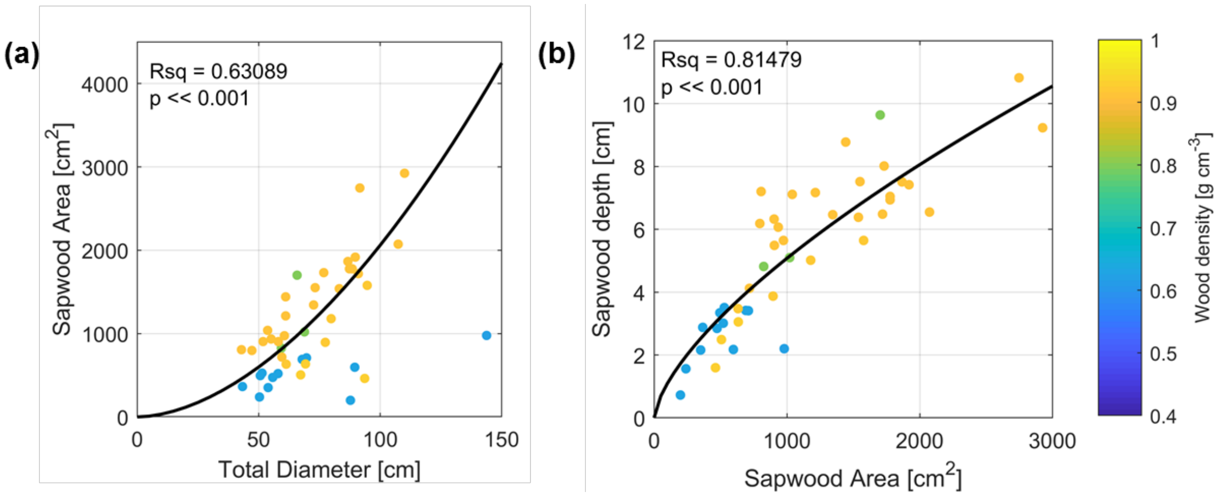

Figure 4.7 (a) Allometric relationship between tree diameter and sapwood area, $A_s = 0.561\ DBH^{1.783}$, with R^2 = 0.63 and p << 0.001. (b) Relationship between sapwood depth and sapwood area, $d_s = 0.051\ A_s^{0.667}$ with R^2 = 0.81 and p << 0.001. Wood density is noted as marker color, given by the color bar on the far right.

4.3.4 Radial sap flow distribution and field calibration

The computed sapwood allometry was used to estimate sapwood depth for the four monitored trees. Allometrically derived sapwood depth ranged from 44-170 mm. Radial distribution fitting parameters were found for each daytime hour in the dataset, with the number of profiles ranging from 3,858-12,539, dependent on the species. Fitting parameters ranged based on hourly environmental conditions, but were clustered around their median value, with binned frequencies ranging from ~0.3 – 0.98 (Fig 4.8 a-d). Fitting parameters were within the ranges previously reported in literature. To control for hourly and daily variations in environmental forcing, the median of each fitting parameter was used as a universal fitting coefficient per Caylor & Dragoni (2009) and Dragoni et al. (2009). Computed sap flow distribution model parameters are summarized in Table 4.4 for the sample population.

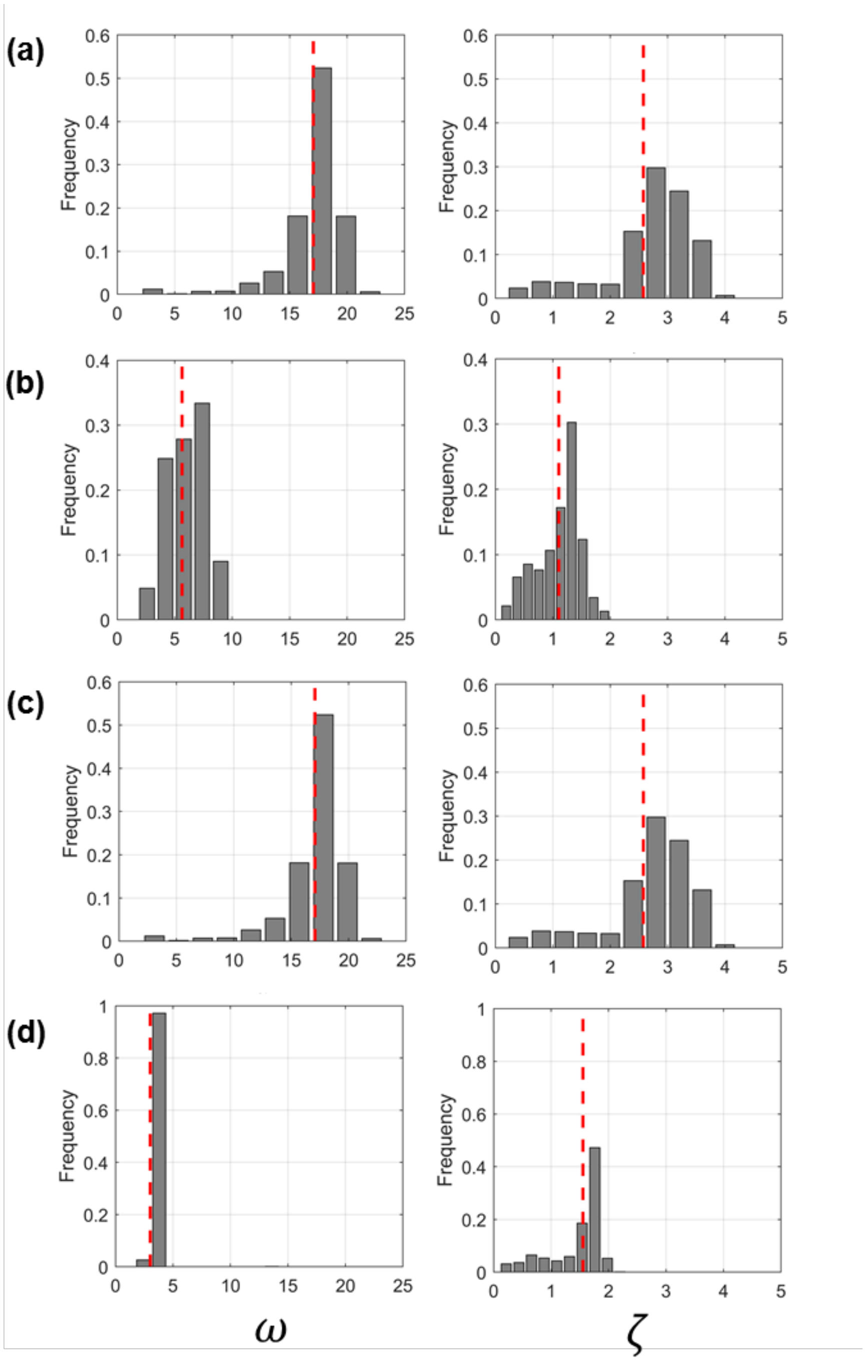

Figure 4.8 Frequency distributions of radial model fit parameters for (a) *T. chrysophylla*, (b) *M. itauba*, (c) *E. uchi*, and (d) *E. uncinatum*. Median values are denoted by the red dashed lines and were used in the final model.

Table 4.4 Summary of fit parameters for radial sap flow distribution model

Species	DBH [cm]	Radial Profiles	Estimated d_s [mm]	$\hat{\omega}$	$\hat{\zeta}$
T. chrysophylla	74.2	3858	75	1.455	0.086
M. itauba	73.2	10370	74	5.853	0.683
E. uchi	47.3	3618	44	17.818	2.154
E. uncinatum	148.1	12539	170	3.081	1.103

The computed $V_{s,15}$ and the relative signal difference ($K = (dT_M - dT)/dT$ from the Granier calibration) were used to find the Granier fitting coefficients (Figure 4.89, Table 4.4). The α fit coefficients ranged from 16.188 – 33.306 cm hr^{-1} and the β from 0.621 – 0.783, with RMSE of 0.75 – 2.15 cm hr^{-1}, with higher scatter at high velocities.

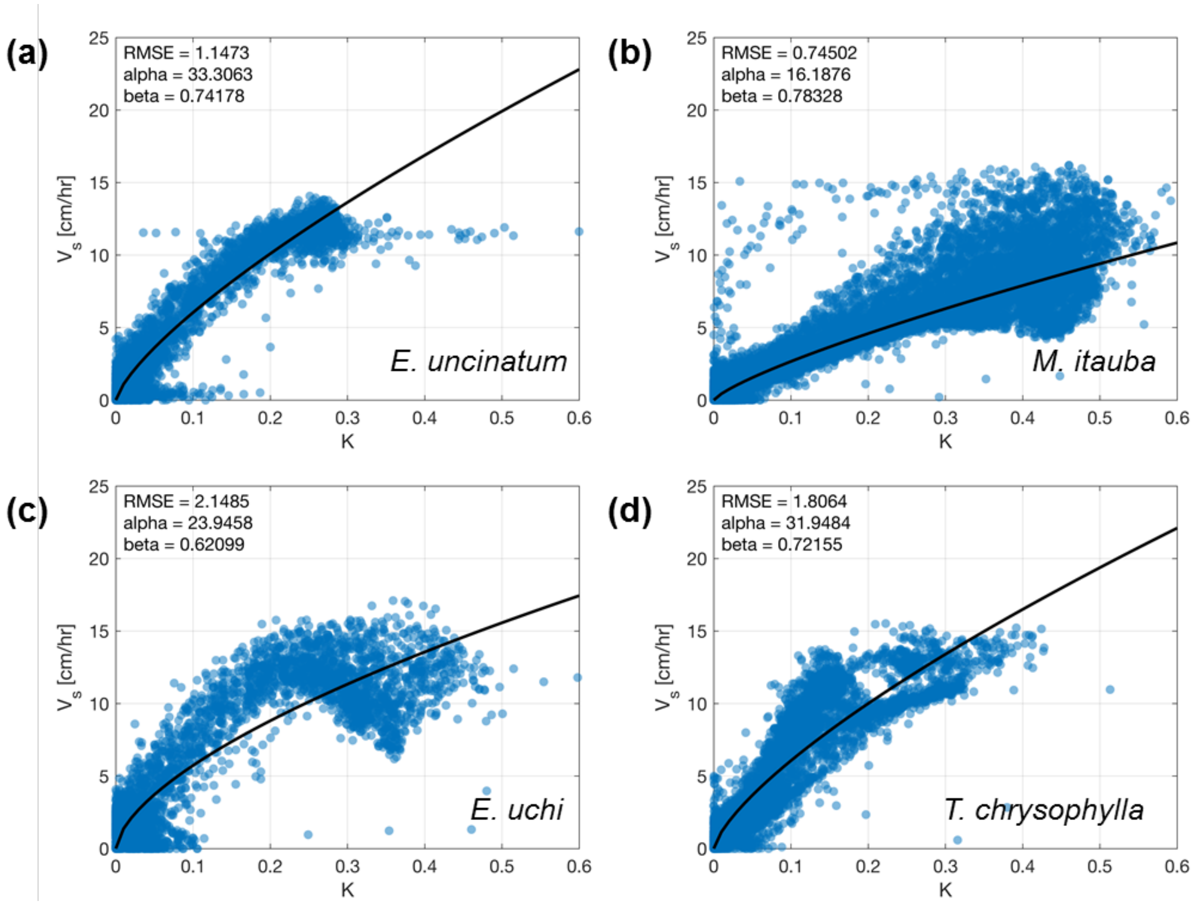

Figure 4.9 Granier calibration fits for the four measured species, (a) *E. uncinatum*, (b) *M. itauba*, (c) *E. uchi*, and (d) *T. chrysophylla*.

Table 4.5 Fit parameters for Granier calibration (α and β) with RMSE. Additional regression statistics are included for the comparison between TDP V_S and commercial HPV V_S.

Species	α	β	RMSE	m	b	R^2
T. chrysophylla	31.948	0.722	1.81	0.808	0.938	0.84
M. itauba	16.188	0.783	0.75	0.770	0.466	0.84
E. uchi	23.946	0.621	2.15	0.822	0.899	0.82
E. uncinatum	33.306	0.742	1.15	0.948	0.337	0.92

The species-specific calibrations were applied for all four species to determine $V_{s,15}$. A comparison between the $V_{s,15}$ computed for HPV and measured by the TDP probes showed strong agreement with all R^2 values >0.80 (Table 4.5, Fig. 4.10a-d). Highest variability was again in the upper sap flow velocities. It is important to note that while the two systems were installed in close proximity, they were not monitoring the exact same location tangentially or circumferentially. Comparisons include both wet and dry season time periods.

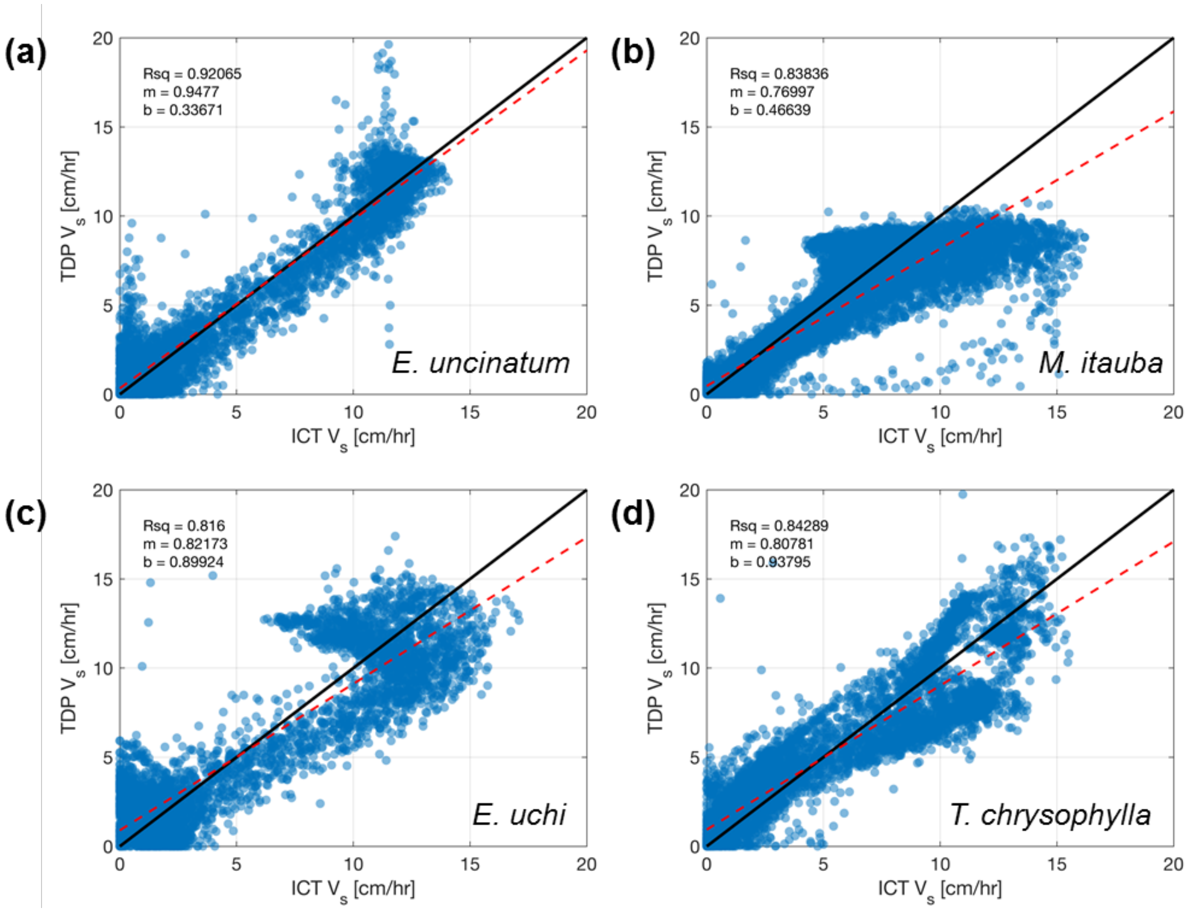

Figure 4.10 Comparison between HPV (measured by ICT sensor) computed and TDP measured $V_{s,15}$ for (a) *E. uncinatum*, (b) *M. itauba*, (c) *E. uchi*, and (d) *T. chrysophylla*.

4.3.5 Sap flow during 2015-2016 dry season

The 2015-2016 dry season was marked by an increase in mean monthly temperature from 26.7°C in July 2015 to a peak of 29.1°C in November 2015 (Fig 4.11, top panel). There was little to no precipitation from July through December, with a marked transition occurring in March 2016 when mean monthly precipitation reached 7.45 mm day^{-1} (Fig 4.11, middle panel). Vapor pressure deficit (VPD) followed the trend in temperature with mean monthly values increasing from 0.68 kPa in July 2015 to a peak of 1.23 kPa in November 2015 (Fig 4.11, bottom panel).

VPD and temperature decreased following the transition from dry to wet seasons starting in January.

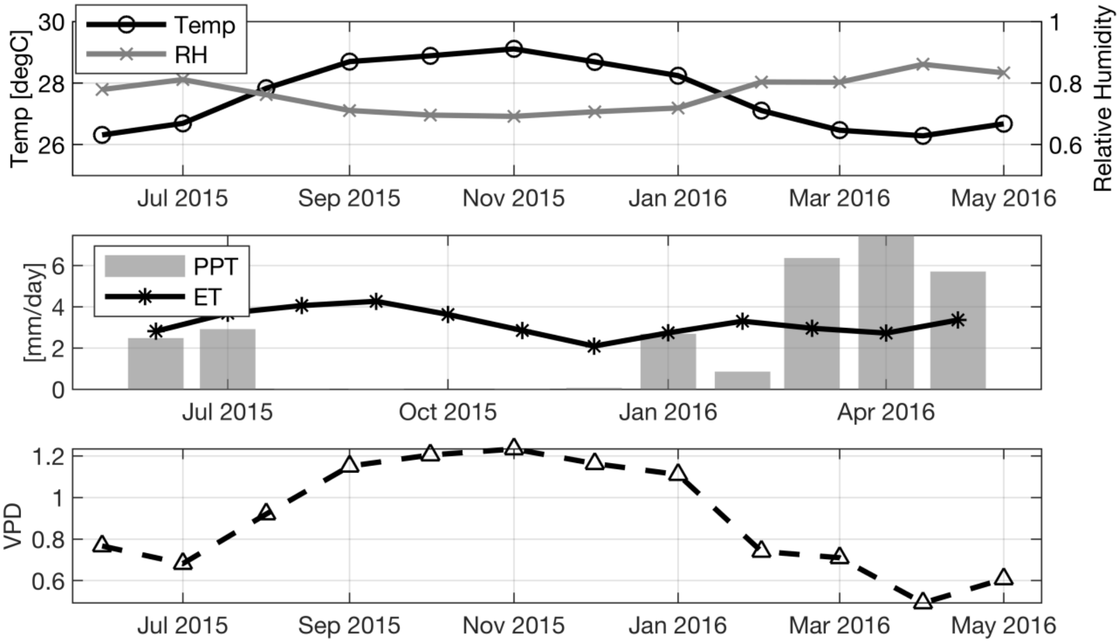

Figure 4.11 Ambient conditions as measured by the K67 eddy covariance tower (described in Chapter 3). (Top panel) Mean monthly temperature [ºC] and relative humidity [-]; (middle panel) mean monthly precipitation and latent heat flux (ET) both given in [mm day^{-1}]; (bottom panel) mean monthly vapor pressure deficit [kPa]. Line symbols and colors follow the legends where appropriate.

Daily mean sap flow velocity was computed for the July 2015-March 2016 period, capturing the dry season and the transitional months on either side (Fig. 4.12). Data were not available for *E.unicinatum* prior to late November 2015. There is a gap in the time series from middle October to middle November, which was due to system power issues. Signal variability is a response to daily variation in ambient conditions which drive transpiration. *T. chrysolphylla* exhibits a dramatic response to water limitation with daily V_S declining from 200-250 cm day^{-1} at the beginning of the dry period to less than 100 cm day^{-1} by end. The decline appears to begin around September 2015 and continues until it reaches a minimum around January 2015. *E. uchi* and *M. itauba* show minimal declines in mean daily V_S throughout the dry period, but maintains smaller flux densities than *T. chyrsolphylla*, with maximum values around 100 cm day^{-1}.

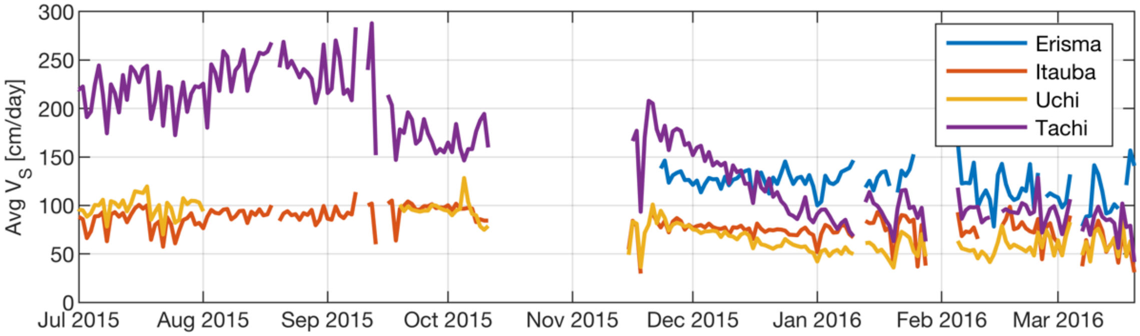

Figure 4.12 Daily mean sap flow velocity [cm day^{-1}] for 7/1/2015 – 3/20/2016. Line colors follow the legend and species are referred to by their genus.

Mean diurnal sap flow velocity was computed for a representative wet period (04/01/2015-07/01/2015) and the dry period (07/01/2015-03/01/2016) at half-hourly resolution (Fig. 4.13). These periods include the data gaps previously mentioned. During the wet and dry periods, V_s begins at around 07:00 local time, reaching a relative maximum at 10:00 which is maintained at a relative constant rate until around 16:00 when rates decline. Mean daily maximum Vs declined from 8.8, 9.6, 19.7 cm hr^{-1} in the wet season to 7.7, 7.0, 13.4 cm hr^{-1} in the dry season for *M. itauba, E. uchi,* and *T. chrysophylla* respectively. *E. uncinatum* had a dry season maximum V_s of 12.1 cm hr^{-1}. As noted from the examination of the seasonal time series, *T. chrysophylla* had the sharpest decline in maximum V_s.

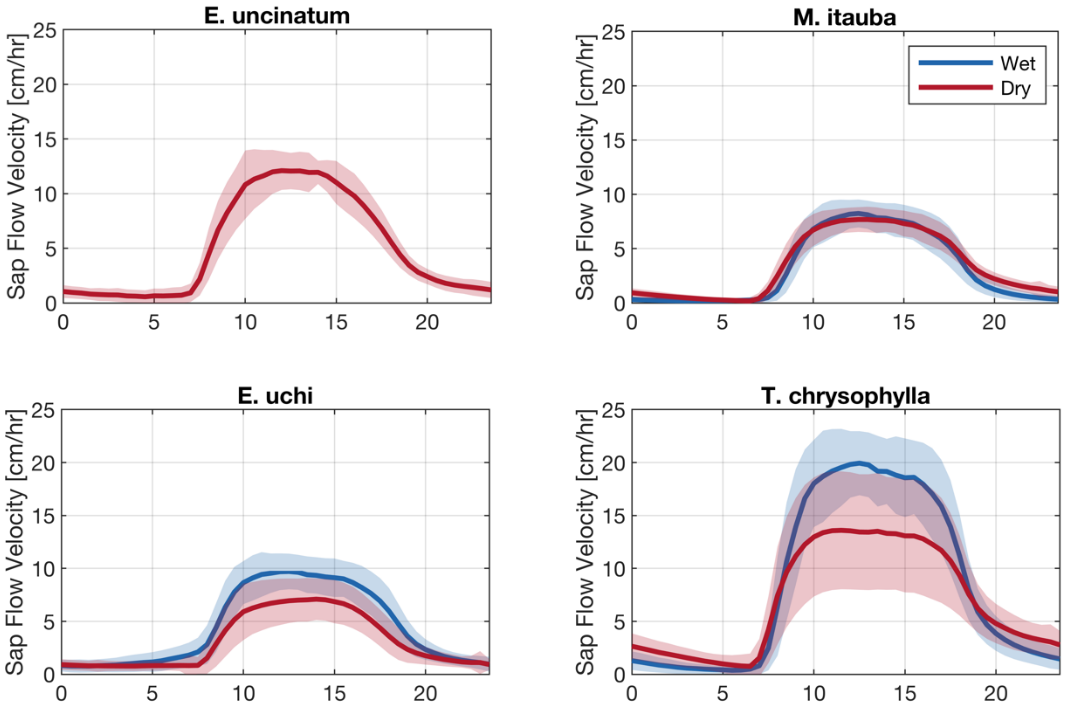

Figure 4.13 Diurnal sap flow velocity for the four sample species with the mean given as a bold line and the half-hourly standard deviation shaded. The representative wet period (04/01/2015-07/01/2015) is shaded blue while the representative dry period (07/01/2015-03/01/2016) is shaded red.

The radial model developed for technology comparison was used to scale the instantaneous sap velocity to whole tree uptake for *M. itauba* and *E.uchi* (Fig 4.14 for the representative wet and dry period). While these two species have very similar daily rates of V_s, scaled transpiration values show tree-scale differences in total water usage. While the data series contains a large gap during the dry period (indicated by flat lines in the cumulative uptakes), it is readily apparent that while V_s rates may be similar between individuals, sapwood area and radial sap flow are produce large differences in scaled fluxes.

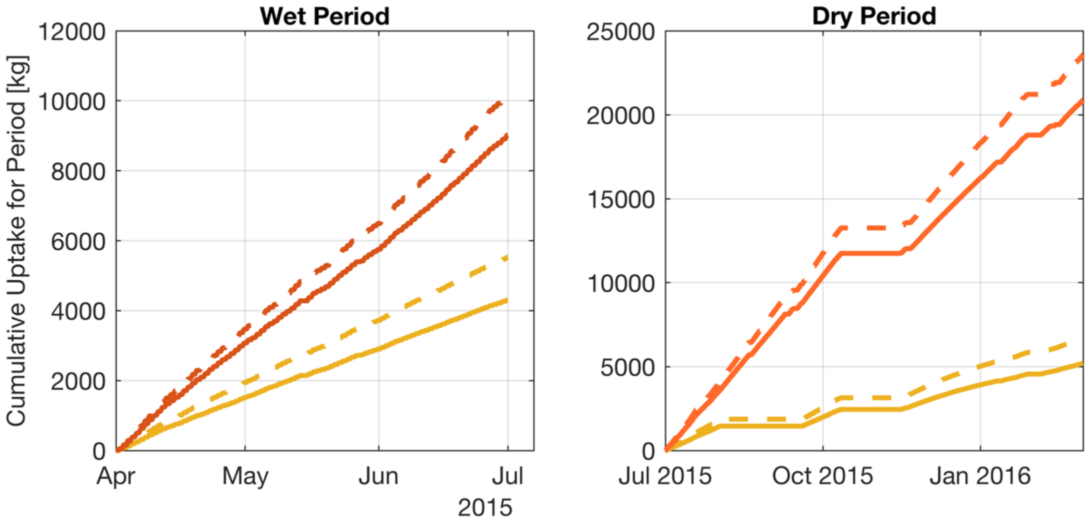

Figure 4.14 Cumulative uptake for M. itauba (orange) and E. uchi (yellow) for the representative wet and dry periods. Whole-tree scaling performed using the radial model is given as a solid line and scaling using sapwood area is given as a dashed line. Color conventions follow Fig. 4.12.

4.3.6 dTm as a proxy for WC

As water content decreases, thermal conductivity of the wood also decreases, consistent with results from (Vergeynst et al. 2014). A comparison between experimental and theoretical impacts of drying show a statistically significant linear correlation between the relative changes in voltage ($r = \frac{x - x_{min}}{x_{max} - x_{min}}$), with $m = 0.8501$, $R^2 = 0.481$, and $p < 0.05$. The theoretical results by (Vergeynst et al. 2014) assume that the heater is an infinitely long, line source with heat applied for 10 minutes ($t = 600$s). To align more closely with the extended length of this experiment, the heating time was adjusted to the actual, $t = 1.728 \cdot 10^7$ s.

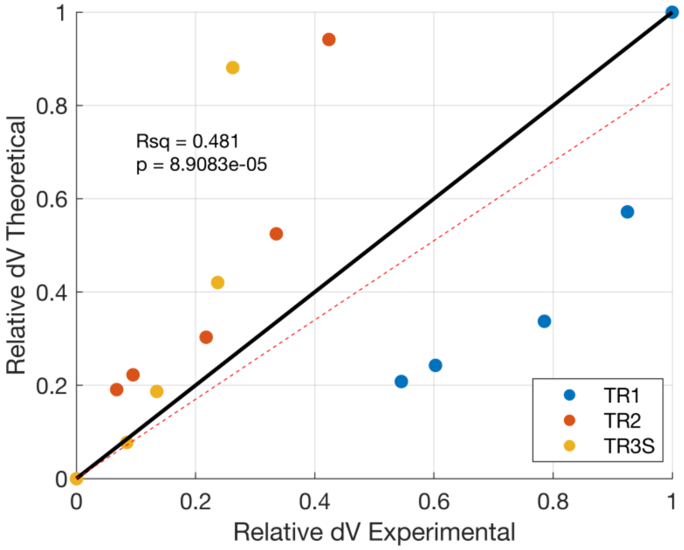

Figure 4.15 One-to-one comparison of the experimental changes in dT_M as a function of moisture content with the theoretical differences, with $m = 0.8501$, $R^2 = 0.481$, and $p < 0.05$.

Differences between the experimental and theoretical can be partially attributed to assumptions made by the theoretical model (e.g., infinite line source, time of heating, etc.). Also, the dry wood density, a primary parameter for the model, was estimated to be 680 kg m^{-3} based on literature values for *Quercus alba* (Chave et al., 2009). Actual dry wood density has intraspecific variability depending on local conditions. Experimental results were adjusted to P = 0.2W using the linear adjustment factor which may result in some systematic error.

Under field conditions, the four monitored species exhibited seasonal changes in dT_M. Raw signal output (Figure 4.16) was variable among species, with raw voltage increases ranging from <0.25V for the *E. uncinatum* to ~ 1V for the *T. chrysophylla*. Variability in absolute voltages result from differences in heating power and wood thermal properties. An additional voltage offset (typically ~0.4V) may also be present from the datalogger design.

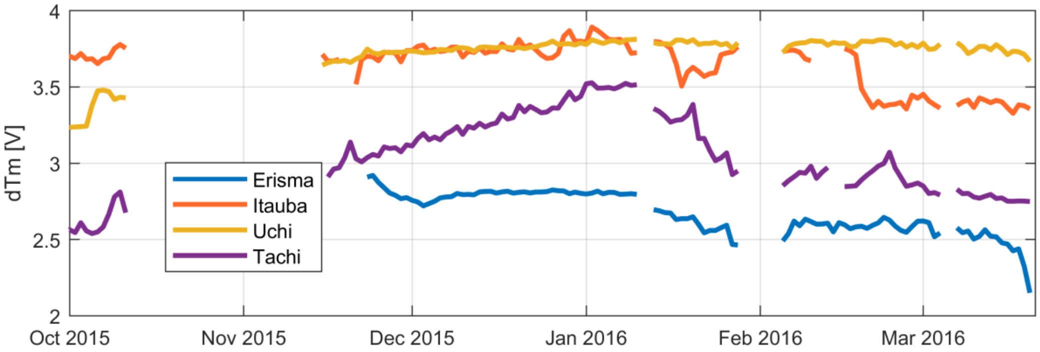

Figure 4.16 Unadjusted daily dT_M for *E. uncinatum*, *M. itauba*, *E. uchi*, and *T. chrysophylla*, with colors given by plot legend. Species are given by their genus.

The theoretical framework was used to estimate daily relative $\Delta\theta$ for the four field species during the 2015 dry season, October 2015 – January 2016 (Figure 4.17). Daily relative $\Delta\theta$ was estimated from the difference between daily θ (from daily dT_M) and the maximum daily θ (from minimum seasonal dT_M) and presented as a 7-day composite. For *M. itauba*, *E. uchi*, and *T. chrysophylla*, the daily relative $\Delta\theta$ is relative to the beginning of the dry season period. Data was unavailable until late November for the *E. uncinatum* and as such, daily relative $\Delta\theta$ was derived using the minimum seasonal dT_M.

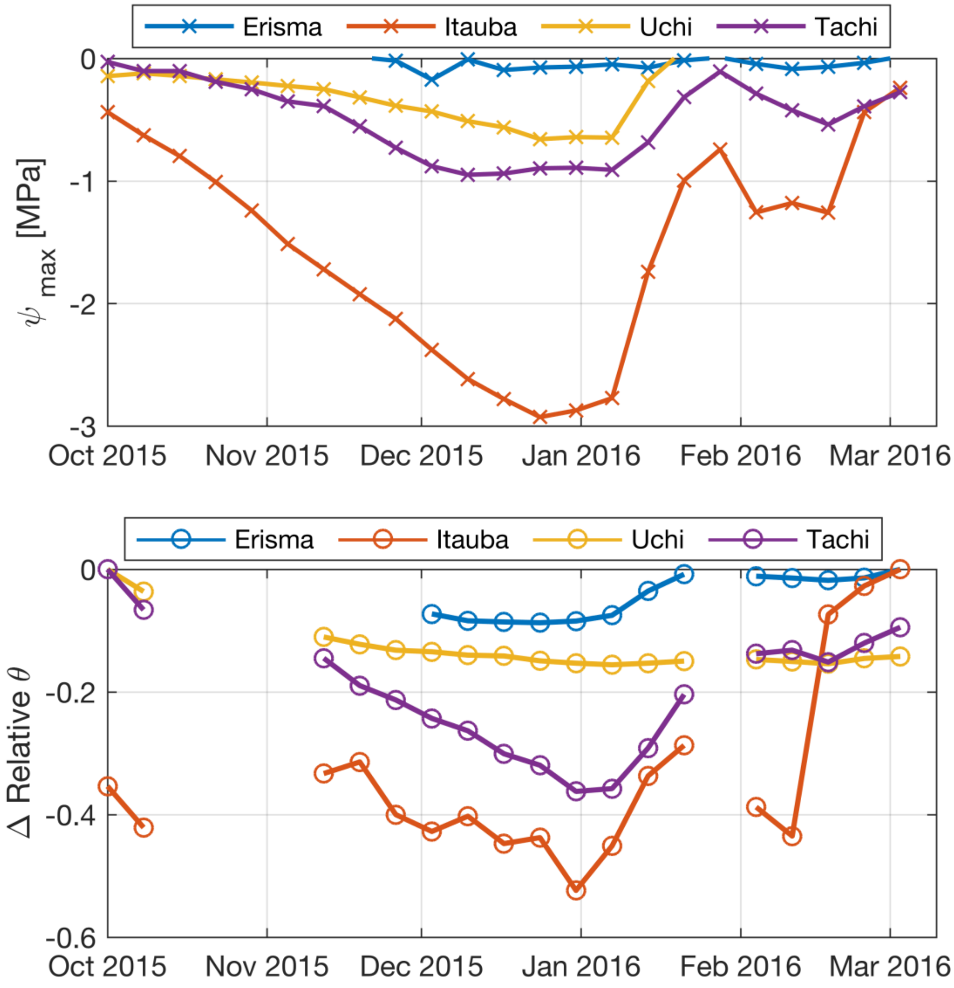

Figure 4.17 (top) Maximum stem water potential, ψ_{max}, (7-day composite) for the four monitored species (Table 4.2) and legend) across the 2015 dry season and 2016 wet season transition. (bottom) Estimated relative change in water content (7-day composite) for the four monitored species. Species are given by their genus.

4. 4 Discussion

4.4.1 Variable power sources and Granier calibration

A tremendous effort has been made to conform to the original 0.2W sensor design presented by Granier (1985). Recent work by Gutierrez Lopez et al. (2019) shows that constant currents of 0.15-0.25 W may be applied without modification of Granier's coefficients for estimation of sap flux density. The results presented here extend the utility of that assertion by demonstrating that the raw signal may be adjusted for variable heating using a simple factor (the ratio of the heating power applied to the Granier 0.2W). The adjustment factor was utilized here both in estimation of thermal properties and for "field calibration" of the TDP probes.

While there is much discussion across the sap flow community about the necessity of species-specific calibration coefficients (Berdanier et al., 2016; Sun et al., 2012), the applicability of these calibrations across sites is unclear. For biodiverse regions like the Amazon, which exhibit a tremendous amount of inter- and intraspecific variability, these calibrations are not feasible given limited resources and sparse complementary datasets. As such, the proposed correction factor may be applied for used for variable power systems, where power or signal sensitivity is a consideration, to help conform to community wide standards of sap flux density estimation.

4.4.2 Sap flow correction factors

A sensitivity analysis was performed for *Quercus alba* to highlight the implications of "corrections" on sap flow velocity (Figure 4.18). Corrections account for wounding and thermal properties of sapwood under variable wood moisture content. Uncertainty is greatest at high velocities where the potential exists to under- or over-estimate actual sap flow velocity, with a scaling factor ranging from 0.6 – 1.4 at 30 cm/hr. While correction variability is high for the range of moisture contents, θ_{FSP} to θ_{sat}, living trees typically exhibit little variability in mean daily θ except under long term water limitation, where hydraulic strategies of water storage could impact θ.

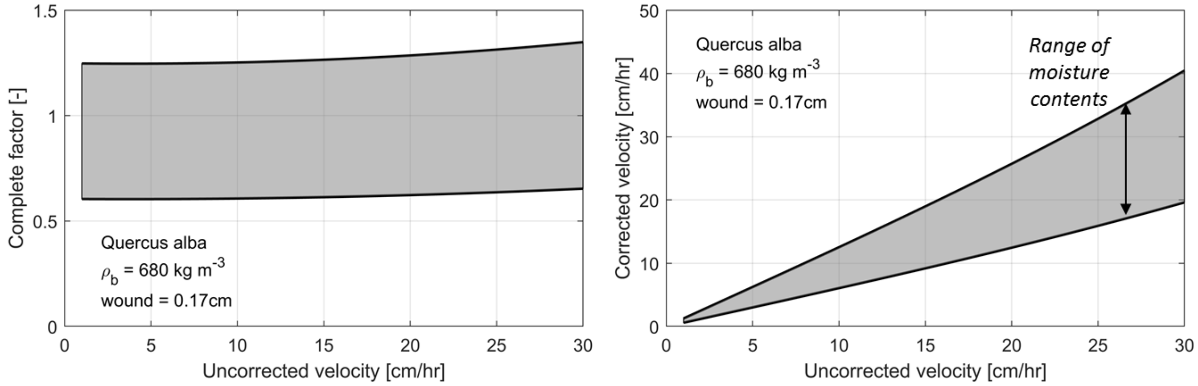

Figure 4.18 (left) The HPV correction factor computed for the range of moisture contents ranging from θ_{FSP} to θ_{max}. (right) The correction factor is applied to uncorrected V_S for Quercus alba, assuming a 0.17 cm wounding coefficient.

The aforementioned calibrations presented in this work use uncorrected values for both HPV and TDP. As both technologies are subject to the same uncertainties due to wounding, thermal variability, and needle asymmetry, both would receive similar corrections. As such, the corrections would not impact the comparison between the two in a significant manner.

4.4.4 Radial sap flow variation

The radial model fit was constrained to 4 data points, which may affect its accuracy. As the radial profile was used primarily for interpolation of a nearby sap flow velocity (2.5mm distance), this was deemed acceptable. For full characterization of radial variability, additional radial points of measurement would be needed to improve estimations of full tree transpiration. The Caylor radial model here was selected due to data availability. Berdanier et al. (2016) compared a selection of radial flow models for temperate tree species across a range of wood anatomies (e.g., tracheids, diffuse porous, and ring porous). In their analysis, they found that absolute xylem depth models performed better than relative depth models, with the gamma model performing best. Overall model performance across distribution types is weakest at a low sap flow velocities, but all radial models performed better than uniform or discrete-weighting scaling methods, improving overall estimations of tree-scale transpiration.

4.4.5 The hidden signal

The shifting seasonal baseline signal (dT_M) from the TDP sensors represents a fundamental shift in the thermal properties of the wood, a function of the wood moisture content. This seasonal change follows shifts in maximum stem water potential. The two variables were compared and a second-order polynomial relationship was fit, with normalized RMSE of 0.044 (Figure 4.19). The measured water potential is a state variable that characterizes the tension (i.e., negative pressures taking atmospheric pressure as the reference) found within the xylem of the tree. When these values become too negative, emboli may form in vessels, impairing the hydraulic pathway and reducing overall transpiration. Variability of stem water potential between individuals representing different species that experience the same environmental conditions (e.g., soil and atmospheric demand) indicates a clear separation of hydraulic strategies among the individuals.

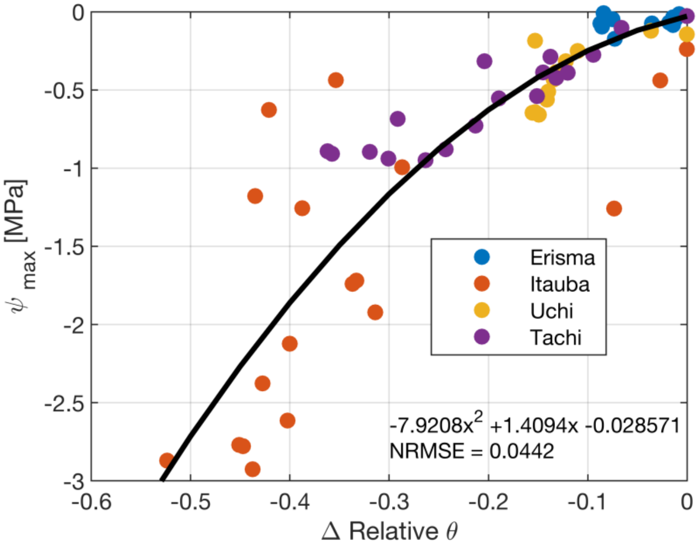

Figure 4.19 Relationship between daily maximum stem water potential and the relative change in wood moisture content (7-day averages). Marker colors for individuals are given by the legend. A second order polynomial was fit to the data, where $\psi_{max} = -7.921\ \Delta\theta_r^2 + 1.409\ \Delta\theta_r - 0.0286$, and the normalized RMSE = 0.044 [-].

These results highlight the “hidden information” embedded in TDP signals. While a substantial effort is made to correct for seasonal changes in moisture content to estimate tree-scale transpiration, these low frequency signals actually present a potential proxy for the hydraulic status of individuals at high temporal frequency. The stem psychrometers used in this study were installed at heights of 24.4 – 29.6 m – regions of the canopy only accessible by trained climbers. Alternative methods for assessing plant water potential require the harvesting of canopy leaves, which again, are only accessible by select means. The implications of this hidden signal are substantial. When coupled with measured vulnerability curves (indicating percent loss conductance in the xylem tissue as a function of water tension), knowledge of plant water potential can give estimates of hydraulic impairment or further insights of individual plant hydraulic strategy. One frequently used in ecophysiological studies parameter, P50, the water potential at which 50% of xylem conductance is lost, has been identified as one key hydraulic trait for assessing plant hydraulic strategy. A number of studies have shown its high correlation with daily maximum stem water potential of the canopy (typically measured at pre-dawn period).

Validation of water uptake processes requires knowledge of not only the quantity of water moving through the system, but also the hydraulic state or stress of the system. Long-term records from inexpensive sap flow technologies can now provide information on both of these fronts, increasing validation sample sizes and providing necessary feedback between the simulated and the observed responses to water limitation.

4.5 Summary

This chapter summarized current thermal theory associated with the measurement of sap flow velocity using heat dissipation technologies. The theory was applied to laboratory and field data collected from FLONA Tapajós in the state of Pará (Brazil) to estimate whole-tree transpiration during the 2015-2016 dry season. It was shown that the baseline signal from TDP sensors may be used as a proxy for stem water content, which provides valuable insights into the hydraulic status of individuals. The “hidden signal” contained within commonly used sap flow technologies has the potential to give further insights into response of individuals to water limitation and provide new, more extensive data sets for trait analyses and models capturing this response in the simulated dynamics.

Appendix 4A – Heat Pulse Velocity Corrections

The estimation of sap flow velocity, V_s, takes into account thermal properties of the wood and the effects of wood wounding caused by probe installation (ICT SFM1 Manual, http://www.ictinternational.com/products/sfm1/sfm1-sap-flow-meter/). The heat pulse velocity, V_h [cm h^{-1}], is given by

$$V_h = \frac{k}{x} \ln\left(\frac{v_1}{v_2}\right) * 3600$$

where k is thermal diffusivity of green wood (0.0025 [cm^2 s^{-1}]), x is distance between heater and reference needles (0.5 [cm]), v_1/v_2 is the ratio [-] of heat pulse velocities of the upstream and downstream reference needles. Wounding caused by needle installation dampens sap flow signals, thus, an empirical wounding correction velocity, V_c, is computed,

$$V_c = bV_h + cV_h^2 + dV_h^3$$

where b, c, and d are fitted parameters (1.6821, -0.0015, and 0.0002, respectively for a 0.17 [cm] diameter wound). The thermal properties of fresh wood change as a function of water content. The final sap flux density (or velocity), V_s, is thus computed by accounting for these properties using,

$$V_s = V_c \frac{\rho_d (c_w + m_c c_s)}{\rho_s c_s}$$

where ρ_d is dry wood density [kg m^{-3}], c_w is the specific heat of the wood matrix (1200 [J kg^{-1} K^{-1}]), m_c is water content of the sapwood [kg kg^{-1}], c_s is the specific heat capacity of sap (4182 [J kg^{-1} K^{-1}]), and ρ_s is the density of sap (1000 [kg m^{-3}]).

Chapter 5 – The Feasibility of High Resolution, Large-Scale Estimation of Evapotranspiration Using Maximum Entropy Production Model

5.1 Introduction

Forest structure and functional composition has direct impacts on water acquisition at individual and community scales. The tropical rainforests of the Amazon River Basin represent 50% of the world's undisturbed tropical biomass (Davidson et al., 2012), with over 200 hyper-dominant and more than 11,000 unique woody species (ter Steege et al., 2013). In contrast with temperate systems, which have a handful of dominant species with distinct functional niches, the high degree of biodiversity within the Amazon likely represents a spectrum of strategies for light, water, and nutrient acquisition. Chapters 2-4 demonstrate the interplay of structural and functional diversity on water uptake processes at individual and community scales – but how these strategies scale to region and basin is unclear. Comprising an area of 5.5 million km^2, the Amazon rainforest plays an important role in global water cycling, with teleconnections extending far beyond its borders (Cox et al., 2008; Duffy et al., 2015).

Evapotranspiration (ET) expresses the exchange of mass and energy between the land surface and the atmosphere and is paramount to understanding vegetation response to drought (Eagleson, 2005). Direct measurements of ET are not feasible and ground observations that lead to ET estimation are resource-intensive and difficult for typical spatiotemporal scales of scientific interest. Remotely sensed satellite observations, given their broad spatiotemporal scales, are an attractive alternative for large, basin-scale analyses. Yet, remote sensing estimations are not without their challenges (Zhang et al., 2016). Widely used products, such as the Moderate Resolution Imaging Spectroradiometer (MODIS) derived MOD16-ET (Mu et al., 2007, 2011), are primarily based upon the Penman-Monteith physical model (Monteith, 1965), which requires intensive parameterization of the vegetation layer for accurate estimates (Bright et al., 2013; Ganguly et al., 2010; Ruhoff et al., 2013; Yang et al., 2014).

A recently introduced Maximum Entropy Production (MEP) model is used to partition surface radiative fluxes as a function of surface net radiation, temperature, and humidity (Wang et al., 2014; Wang & Bras, 2009, 2011). The MEP theory has been widely applied in land surface hydrology (Kleidon & Schymanski, 2008) and bio-ecological systems (Juretić & Županović, 2003; Kleidon et al., 2010; Kleidon & Fraedrich, 2005; Shipley, 2010). MEP has shown great utility in estimating surface energy fluxes and was first applied to Amazonia by (Xu et al., 2019). In that application, the MEP model was first driven and validated using inputs and estimations from regional eddy covariance (EC) towers (summarized in Appendix 5A) spanning several land cover types. Hourly comparisons of daytime modeled latent heat flux and the corrected observed latent heat fluxes show strong agreement with a $R^2 > 0.87$ across all sites (Figure 5.1).

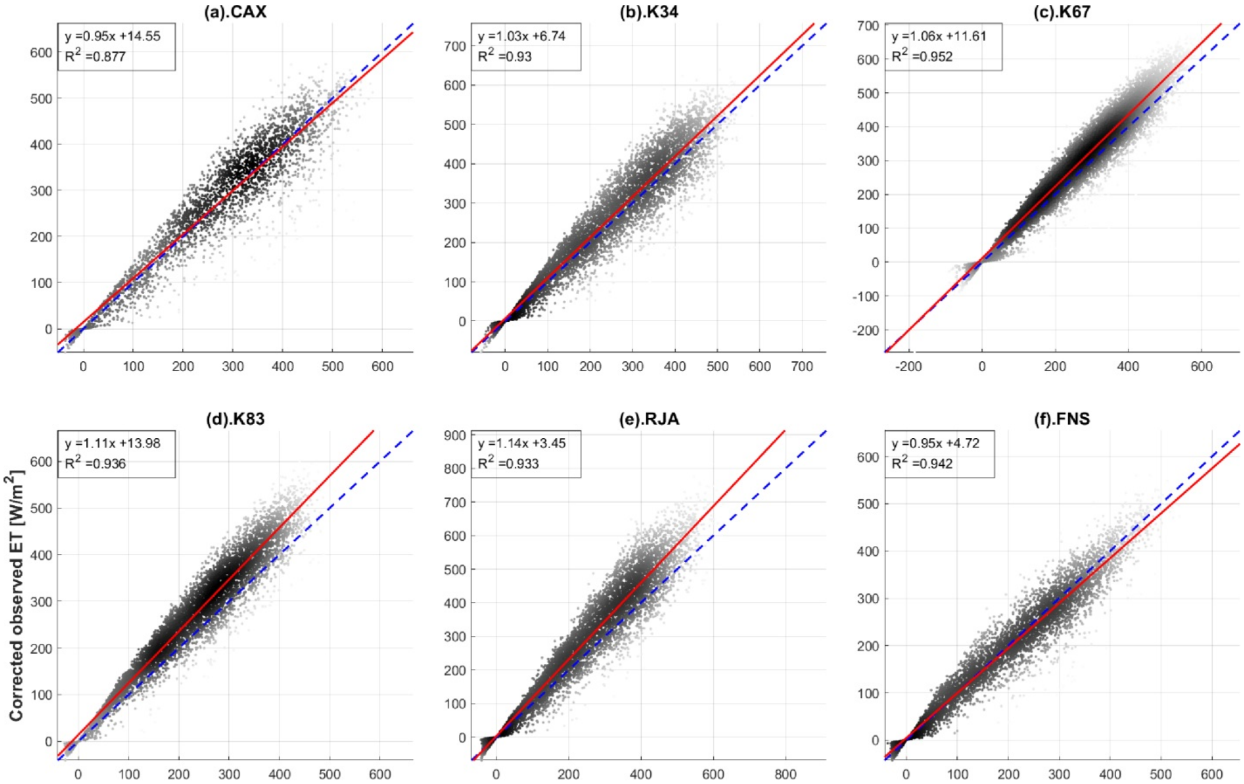

Figure 5.1 Scatter plots of MEP estimated ET (X-axis) against observed ET (Y-axis) corrected using the Bowen ratio closure method (Eq. (8)) for selected study sites at hourly scale (subplot (a) to subplot (f)) and at monthly scale (subplot (g) and subplot(h)). Comparison only for the daytime hours (6:00am – 19:00pm) at hourly scale is presented. Reproduced from (D. Xu et al., 2019).

Xu et al. (2019) further showed the utility of MEP at the basin scale, estimating monthly ET at 1^{o} spatial resolution for the basin. Despite discrepancies in spatial distribution and local maxima and minima, long-term annual ET from MEP agreed well with similar estimates from MODIS (MOD16A2). For 2003-2013, MEP estimated ET was 1280 mm compared to 1284 mm from MODIS. Both estimates were higher than those obtained from a traditional water budget method (108 mm), where ET is assumed to be the difference between precipitation and runoff (assuming long term storage is negligible).

The successful application of the MEP method at the basin scale provides an attractive analytical tool for examining the spatiotemporal trends of ET at finer spatiotemporal resolutions. This chapter addresses the following research questions: (1) What is the feasibility and performance of the Maximum Entropy Production method at the basin scale at the hourly timescale across seasons? (2) Does the MEP method capture the drought signal caused by the 2015-2016 ENSO event? This chapter explores these questions by applying the MEP model to partition surface energy fluxes at the hourly scale using climate forcing from two EC towers in central and eastern Amazonia and basin-wide remotely sensed data. The performance and feasibility of the method is tested under extreme water limitation and compared to other ET estimation methods.

5.2 Methods

5.2.1 Maximum entropy model (MEP)

With roots in statistical mechanics and non-equilibrium thermodynamics, MEP (Dewar, 2005; Dewar & Maritan, 2014) is a special case of the well-established principle of maximum entropy (MaxENT) (Jaynes, 2003), a framework that utilizes Bayesian interpretation of probability theory to determine the most likely distribution or physical macrostate for a system, given a set of constraints. The MEP model differs from classical energy partition models in three major ways: (1) it requires only single-level input of net radiation, temperature, and humidity, resulting in fewer model parameters thus avoiding transfer coefficients used in bulk flux formulas; (2) it does not require wind speed, roughness lengths, etc., that are more difficult to measure using remote sensing technology; and (3) it is less sensitive to the uncertainty of input data and model parameters.

Net radiation, R_n, is partitioned into surface heat fluxes λE, H, and G as follows:

$$R_n = \lambda E + H + G. \tag{5.1}$$

In MEP theory, a dissipation function of energy fluxes *D* is expressed as:

$$D(\lambda E, H, G) \equiv \frac{2\lambda E^2}{I_e} + \frac{2H^2}{I_a} + \frac{2G^2}{I_s} \qquad (5.2)$$

where I_e, I_a, and I_s are thermal inertia of water vapor, air, and soil, respectively (Wang & Bras, 2009, 2011).

A unique solution of the heat fluxes above corresponds to the maximization of *D* under the constraint of energy conservation. For the case of the closed canopy where the energy balance is defined at the canopy top, the ground heat flux, *G*, is negligible compared to the latent and sensible fluxes, λE and *H*. Thus, the solution for latent and sensible heat reduces to:

$$R_n = \lambda E + H \qquad (5.3)$$

$$\lambda E = B(\sigma)H \qquad (5.4)$$

where the Bowen ratio, *B(σ)*, is a function of the a dimensionless parameter *σ* characterizing the water and thermal state of the evaporating surface (Wang & Bras, 2011).

$$B(\sigma) = 6\left(\sqrt{1 + \frac{11}{36}\sigma} - 1\right) \qquad (5.5)$$

where:

$$\sigma = \frac{\lambda^2}{c_p R_v} \frac{q_s}{T_s^2} \qquad (5.6)$$

λ is the vaporization heat of liquid water, R_v, is the gas constant for water vapor and q_s and T_s are the specific humidity and temperature of the transpiring surface, respectively.

5.2.2 Model Forcing

The primary inputs for the MEP model are net radiation, temperature, and specific humidity. The following section presents the data products used for model forcing and comparison. Where relevant for error sensitivity, a summary of retrieval algorithms are presented.

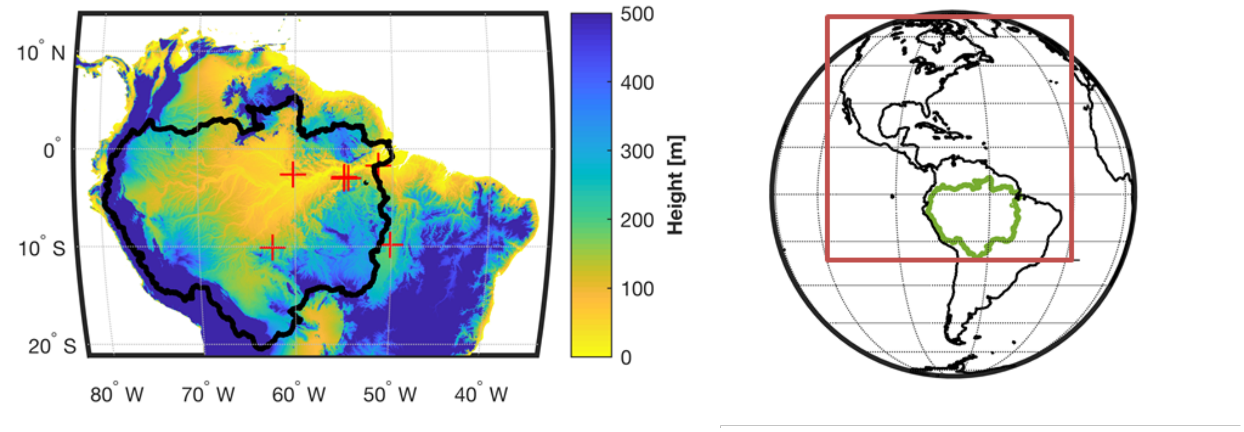

Figure 5.2 (Left) Digital elevation model for the Amazon Basin region (SRTM at 30 arc-sec or about 1 km). The Amazon River Basin boundary is outlined in black. Eddy covariance tower locations are denoted as red markers. (Right) Boundary of the GOES Northern Hemisphere Extended scan sector which provides hourly observations for the region including the Amazon River Basin (green outline).

5.2.2.1 Net radiation

Surface net radiation is taken from the GOES Surface and Insolation Product (GSIP) version 3 product, derived from NOAA's GOES geostationary satellites. GSIP v3 provides the components of the surface radiative budget at hourly temporal resolution and ~4 km spatial resolution. Product coverage spans from 03/01/2014 to 01/01/2018, ending with the removal of GOES-13 from operational status. The previous version of GSIP (v2) provides additional historical coverage from 03/01/2009 to 01/01/2018, but at a coarser spatial resolution of 0.125

degrees. The variables available with the GSIP product are summarized in Appendix 5A.

Net surface radiation [W m^{-2}] is computed from the radiative components as follows:

$$R_n = (S_{\downarrow} - S_{\uparrow}) + (L_{\downarrow} - L_{\uparrow}) \tag{5.7}$$

where $S_{\downarrow}$ is downward welling shortwave radiation at the surface [W m^{-2}], $S_{\uparrow}$ is upward welling shortwave radiation at the surface [W m^{-2}], $L_{\downarrow}$ is downward welling longwave radiation at the surface [W m^{-2}], and $L_{\uparrow}$ is upward welling longwave radiation at the surface [W m^{-2}].

Upward and downward welling radiative fluxes are computed from raw GOES scenes using a heavily modified algorithm developed by (Ohmura et al., 1998; Pinker & Laszlo, 1992; Whitlock et al., 1995). GSIP estimated outgoing longwave radiation is estimated using the High-resolution Infrared Sounder (HIRS) outgoing longwave radiation (OLR) algorithm (Ellingson et al. 1989). The multi-spectral OLR algorithm can be described by

$$I_{\nu}^{\uparrow}(z_t; \theta, \phi) = \varepsilon_{\nu}^{*} B_{\nu}^{*}(0) T_{\nu}^{*}(z_t, 0; \theta, \phi) + \int_0^{z_t} B_{\nu}(z') \left(\frac{\delta T_{\nu}(z_t, z'; \theta, \phi)}{\delta z'} \right) dz' \tag{5.8}$$

where $I_{\nu}^{\uparrow}$ is the specific intensity of upward longwave radiation at the top of the atmosphere z_t at local zenith angle θ and azimuth angle ϕ; ε_{ν}^{*} is surface emissivity, T_{ν} is atmospheric transmittance, $B_{\nu}(z')$ is the Planck function evaluated at wave number ν with the temperature at level z'. A perfect blackbody is assumed (i.e., everything that is absorbed is emitted). The first term of the equation represents the longwave radiation emitted from the surface. The second term represents longwave radiation emitted from or reflected from any point between the surface and the top of atmosphere (TOA). OLR is related to the specific intensity by integrating over wavenumbers and hemispheric solid angles and is given by

$$OLR = \int_0^{2\pi} \int_0^{\pi/2} \int_0^{\infty} I_\nu^{\uparrow}(z_t; \theta, \phi) \cos\theta \, d\nu \sin\theta \, d\theta d\phi \tag{5.9}$$

Outgoing longwave radiation can be estimated as a linear combination of selected narrowband radiances, weighted according to band significance. Regression coefficients and radiances are functions of the local zenith angle θ:

$$OLR = a_0(\theta) + \sum_i a_0(\theta) \cdot N_i(\theta) \tag{5.10}$$

where a_0 is the regression coefficients and N_i are the satellite-observed narrowband radiance of channel i.

5.2.2.2 Land surface temperature

Land surface temperature (LST) is difficult to estimate from satellite imagery as cloud contamination often biases measurements. In GSIP, LST is derived from the 11μm channel of GOES Imager using a single-channel approach (Sun & Pinker, 2003). A detailed assessment and uncertainty analysis of the single-channel approach was made by Heidinger et al. (2013). The methodology provides the high compatibility and modest accuracy across a variety of satellite imagers, facilitating decadal records of LST. Yet, despite support for this approach, GSIP LST values for the Amazon basin, where cloud and vapor contamination are prevalent, were outside the feasible range and excluded (Figure 5.3).

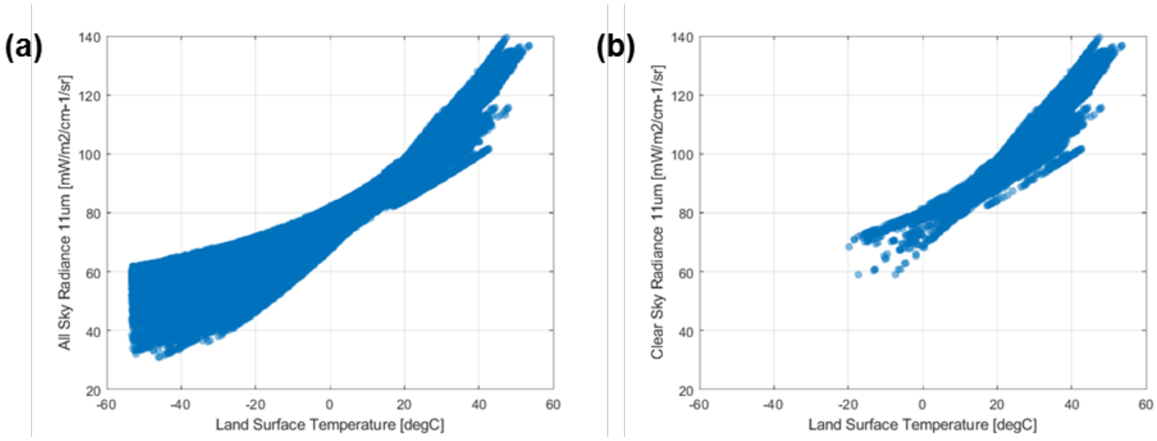

Figure 5.3 Comparison of basin wide 11µm radiance and LST for (a) "all sky" conditions and (b) "clear sky" conditions for a sample hour (July 19, 2015 15:45 UTC). LST values range from -60 to +60oC under all sky conditions which include partial and full clouds. Removal of partial and full cloud conditions (i.e., clear sky) limits the range to -20 to +60oC, outside the feasible temperature range for LST.

In lieu of these "direct" observations, near surface air temperature (at 2m) from the ERA5 reanalysis product ("ERA5 Reanalysis," 2017) was used for model forcing. ERA5 is the fifth generation of reanalysis product produced by the European Centre for Medium-Range Weather Forecasts (ECMWF) and uses a 4D-Var assimilation scheme which couples actual observations with forecast models to produce historical and near-real time estimates of atmospheric and near surface parameters. Single level estimates of precipitation, air temperature, and dew point temperature are provided at hourly temporal frequency and 0.25° spatial resolution. Gridded observations were resampled using a 'nearest-neighbor' approach to harmonize spatial resolutions between GSIP and ERA5.

When air temperature was previously used as a proxy for surface temperature by Xu et al. (2019), MEP modeled energy partitions showed minimal sensitivity to temperature. As air and canopy temperatures can differ as much 7°C (Pau et al., 2018), further sensitivity analysis was performed to quantify parameter uncertainty.

5.2.2.3 Specific humidity

Two parameterizations of specific humidity, q_s, were used to drive the model, both derived from single level ERA5 variables. Given the dew point temperature, T_d, the specific humidity is given as:

$$q_s = \frac{0.622\ e}{p - 0.378e} \tag{5.11}$$

where p is the surface pressure in [Pa] and e is the vapor pressure in [Pa]. Vapor pressure in [hPa] is found using the August-Roche-Magnus approximation of Clausius-Clayperon:

$$e(T_d) = 6.1094 \exp\left(\frac{17.625 T_d}{T_d + 243.04}\right) \tag{5.12}$$

where T_d is the dewpoint temperature in [ºC]. In the absence of observations, q_s may be parameterized as saturated humidity within the stomatal cavity, $q^{sat}(T_s, \psi_s)$. Wang and Bras (2011) give $q^{sat}(T_s, \psi_s)$ as:

$$q_s(T_s, \psi_s) = \varepsilon\left(\frac{e_0}{p}\right) \exp\left(\frac{\lambda}{R_v}\left(\frac{1}{T_0} - \frac{1}{T_s}\right)\right) \exp\left(-\frac{g\psi_s}{R_v T_s}\right) \tag{5.13}$$

where T_0 is the reference temperature taken to 0 ºC, e_0 is the saturation vapor pressure at T_0, p the ambient pressure, and R_v the gas constant for water vapor.

5.2.2.4 Eddy covariance measurements

The MEP ET model was initially validated against eddy covariance (EC) estimations of latent heat and sensible heat for historical data ranging from 1999-2006 (Xu et al., 2019). EC estimations of latent and sensible heat for the 2015-2016 El Nino period are only available for the BR-MA2 and BR-SA1 towers. These towers will be referred to by their common names, "K34" and "K67", to conform with previous discussion. Results and analysis from K67 was also presented in Chapters 3 and 4.

Measurement errors from the EC method are approximately 20% of the total energy budget, resulting in an imbalance between measured net radiation and the component surface energy fluxes (Gerken et al., 2018; Wilson et al., 2002). These errors complicate comparisons between modeled MEP fluxes and observations. Specifically, energy conservation is automatically satisfied following the underlying structure of the MEP solution, while energy conservation of EC measurements is not guaranteed. EC surface energy fluxes are thus corrected using the Bowen Ratio method (Xu et al., 2019). R_n and the Bowen Ratio (B_0) obtained directly from measurements of λE_{OBS} and H_{OBS} is assumed to be valid. The net energy imbalance is redistributed to surface heat fluxes through the system of equations:

$$B_0 = \frac{H_{OBS}}{\lambda E_{OBS}},\ \lambda\tilde{E} = \frac{R_{n\,OBS}}{1+B_0} \tag{5.14}$$

where "OBS" refers to the observed fluxes and $\lambda\tilde{E}$ is the corrected flux.

5.2.2.5 Precipitation

Precipitation is an essential climate variable used to determine conditions of hydrological drought. With limited gaging per unit area, remotely sensed and reanalysis products were used as observational data across the basin. While several products were examined, the primary product used for analysis was the ERA-I/5 reanalysis product. The ERA reanalysis precipitation product has been shown to outperform similar products for Amazonia, where closure of the terrestrial water budget is especially problematic due to sparse gaging (Lorenz & Kunstmann, 2012).

While gaged precipitation is available for both K67 and K34, the historical reliability of the data is unknown. For example, when compared to a gage of known reliability, the reported K67 values were found to grossly underestimate actual precipitation. Given this, and that this analysis is more broadly focused on basin scale processes, ERA data is used for both tower scale and basin scale comparisons.

5.3 Results

5.3.1 Ambient conditions at tower sites

Surface energy fluxes were simulated using tower forcing from K67 and K34 for the period 06/01/2015 – 06/01/2016, which includes the 2015-2015 ENSO dry season. Climate conditions from the two towers show similar seasonality, with the dry season period showing increased temperatures and decreased precipitation at both sites (Figure 5.4). Net radiation remains relatively constant for K34, showing little seasonality. K67 shows a slight decline in R_n with the onset of the 2016 wet season. As previously mentioned, the reliability and continuity of tower precipitation gages in remote regions is dubious at best. This is highlighted by the precipitation values reported at K34 (Figure 5.4, middle panel). Despite having higher mean annual precipitation, reported mean monthly precipitation at K34 is lower than K67 for all months except January, March, and April 2016. These potential gaging issues lends further support for the use of the ERA reanalysis product over tower product for further analysis.

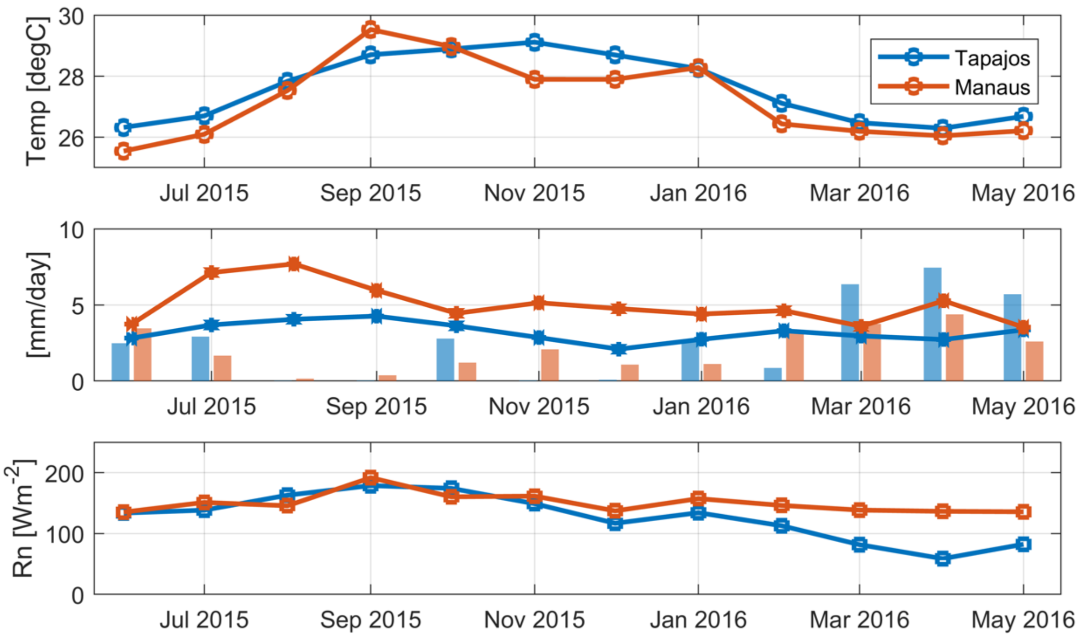

Figure 5.4 Mean monthly observational data (6/2015 – 6/2016) from the K67 (Tapajós) and K34 (Manaus) sites with: (top panel) air temperature [ºC]; (middle panel) precipitation as bars and ET as lines, both in [mm day^{-1}]; (bottom panel) net radiation [W m^{-2}].

Site level precipitation (ERA) highlights the differences in seasonality between the K67 and K34 sites, with K67 exhibiting stronger seasonality than K34. An area is considered under dry season conditions when precipitation drops below 100mm per month. K67 more consistently falls below this threshold with dry season conditions persisting 3-4 months as opposed to the 1-2 months at K34. The difference between the two sites is especially pronounced in the 2005 and 2010 basin drought years (Figure 5.5). Monthly precipitation from the 2015 ENSO event highlights the unique nature of the drought event, with monthly precipitation values at both K67 and K34 reaching near or below dry season conditions from August 2015 – January 2016.

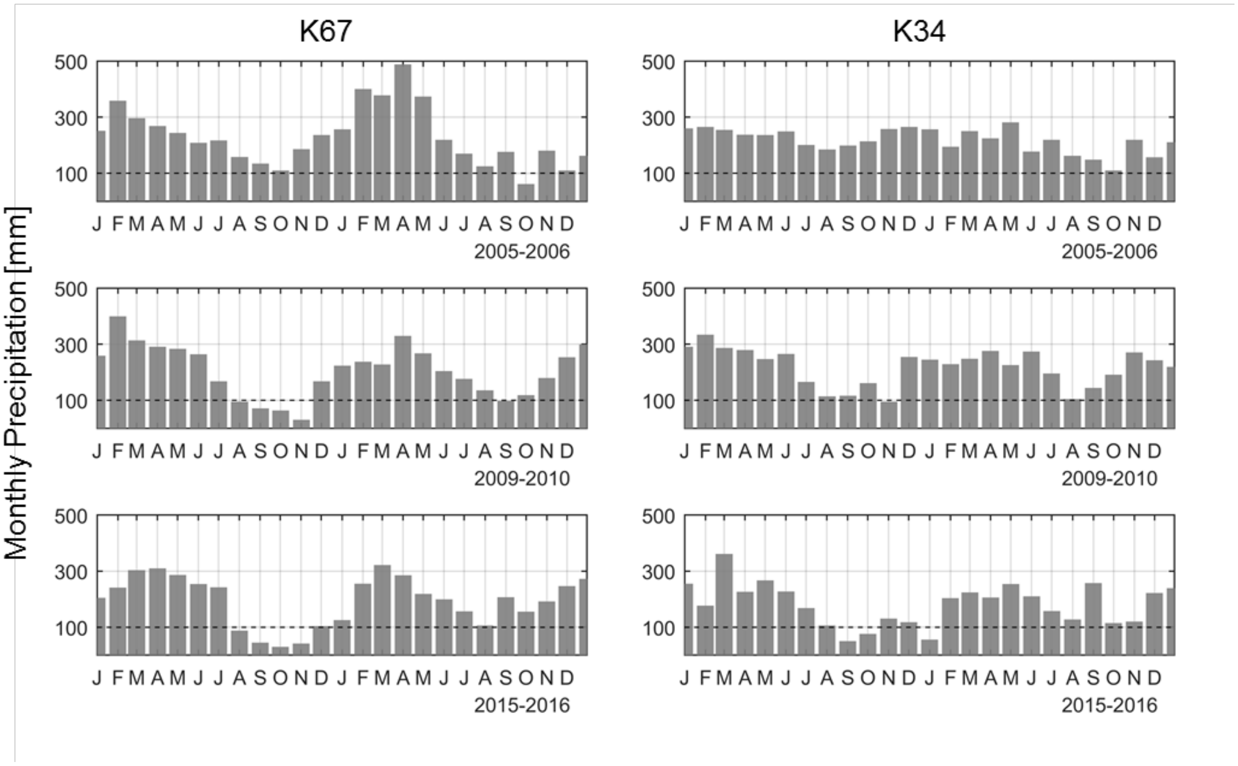

Figure 5.5 ERA monthly precipitation for K67 and K34 for the 2005, 2010, and 2015 drought periods with antecedent and subsequent periods. The 100mm “dry season threshold” is plotted as a black dashed line following Restrepo-Coupe et al. (2013).

4.3.2 Tower-driven MEP

The performance of the MEP modeled surface energy fluxes for the 2015-2016 was evaluated using hourly Bowen ratio corrected energy fluxes from K67 and K34 (Fig. 5.6). Model performance was assessed by fitting a linear model to a one-to-one comparison of the modeled and simulated fluxes. Over the entire data period, which includes both wet and dry seasons, modeled performance is high at the hourly resolution. Modeled ET had the strongest performance at both K67 and K34 with regression statistics of m = 0.96, 1.03 and R^2 = 0.91 and 0.93, respectively. Modeled sensible heat, H, showed weaker performance with m = 1.09, 0.94 and R^2 = 0.82, 0.79 at K67 and K34 sites, respectively. When compared to the 1999-2006 period modeled by Xu et al. (2019), model performance at K67 decreased, with the R^2 value declining from 0.95 to 0.91. Visual inspection highlights increased scatter, with MEP *overestimating* latent heat fluxes.

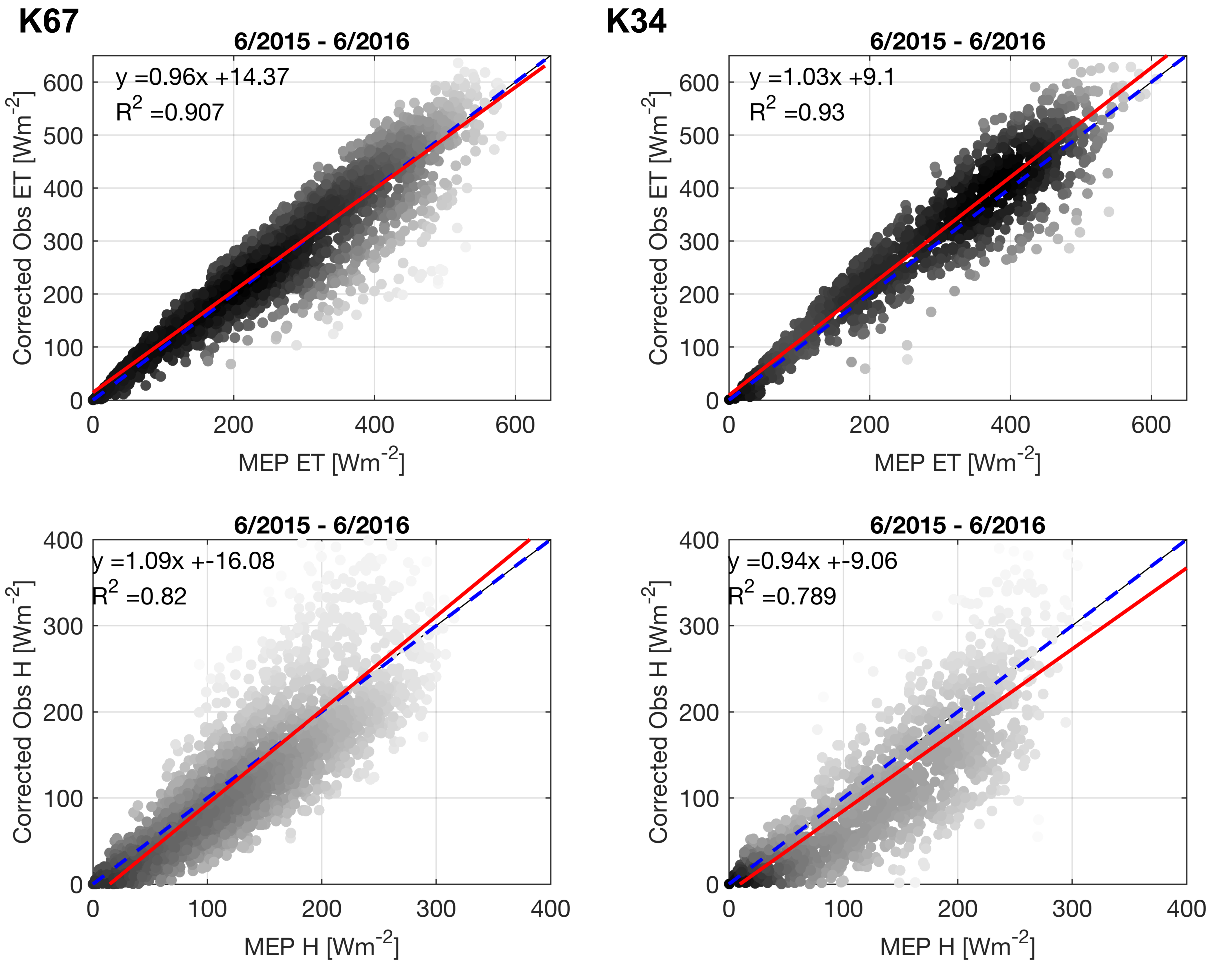

Figure 5.6 A comparison of MEP modeled hourly latent and sensible heat fluxes and corrected tower observations for (left panels) K67-Santarém and (right panels) K34-Manaus for 6/2015 – 6/2016. One to one reference line is given in dashed blue and a linear regression fit to the data as a red solid line. Regression statistics are noted in the upper right corner of the plot.

The diurnal partition of surface fluxes shows similar patterns of mean modeled and observed energy fluxes (Fig. 5.7). Mean observed ET fluxes have a slightly higher amplitude than modeled ET for both sites. The modeled sensible heat partition shows less variability than the observed. Net radiation is displayed for reference, but is the same between modeled and observed as R_n serves as an input variable for the MEP model.

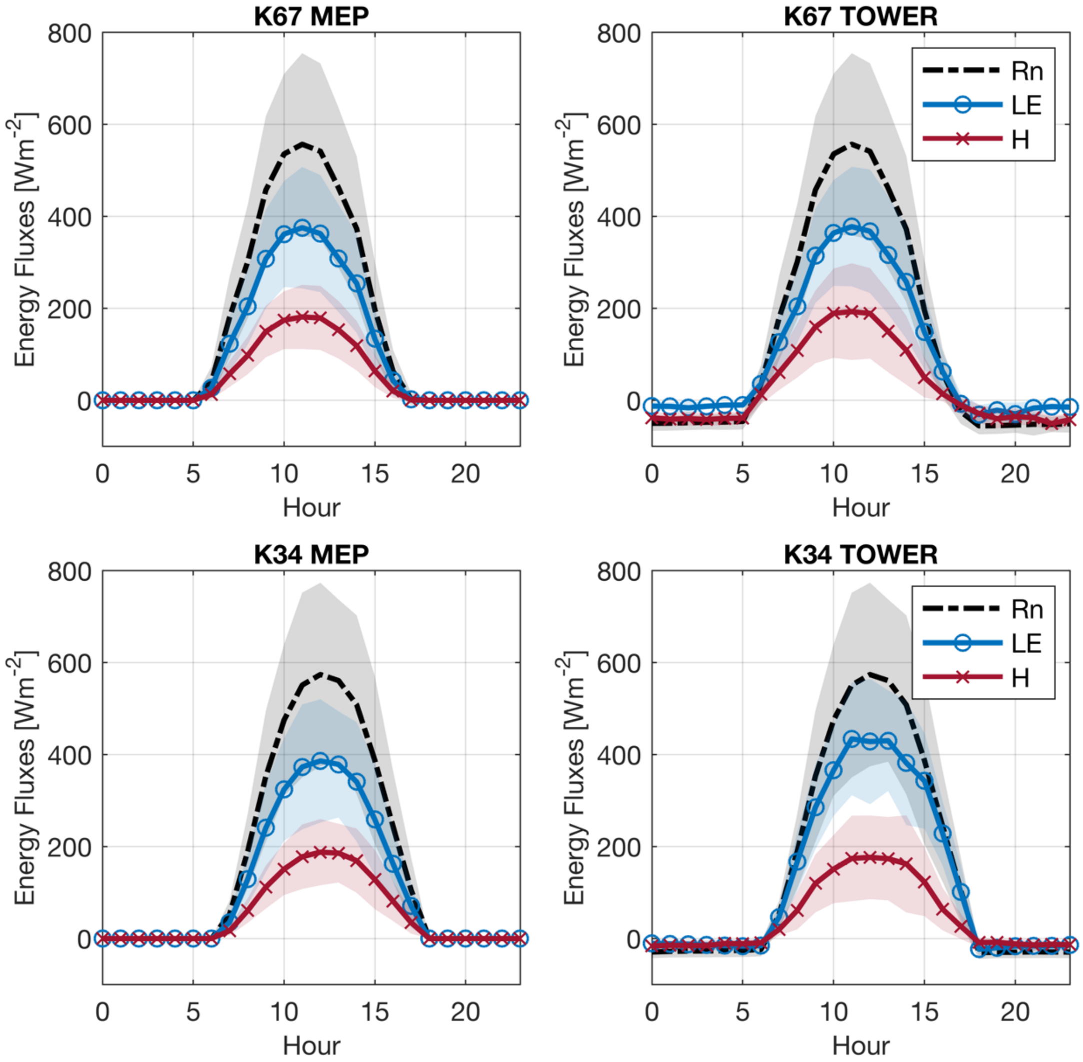

Figure 5.7 Diurnal surface energy partition for the modeled and observed fluxes for (top panels) K67 and (bottom panels) K34. Markered lines represent mean values with colors given by the legend. The shaded regions of the same color representing one standard deviation from the mean.

5.3.3 Performance of MEP model during 2015 ENSO dry season

The marked decrease in MEP performance for K67 prompted a detailed analysis of the temporal evolution of performance during the onset of the unprecedented dry season. As an illustrative example, the time series of modeled and observed daytime ET for a two week period at the onset of the dry season (9/16/2015-9/30/2015) and deep in the dry season (12/16/2015-

12/31/2015) is presented (Figure 5.8). At the onset of the dry season, MEP is able to capture observed ET, but two months later, the magnitudes of MEP modeled fluxes are substantially higher than observations.

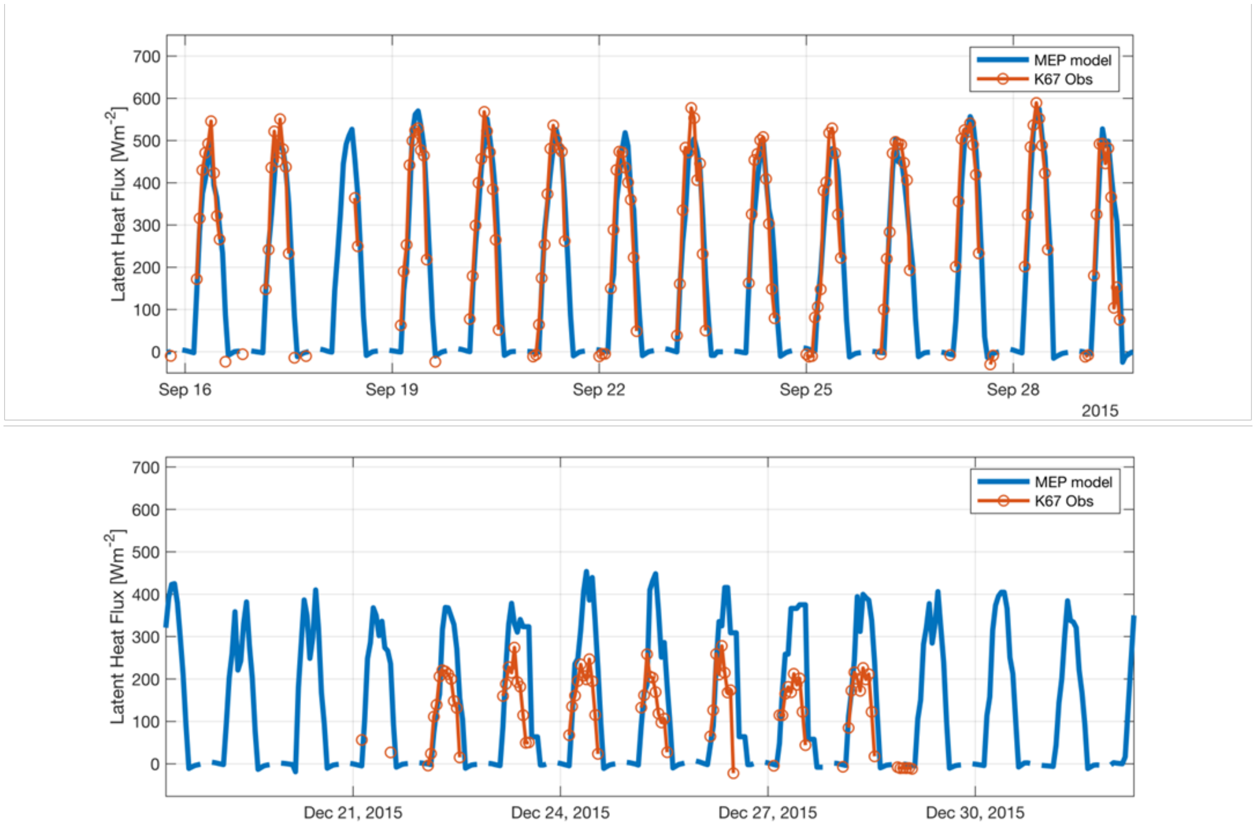

Figure 5.8 Time series of model and observed daytime ET at K67 for (a) 9/16/2015-9/30/2015 at the onset of the dry season and (b) 12/16/2015-12/31/2015 in the heart of the dry season. Modeled fluxes are in blue and observations in orange. Periods without markers are from data availability gaps.

Hourly comparisons were made for three periods, pre-, during, and post-water limitation: 6/01/2015-10/31/2015, 11/01/2015-2/29/2016, and 3/1/2016-7/31/2016 respectively. Model performance for K67 was high during the pre- and post-water limitation periods, with $R^2 = 0.97$ for both and m = 1.08 and 1.01 respectively (Fig 5.9 top row). The water limitation period showed the lowest model performance with $R^2 = 0.84$ and m = 0.74. Poor performance was biased during at magnitudes >100 Wm^{-2}, values that typically occur in the midday. During the midday, MEP over-estimated ET by as much as a factor of 2. A similar comparison of results from the K34 tower did not show any appreciable change in the model performance across the dry season (Fig. 5.9 bottom row).

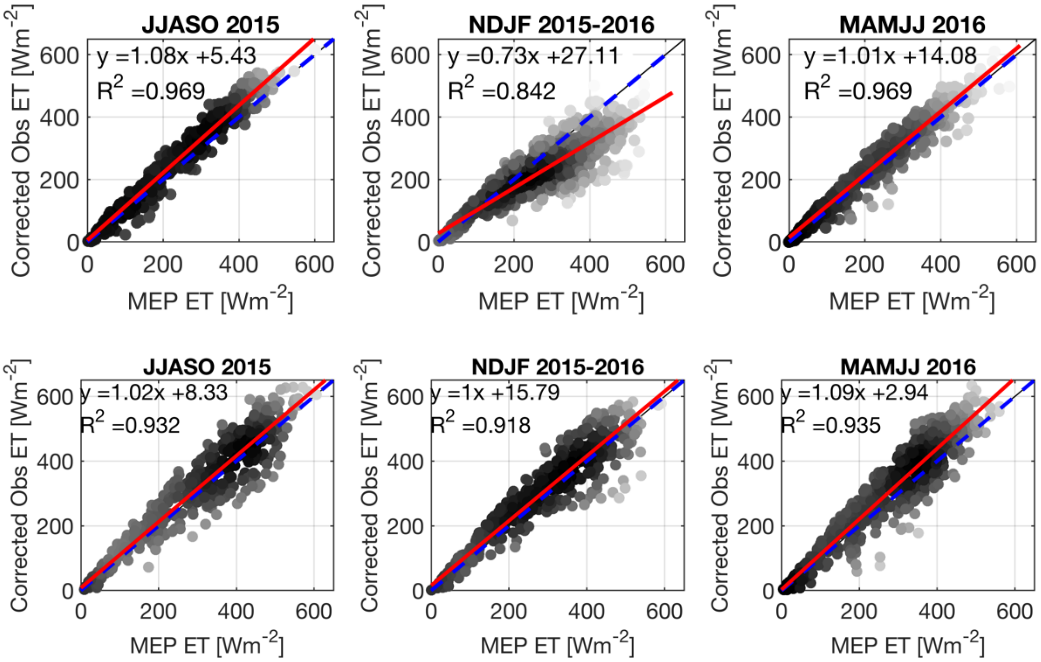

Figure 5.9 Comparison of corrected observations of ET versus MEP modeled ET for the pre-, during, and post-water limitation periods for (top row: K67; bottom row: K34). One to one reference line is given in dashed blue and a linear regression fit to the data as a red solid line. Regression statistics are noted in the upper right corner of the plot.

5.3.4 Satellite-driven MEP

The MEP model was forced using observations from GSIP and ERA5 to estimate ET at 4 km spatial resolution and hourly temporal resolution. A comparison with hourly corrected ET from the K34 and K67 show model performance at m = 0.71 and 0.82 and R^2 = 0.57 and 0.62 for the period spanning 11/2015-2/2016 (Figure 5.10). Given the different spatial footprints between EC towers and pixel resolution of the satellite imagery, weaker model performance is expected.

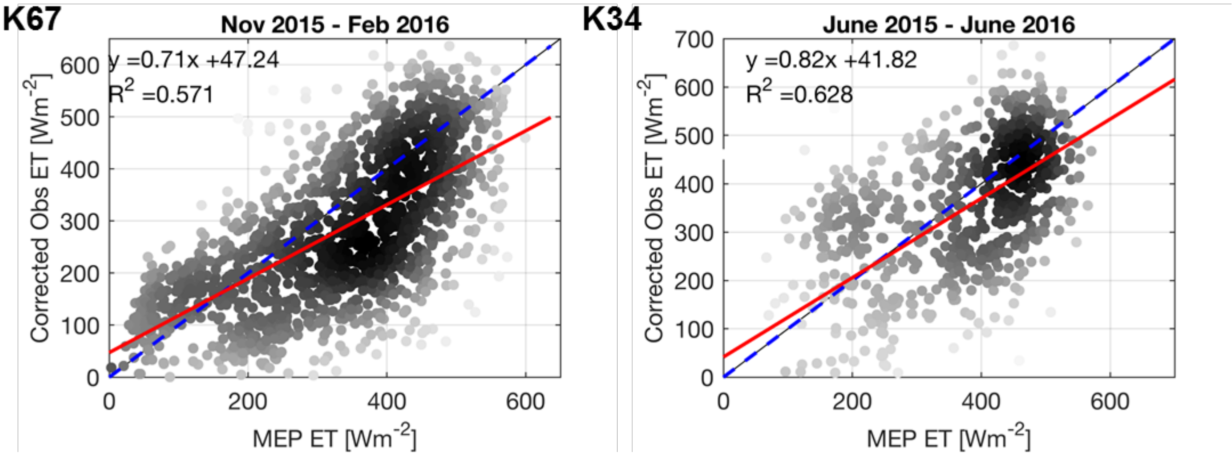

Figure 5.10 Comparison between satellite driven MEP fluxes and corrected tower observations for (left) K67 and (right) K34. One to one reference line is given in dashed blue and a linear regression fit to the data as a red solid line. Regression statistics are noted in the upper right corner of the plot.

A more detailed analysis at the K67 site shows that the satellite driven model exhibited the same water limited behavior as the tower forced simulations (Figure 5.11). Model performance from 7/2015-10/2015 is stronger with m = 0.83 and $R^2 = 0.68$, versus the water limited period which has m = 0.52 and $R^2 = 0.51$.

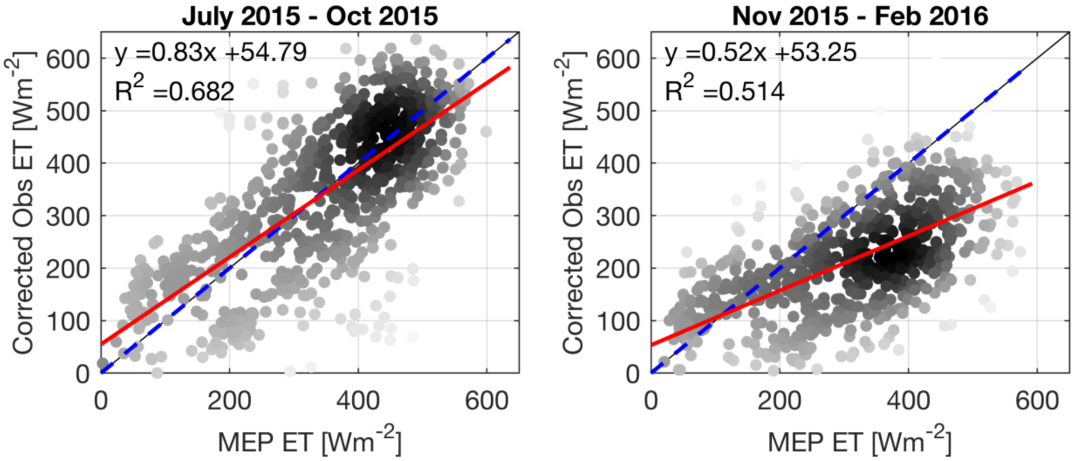

Figure 5.11 Comparison between satellite driven MEP fluxes and corrected tower observations for (left) the non-limited and (right) water-limited periods. One to one reference line is given in dashed blue and a linear regression fit to the data as a red solid line. Regression statistics are noted in the upper right corner of the plot.

An illustrative example (9/1/2015-9/15/2015) shows the ability of the satellite-driven

MEP model to capture diurnal variation in ET at the K67 site (Figure 5.12). These results highlight the utility of using remotely sensed observations to drive the MEP model and estimate ET in areas without high fidelity data. However, differences in land-use and micrometeorological variability may result in inaccuracies when downscaling results. As such, estimates are more appropriate at larger scales.

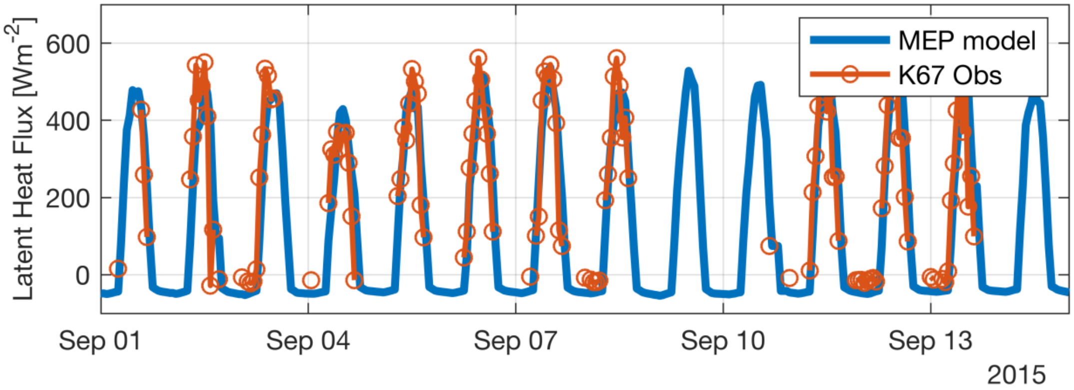

Figure 5.12 Time series of model and observed daytime ET at K67 for 9/1/2015-9/15/2015. Modeled fluxes are in blue and observations in orange. Periods without markers are from data availability gaps.

Mean monthly estimates of surface energy fluxes from the GSIP driven MEP model capture the seasonality in surface energy fluxes expected from the Amazon region (Figure 5.13). Net radiation R_n decreases during the wet season periods as cloud cover dominants the area and increases during the dry season periods. The partition of latent heat and sensible heat follows, showing seasonality across the basin.

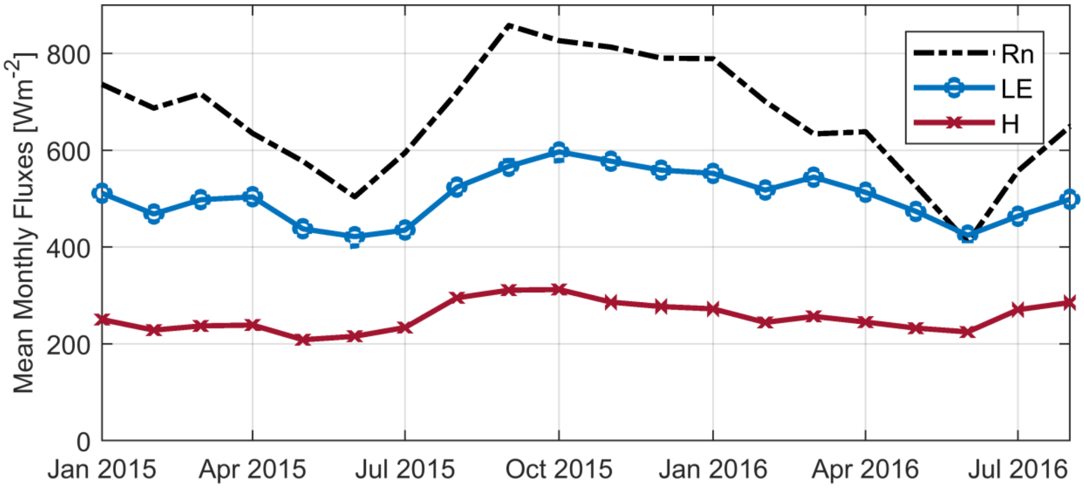

Figure 5.13 Mean monthly surface energy fluxes for the Amazon Basin for 1/2015 – 8/2016. The legend gives line styles for net radiation, latent heat, and sensible heat energy fluxes.

5.4 Discussion

5.4.1 Performance of MEP model during ENSO droughts

The results highlight excellent skill of the MEP model during periods with no soil control on energy partition and the inability of the model to capture observed ET under *severe* water limitation, with actual ET being constrained due to ecophysiological feedbacks. Previous ENSO drought periods were examined to determine if this failure was recurrent or if the conditions of the 2015-2016 ENSO event were unique. MEP estimated ET was compared to corrected tower observations for ENSO anomaly periods as defined by Panisset et al. (2018). For K67, MEP performance was strong for the JJAS 2005 and 2010 anomalies ($R^2 = 0.95$, 0.97 respectively), but there is a large reduction in model performance for the ONDJ 2015 period ($R^2 = 0.84$). In contrast, K34 shows the weakest agreement during the JJAS 2005 period ($R^2 = 0.76$), opposed to JJAS 2010 and ONDJ 2015 where agreement is relatively strong ($R^2 = 0.94$, 0.90 respectively). While agreement is high during ONDJ 2015 for K34, there is visually more scatter present at high magnitudes, suggesting slightly constrained transpiration.

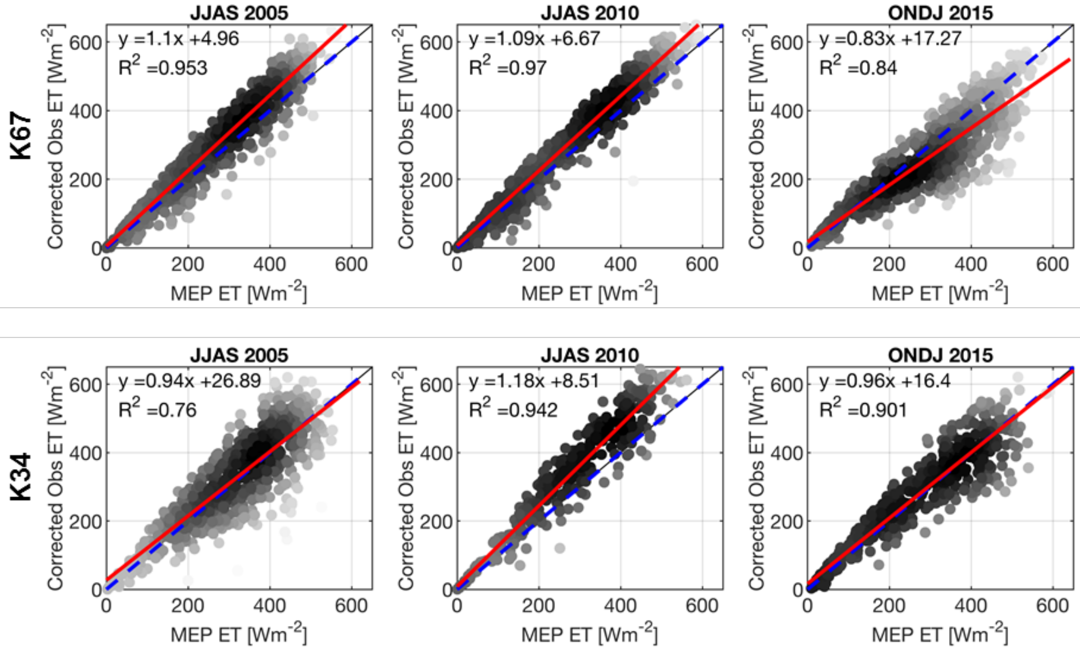

Figure 5.14 Comparison of corrected observations of ET versus MEP modeled ET for three significant drought periods at the K67 (top) and K34 (bottom). One to one reference line is given in dashed blue and a linear regression fit to the data as a red solid line. Regression statistics are noted in the upper right corner of the plot.

This comparison highlights the ability of MEP to capture ET fluxes during anomalous dry seasons up to a certain severity threshold. This is not to say that during the 2005 and 2010 events transpiration was not limited at the individual tree scale. Instead, it suggests that to some degree, decrease in ET during mild water limitation is captured by state variables such as specific humidity and air temperature. When less net radiation is partitioned into latent heat, it will become sensible heat (under the zero ground flux assumption). This increase in sensible heat will be partially reflected by rising air temperature. Decreases in ET may also cause a decline in specific humidity imposing a further feedback to the MEP model.

5.4.2 Identifying threshold variables

Ambient conditions were examined during the water limitation period at K67. Vapor pressure deficit (VPD) is a key metric for determining stomatal response. When VPD values become too high, this may trigger stomatal closure, decreasing water loss at the leaf level and ET at the system scale. The ratio of observed and modeled ET was examined for the 2015-2016 data period and compared to the VPD during that same time period. A ratio of 1 represents unity between observed and modeled fluxes, while values <1 represent periods when MEP is over-estimating ET. Data was resampled at 5-day mean value to remove signal noise. The ratio hovers around 1 during the pre-water limitation period and declines to around 0.8 during the water limitation period before rebounding around March 2016. VPD values show slight seasonality, with higher 5-day average values during the water limitation period (Fig. 5.15).

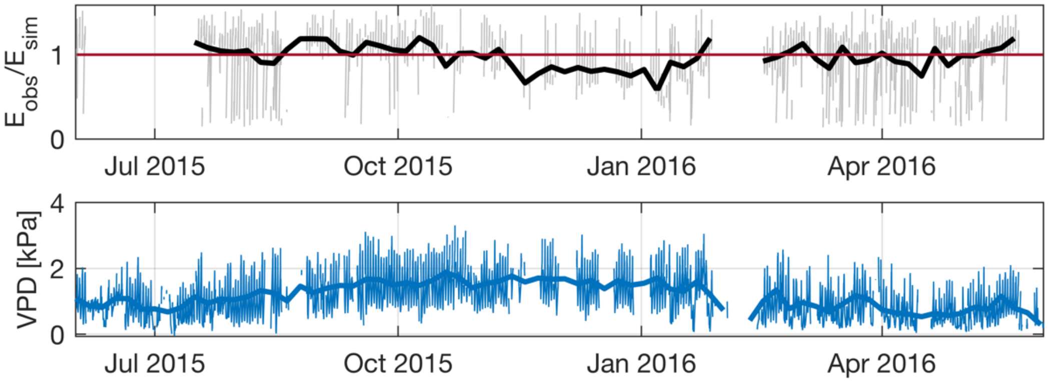

Figure 5.15 Time series analysis of the observed versus simulated ET ratio (top) and observed VPD (bottom). The hourly observations are shown as the lighter line in the plot while a resampled 5-day mean is shown as a bold line. The unity line is shown in red for the ratio time series.

When 5-day average values of the ET ratio and VPD are compared, a clear demarcation can be seen for the lowest ET ratios (Fig. 5.16). While ratios of 0.8 and higher occur for the range of VPD values, the lowest ratios only occur at mean VPD values higher than 1.25 kPa. While the correlation is not strong enough to build a correction model purely on VPD, it does present a potential avenue for future research for correcting MEP fluxes during periods of severe water limitation.

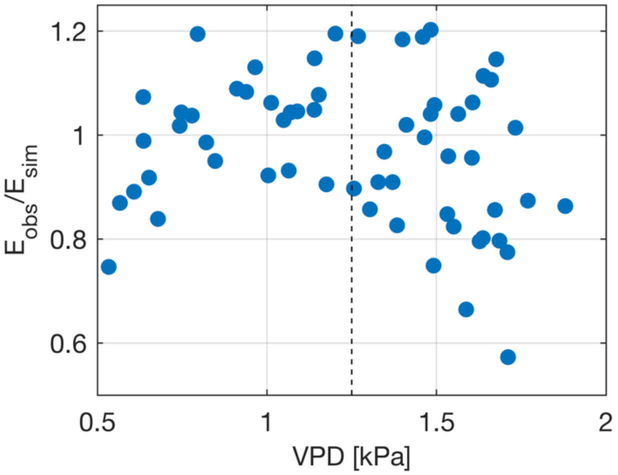

Figure 5.16 5-day mean values of the ratio between observed ET and simulated ET and observed VPD at K67. The comparison includes both wet and water-limiting periods. The 1.25 kPa threshold is denoted as a dashed black line.

5.4.3 Improved estimates of potential ET

While MEP was unable to capture observed ET during the period of severe water limitation for K67, it retains value as an estimation of potential ET. Potential ET is an important analysis variable and is used for model forcing. Models of PET are subject to the same parameterizations mentioned for physical models of ET, with parsimonious formulations only modestly capturing observations. For example, The Hargreaves & Samani (1985) formulation used in Chapter 3 as forcing is a parsimonious model requiring only single-level air temperature for parameterization. For data scarce spaces this is attractive, but performance is not robust (Figure 5.17). Requiring only 3 inputs – air temperature, specific humidity, and net radiation – MEP may serve as a parsimonious model of PET that does not sacrifice performance during non-limiting periods.

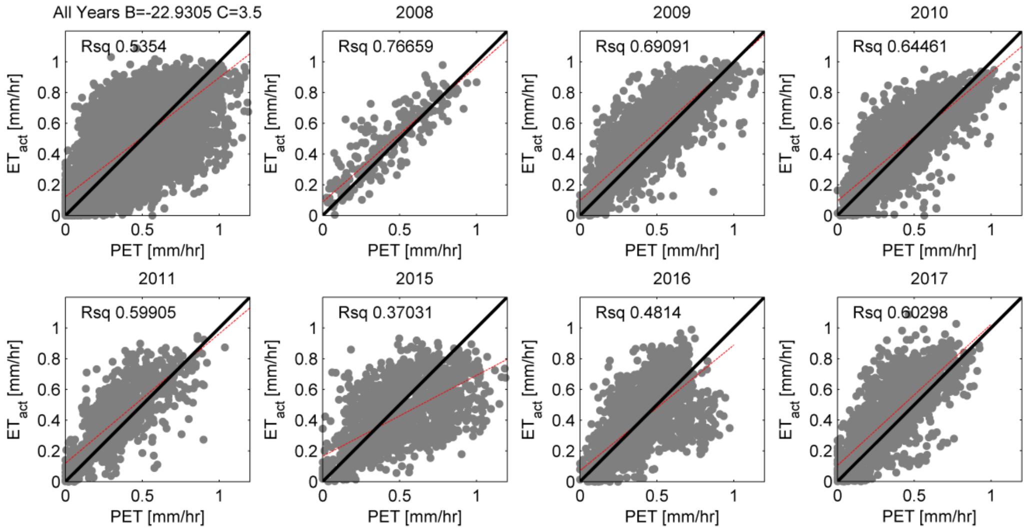

Figure 5.17 Hargreaves-Semani estimation of PET using K67 air temperature. PET was calibrated using an optimization function with HS parameters of B = -22.9 and C = 3.5. Model performance is much weaker than that found with the MEP method.

5.4.4 Model forcing needs

A sensitivity analysis of model forcing showed MEP is most sensitive to net radiation, and to a lesser degree, air temperature (Xu et al., 2019). Basin scale analysis indicated that the source of q_s may be important to overall analysis of basin scale processes. As much attention has been paid to the uncertainty of net radiation and temperature by this previous work, this discussion will focus primarily on specific humidity.

Direct observations of q_s were not available from the GSIP product. A study by Ruckstuhl et al., (2007) suggests that q_s may be derived from total precipitable water (TPW) for high altitude environments. While not high altitude, this approach was nevertheless tested using radiosonde returns collected at Belterra, Para, Brazil (a small town within the vicinity of the Tapajos National Forest). Near surface q_s was compared to TPW, but no significant correlation was found for any time period (not shown).

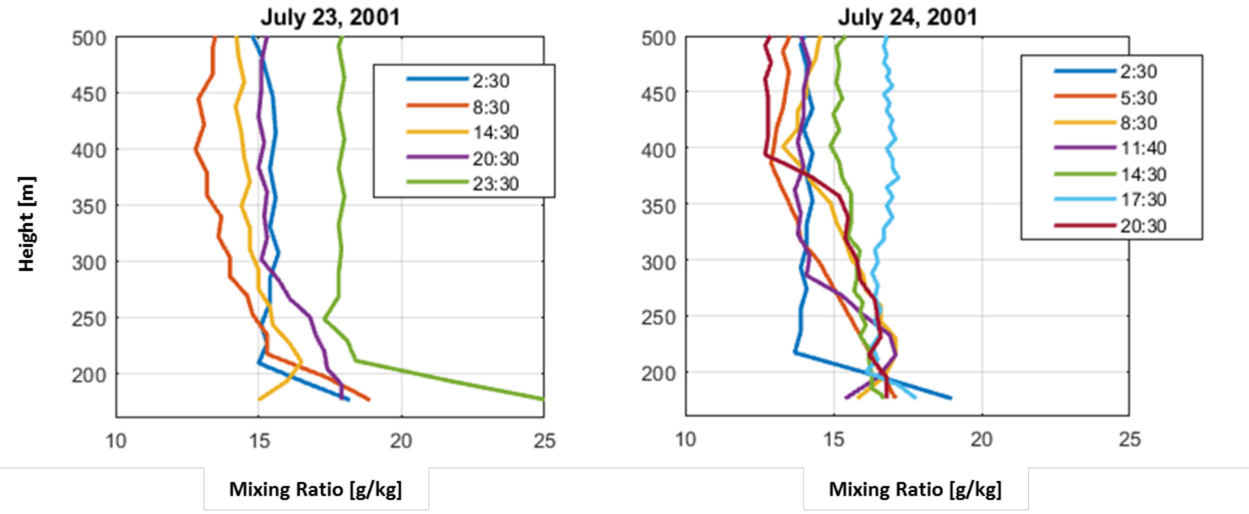

Figure 5.18 Radiosonde data for Belterra, Pará, Brazil for 7/23/2001 and 7/24/201 showing the mixing ratio as a function of height. Uniform layers of moisture up through 500m prohibit estimation of surface specific humidity using TPW.

5.5 Summary

The Maximum Entropy Production model provides a parsimonious model for estimation of surface energy fluxes at a variety of scales. Previous applications of the model have shown strong performance in the Amazon Basin region. This chapter applied the model to the 2015-2016 ENSO period using tower and satellite forcing to examine the feasibility of using MEP at fine spatiotemporal resolutions under extreme drought events. The model performed well under mild water limitation, but performance declined under severe water limitation: MEP over-estimated latent heat fluxes, in some instances, by a factor of 2. VPD was explored as a potential proxy to indicate severe water limitation and thus pointing to the need of adjusting the model behavior but further work is needed. Despite this, the MEP model may serve as a good proxy for ET for well-watered to mild-water limitation and to provide estimates of potential ET during extreme water limitation. Basin scale estimates of ET using the GSIP satellite product captured local diurnal variability in ET and basin-scale seasonality of net radiation, latent heat, and sensible heat fluxes.

Appendix 5A Eddy covariance and satellite data information

Table 5.1 FLUXNET eddy covariance towers located in the Amazon Basin region (Restrepo-Coupe et al., 2013) used for ground truthing of the MEP method.

Site ID	Name	Lat/Long	Description	Years Available
BR-CAX	Caxiuana	-1.720 / -51.459	Tropical lowland forest	1999 – 2003
BR-MA2	Manaus	-2.609 / -60.209	Tropical rainforest	1999 – 2006
BR-SA1	Santarem K67	-2.857 / -54.959	Tropical rainforest	2002 – 2006
BR-SA2	Santarem K77	-3.012 / -54.537	Pasture/agriculture	2000 – 2005
BR-SA3	Santarem K83	-3.018 / -54.971	Tropical rainforest	2000 – 2004
BR-BAN	Bananal Island	-9.821 / -50.149	Seasonally flooded forest	2003 – 2006
BR-RJA	Reserva Jaru	-10.095 / -62.358	Tropical dry forest	1999 – 2002

Table 5.2 GSIP v3 variables, available from the NOAA Comprehensive Large Array-data Stewardship System (http://www.class.noaa.gov/)

Variable	Unit
Radiative Fluxes	
shortwave downward surface radiative flux	W m^{-2}
shortwave upward surface radiative flux	W m^{-2}
longwave downward surface radiative flux	W m^{-2}
longwave upward surface radiative flux	W m^{-2}
PAR downward surface diffuse radiative flux	W m^{-2}
PAR downward surface diffuse clear-sky radiative flux	W m^{-2}
PAR upward surface diffuse clear-sky radiative flux	W m^{-2}
shortwave downward TOA radiative flux	W m^{-2}
shortwave upward TOA radiative flux	W m^{-2}
shortwave upward TOA clear radiative flux	W m^{-2}
longwave upward TOA radiative flux	W m^{-2}
Cloud Properties	
cloud mask (cloudy, probably cloudy, probably clear, clear)	0-3
cloud type (clear, fog, liquid, supercooled/mixed, opaque ice, cirrus, multilayered)	0-6
cloud type layer height (clear, low, middle, high)	0-3
cloud top temperature	K
cloud top pressure	HPa
cloud liquid water path	kg m^{-2}
cloud ice water path	kg m^{-2}
cloud optical depth	-
Temperature and Column Properties	
surface temperature	K
radiative temperature	K
total column ozone	atm cm
total precipitable water	cm
snow fraction	fraction 0-1

Chapter 6 – Summary and Future Directions

6.1 Summary of dissertation work

6.1.1 Ch 2: Root structure and lateral interactions

A coupled model of three-dimensional root hydraulic architecture and soil water dynamics was used to explore the impact of below-ground structure, specifically degree of root system interaction on water uptake during water limitation. A root competition index was introduced to help classify the degree of below ground interaction and formed the basis of a cluster-based sampling protocol. Root hydraulic architectures of different form and lateral interaction were tested, highlighting a trade-off between carbon investment in root structure and water uptake. Trees which faced water limitation under the low interaction scenario increased their water access by expanding their root systems laterally, but this gain in benefit declines as the system becomes more homogeneous. To achieve additional water resources and alleviate water stress, systems would need to root deeper or by alter functional properties like root hydraulic conductivity. This suggests a system scale optimal configuration where roots expand laterally to exploit all available soil resources, homogenizing the field, but no further. Once the system has reached a state of homogeneity, then additional benefit can only be gained by utilizing other root traits.

6.1.2 Ch 3: Functional diversity and response to ENSO dry seasons

The work of chapter 2 is expanded to examine the role of root functional strategy on water uptake processes during the unprecedented 2015-2016 ENSO dry season for a highly seasonal rainforest located in the eastern Amazon River Basin. The work compiles heterogeneous streams of data to compose a three-dimensional representation of root structure under three separate scenarios of rooting depth. Root water uptake is simulated during the dry season showing the onset of severe water limitation and the constraint of water uptake. Water stress is alleviated somewhat by partitioning of roots along different depth strata, supporting prior evidence of root niche segregation or hydrologic niche partitioning.

6.1.3 Ch 4: Sap flow and the hidden signals

While the representation of below-ground structural and functional dynamics provide valuable insights into ecophysiological feedbacks and controls on uptake during water limitation, metrics are needed to quantify this response *in situ*. Measurements of sap flow velocity have proliferated as access to low-cost sensing technology has risen. Chapter 4 presents sap flow measurements for four trees at FLONA Tapajós, a highly seasonal forest in the eastern Amazon River Basin. Utilizing thermodynamic theory, changes in raw baseline sap flow signal are used to quantify changes in wood moisture content during the 2015-2016 dry season. Decreases in moisture content strongly correlated with decreases in stem water potential, a state variable that is used as a proxy for plant water stress. The identification of this low frequency signal increases the utility of sap flow measurements in general, allowing one sensor to quantify water quantity and hydraulic status.

6.1.4 Ch 5: Feasibility of hourly scale PET estimation

The maximum entropy production model provides a parsimonious model for estimation of surface energy fluxes at a variety of scales. Previous applications of the model have shown strong performance in the Amazon Basin region. This chapter applies the model to the 2015-2016 ENSO period using tower and satellite forcing. The model performs well under mild water limitation, but performance declines under severe water limitation with the model over-estimating latent heat fluxes by a factor of 2. VPD was identified as a potential variable that may serve as a correction or indicator of model behavior under severe water limitation. Despite this, the MEP model may serve as a good proxy for potential ET at the tower and basin scale. Basin scale estimates of ET using the GSIP satellite product captured local diurnal variability in ET and basin-scale seasonality of net radiation, latent heat, and sensible heat fluxes.

6.2 Future directions

Disturbance plays a major role in shaping forest structure and function (Pan et al., 2011), including water cycling. In the upper-Midwest, disturbances have largely transitioned away from severe events that cause stand replacement, to more moderate disturbances resulting in only partial canopy defoliation or species loss (Birdsey et al., 2006; Canham et al., 2013; Cohen et al., 2016; Lu et al., 2015; Luyssaert et al., 2007; Pregitzer & Euskirchen, 2004; Radeloff et al., 2012; Williams et al., 2012). These subtler disturbances include insect-infestation, pathogens, wind, age-related senescence, and partial harvest (Birdsey et al., 2006; Clark et al., 2010; Cohen et al., 2016; Hicke et al., 2012; Williams et al., 2012), which contribute to a gradient of disturbance intensities across the landscape. Unlike stand-replacing disturbance, moderate disturbances tend to increase canopy structural complexity (Hardiman et al., 2011), with entirely different consequences for ecosystems (Anderegg, 2015; Dietze & Matthes, 2014; Peters et al., 2013; Trumbore et al., 2015) . Research on the impact of disturbance severity on ecosystem water cycling has been limited and overall responses difficult to disentangle, with many studies reporting nonlinear or conflicting responses (see review by Adams et al. (2012)). Beyond the immediate consequences of disturbance, further questions arise surrounding the legacy of disturbance on forest water cycling and the resilience of restructured forests to climate change.

Beyond changing the above-ground landscape, tree mortality from disturbance also alters the below-ground landscape. A future direction for the work presented here would be to study the impact of disturbance severity on the spatiotemporal evolution of forest water cycling using computational models of below-ground structure and root water uptake. The results from Chapter 2 demonstrated that root lateral interaction has a significant impact on the ability of individuals to meet their demand and also where they access the majority of their water. The removal of individuals from a stable system may have important implications for forest water cycling and forest management under changing climate. This type of work can also be used to inform hypotheses and data acquisition at ongoing disturbance experiments. A current example is the Forest Threshold Resilience Experiment (FoRTE) currently ongoing at the University of Michigan Biological Station (Fig. 6.1). This experiment is examining the impact of disturbance severity from a variety of angles including carbon and nutrient cycling. A natural next step of this experiment would be to examine water cycling.

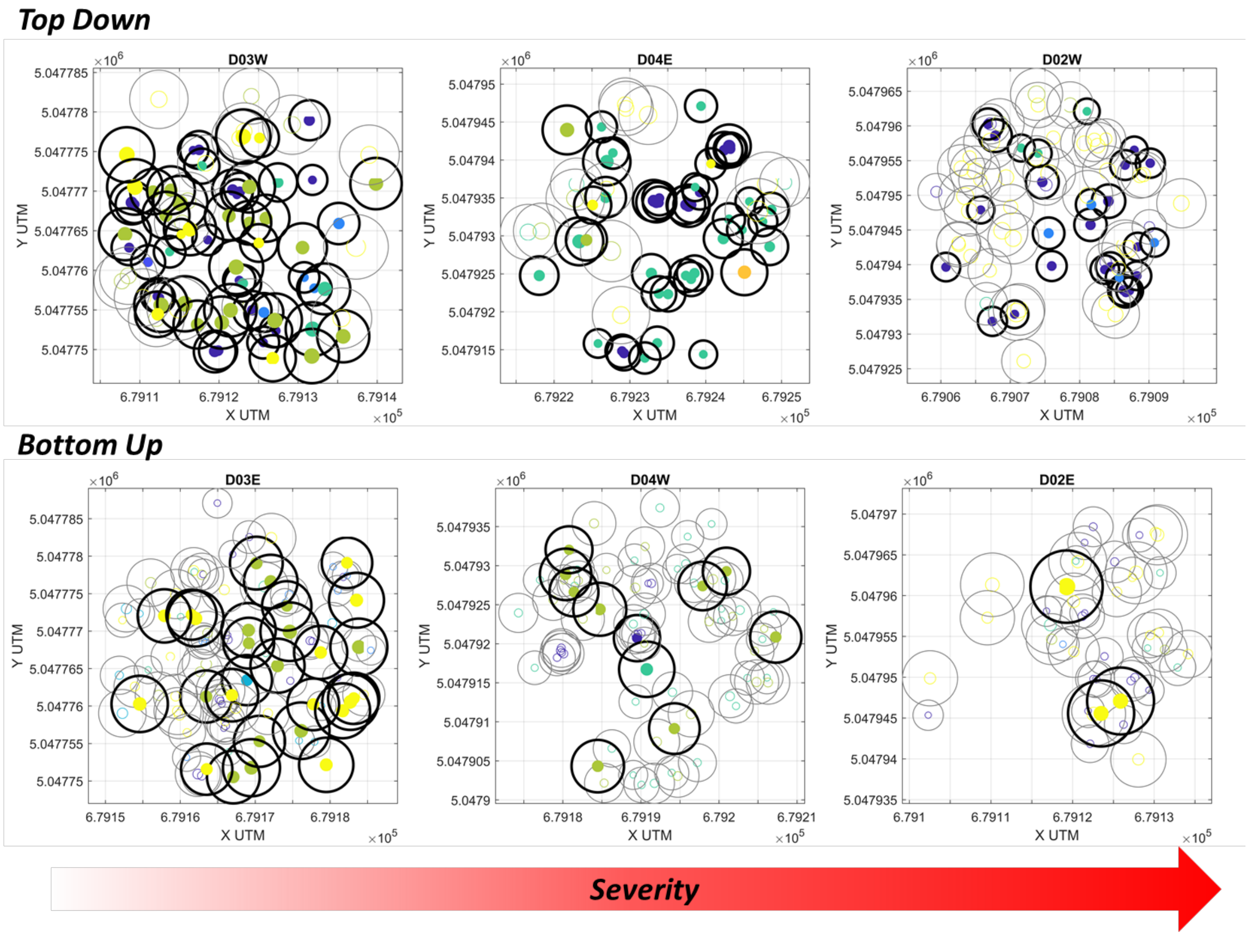

Figure 6.1 Illustrative example of root lateral interaction changes as a function of disturbance severity. Data was taken from the FoRTE experiment currently being conducted at the University of Michigan Biological Station.

An additional future direction would be to further examine the hidden signals found in long term sap flow data. The results from this chapter found that the low frequency signal embedded in continuous TDP sensors may be used as a proxy for hydraulic state in tropical rainforest trees. This may be further explored by comparing the low frequency signal with measurements of wood moisture content as gathered by ruggedized capacitance sensors (Matheny et al., 2015). This comparison could help draw a more direct comparison between actual wood moisture content and hydraulic state instead of relying purely on relative measures of moisture content. The proliferation of TDP technology means that with further testing, this methodology has the potential to be applied across ecosystems to help elucidate plant hydraulic state in real-time.

References

Adams, H. D., Luce, C. H., Breshears, D. D., Allen, C. D., Weiler, M., Hale, V. C., et al. (2012). Ecohydrological consequences of drought- and infestation- triggered tree die-off: insights and hypotheses. *Ecohydrology*, *5*(2), 145–159. https://doi.org/10.1002/eco.233

Allen, C. D., Macalady, A. K., Chenchouni, H., Bachelet, D., McDowell, N., Vennetier, M., et al. (2010). A global overview of drought and heat-induced tree mortality reveals emerging climate change risks for forests. *Forest Ecology and Management*, *259*(4), 660–684. https://doi.org/10.1016/j.foreco.2009.09.001

Anderegg, W. R. L. (2015). Spatial and temporal variation in plant hydraulic traits and their relevance for climate change impacts on vegetation. *New Phytologist*, *205*(3), 1008–1014. https://doi.org/10.1111/nph.12907

Ansley, R. J., Boutton, T. W., & Jacoby, P. W. (2014). Root Biomass and Distribution Patterns in a Semi-Arid Mesquite Savanna: Responses to Long-Term Rainfall Manipulation. *Rangeland Ecology & Management*, *67*(2), 206–218. https://doi.org/10.2111/REM-D-13-00119.1

Aparecido, L. M. T., Santos, J. dos, Higuchi, N., Kunert, N., Aparecido, L. M. T., Santos, J. dos, et al. (2019). Relevance of wood anatomy and size of Amazonian trees in the determination and allometry of sapwood area. *Acta Amazonica*, *49*(1), 1–10. https://doi.org/10.1590/1809-4392201800961

Arney, J. D. (1973). *Tables for quantifying competitive stress on individual trees* (Inf Report No. BC-X-78) (p. 10). Pacific Forest Research Centre: Canadian Forestry Service.

Barbeta, A., Mejía-Chang, M., Ogaya, R., Voltas, J., Dawson, T. E., & Peñuelas, J. (2015). The combined effects of a long-term experimental drought and an extreme drought on the use of plant-water sources in a Mediterranean forest. *Global Change Biology*, *21*(3), 1213–1225. https://doi.org/10.1111/gcb.12785

Barros, F. de V., Bittencourt, P. R. L., Brum, M., Restrepo-Coupe, N., Pereira, L., Teodoro, G. S., et al. (2019). Hydraulic traits explain differential responses of Amazonian forests to the 2015 El Niño-induced drought. *New Phytologist*, *223*(3), 1253–1266. https://doi.org/10.1111/nph.15909

Bayala, J., Teklehaimanot, Z., & Ouedraogo, S. J. (2004). Fine root distribution of pruned trees and associated crops in a parkland system in Burkina Faso. *Agroforestry Systems*, *60*(1), 13–26. https://doi.org/10.1023/B:AGFO.0000009401.96309.12

Berdanier, A. B., Miniat, C. F., & Clark, J. S. (2016). Predictive models for radial sap flux variation in coniferous, diffuse-porous and ring-porous temperate trees. *Tree Physiology*, *36*(8), 932–941. https://doi.org/10.1093/treephys/tpw027

Birdsey, R., Pregitzer, K., & Lucier, A. (2006). Forest Carbon Management in the United States. *Journal of Environment Quality*, *35*(4), 1461. https://doi.org/10.2134/jeq2005.0162

Bogeat-Triboulot, M.-B., Martin, R., Chatelet, D., & Cochard, H. (2002). Hydraulic conductance of root and shoot measured with the transient and dynamic modes of the high-pressure flowmeter. *Annals of Forest Science*, *59*(4), 389–396. https://doi.org/10.1051/forest:2002010

Bouttier, L., Paquette, A., Messier, C., Rivest, D., Olivier, A., & Cogliastro, A. (2014). Vertical root separation and light interception in a temperate tree-based intercropping system of

Eastern Canada. *Agroforestry Systems*, *88*(4), 693–706. https://doi.org/10.1007/s10457-014-9721-6

Bright, B. C., Hicke, J. A., & Meddens, A. J. H. (2013). Effects of bark beetle-caused tree mortality on biogeochemical and biogeophysical MODIS products. *Journal of Geophysical Research: Biogeosciences*, *118*(3), 974–982. https://doi.org/10.1002/jgrg.20078

Brown, W. G. E., Lacate, D. S., & others. (1961). Rooting habits of white and red pine. Retrieved from http://www.cfs.nrcan.gc.ca/bookstore_pdfs/31370.pdf

Brum, M., Vadeboncoeur, M. A., Ivanov, V., Asbjornsen, H., Saleska, S., Alves, L. F., et al. (2018). Hydrological niche segregation defines forest structure and drought tolerance strategies in a seasonal Amazon forest. *Journal of Ecology*, *0*(0). https://doi.org/10.1111/1365-2745.13022

Brum, M., Gutiérrez López, J., Asbjornsen Heidi, Licata Julian, Pypker Thomas, Sanchez Gilson, & Oiveira Rafael S. (2018). ENSO effects on the transpiration of eastern Amazon trees. *Philosophical Transactions of the Royal Society B: Biological Sciences*, *373*(1760), 20180085. https://doi.org/10.1098/rstb.2018.0085

Burgess, S. S., Adams, M. A., Turner, N. C., Beverly, C. R., Ong, C. K., Khan, A. A., & Bleby, T. M. (2001). An improved heat pulse method to measure low and reverse rates of sap flow in woody plants. *Tree Physiology*, *21*(9), 589–598.

Burgess, S. S. O., Adams, M. A., Turner, N. C., & Ong, C. K. (1998). The redistribution of soil water by tree root systems. *Oecologia*, *115*(3), 306–311. https://doi.org/10.1007/s004420050521

Canadell, J., Jackson, R. B., Ehleringer, J. B., Mooney, H. A., Sala, O. E., & Schulze, E.-D. (1996). Maximum rooting depth of vegetation types at the global scale. *Oecologia*, *108*(4), 583–595. https://doi.org/10.1007/BF00329030

Canham, C. D., Rogers, N., & Buchholz, T. (2013). Regional variation in forest harvest regimes in the northeastern United States. *Ecological Applications*, *23*(3), 515–522. https://doi.org/10.1890/12-0180.1

Casper, B. B., & Jackson, R. B. (1997). Plant Competition Underground. *Annual Review of Ecology and Systematics*, *28*(1), 545–570. https://doi.org/10.1146/annurev.ecolsys.28.1.545

Casper, B. B., Schenk, H. J., & Jackson, R. B. (2003). Defining a plant's belowground zone of influence. *Ecology*, *84*(9), 2313–2321. https://doi.org/10.1890/02-0287

Caylor, K. K., & Dragoni, D. (2009). Decoupling structural and environmental determinants of sap velocity: Part I. Methodological development. *Agricultural and Forest Meteorology*, *149*(3–4), 559–569. https://doi.org/10.1016/j.agrformet.2008.10.006

Chave, J., Coomes, D., Jansen, S., Lewis, S. L., Swenson, N. G., & Zanne, A. E. (2009). Towards a worldwide wood economics spectrum. *Ecology Letters*, *12*(4), 351–366. https://doi.org/10.1111/j.1461-0248.2009.01285.x

Cheng, S. (2009). Changes in root growth and relationships between plant organs and root hydraulic traits in American elm (Ulmus americana L.) and red oak (Quercus rubra L.) seedlings due to elevated CO2 level. *Forestry Studies in China*, *11*(2), 65–76. https://doi.org/10.1007/s11632-009-0013-6

Ciais, P., Reichstein, M., Viovy, N., Granier, A., Ogée, J., Allard, V., et al. (2005). Europe-wide reduction in primary productivity caused by the heat and drought in 2003. *Nature*, *437*(7058), 529–533. https://doi.org/10.1038/nature03972

Clark, K. L., Skowronski, N., & Hom, J. (2010). Invasive insects impact forest carbon dynamics: defoliation and forest carbon dynamics. *Global Change Biology*, *16*(1), 88–101. https://doi.org/10.1111/j.1365-2486.2009.01983.x

Clearwater, M. J., Meinzer, F. C., Andrade, J. L., Goldstein, G., & Holbrook, N. M. (1999). Potential errors in measurement of nonuniform sap flow using heat dissipation probes. *Tree Physiology*, *19*(10), 681–687.

Cochard, H., Badel, E., Herbette, S., Delzon, S., Choat, B., & Jansen, S. (2013). Methods for measuring plant vulnerability to cavitation: a critical review. *Journal of Experimental Botany*, *64*(15), 4779–4791. https://doi.org/10.1093/jxb/ert193

Cohen, W. B., Yang, Z., Stehman, S. V., Schroeder, T. A., Bell, D. M., Masek, J. G., et al. (2016). Forest disturbance across the conterminous United States from 1985–2012: The emerging dominance of forest decline. *Forest Ecology and Management*, *360*, 242–252. https://doi.org/10.1016/j.foreco.2015.10.042

Cornelissen, J., Lavorel, S., Garnier, E., Diaz, S., Buchmann, N., Gurvich, D. E., et al. (2003). A handbook of protocols for standardised and easy measurement of plant functional traits worldwide. *Australian Journal of Botany*, *51*, 335–380.

Couvreur, V., Vanderborght, J., & Javaux, M. (2012). A simple three-dimensional macroscopic root water uptake model based on the hydraulic architecture approach. *Hydrology and Earth System Sciences*, *16*(8), 2957–2971. https://doi.org/10.5194/hess-16-2957-2012

Cox, P. M., Harris, P. P., Huntingford, C., Betts, R. A., Collins, M., Jones, C. D., et al. (2008). Increasing risk of Amazonian drought due to decreasing aerosol pollution. *Nature*, *453*(7192), 212–215. https://doi.org/10.1038/nature06960

Danjon, F., & Reubens, B. (2007). Assessing and analyzing 3D architecture of woody root systems, a review of methods and applications in tree and soil stability, resource acquisition and allocation. *Plant and Soil*, *303*(1–2), 1–34. https://doi.org/10.1007/s11104-007-9470-7

Davidson, E. A., de Araújo, A. C., Artaxo, P., Balch, J. K., Brown, I. F., C. Bustamante, M. M., et al. (2012). The Amazon basin in transition. *Nature*, *481*(7381), 321–328. https://doi.org/10.1038/nature10717

Davis, T. W., Kuo, C. M., Liang, X., & Yu, P. S. (2012). Sap Flow Sensors: Construction, Quality Control and Comparison. *Sensors*, *12*(12), 954–971. https://doi.org/10.3390/s120100954

Dewar, R C. (2005). Maximum entropy production and the fluctuation theorem. *Journal of Physics A: Mathematical and General*, *38*(21), L371–L381. https://doi.org/10.1088/0305-4470/38/21/L01

Dewar, R. C., & Maritan, A. (2014). A Theoretical Basis for Maximum Entropy Production. In R. C. Dewar, C. H. Lineweaver, R. K. Niven, & K. Regenauer-Lieb (Eds.), *Beyond the Second Law* (pp. 49–71). Springer Berlin Heidelberg. https://doi.org/10.1007/978-3-642-40154-1_3

Dietze, M. C., & Matthes, J. H. (2014). A general ecophysiological framework for modelling the impact of pests and pathogens on forest ecosystems. *Ecology Letters*, *17*(11), 1418–1426. https://doi.org/10.1111/ele.12345

Dixon, M. A., & Tyree, M. T. (1984). A new stem hygrometer, corrected for temperature gradients and calibrated against the pressure bomb. *Plant, Cell & Environment*, *7*(9), 693–697. https://doi.org/10.1111/1365-3040.ep11572454

Doussan, C., Pagès, L., & Vercambre, G. (1998). Modelling of the hydraulic architecture of root systems: an integrated approach to water absorption—model description. *Annals of Botany*, *81*(2), 213–223.

Doussan, C., Pierret, A., Garrigues, E., & Pagès, L. (2006). Water Uptake by Plant Roots: II – Modelling of Water Transfer in the Soil Root-system with Explicit Account of Flow within the Root System – Comparison with Experiments. *Plant and Soil*, *283*(1–2), 99–117. https://doi.org/10.1007/s11104-004-7904-z

Dragoni, D., Caylor, K. K., & Schmid, H. P. (2009). Decoupling structural and environmental determinants of sap velocity. *Agricultural and Forest Meteorology*, *149*(3–4), 570–581. https://doi.org/10.1016/j.agrformet.2008.10.010

Duffy, P. B., Brando, P., Asner, G. P., & Field, C. B. (2015). Projections of future meteorological drought and wet periods in the Amazon. *Proceedings of the National Academy of Sciences*, *112*(43), 13172–13177. https://doi.org/10.1073/pnas.1421010112

Eagleson, P. S. (2005). *Ecohydrology: Darwinian expression of vegetation form and function*. Cambridge ; New York: Cambridge University Press. Retrieved from http://mirlyn.lib.umich.edu/Record/005094999

ERA5 Reanalysis. (2017). Research Data Archive at the National Center for Atmospheric Research, Computational and Information Systems Laboratory. https://doi.org/10.5065/D6X34W69

Fatichi, S., Pappas, C., & Ivanov, V. Y. (2015). Modeling plant–water interactions: an ecohydrological overview from the cell to the global scale. *Wiley Interdisciplinary Reviews: Water*, n/a-n/a. https://doi.org/10.1002/wat2.1125

Feddes, R. A., & Raats, P. A. (2005). Parameterizing the soil-water-plant root system. *Frontis*, *6*(0), 95–141.

Feddes, R. A., Kowalik, P., Kolinska-Malinka, K., & Zaradny, H. (1976). Simulation of field water uptake by plants using a soil water dependent root extraction function. *Journal of Hydrology*, *31*(1), 13–26. https://doi.org/10.1016/0022-1694(76)90017-2

Feddes, R. A., Hoff, H., Bruen, M., Dawson, T., de Rosnay, P., Dirmeyer, P., et al. (2001). Modeling root water uptake in hydrological and climate models. *Bulletin of the American Meteorological Society*, *82*(12), 2797–2809.

Ferrara, C., Salvati, L., & Barone, P. M. (2017). Tree root system imaging using Ground Penetrating Radar. https://doi.org/10.12899/asr-1314

Fiscus, E. L. (1975). The Interaction between Osmotic- and Pressure-Induced Water Flow in Plant Roots. *Plant Physiology*, *55*(5), 917–922.

Fisher, R. A., Williams, M., Do, V., Lobo, R., da Costa, A. L., & Meir, P. (2006). Evidence from Amazonian forests is consistent with isohydric control of leaf water potential. *Plant, Cell & Environment*, *29*(2), 151–165.

Fisher, R. F., & Binkley, D. (Eds.). (2012). Life in Forest Soils. In *Ecology and Management of Forest Soils* (pp. 75–98). John Wiley & Sons, Ltd. https://doi.org/10.1002/9781118422342.ch6

Fontes, C. G., Dawson, T. E., Jardine, K., McDowell, N., Gimenez, B. O., Anderegg, L., et al. (2018). Dry and hot: the hydraulic consequences of a climate change–type drought for

Amazonian trees. *Phil. Trans. R. Soc. B*, *373*(1760), 20180209. https://doi.org/10.1098/rstb.2018.0209

Fukuzawa, K., Shibata, H., Takagi, K., Satoh, F., Koike, T., & Sasa, K. (2013). Temporal variation in fine-root biomass, production and mortality in a cool temperate forest covered with dense understory vegetation in northern Japan. *Forest Ecology and Management*, *310*, 700–710. https://doi.org/10.1016/j.foreco.2013.09.015

Ganguly, S., Friedl, M. A., Tan, B., Zhang, X., & Verma, M. (2010). Land surface phenology from MODIS: Characterization of the Collection 5 global land cover dynamics product. *Remote Sensing of Environment*, *114*(8), 1805–1816. https://doi.org/10.1016/j.rse.2010.04.005

Gardner, W. R. (1960). Dynamic Aspects of Water Availability to Plants. *Soil Science*, *89*(2), 63–73.

Gebauer, T., Horna, V., & Leuschner, C. (2008). Variability in radial sap flux density patterns and sapwood area among seven co-occurring temperate broad-leaved tree species. *Tree Physiology*, *28*(12), 1821–1830.

Hargreaves, G.H. & Samani, Z. A. (1985). Reference Crop Evapotranspiration from Temperature. *Applied Engineering in Agriculture*, *1*(2), 96–99. https://doi.org/10.13031/2013.26773

Gerken, T., Ruddell, B. L., Fuentes, J. D., Araújo, A., Brunsell, N. A., Maia, J., et al. (2018). Investigating the mechanisms responsible for the lack of surface energy balance closure in a central Amazonian tropical rainforest. *Agricultural and Forest Meteorology*, *255*, 92–103. https://doi.org/10.1016/j.agrformet.2017.03.023

Gimenez, B. O., Jardine, K. J., Higuchi, N., Negrón-Juárez, R. I., Sampaio-Filho, I. de J., Cobello, L. O., et al. (2019). Species-Specific Shifts in Diurnal Sap Velocity Dynamics and Hysteretic Behavior of Ecophysiological Variables During the 2015–2016 El Niño Event in the Amazon Forest. *Frontiers in Plant Science*, *10*. https://doi.org/10.3389/fpls.2019.00830

Gonçalves, F. G. (2014). *Vertical structure and aboveground biomass of tropical forests from lidar remote sensing*. (Doctoral Thesis). Oregon State University, Corvallis, OR.

Gradmann, H. (1928). Untersuchungen iiber die Wasserverhaltnisse des Bodens als Grundlage des Pflan-zenwachstums. *Jahrb Wiss Bot*, *69*(1), 1–100.

Granier, A. (1985). Une nouvelle méthode pour la mesure du flux de sève brute dans le tronc des arbres. *Annales des Sciences Forestières*, *42*(2), 193–200. https://doi.org/10.1051/forest:19850204

Gutierrez Lopez, J., Licata, J., Pypker, T., & Asbjornsen, H. (2019). Effects of heater wattage on sap flux density estimates using an improved tree-cut experiment. *Tree Physiology*, *39*(4), 679–693. https://doi.org/10.1093/treephys/tpy137

Hammond, G. E., Lichtner, P. C., & Mills, R. T. (2014). Evaluating the performance of parallel subsurface simulators: An illustrative example with PFLOTRAN: Evaluating the Parallel Performance of Pflotran. *Water Resources Research*, *50*(1), 208–228. https://doi.org/10.1002/2012WR013483

Hardiman, B. S., Bohrer, G., Gough, C. M., Vogel, C. S., & Curtis, P. S. (2011). The role of canopy structural complexity in wood net primary production of a maturing northern deciduous forest. *Ecology*, *92*(9), 1818–1827. https://doi.org/10.1890/10-2192.1

Hatton, T. J., Catchpole, E. A., & Vertessy, R. A. (1990). Integration of sapflow velocity to estimate plant water use. *Tree Physiology*, *6*(2), 201–209. https://doi.org/10.1093/treephys/6.2.201

He, L. (2014). *Impact of Fine-Scale Spatially Heterogeneous Canopy and Soil Moisture, and Three-Dimensional Root Water Uptake on Large-Scale Energy Fluxes in Vegetated Environments* (Doctoral Thesis). University of Michigan, Ann Arbor, MI.

He, L., Ivanov, V. Y., Bohrer, G., Thomsen, J. E., Vogel, C. S., & Moghaddam, M. (2013). Temporal dynamics of soil moisture in a northern temperate mixed successional forest after a prescribed intermediate disturbance. *Agricultural and Forest Meteorology*, *180*, 22–33. https://doi.org/10.1016/j.agrformet.2013.04.014

He, L., Ivanov, V. Y., Bohrer, G., Maurer, K. D., Vogel, C. S., & Moghaddam, M. (2014). Effects of fine-scale soil moisture and canopy heterogeneity on energy and water fluxes in a northern temperate mixed forest. *Agricultural and Forest Meteorology*, *184*, 243–256. https://doi.org/10.1016/j.agrformet.2013.10.006

Heidinger, A. K., Laszlo, I., Molling, C. C., & Tarpley, D. (2013). Using SURFRAD to Verify the NOAA Single-Channel Land Surface Temperature Algorithm. *Journal of Atmospheric and Oceanic Technology*, *30*(12), 2868–2884. https://doi.org/10.1175/JTECH-D-13-00051.1

Hicke, J. A., Allen, C. D., Desai, A. R., Dietze, M. C., Hall, R. J., Ted Hogg, E. H., et al. (2012). Effects of biotic disturbances on forest carbon cycling in the United States and Canada. *Global Change Biology*, *18*(1), 7–34. https://doi.org/10.1111/j.1365-2486.2011.02543.x

Honert, T. H. van den. (1948). Water transport in plants as a catenary process. *Discussions of the Faraday Society*, *3*(0), 146–153. https://doi.org/10.1039/DF9480300146

Hunt, E. R., Running, S., & Federer, C. A. (1991). Extrapolating plant water flow resistances and capacitances to regional scales. *Agricultural and Forest Meteorology*, *54*, 169–195.

Hunter, M. O., Keller, M., Victoria, D., & Morton, D. C. (2013). Tree height and tropical forest biomass estimation. *Biogeosciences*, *10*(12), 8385–8399. https://doi.org/10.5194/bg-10-8385-2013

Imada, S., Taniguchi, T., Acharya, K., & Yamanaka, N. (2013). Vertical distribution of fine roots of Tamarix ramosissima in an arid region of southern Nevada. *Journal of Arid Environments*, *92*, 46–52. https://doi.org/10.1016/j.jaridenv.2013.01.006

Ivanov, V. Y., Bras, R. L., & Vivoni, E. R. (2008). Vegetation-hydrology dynamics in complex terrain of semiarid areas: 1. A mechanistic approach to modeling dynamic feedbacks: Modeling Vegetation-Hydrology Feedbacks. *Water Resources Research*, *44*(3), n/a-n/a. https://doi.org/10.1029/2006WR005588

Ivanov, V. Y., Fatichi, S., Jenerette, G. D., Espeleta, J. F., Troch, P. A., & Huxman, T. E. (2010). Hysteresis of soil moisture spatial heterogeneity and the “homogenizing” effect of vegetation: Soil Moisture Spatial Heterogeneity. *Water Resources Research*, *46*(9), n/a-n/a. https://doi.org/10.1029/2009WR008611

Ivanov, V. Y., Hutyra, L. R., Wofsy, S. C., Munger, J. W., Saleska, S. R., de Oliveira, R. C., & de Camargo, P. B. (2012). Root niche separation can explain avoidance of seasonal drought stress and vulnerability of overstory trees to extended drought in a mature Amazonian forest: Root Niche Separation As Drought Avoidance Strategy. *Water Resources Research*, *48*(12). https://doi.org/10.1029/2012WR011972

James, S. A., Clearwater, M. J., Meinzer, F. C., & Goldstein, G. (2002). Heat dissipation sensors of variable length for the measurement of sap flow in trees with deep sapwood. *Tree Physiology*, *22*(4), 277–283.

Jarvis, N. J. (1989). A simple empirical model of root water uptake. *Journal of Hydrology*, *107*(1), 57–72. https://doi.org/10.1016/0022-1694(89)90050-4

Jarvis, N. J. (2011). Simple physics-based models of compensatory plant water uptake: concepts and eco-hydrological consequences. *Hydrol. Earth Syst. Sci.*, *15*(11), 3431–3446. https://doi.org/10.5194/hess-15-3431-2011

Javaux, M., Schröder, T., Vanderborght, J., & Vereecken, H. (2008). Use of a Three-Dimensional Detailed Modeling Approach for Predicting Root Water Uptake. *Vadose Zone Journal*, *7*(3), 1079. https://doi.org/10.2136/vzj2007.0115

Javaux, M., Couvreur, V., Vanderborght, J., & Vereecken, H. (2013). Root Water Uptake: From Three-Dimensional Biophysical Processes to Macroscopic Modeling Approaches. *Vadose Zone Journal*, *12*(4), 0. https://doi.org/10.2136/vzj2013.02.0042

Jaynes, E. T. (2003). *Probability theory: The logic of science*. Cambridge university press.

Jiménez-Muñoz, J. C., Mattar, C., Barichivich, J., Santamaría-Artigas, A., Takahashi, K., Malhi, Y., et al. (2016). Record-breaking warming and extreme drought in the Amazon rainforest during the course of El Niño 2015–2016. *Scientific Reports*, *6*, 33130. https://doi.org/10.1038/srep33130

Johnsen, K. H., McConnell, S. P., Regelbrugge, J. C., & Seiler, J. R. (1988). Hydraulic conductance of roots present at the time of lifting and newly regenerated roots of 2+ 0 eastern white pine seedlings. *Tree Planters Notes*, *39*(3), 5–8.

de Jong van Lier, Q., van Dam, J. C., Metselaar, K., de Jong, R., & Duijnisveld, W. H. M. (2008). Macroscopic Root Water Uptake Distribution Using a Matric Flux Potential Approach. *Vadose Zone Journal*, *7*(3), 1065. https://doi.org/10.2136/vzj2007.0083

Juretić, D., & Županović, P. (2003). Photosynthetic models with maximum entropy production in irreversible charge transfer steps. *Computational Biology and Chemistry*, *27*(6), 541–553. https://doi.org/10.1016/j.compbiolchem.2003.09.001

Kleidon, A., & Schymanski, S. (2008). Thermodynamics and optimality of the water budget on land: A review. *Geophysical Research Letters*, *35*(20). https://doi.org/10.1029/2008GL035393

Kleidon, A., Malhi, Y., & Cox, P. M. (2010). Maximum entropy production in environmental and ecological systems. *Philosophical Transactions of the Royal Society B: Biological Sciences*, *365*(1545), 1297–1302. https://doi.org/10.1098/rstb.2010.0018

Kleidon, A., & Fraedrich, K. (2005). Biotic Entropy Production and Global Atmosphere-Biosphere Interactions. In Axel Kleidon & R. D. Lorenz (Eds.), *Non-equilibrium Thermodynamics and the Production of Entropy* (pp. 173–189). Springer Berlin Heidelberg. https://doi.org/10.1007/11672906_14

Kolb, T. E., Fettig, C. J., Ayres, M. P., Bentz, B. J., Hicke, J. A., Mathiasen, R., et al. (2016). Observed and anticipated impacts of drought on forest insects and diseases in the United States. *Forest Ecology and Management*, *380*, 321–334. https://doi.org/10.1016/j.foreco.2016.04.051

Kostner, B., Granier, A., & Cermak, J. (1998). Sapflow measurements in forest stands: methods and uncertainties. *Annals of Forest Science*, *55*, 13–27.

Kramer-Walter, K. R., Bellingham, P. J., Millar, T. R., Smissen, R. D., Richardson, S. J., & Laughlin, D. C. (2016). Root traits are multidimensional: specific root length is independent from root tissue density and the plant economic spectrum. *Journal of Ecology*, *104*(5), 1299–1310. https://doi.org/10.1111/1365-2745.12562

Kruger, E., & Sucoff, E. (1989). Aluminium and the Hydraulic Conductivity of Quercus rubra L. Root Systems. *Journal of Experimental Botany*, *40*(6), 659–665. https://doi.org/10.1093/jxb/40.6.659

Landsberg, J. J., & Fowkes, N. D. (1978). Water Movement Through Plant Roots. *Annals of Botany*, *42*(3), 493–508. https://doi.org/10.1093/oxfordjournals.aob.a085488

Lang, C., Dolynska, A., Finkeldey, R., & Polle, A. (2010). Are beech (Fagus sylvatica) roots territorial? *Forest Ecology and Management*, *260*(7), 1212–1217. https://doi.org/10.1016/j.foreco.2010.07.014

Larocque, G. R., Luckai, N., Adhikary, S. N., Groot, A., Bell, F. W., & Sharma, M. (2012). Competition theory — science and application in mixed forest stands: review of experimental and modelling methods and suggestions for future research. *Environmental Reviews*, *21*(2), 71–84. https://doi.org/10.1139/er-2012-0033

Lechuga, V., Carraro, V., Viñegla, B., Carreira, J. A., & Linares, J. C. (2017). Managing drought-sensitive forests under global change. Low competition enhances long-term growth and water uptake in Abies pinsapo. *Forest Ecology and Management*, *406*, 72–82. https://doi.org/10.1016/j.foreco.2017.10.017

Leitner, D., Klepsch, S., Bodner, G., & Schnepf, A. (2010). A dynamic root system growth model based on L-Systems. *Plant and Soil*, *332*(1–2), 177–192. https://doi.org/10.1007/s11104-010-0284-7

Leuschner, C., Hertel, D., Coners, H., & Büttner, V. (2001). Root competition between beech and oak: a hypothesis. *Oecologia*, *126*(2), 276–284. https://doi.org/10.1007/s004420000507

Lichtner, P. C., Hammond, G. E., Lu, C., Karra, S., Bisht, G., Andre, B., et al. (2017). *PFLOTRAN User Manual*.

Lima, J. R. de S., Antonino, A. C. D., Souza, E. S. de, Hammecker, C., Montenegro, S. M. G. L., & Lira, C. A. B. de O. (2013). Calibration of Hargreaves-Samani Equation for Estimating Reference Evapotranspiration in Sub-Humid Region of Brazil. *Journal of Water Resource and Protection*, *05*(12), 1–5. https://doi.org/10.4236/jwarp.2013.512A001

Lindenmayer, A. (1977). Paracladial Relationships in Leaves. *Berichte Der Deutschen Botanischen Gesellschaft*, *90*(1), 287–301. https://doi.org/10.1111/j.1438-8677.1977.tb02822.x

Littell, J. S., Peterson, D. L., Riley, K. L., Liu, Y., & Luce, C. H. (2016). A review of the relationships between drought and forest fire in the United States. *Global Change Biology*, *22*(7), 2353–2369. https://doi.org/10.1111/gcb.13275

Lloyd, S. P. (1982). Least squares quantization in pcm. *IEEE Transactions on Information Theory*, *28*, 129–137.

Lorenz, C., & Kunstmann, H. (2012). The Hydrological Cycle in Three State-of-the-Art Reanalyses: Intercomparison and Performance Analysis. *Journal of Hydrometeorology*, *13*(5), 1397–1420. https://doi.org/10.1175/JHM-D-11-088.1

Lu, P., Urban, L., & Zhao, P. (2004). Granier's Thermal Dissipation Probe (TDP) Method for Measuring Sap Flow in Trees: Theory and Practice. *Acta Botanica Sinica*, *46*(6), 631–646.

Lu, X., Kicklighter, D. W., Melillo, J. M., Reilly, J. M., & Xu, L. (2015). Land carbon sequestration within the conterminous United States: Regional- and state-level analyses: Regional U.S. land sinks and legacies. *Journal of Geophysical Research: Biogeosciences*, *120*(2), 379–398. https://doi.org/10.1002/2014JG002818

Luyssaert, S., Inglima, I., Jung, M., Richardson, A. D., Reichstein, M., Papale, D., et al. (2007). CO $_2$ balance of boreal, temperate, and tropical forests derived from a global database. *Global Change Biology*, *13*(12), 2509–2537. https://doi.org/10.1111/j.1365-2486.2007.01439.x

Makita, N., Hirano, Y., Dannoura, M., Kominami, Y., Mizoguchi, T., Ishii, H., & Kanazawa, Y. (2009). Fine root morphological traits determine variation in root respiration of Quercus serrata. *Tree Physiology*, *29*(4), 579–585. https://doi.org/10.1093/treephys/tpn050

Manoli, G., Bonetti, S., Domec, J.-C., Putti, M., Katul, G., & Marani, M. (2014). Tree root systems competing for soil moisture in a 3D soil–plant model. *Advances in Water Resources*, *66*, 32–42. https://doi.org/10.1016/j.advwatres.2014.01.006

Mares, R., Barnard, H. R., Mao, D., Revil, A., & Singha, K. (2016). Examining diel patterns of soil and xylem moisture using electrical resistivity imaging. *Journal of Hydrology*, *536*, 327–338. https://doi.org/10.1016/j.jhydrol.2016.03.003

Matheny, A. M., Bohrer, G., Vogel, C. S., Morin, T. H., He, L., Frasson, R. P. de M., et al. (2014). Species-specific transpiration responses to intermediate disturbance in a northern hardwood forest. *Journal of Geophysical Research: Biogeosciences*, *119*(12), 2014JG002804. https://doi.org/10.1002/2014JG002804

Matheny, A. M., Bohrer, G., Garrity, S. R., Morin, T. H., Howard, C. J., & Vogel, C. S. (2015). Observations of stem water storage in trees of opposing hydraulic strategies. *Ecosphere*, *6*(9), 1–13. https://doi.org/10.1890/ES15-00170.1

Matheny, A. M., Fiorella, R. P., Bohrer, G., Poulsen, C. J., Morin, T. H., Wunderlich, A., et al. (2017). Contrasting strategies of hydraulic control in two codominant temperate tree species. *Ecohydrology*, *10*(3), e1815. https://doi.org/10.1002/eco.1815

Mathias, C., Nouvellon, Y., Laclau, J.-P., Stape, J. L., Bouillet, J.-P., Lambais, G. R., & Maire, G. le. (2016). Importance of deep water uptake in tropical eucalypt forest. *Functional Ecology*, *31*(2), 509–519. https://doi.org/10.1111/1365-2435.12727

McCormack, M. L., Guo, D., Iversen, C. M., Chen, W., Eissenstat, D. M., Fernandez, C. W., et al. (2017). Building a better foundation: improving root-trait measurements to understand and model plant and ecosystem processes. *New Phytologist*, *215*(1), 27–37. https://doi.org/10.1111/nph.14459

McDowell, N., Pockman, W. T., Allen, C. D., Breshears, D. D., Cobb, N., Kolb, T., et al. (2008). Mechanisms of plant survival and mortality during drought: why do some plants survive while others succumb to drought? *New Phytologist*, *178*(4), 719–739. https://doi.org/10.1111/j.1469-8137.2008.02436.x

McDowell, N. G., Fisher, R. A., Xu, C., Domec, J. C., Hölttä, T., Mackay, D. S., et al. (2013). Evaluating theories of drought-induced vegetation mortality using a multimodel-experiment framework. *New Phytologist*, *200*(2), 304–321. https://doi.org/10.1111/nph.12465

Medvigy, D., Walko, R. L., & Avissar, R. (2011). Effects of Deforestation on Spatiotemporal Distributions of Precipitation in South America. *Journal of Climate*, *24*(8), 2147–2163. https://doi.org/10.1175/2010JCLI3882.1

Medvigy, D., Walko, R. L., Otte, M. J., & Avissar, R. (2013). Simulated Changes in Northwest US Climate in Response to Amazon Deforestation*. *Journal of Climate*, *26*(22), 9115–9136.

Meinen, C., Leuschner, C., Ryan, N. T., & Hertel, D. (2009). No evidence of spatial root system segregation and elevated fine root biomass in multi-species temperate broad-leaved forests. *Trees*, *23*(5), 941–950. https://doi.org/10.1007/s00468-009-0336-x

Miner, G. L., Ham, J. M., & Kluitenberg, G. J. (2017). A heat-pulse method for measuring sap flow in corn and sunflower using 3D-printed sensor bodies and low-cost electronics. *Agricultural and Forest Meteorology*, *246*, 86–97. https://doi.org/10.1016/j.agrformet.2017.06.012

Montagnoli, A., Terzaghi, M., Di Iorio, A., Scippa, G. S., & Chiatante, D. (2012). Fine-root morphological and growth traits in a Turkey-oak stand in relation to seasonal changes in soil moisture in the Southern Apennines, Italy. *Ecological Research*, *27*(6), 1015–1025. https://doi.org/10.1007/s11284-012-0981-1

Monteith, J. L. (1965). Evaporation and environment. In *Symposia of the Society for Experimental Biology* (Vol. 19, pp. 205–224). Retrieved from https://www.unc.edu/courses/2007fall/geog/801/001/www/ET/Monteith65.pdf

Mu, Q., Heinsch, F. A., Zhao, M., & Running, S. W. (2007). Development of a global evapotranspiration algorithm based on MODIS and global meteorology data. *Remote Sensing of Environment*, *111*(4), 519–536. https://doi.org/10.1016/j.rse.2007.04.015

Mu, Q., Zhao, M., & Running, S. W. (2011). Improvements to a MODIS global terrestrial evapotranspiration algorithm. *Remote Sensing of Environment*, *115*(8), 1781–1800. https://doi.org/10.1016/j.rse.2011.02.019

Nardini, A., & Tyree, M. T. (1999). Root and shoot hydraulic conductance of seven Quercus species. *Annals of Forest Science*, *56*(5), 371–377.

Nave, L. E., Gough, C. M., Maurer, K. D., Bohrer, G., Hardiman, B. S., Moine, J. L., et al. (2011). Disturbance and the resilience of coupled carbon and nitrogen cycling in a north temperate forest. *Journal of Geophysical Research: Biogeosciences*, *116*(G4). Retrieved from https://agupubs.onlinelibrary.wiley.com/doi/abs/10.1029/2011JG001758

Nepstad, D., Lefebvre, P., Lopes da Silva, U., Tomasella, J., Schlesinger, P., Solórzano, L., et al. (2004). Amazon drought and its implications for forest flammability and tree growth: a basin-wide analysis. *Global Change Biology*, *10*(5), 704–717. https://doi.org/10.1111/j.1529-8817.2003.00772.x

Nepstad, D. C., Carvalho, C. R. de, Davidson, E. A., Jipp, P. H., Lefebvre, P. A., Negreiros, G. H., et al. (1994). The role of deep roots in the hydrological and carbon cycles of Amazonian forests and pastures. *Nature*, *372*(6507), 372666a0. https://doi.org/10.1038/372666a0

Nepstad, D. C., de Carvalho, C. R., Davidson, E. A., Jipp, P. H., Lefebvre, P. A., Negreiros, G. H., et al. (1994). The role of deep roots in the hydrological and carbon cycles of Amazonian forests and pastures. *Nature*, *372*(6507), 666–669. https://doi.org/10.1038/372666a0

Nepstad, D. C., Tohver, I. M., Ray, D., Moutinho, P., & Cardinot, G. (2007). Mortality of Large Trees and Lianas Following Experimental Drought in an Amazon Forest. *Ecology*, *88*(9), 2259–2269. https://doi.org/10.1890/06-1046.1

Nizinski, J. J., Montoroi, J.-P., Silvera, N., & Lointier, M. (2013). Use of the Dixon-Tyree stem hygrometer in a rubber tree plantation. *Agricultural and Forest Meteorology*, *173*, 100–106. https://doi.org/10.1016/j.agrformet.2013.01.006

Oh, S., Montanari, A., & Karbasi, A. (2010). Sensor network localization from local connectivity: Performance analysis for the MDS-MAP algorithm. In *2010 IEEE Information Theory Workshop on Information Theory (ITW 2010, Cairo)* (pp. 1–5). https://doi.org/10.1109/ITWKSPS.2010.5503144

Ohmura, A., Dutton, E. G., Forgan, B., Fröhlich, C., Gilgen, H., Hegner, H., et al. (1998). Baseline Surface Radiation Network (BSRN/WCRP): New Precision Radiometry for Climate Research. *Bulletin of the American Meteorological Society*, *79*(10), 2115–2136. https://doi.org/10.1175/1520-0477(1998)079<2115:BSRNBW>2.0.CO;2

Oishi, A. C., Oren, R., & Stoy, P. C. (2008). Estimating components of forest evapotranspiration: A footprint approach for scaling sap flux measurements. *Agricultural and Forest Meteorology*, *148*(11), 1719–1732. https://doi.org/10.1016/j.agrformet.2008.06.013

Oliveira, R. S., Dawson, T. E., Burgess, S. S. O., & Nepstad, D. C. (2005). Hydraulic redistribution in three Amazonian trees. *Oecologia*, *145*(3), 354–363. https://doi.org/10.1007/s00442-005-0108-2

Orfánus, T., Stojkovová, D., Nagy, V., & Németh, T. (2016). Variability of soil water content controlled by evapotranspiration and groundwater–root zone interaction. *Archives of*

Agronomy and Soil Science, *62*(11), 1602–1613. https://doi.org/10.1080/03650340.2016.1155700

Pan, Y., Birdsey, R. A., Fang, J., Houghton, R., Kauppi, P. E., Kurz, W. A., et al. (2011). A Large and Persistent Carbon Sink in the World's Forests. *Science*, *333*(6045), 988–993. https://doi.org/10.1126/science.1201609

Panisset, J. S., Libonati, R., Gouveia, C. M. P., Machado-Silva, F., França, D. A., França, J. R. A., & Peres, L. F. (2018). Contrasting patterns of the extreme drought episodes of 2005, 2010 and 2015 in the Amazon Basin. *International Journal of Climatology*, *38*(2), 1096–1104. https://doi.org/10.1002/joc.5224

Parotta, J. A., Francis, J. K., & Rolo de Almeida, R. (1995). *Trees of the Tapajós*. Río Piedras: International Institute of Tropical Forestry.

Pau, S., Detto, M., Kim, Y., & Still, C. J. (2018). Tropical forest temperature thresholds for gross primary productivity. *Ecosphere*, *9*(7), e02311. https://doi.org/10.1002/ecs2.2311

Paudel, I., Kanety, T., & Cohen, S. (2013). Inactive xylem can explain differences in calibration factors for thermal dissipation probe sap flow measurements. *Tree Physiology*, *33*(9), 986–1001. https://doi.org/10.1093/treephys/tpt070

Paz, H., Pineda-García, F., & Pinzón-Pérez, L. F. (2015). Root depth and morphology in response to soil drought: comparing ecological groups along the secondary succession in a tropical dry forest. *Oecologia*, *179*(2), 551–561. https://doi.org/10.1007/s00442-015-3359-6

Peters, E. B., Wythers, K. R., Bradford, J. B., & Reich, P. B. (2013). Influence of Disturbance on Temperate Forest Productivity. *Ecosystems*, *16*(1), 95–110. https://doi.org/10.1007/s10021-012-9599-y

Phillips, O. L., Aragão, L. E., Lewis, S. L., Fisher, J. B., Lloyd, J., López-González, G., et al. (2009). Drought sensitivity of the Amazon rainforest. *Science*, *323*(5919), 1344–1347.

Phillips, R. P., Ibáñez, I., D'Orangeville, L., Hanson, P. J., Ryan, M. G., & McDowell, N. G. (2016). A belowground perspective on the drought sensitivity of forests: Towards improved understanding and simulation. *Forest Ecology and Management*, *380*, 309–320. https://doi.org/10.1016/j.foreco.2016.08.043

Pierret, A., Gonkhamdee, S., Jourdan, C., & Maeght, J.-L. (2013). IJ_Rhizo: an open-source software to measure scanned images of root samples. *Plant and Soil*, *373*(1–2), 531–539. https://doi.org/10.1007/s11104-013-1795-9

Pierret, A., Maeght, J.-L., Clément, C., Montoroi, J.-P., Hartmann, C., & Gonkhamdee, S. (2016). Understanding deep roots and their functions in ecosystems: an advocacy for more unconventional research. *Annals of Botany*, *118*(4), 621–635. https://doi.org/10.1093/aob/mcw130

Pinker, R. T., & Laszlo, I. (1992). Modeling Surface Solar Irradiance for Satellite Applications on a Global Scale. *Journal of Applied Meteorology*, *31*(2), 194–211. https://doi.org/10.1175/1520-0450(1992)031<0194:MSSIFS>2.0.CO;2

Poyatos, R., Granda, V., Molowny-Horas, R., Mencuccini, M., Steppe, K., & Martínez-Vilalta, J. (2016). SAPFLUXNET: towards a global database of sap flow measurements. *Tree Physiology*, *36*(12), 1449–1455. https://doi.org/10.1093/treephys/tpw110

Pregitzer, K. S., & Euskirchen, E. S. (2004). Carbon cycling and storage in world forests: biome patterns related to forest age. *Global Change Biology*, *10*(12), 2052–2077. https://doi.org/10.1111/j.1365-2486.2004.00866.x

Preisler, H. K., Grulke, N. E., Heath, Z., & Smith, S. L. (2017). Analysis and out-year forecast of beetle, borer, and drought-induced tree mortality in California. *Forest Ecology and Management*, *399*, 166–178. https://doi.org/10.1016/j.foreco.2017.05.039

Quijano, J. C., & Kumar, P. (2015). Numerical simulations of hydraulic redistribution across climates: The role of the root hydraulic conductivities. *Water Resources Research*, *51*(10), 8529–8550. https://doi.org/10.1002/2014WR016509

Raats, P. A. C. (2007). Uptake of water from soils by plant roots. *Transport in Porous Media*, *68*(1), 5–28. https://doi.org/10.1007/s11242-006-9055-6

Radeloff, V. C., Nelson, E., Plantinga, A. J., Lewis, D. J., Helmers, D., Lawler, J. J., et al. (2012). Economic-based projections of future land use in the conterminous United States under alternative policy scenarios. *Ecological Applications*, *22*(3), 1036–1049. https://doi.org/10.1890/11-0306.1

Rajkai, K., & Várallyay, G. (1992). Estimating soil water retention from simpler properties by regression techniques. In *Proc. Int. Workshop on Indirect Methods for Estimating the Hydraulic Properties of Unsaturated Soils. University of California, Riverside* (pp. 417–426).

Rasheed-Depardieu, C., Parelle, J., Tatin-Froux, F., Parent, C., & Capelli, N. (2015). Short-term response to waterlogging in *Quercus petraea* and *Quercus robur*: A study of the root hydraulic responses and the transcriptional pattern of aquaporins. *Plant Physiology and Biochemistry*, *97*, 323–330. https://doi.org/10.1016/j.plaphy.2015.10.016

Reich, P. B. (2014). The world-wide 'fast–slow' plant economics spectrum: a traits manifesto. *Journal of Ecology*, *102*(2), 275–301. https://doi.org/10.1111/1365-2745.12211

Restrepo-Coupe, N., da Rocha, H. R., Hutyra, L. R., da Araujo, A. C., Borma, L. S., Christoffersen, B., et al. (2013). What drives the seasonality of photosynthesis across the Amazon basin? A cross-site analysis of eddy flux tower measurements from the Brasil flux network. *Agricultural and Forest Meteorology*, *182–183*, 128–144. https://doi.org/10.1016/j.agrformet.2013.04.031

Reyes-Acosta, J. L., Vandegehuchte, M. W., Steppe, K., & Lubczynski, M. W. (2012). Novel, cyclic heat dissipation method for the correction of natural temperature gradients in sap flow measurements. Part 2. Laboratory validation. *Tree Physiology*, tps042. https://doi.org/10.1093/treephys/tps042

Richards, L. A. (1931). Capillary conduction of liquids through porous mediums. *Physics*, *1*(5), 318–333. https://doi.org/10.1063/1.1745010

Ruckstuhl, C., Philipona, R., Morland, J., & Ohmura, A. (2007). Observed relationship between surface specific humidity, integrated water vapor, and longwave downward radiation at different altitudes. *Journal of Geophysical Research: Atmospheres*, *112*(D3), D03302. https://doi.org/10.1029/2006JD007850

Ruhoff, A. L., Paz, A. R., Aragao, L. E. O. C., Mu, Q., Malhi, Y., Collischonn, W., et al. (2013). Assessment of the MODIS global evapotranspiration algorithm using eddy covariance measurements and hydrological modelling in the Rio Grande basin. *Hydrological Sciences Journal*, *58*(8), 1658–1676. https://doi.org/10.1080/02626667.2013.837578

Sands, R., Fiscus, E. L., & Reid, C. P. P. (1982). Hydraulic properties of pine and bean roots with varying degrees of suberization, vascular differentiation, and mycorrhizal infection. *Australian Journal of Plant Physiology*, *9*, 559–569.

Schenk, H. J., Callaway, R. M., & Mahall, B. E. (1999). Spatial Root Segregation: Are Plants Territorial? In A. H. Fitter & D. Raffaelli (Eds.), *Advances in Ecological Research* (Vol. 28, pp. 145–180). Academic Press. https://doi.org/10.1016/S0065-2504(08)60032-X

Schlesinger, W. H., Dietze, M. C., Jackson, R. B., Phillips, R. P., Rhoades, C. C., Rustad, L. E., & Vose, J. M. (2016). Forest biogeochemistry in response to drought. *Global Change Biology*, *22*(7), 2318–2328. https://doi.org/10.1111/gcb.13105

Schneider, C. L., Attinger, S., Delfs, J.-O., & Hildebrandt, A. (2010). Implementing small scale processes at the soil-plant interface–the role of root architectures for calculating root water uptake profiles. *Hydrology and Earth System Sciences*, *14*(2), 279–289.

Shimizu, M., Ishida, A., & Hogetsu, T. (2005). Root Hydraulic Conductivity and Whole-Plant Water Balance in Tropical Saplings following a Shade-to-Sun Transfer. *Oecologia*, *143*(2), 189–197.

Shipley, B. (2010). *From Plant Traits to Vegetation Structure - Chance and Selection in the Assembly of Ecological Communities*. New York: Cambridge University Press. Retrieved from http://admin.cambridge.org/sb/academic/subjects/life-sciences/ecology-and-conservation/plant-traits-vegetation-structure-chance-and-selection-assembly-ecological-communities?format=HB&isbn=9780521117470

Siemens, J. A., & Zwiazek, J. J. (2003). Effects of water deficit stress and recovery on the root water relations of trembling aspen (*Populus tremuloides*) seedlings. *Plant Science*, *165*(1), 113–120. https://doi.org/10.1016/S0168-9452(03)00149-3

Siemens, J. A., & Zwiazek, J. J. (2008). Root hydraulic properties and growth of balsam poplar (Populus balsamifera) mycorrhizal with *Hebeloma crustuliniforme* and *Wilcoxina* *mikolae var. mikolae*. *Mycorrhiza*, *18*(8), 393–401. https://doi.org/10.1007/s00572-008-0193-2

Sinacore, K., Hall, J. S., Potvin, C., Royo, A. A., Ducey, M. J., & Ashton, M. S. (2017). Unearthing the hidden world of roots: Root biomass and architecture differ among species within the same guild. *PLOS ONE*, *12*(10), e0185934. https://doi.org/10.1371/journal.pone.0185934

Sitch, S., Huntingford, C., Gedney, N., Levy, P. E., Lomas, M., Piao, S. L., et al. (2008). Evaluation of the terrestrial carbon cycle, future plant geography and climate-carbon cycle feedbacks using five Dynamic Global Vegetation Models (DGVMs). *Global Change Biology*, *14*(9), 2015–2039. https://doi.org/10.1111/j.1365-2486.2008.01626.x

Skelton, R. P., West, A. G., & Dawson, T. E. (2015). Predicting plant vulnerability to drought in biodiverse regions using functional traits. *Proceedings of the National Academy of Sciences*, *112*(18), 5744–5749. https://doi.org/10.1073/pnas.1503376112

Smit, A. L. (2000). Root methods : a handbook.

Sperry, J. S., & Love, D. M. (2015). What plant hydraulics can tell us about responses to climate-change droughts. *New Phytologist*, *207*(1), 14–27. https://doi.org/10.1111/nph.13354

Stark, S. C., Leitold, V., Wu, J. L., Hunter, M. O., de Castilho, C. V., Costa, F. R. C., et al. (2012). Amazon forest carbon dynamics predicted by profiles of canopy leaf area and light environment. *Ecology Letters*, *15*(12), 1406–1414. https://doi.org/10.1111/j.1461-0248.2012.01864.x ter Steege, H., Pitman, N. C. A., Sabatier, D., Baraloto, C., Salomao, R. P., Guevara, J. E., et al. (2013). Hyperdominance in the Amazonian Tree Flora. *Science*, *342*(6156), 1243092–1243092. https://doi.org/10.1126/science.1243092

Steudle, E., & Meshcheryakov, A. B. (1996). Hydraulic and osmotic properties of oak roots. *Journal of Experimental Botany*, *47*(3), 387–401.

Stone, E. L., & Kalisz, P. J. (1991). On the maximum extent of tree roots. *Forest Ecology and Management*, *46*, 59–102.

Sulis, M., Couvreur, V., Keune, J., Cai, G., Trebs, I., Junk, J., et al. (2019). Incorporating a root water uptake model based on the hydraulic architecture approach in terrestrial systems simulations. *Agricultural and Forest Meteorology*, *269–270*, 28–45. https://doi.org/10.1016/j.agrformet.2019.01.034

Sun, D., & Pinker, R. T. (2003). Estimation of land surface temperature from a Geostationary Operational Environmental Satellite (GOES-8). *Journal of Geophysical Research: Atmospheres*, *108*(D11). https://doi.org/10.1029/2002JD002422

Sun, H., Aubrey, D. P., & Teskey, R. O. (2012). A simple calibration improved the accuracy of the thermal dissipation technique for sap flow measurements in juvenile trees of six species. *Trees*, *26*(2), 631–640. https://doi.org/10.1007/s00468-011-0631-1

Sutton, R. F., & Tinus, R. W. (1983). Root and Root System Terminology. *Forest Science*, *29*(suppl_1), a0001-z0001. https://doi.org/10.1093/forestscience/29.s1.a0001

Thomsen, J. E., Bohrer, G., Matheny, A. M., Ivanov, V. Y., He, L., Renninger, H. J., & Schäfer, K. V. R. (2013). Contrasting Hydraulic Strategies during Dry Soil Conditions in *Quercus rubra* and *Acer rubrum* in a Sandy Site in Michigan. *Forests*, *4*(4), 1106–1120. https://doi.org/10.3390/f4041106

Tron, S., Bodner, G., Laio, F., Ridolfi, L., & Leitner, D. (2015). Can diversity in root architecture explain plant water use efficiency? A modeling study. *Ecological Modelling*, *312*, 200–210. https://doi.org/10.1016/j.ecolmodel.2015.05.028

Trumbore, S., Brando, P., & Hartmann, H. (2015). Forest health and global change. *Science*, *349*(6250), 814–818. https://doi.org/10.1126/science.aac6759

Tyree, M. T., Velez, V., & Dalling, J. W. (1998). Growth dynamics of root and shoot hydraulic conductance in seedlings of five neotropical tree species: scaling to show possible adaptation to differing light regimes. *Oecologia*, *114*(3), 293–298.

Valverde-Barrantes, O. J., Smemo, K. A., Feinstein, L. M., Kershner, M. W., & Blackwood, C. B. (2015). The distribution of below-ground traits is explained by intrinsic species differences and intraspecific plasticity in response to root neighbours. *Journal of Ecology*, *101*(4), 933–942. https://doi.org/10.1111/1365-2745.12087

Vandegehuchte, M. W., & Steppe, K. (2012). Improving sap flux density measurements by correctly determining thermal diffusivity, differentiating between bound and unbound water. *Tree Physiology*, *32*(7), 930–942. https://doi.org/10.1093/treephys/tps034

Vergeynst, L. L., Vandegehuchte, M. W., McGuire, M. A., Teskey, R. O., & Steppe, K. (2014). Changes in stem water content influence sap flux density measurements with thermal dissipation probes. *Trees*, *28*(3), 949–955. https://doi.org/10.1007/s00468-014-0989-y

Vivoni, E. R., Rinehart, A. J., Méndez-Barroso, L. A., Aragón, C. A., Bisht, G., Cardenas, M. B., et al. (2008). Vegetation controls on soil moisture distribution in the Valles Caldera, New Mexico, during the North American monsoon. *Ecohydrology*, *1*(3), 225–238. https://doi.org/10.1002/eco.11

Wan, X., Landhäusser, S. M., Zwiazek, J. J., & Lieffers, V. J. (1999). Root water flow and growth of aspen (*Populus tremuloides*) at low root temperatures. *Tree Physiology*, *19*(13), 879–884. https://doi.org/10.1093/treephys/19.13.879

Wan, X., Zwiazek, J. J., Lieffers, V. J., & Landhäusser, S. M. (2001). Hydraulic conductance in aspen (*Populus tremuloides*) seedlings exposed to low root temperatures. *Tree Physiology*, *21*(10), 691–696. https://doi.org/10.1093/treephys/21.10.691

Wang, J., & Bras, R. L. (2009). A model of surface heat fluxes based on the theory of maximum entropy production: MEP and Surface Heat Fluxes. *Water Resources Research*, *45*(11). https://doi.org/10.1029/2009WR007900

Wang, J., & Bras, R. L. (2011). A model of evapotranspiration based on the theory of maximum entropy production: MEP and Surface Heat Fluxes. *Water Resources Research*, *47*(3). https://doi.org/10.1029/2010WR009392

Wang, J., Bras, R. L., Nieves, V., & Deng, Y. (2014). A model of energy budgets over water, snow, and ice surfaces. *Journal of Geophysical Research: Atmospheres*, *119*(10), 6034–6051. https://doi.org/10.1002/2013JD021150

Wang, T., Wedin, D. A., Franz, T. E., & Hiller, J. (2015). Effect of vegetation on the temporal stability of soil moisture in grass-stabilized semi-arid sand dunes. *Journal of Hydrology*, *521*, 447–459. https://doi.org/10.1016/j.jhydrol.2014.12.037

Warren, J. M., Hanson, P. J., Iversen, C. M., Kumar, J., Walker, A. P., & Wullschleger, S. D. (2015). Root structural and functional dynamics in terrestrial biosphere models - evaluation and recommendations. *New Phytologist*, *205*(1), 59–78. https://doi.org/10.1111/nph.13034

Weemstra, M., Mommer, L., Visser, E. J. W., van Ruijven, J., Kuyper, T. W., Mohren, G. M. J., & Sterck, F. J. (2016). Towards a multidimensional root trait framework: a tree root review. *New Phytologist*, *211*(4), 1159–1169. https://doi.org/10.1111/nph.14003

Whitlock, C. H., Charlock, T. P., Staylor, W. F., Pinker, R. T., Laszlo, I., Ohmura, A., et al. (1995). First Global WCRP Shortwave Surface Radiation Budget Dataset. *Bulletin of the American Meteorological Society*, *76*(6), 905–922. https://doi.org/10.1175/1520-0477(1995)076<0905:FGWSSR>2.0.CO;2

Williams, C. A., Collatz, G. J., Masek, J., & Goward, S. N. (2012). Carbon consequences of forest disturbance and recovery across the conterminous United States: Forest Disturbance and Carbon Dynamics. *Global Biogeochemical Cycles*, *26*(1), n/a-n/a. https://doi.org/10.1029/2010GB003947

Wilson, K., Goldstein, A., Falge, E., Aubinet, M., Baldocchi, D., Berbigier, P., et al. (2002). Energy balance closure at FLUXNET sites. *Agricultural and Forest Meteorology*, *113*(1–4), 223–243. https://doi.org/10.1016/S0168-1923(02)00109-0

Xu, D., Agee, E., Wang, J., & Ivanov, V. Y. (2019). Estimation of Evapotranspiration of Amazon Rainforest Using the Maximum Entropy Production Method. *Geophysical Research Letters*, *46*(3), 1402–1412. https://doi.org/10.1029/2018GL080907

Xu, L., Samanta, A., Costa, M. H., Ganguly, S., Nemani, R. R., & Myneni, R. B. (2011). Widespread decline in greenness of Amazonian vegetation due to the 2010 drought: BROWNING OF AMAZONIA IN THE 2010 DROUGHT. *Geophysical Research Letters*, *38*(7), n/a-n/a. https://doi.org/10.1029/2011GL046824

Yang, Y., Guan, H., Shang, S., Long, D., & Simmons, C. T. (2014). Toward the Use of the MODIS ET Product to Estimate Terrestrial GPP for Nonforest Ecosystems. *IEEE*

Geoscience and Remote Sensing Letters, *11*(9), 1624–1628. https://doi.org/10.1109/LGRS.2014.2302796

Yang, Y., Donohue, R. J., & McVicar, T. R. (2016). Global estimation of effective plant rooting depth: Implications for hydrological modeling. *Water Resources Research*, *52*(10), 8260–8276. https://doi.org/10.1002/2016WR019392

Yu, T., Feng, Q., Si, J., Xi, H., Li, Z., & Chen, A. (2013). Hydraulic redistribution of soil water by roots of two desert riparian phreatophytes in northwest China's extremely arid region. *Plant and Soil*, *372*(1–2), 297–308. https://doi.org/10.1007/s11104-013-1727-8

Zhang, K., Kimball, J. S., & Running, S. W. (2016). A review of remote sensing based actual evapotranspiration estimation: A review of remote sensing evapotranspiration. *Wiley Interdisciplinary Reviews: Water*, *3*(6), 834–853. https://doi.org/10.1002/wat2.1168

Zhang, W., & Zwiazek, J. J. (2016). Effects of root medium pH on root water transport and apoplastic pH in red-osier dogwood (Cornus sericea) and paper birch (Betula papyrifera) seedlings. *Plant Biology*, *18*(6), 1001–1007. https://doi.org/10.1111/plb.12483

Zhao, M., & Running, S. W. (2010). Drought-Induced Reduction in Global Terrestrial Net Primary Production from 2000 Through 2009. *Science*, *329*(5994), 940–943. https://doi.org/10.1126/science.1192666

Zhao Y., Ma, J., Sun X., & Guo X.. (2014). Spatial Distribution of Soil Moisture and Fine Roots of Apple Trees under Water Storage Pit Irrigation. *Journal of Irrigation and Drainage Engineering*, *140*(1), 06013001. https://doi.org/10.1061/(ASCE)IR.1943-4774.0000624